Design and Analysis of Composite Rotor Blades for Active/Passive Vibration Reduction

by

Devesh Kumar

A dissertation submitted in partial fulfillment
of the requirements for the degree of
Doctor of Philosophy
(Aerospace Engineering)
in The University of Michigan
2013

Doctoral Committee:

Professor Carlos E. S. Cesnik, Chair
Professor Peretz P. Friedmann
Associate Professor Joaquim R. R. A. Martins
Professor Kon-Well Wang

To my parents, sister and brother

ACKNOWLEDGEMENTS

I would like to extend my sincere thanks to my family, teachers, friends and colleagues who helped me immensely during my days in the graduate school.

First of all, I would like to thank my family for providing unyielding support and encouragement over the years. They not only provided me with the best opportunities but also created a protected environment around to help me to succeed. The values instilled in me by my family have been a constant guiding force for me. I hope the completion of my thesis gives them some happiness and relief which they truly deserve.

Next, I would like to thank Prof. Cesnik for being my advisor and mentor during the course of my long and uneventful (fortunately!) doctoral research. I appreciate the encouragement and opportunities that he has provided me at different times during the graduate school to help me learn better, to grow as a researcher and to build my confidence. I am also very grateful for the patience and effort that he has put in improving my writing and presentation skills to reach the high standards that he has set. His enthusiasm for research and the ability to pay attention to finer details has been very inspiring. Besides these, his passion for sports, flying, food and johnnies has always been very contagious.

I deeply appreciate the time and effort and useful feedback from my thesis committee members, Prof. Friedmann, Prof. Martins and Prof. Wang. I would specially like to acknowledge encouragement and guidance provided by Prof. Friedmann during my

research and graduate courses. I would also like to thank my collaborators at Advatech Pacific Inc, Dr. Peter Röhl and Mark Sutton, for their help in the implementation of ModelCenter solution. I am very grateful to Dr. Bryan Glaz for his help in the implementation of the basic surrogate-based optimization technique. I also benefitted greatly from technical discussions with Dr. Li Liu, Dr. Rafael Palacios, and Dr. Ashwani Padthe.

My research group, A^2SRL, has always been very supportive and I have had the opportunity to learn something new from each of my group members. I wish to thank Dr. Weihua Su, Dr. Jiwon Mok, Dr. Satish Chimakurthi, Dr. Ken Salas, Dr. Torsten Skujins, Dr. Nate Falkiewicz, Kalyan Nadella, Smith Thepvongs, Ben Hallisy, Matt Dillsaver, Matt Obenchain, Jessica Jones, and members of X-HALE team (Blake Davis, Elizabeth Prentice, etc.) for making the research in a windowless office and basement lab a very enjoyable experience. I would specially like to thank Dr. Jiwon Mok and Smith Thepvongs for help with their numerical codes, and Dr. Ken Salas for help in the experimental laboratory.

The experimental study presented in my thesis would not have been possible without the help of the technical staff in the Department of Aerospace Engineering. I am very grateful to Terry “it will never work” Larrow for being patient with me and for fabricating all my crazy and tiny parts multiple times. I would like to thank Eric Kirk, Chris Chartier, and Thomas Griffin for being readily available whenever required and for providing useful suggestions. I would also like to thank Amit Salvi for his help with tensile testing of fabricated blade sections.

My long stay in Ann Arbor was made wonderful by friends around me. I would like to thank my friend Dr. Pavana Prabhakar for her joyous company, for being part of innumerable happy memories and for smoothing out the difficult part of my PhD. I would like to thank my friend Dr. Gayathri Seenumani for trusting in me and for giving me lot of confidence when it was needed the most. I also wish to thank Kalyan Nadella, Dr. Rajeev Verma and Pritam Sukumar for their friendship and belief in me. I will also cherish the time spent with my friends: Dr. Christian Heinrich, Dr. Saumil Ambani, Nicholas Lamorte, Dr. Daniel Zaide, Dr. Qing Zhu, Nhung Nguyen, Karthik Ananthraman, Dipankar Dua, Dr. Amit Kaushik and my lunch group.

And finally, I would like to acknowledge the financial support provided by Georgia Tech/University of Michigan/Washington University Vertical Lift Rotorcraft Center of Excellence (VLRCOE), funded by the U.S. Army, with Dr. Michael Rutkowski as the technical monitor. This work was also supported by U.S. Army Research, Development and Engineering Command (AMRDEC), Aviation Applied Technology Directorate (AATD) through SBIR Phase II contract W911W6-10-C-0030.

TABLE OF CONTENTS

LIST OF FIGURES

LIST OF TABLES

LIST OF APPENDICES

ABSTRACT

The problem of vibration has limited the use of helicopters in both civil and military applications. In this research, further analysis has been performed for the various on-blade approaches available for vibration reduction using a unique optimization framework.

For *passive optimization*, an aeroelastic environment with several well-established analysis codes from different sources was developed that can be used to analyze and design composite rotor blades for minimum vibration or maximum performance. This design environment enables conceptual/early preliminary multidisciplinary rotor blade design with realistic structural properties for modern composite rotor blades.

For the design of a rotor blade with *active twist*, a new design strategy was introduced where the amplitude of dynamic twist is maximized. The optimization framework included the aeroelastic design environment described earlier along with surrogate based optimization technique. The surrogate based optimization is performed in combination with Efficient Global Optimization algorithm. Results showed that the amplitude of dynamic twist is a true indicator of control authority of active twist rotor for vibration reduction. Furthermore, the optimization framework was extended to include discrete design variables in the optimization and the solution for mixed-variable design problem was obtained using three different techniques.

After modifying the aeroelastic analysis to account for the presence of *active flaps*, a Mach-scaled composite rotor blade was designed using the same mixed design variable

optimization framework to enhance the vibration reduction capabilities of the active flap. In this case also, the amplitude of dynamic twist was used as the objective function and the analysis was carried out at three different spanwise flap locations. This thesis also includes work related to the design and fabrication of a composite rotor blade with dual flaps which can be tested in a Mach-scaled spin test stand.

Finally, the use of *camber actuation* with quadratic and cubic camber deformation shapes for vibration reduction and performance enhancement in dynamic stall region was studied. The aeroelastic analysis was augmented with a modified version of the ONERA dynamic stall model that accounts for morphing airfoil section.

Chapter 1. Introduction

A helicopter can take off and land, fly forward or backward, climb and descend and move in almost any direction. These combinations of maneuvers, which are not possible with a fixed-wing aircraft, have made the helicopter an ideal vehicle for a number of challenging tasks in both civil and military operations. Modern civilian roles of the helicopter include sea and land rescue mission, police surveillance, oil rig servicing, homeland security etc. However, the issues of high vibration and noise have limited the helicopter`s community acceptance and reduced its mission effectiveness.

The current chapter provides an introduction to the problem of vibration reduction in helicopters. It highlights the main sources of vibration in helicopter and various techniques currently being used to obtain vibration reduction. Different methods available for vibration reduction are classified depending upon their nature (active/passive) and implementation (components of the helicopter that it influences). Based on the literature review, key areas where further improvement can be made in the vibration reduction techniques are identified and that forms the motivation for the research presented in this thesis. Finally, an outline of the thesis is presented.

1.1 Introduction to Vibration in Helicopters

Vibration in a helicopter leads to passenger/pilot discomfort and fatigue and it affects the reliability and fatigue life of the airframe and its components. Other effects of vibration are reduced weapon effectiveness, difficulty in reading instruments, etc. A

study done by Sikorsky Aircraft in 1973 [1] showed that reduction in vibration can significantly improve the reliability and reduce the costs associated with maintenance and life cycle. The current overall level of vibration in helicopters (approximately 0.05g to 0.1g) [2] remains significantly higher than those for a fixed-wing aircraft (0.01g). Even though a significant reduction in helicopter vibration has been obtained over the last few decades due to improved designs**,** the modern helicopters still do not meet the ultimate goal of a jet smooth ride, as highlighted in Figure 1-1.

The main sources of vibration in a helicopter are the main rotor, tail rotor, engine, gearbox and fuselage. However, the most dominant source of vibration is the main rotor (more than 90% for a UH-60 Helicopter). The vibratory loads are produced by the main rotor in the rotating frame. However, when the loads are transferred to the hub or the fuselage in the fixed system, only the loads corresponding to the N_b/rev frequency are observed, where N_b is the number of rotor blades. Thus, the rotor acts as a filter for the vibratory loads. Figure 1-2 shows a typical vibration amplitude spectrum of a BO 105 helicopter in cruise condition.

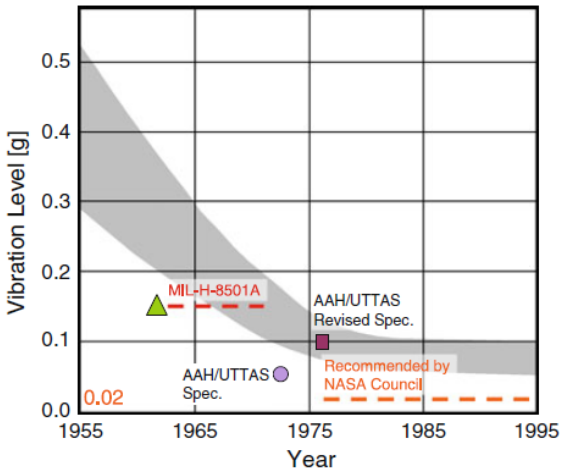

Figure 1-1: Trends for Helicopter Vibration Levels [3]

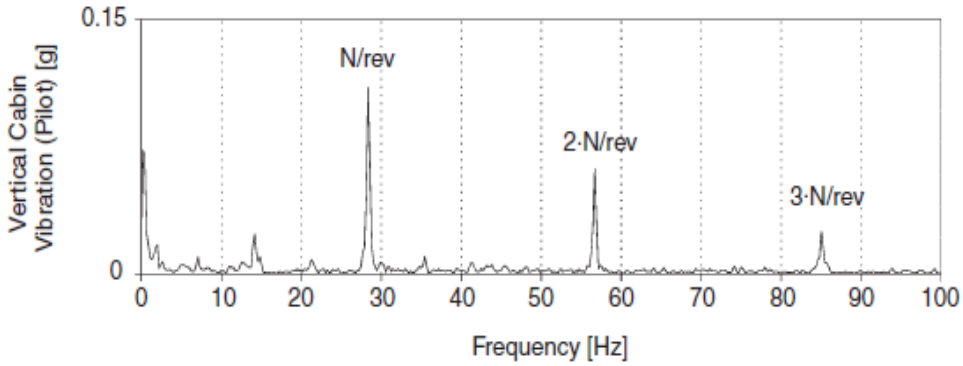

Figure 1-2: Vibration Amplitude Spectrum for BO 105 in Level Cruise Flight [4]

The main rotor blade in a helicopter experiences highly unsteady aerodynamic loads [5] as shown in the Figure 1-3, in addition to the time varying pitch angles. For a rotor in forward flight, the advancing side of the blade experiences different aerodynamic conditions as compared to the retreating side. On the advancing side, highly unsteady aerodynamic loads are produced due to the blade-vortex interactions. This occurs when the rotating blades encounter tip vortices shed by the preceding blades. The effects of blade-vortex interaction are more pronounced at low forward flight speeds ($\mu = 0.15$). At higher advance ratios ($\mu = 0.35$), very high mach numbers are observed at the blade tip on the advancing side, and the flow reaches transonic conditions (supercritical flow). On the retreating side, the dynamic stall condition is observed which is characterized by flow separation. Also, near the root section on the retreating side, reverse flow occurs in the region where the rotational speed at a radial location is smaller than the forward flight speed. In this region, the flow over the airfoil section is from the trailing edge to the leading edge. In addition to these, the finite length of the rotor blade results in tip vortices, as in a fixed wing aircraft. Thus, the combination of unsteady aerodynamics and large structural deformations in flap, torsion and lag due to blade flexibility and slenderness leads to the generation of large oscillatory loads by the main rotor blades.

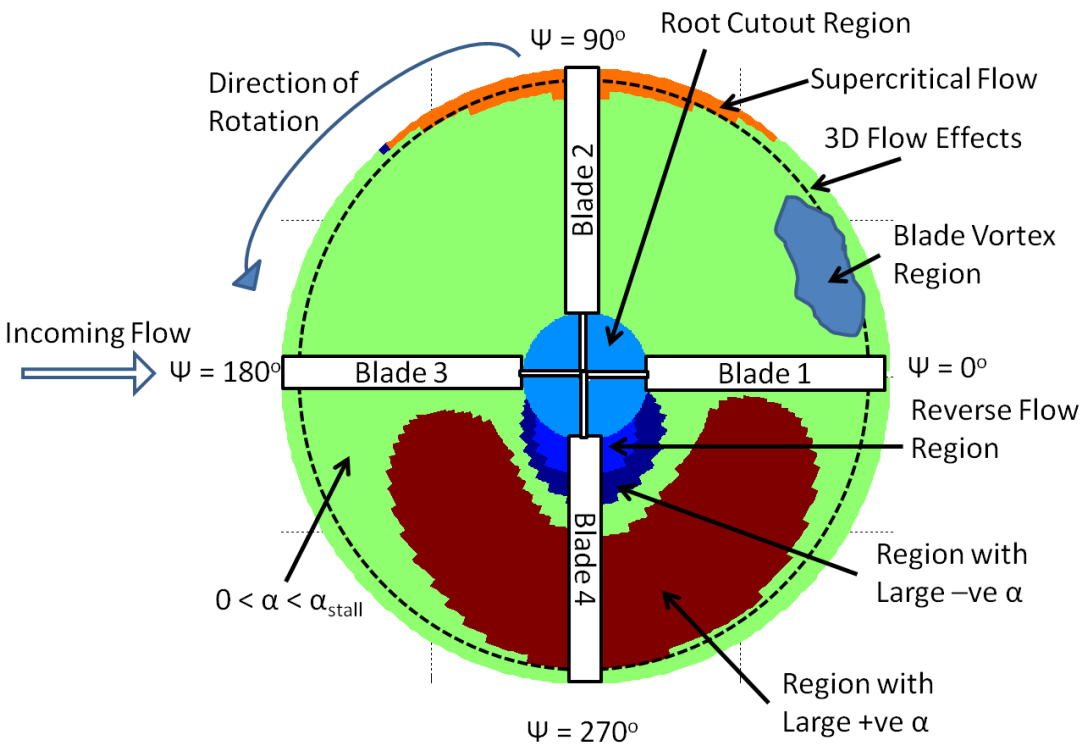

Figure 1-3: Unsteady Aerodynamics on the Main Rotor Disk

The variation in the vibratory loads at the cabin in a BO 105 helicopter with forward flight speed is shown in Figure 1-4. As discussed above, large vibration is observed at low flight speeds due to the blade-vortex interaction and then at high forward flight speeds due to the dynamic stall and high speed flow effects. The vibrations due to the blade-vortex interactions are increased by the maneuvers that retain the wake near the plane of the disk, such as decelerating or descending flight (flare condition as shown in Figure 1-4).

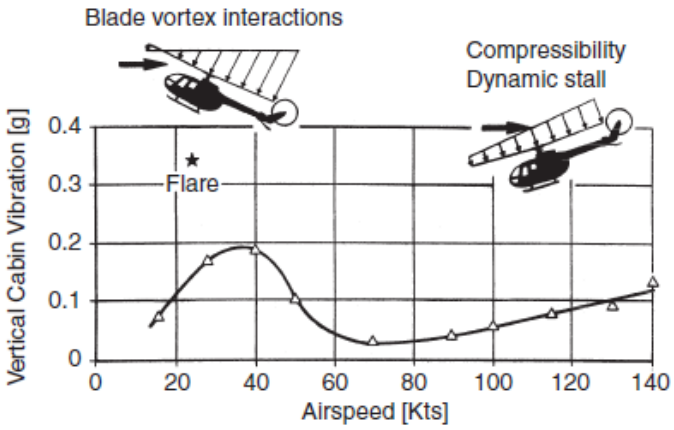

Figure 1-4: Vertical Cabin Vibration in BO 105 as a function of Airspeed [6]

The noise generated by helicopters has constrained the rotorcraft operation near cities and have resulted in restrictions on the frequency of operation, time of day of specific operation and types of rotorcraft that can be used. In a helicopter, main sources of noise are the main rotor, the tail rotor and the engine. Among these, the most important one is the main rotor. The low frequency noise that the main rotor generates is made up of basic loading noise and broadband turbulence noise, each a function of lift and rotor speed. In addition to these, BVI noise and High Speed Impulsive (HSI) noise become dominant in descents and forward flight airspeeds, respectively. Further details related to the physical mechanism of noise generation and acoustic modeling can be found in [7-9]. In the research presented in this thesis, the main focus will be on vibration reduction.

1.2 Methods for Vibration Reduction

From the earliest days of rotorcraft development, the problem of airframe vibration has been a serious concern. In a very early study [10], researchers identified three different approaches to obtain vibration reduction, namely: a) by minimizing the source of vibration, b) by reducing the response of the structure to the vibration, and c) by

isolating the structure from the source of vibration. Based on these approaches, the problem of vibration reduction can be solved by both passive and active techniques. Different methods for vibration reduction that have been discussed in the literature are graphically summarized in Figure 1-5.

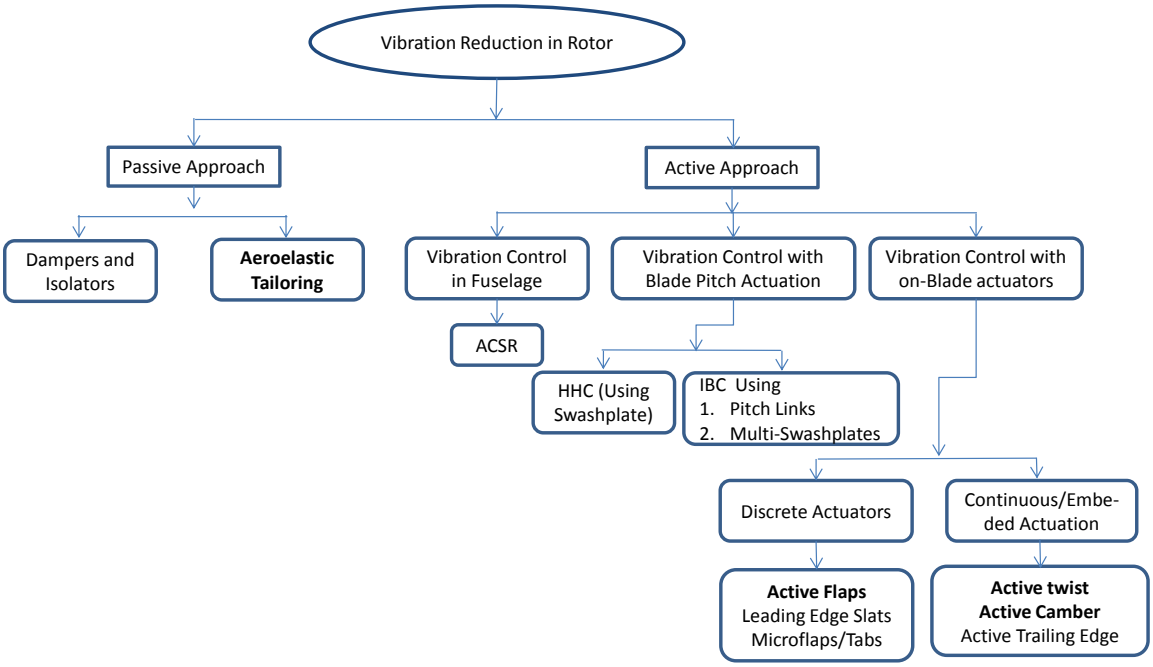

Figure 1-5: Methods used for Vibration Reduction in Rotor Blades

1.2.1 Passive Approaches

The earliest approach for vibration reduction involved the usage of passive and semi-passive devices like pendulum absorbers and isolators to reduce vibration. It is usually a single DOF system with a small mass and a spring. Good reviews of passive vibration reduction methods are given by Reichert [3] and Loewy [11]. Although the aerodynamic vibratory loads persist, the transmission of these loads to the rest of the helicopter is reduced. The passive devices have been used in many operational helicopters by tuning their characteristics to filter out specific frequencies [12]. A brief description of the

passive systems like SARIB (Vibration reduction system using integral bar absorption) and ARIS (Anti-Resonance Isolation Systems) implemented in the pylon assembly of various Eurocopter helicopters to filter the dynamic loads transmitted to the airframe is provided in [13]. However, these devices introduce weight penalties and are designed to be effective over a narrow range of operating conditions only. Some of the studies have considered the use of passive devices on the rotor blade themselves like the bifilar pendulum implemented on the S-76 helicopters [14].

The second passive approach involves the tailoring of the structural and the aerodynamic properties of a rotor blade using optimization techniques [15-17]. The increased use of composite material in the blade allows easier fabrication of advanced geometry blades and provides the potential of aeroelastic tuning. In this approach, the vibration reduction problem is formulated as a mathematical optimization function with appropriate objective function and constraints. For a composite rotor blade, the ply angles, the ply thicknesses or any other cross-sectional parameters can be used as design variables. For the aerodynamic shape, sweep, anhedral, droop, etc., at the blade tip are considered as the design variables. In many cases, both structural and aerodynamic shape optimization design variables are used simultaneously. Further discussion on multidisciplinary optimization frameworks is provided in Section 1.3.2.

1.2.2 Active Approaches

An active control approach for the rotor has the potential to be a more effective solution for vibration reduction since it can directly influence the source of vibratory loads which are the main rotor blades [18]. This is fundamentally different from the

passive devices which attempt to reduce vibratory loads in the hub or the fuselage, which are far away from the source. Also, the optimization technique has limited capability for vibration reduction (20-40%) and in most of the cases, the final design is optimum at one flight condition only. Most recent review of the active control methods for vibration reduction is given by Kessler [19, 20]. A summary of all the methods shown in Figure 1-5 is given next.

1.2.3 Active Vibration Control in Fuselage

The ACSR (Active Control of Structural Response) scheme is based on the fact that in a linear system it is possible to superimpose two independent responses such that the total response is minimized [21]. In practice, the principle consists of connecting a number of (hydraulic) actuators among strategic points on the fuselage and applying control forces to the structure so to destruct the vibration signal [22, 23]. It has the advantage that it is easy to maintain and the potential for vibration reduction is high since the actuator can always produce the right amount of load at the right amplitude and phase to counteract the primary vibration. In most of these cases, the vibration reduction is localized e.g., pilot seat, instrumentation panel, passenger cabin, etc. The ACSR technology has been implemented for vibration reduction in the EH101 helicopter produced in Europe. An AVCS (active anti-vibration control system) based on electromagnetic actuation was implemented on the EC225 helicopter, while a piezo-based AVCS was successfully tested on the EC135 [13]. The drawbacks of this system are that it requires a detailed model for the rotor-fuselage dynamics in order to determine the optimum placement of the actuator for maximum vibration reduction and it does not address the noise and performance issues of the rotor.

In the early studies of vibration reduction, it was observed that the built-in twist of the blade has a strong influence on blade vibratory loads. For vibration reduction, a decreased negative twist is desired on the advancing side and a simultaneous increased negative twist is required on the retreating side [24, 25]. This effect can either be obtained by changing the pitch of the entire rotor blade, as described in Section 1.2.4, or by using the twisting moment generated by the on-blade actuators to twist the rotor blade, as described in Section 1.2.5.

1.2.4 Vibration Control with Blade Pitch Actuation

In the case of HHC (Higher Harmonic Control) and conventional IBC (Individual Blade Control) methods, the aeroelastic behavior of a rotor blade is influenced by using the actuators either mounted on the swashplate or by the use of pitch links to induce rigid body actuation of the blade in pitch, respectively. The pitching motion consists of a high frequency actuation signal on top of the primary collective and cyclic commands. This method has potential for influencing the vibratory loads as they reduce the loads at the source in rotating system.

In the HHC technique, the blade pitch actuation is introduced in the non-rotating swashplate by superimposing the appropriate time dependent pitch commands [26]. The HHC approach is the most mature active control approach for vibration reduction. Here, all the blades experience the same input. The vibration levels in the fuselage or at the hub are modified at their source before they propagate into the airframe. Numerical simulations demonstrating the effectiveness of HHC technique for vibration reduction are presented in [27, 28], while various experimental tests on model scale and full scale rotors in wind tunnel are discussed in [29-32]. Some of the limitations of the HHC

approach are: 1) the considerable cost of implementing the HHC on a production helicopter, 2) the power required for actuating the blades at the root and 3) limitations on the objective that can be achieved with an HHC implemented through a conventional swashplate as the actuation frequencies available are limited.

In the conventional IBC approach, each blade is actuated independently in the rotating frame [33, 34] at any desired frequency, thus overcoming some of the limitations of the HHC technique. The IBC approach involves independent feedback control of each blade in the rotating frame. As compared to HHC, which provides a maximum of three DOF, the IBC approach provides more freedom for vibration control. IBC can be obtained by using active pitch link for each of the blades or by using multiple swashplates [20]. Experimental tests demonstrating the feasibility of the IBC for vibration reduction, performance enhancement and noise reduction have been done in both the U.S. [35, 36] and Europe [37]. Implementing the IBC approach brings significant challenges since supplying hydraulic power to the rotating system is only possible by means of hydraulic slip rings which are heavy and complex.

1.2.5 Vibration Control with on-Blade Actuators

In another approach, the actuation was moved onto the rotor blade. Unlike the HHC and the conventional IBC, failure of the on-blade actuation system would not catastrophically affect the flight safety. The actuation with the on-blade actuators requires significantly less power as compared to HHC and conventional IBC [18] and it is relatively less complex to implement them in the rotor blades. Vibration control with the on-blade actuators can be considered as a subset of the IBC approach since the controller

has the freedom to control the actuator on each blade individually. (Hence, the IBC approach described in the previous section is referred as “Conventional IBC.”)

The possibility of using an on-blade actuator to reduce vibration and noise was also supported by the advent of smart materials. These are light weight, compact and have small power requirements. A summary for the applications of smart material based actuations for aeroelastic and vibration control is provided in the following references. Giurgiutiu and co-workers [38-41] demonstrated the use of induced strain actuation principles and capabilities for a smart rotor blade application like inducing twist, active blade tip and active flaps. The application of these technologies for a fixed wing aircraft was also discussed for active flutter control, buffet suppression, gust load alleviation and sonic fatigue reduction. Straub [42, 43] stressed on the use of smart materials for “on the blade” actuation to overcome the size, weight and complexity issues associated with the hydraulic and electrical on-rotor actuation. Preliminary results showed the servoflap control to be more effective as compared to the embedded actuators concepts like pitch twist and camber control. Chopra [44] highlighted that the use of smart materials methodology is equally applicable to other helicopter problems like aeromechanical stability augmentation, handling qualities enhancement, stall alleviation, reduction of interior/exterior acoustic signatures, minimization of the blade dynamic stresses and rotor head health monitoring. Friedmann [45] obtained the scaling laws for the rotary-wing aeroelastic and aeroservoelastic problem to be used for the scale model tests intended to demonstrate the active control of vibration using an adaptive materials based actuation.

The on-blade actuation system mechanism can be further classified into discrete actuation system and embedded actuation system.

1.2.5.1 Discrete Actuators

This approach includes an actuator installed inside the rotor blade and it is connected to a movable device usually mounted on the trailing edge of the blade. The actuator mainly consists of active materials capable of operating at large actuation frequencies and an amplification mechanism to amplify the displacement produced by the active material. Examples of discrete actuators are active flaps, active microflaps/tabs, leading edge slats, etc. Discrete actuators modify the sectional aerodynamic properties of the region where they are installed. The aerodynamic parameters that may be influenced by a discrete actuator are $c_{L\alpha}$, $c_{L,max}$, $c_{M\alpha}$, or c_L/c_D for the cross section. The control of the aerodynamic loads acting on the blade is obtained either through changes in lift (lift effect) or by elastically twisting the blade using the pitching moment generated by the movable surface (servo-effect).

Actively controlled flaps (ACF) are usually installed between 0.6R to 0.9R along the span of a rotor blade. The ACF can be implemented in a single, dual or multiple flap configurations. ACF influences the blade vibrations by the combination of the servoeffect and the direct lift effect [46]. Thus, like the HHC and conventional IBC, it reduces vibration at the source which is the main rotor, but the power it consumes is an order of magnitude less than IBC [18]. Substantial amount of work has been done to model the effect of active flaps and use them for vibration reduction, performance enhancement and noise reduction. Most of this work has been summarized in [47-49]. In these studies, it was concluded that a flap deflection of ±4 deg at full RPM is sufficient to obtain substantial benefit without incurring penalties on the stability or performance of the helicopter.

As an active control device, microflaps have the potential for a high bandwidth control with low actuation power requirement and minimal loss in the stiffness due to their small size and low inertia. Microflaps are small, usually less than 5% of chord in height and are mounted normal to the pressure surface and produce an increase in sectional $c_{L,max}$ by approximately 25%. Since microflaps work within the boundary of the airfoil, they produce a very small profile drag and are expected to have even smaller performance penalty as compared to the active flaps. Microflaps were first proposed for fixed wing aircraft [50, 51] to solve the problem of flutter. Many numerical studies with microflaps for vibration reduction in helicopters [52-55] have been conducted in the last few years; however, the experimental tests with microflaps mounted on a rotor blade in rotating condition have yet to be performed. This is due to the difficulty in identifying an actuator suitable for actuating [56] microflaps and the size constraints on the airfoil thickness.

Besides active flaps and microflaps, another on-blade discrete actuator called Active Tab was developed by the research cooperation between JAXA and Kawada Industries Ltd [57]. The low-speed wind tunnel test was conducted to prove the capability of BVI noise reduction for a helicopter using the active tab control.

1.2.5.2 Continuous/Embedded Actuators

In this approach, the active material is usually embedded in the cross section or bonded on the surface of the rotor blade. In most of the cases, the deformation is obtained by the use of piezoceramic layers inducing shear strains. As compared to discrete actuators, it does not have any external moving parts like hinges or bearing and, hence,

they have less profile drag. A possible disadvantage is that the maintenance of the actuator is difficult since they are integrated inside the blade.

Active twist in the rotor blade is obtained by the active torsional moment generated by embedded active piezoelectric fibers at ±45 deg orientation. The advantages of active twist lies in the simplicity of the mechanism and no increase in the profile drag. Review for the recent advances made in active twist technology is provided in [38, 58-62]. Numerical results have shown that a tip twist of ±2 deg obtained due to active twist actuation is sufficient for vibration and noise reductions.

Active camber approach is relatively new as compared to the active twist and active flap methods proposed in the earlier sections. Camber deformation is considered to be a more efficient way of modifying blade sectional loads to influence vibratory loads at the hub in fixed system. A good review of the active camber methodology is provided in [63] and it discusses the use of camber deformation for vibration reduction. Active trailing edge [64] is a new concept being developed as part of the Friendcopter program in Europe and it consists of a trimorph bender integrated into the blade cross section. Like active flaps, it moves the blade trailing edge upwards and downwards to generate servo effects, but unlike the active flaps, there are neither moving parts nor discrete hinges.

1.3 Literature Review Relevant to the Thesis

This thesis focuses on the methods of vibration reduction where the vibration is reduced at the source, that is, the main rotor. These include:

a) Active Twist Rotors

b) Rotor Blade with Active Flaps

c) Rotor Blade with Morphing Airfoil Section

d) Aeroelastically tailored Blades

1.3.1 Active Twist Rotors

Active twist is obtained in the rotor blades by including active MFC (macro fiber composite) or AFC (active fiber composite) plies in the cross-sectional layup of the rotor blade. Modeling and design of a rotor blade with active fiber plies present many challenges since the actuator itself is part of the rotor blade and it is a load-bearing member.

1.3.1.1 Modeling of Active Twist

The structural modeling of a cross section with embedded piezoelectric fibers must take into account not only the contribution to mass and stiffness of the integral actuators, but also the induced strain effects. Some of the works related to capturing these effects is presented here.

Cesnik and Shin (2001) [65, 66] developed an asymptotic analysis that takes into account the electromechanical three-dimensional nature of the problem and reduces it into a linear analysis over the cross section and a nonlinear analysis of the resulting beam reference line. The analysis results showed very good correlation with experimental data obtained at MIT for active model blades. In [67], they analyzed the active cross section of a rotor blade with multiple cell and showed that an increase in torsional stiffness does not necessarily reduce the twist actuation. This approach was used in the design of the NASA/ARMY/MIT Active Twist rotor [68]. The closed loop vibration control tests were

carried out with this rotor blade in NASA Langley's Transonic Dynamic Tunnel in forward flight conditions [69]. The experimental test results showed 40db reduction in vertical shear vibratory loads and some reduction in other hub force and moment components. This analytical work was further extended by Palacios and Cesnik to include a modal solution procedure that allows arbitrary definition of the one dimensional elastic, thermal and electric variables [70]. This methodology has been implemented in a software code called UM/VABS [71] providing cross-sectional parameters for the active beam model of the blades. For the nonlinear beam analysis of active rotor blades, an in-house analysis code called UM/NLABS (University of Michigan, Nonlinear Active Beam Solver) was developed [72]. It includes the mixed form of beam dynamic equations and is expanded to account for the deformation of cross section through a set of finite section modes. This resulting beam formulation explicitly captures both large elastic beam deformation of the beam reference line and small local deformations at the cross section for active/passive beams.

In the European Friendcopter Project, an FEA based procedure was used to determine the stiffness and piezoelectric properties of an active twist rotor blade [73]. The cross-sectional properties obtained were used in a multibody analysis of the active twist rotor to obtain vibration suppression by open and closed loop controls [74]. Glukhikh et al. [75] modeled the piezoelectric effect by the means of temperature analogy and thus converting the electro-elastic problem to a thermo-elastic problem, which was solved using FEA in ANSYS. Hoffman et al. [76] presented two simulation models for active twist by prescribing active twist and twist moment based on modal shape function and validated results from whirl tower test data. Brockmann and Lammering [77] derived a three

dimensional beam finite element model with regard to all the gyroscopic terms and the actuation capabilities in a shear-flexible formulation with out-of-plane torsional warping. Results obtained were compared with analytical solution for the static case and results from the finite element shell model. The model showed good agreement with the finite element shell model except in the cases where deformation in the cross-sectional plane was observed since the beam formulation assumed undeformable shape.

1.3.1.2 Design and Parametric Studies

Cesnik et al. [78] performed numerical parametric studies with UM/VABS for wing sections with double and triple cells to determine a cost effective way to add active material to the cross section. Sekula and Wilbur conducted a series of parametric design studies with structural and aerodynamic parameters to understand the twist actuation in rotor blades [79-81]. In the parametric study with structural variables [80], the effect on blade active twist, rotor power required, blade loads and vibratory hub loads were studied due to the variation in blade torsional, flap-wise and lead-lag stiffnesses, sectional mass and torsional inertia, and center of gravity and elastic axis locations. The analysis was done using CAMARAD II [82] and the effect of actuators was represented by two torsion moments producing equal but opposing loads at the blade ends. In a similar study, the effect of aerodynamic parameters like linear blade twist, blade tip sweep, droop and taper on active twist performance was studied [79, 81]. Based on the analysis, a candidate design of AATR (Advance Active Twist Rotor) with −10 deg linear twist, 30 deg sweep, 10 deg droop and 2.5:1 taper ratio was proposed. In these studies, the external active twisting moment applied was assumed to be independent of the variation in blade

structural and aerodynamic properties. Thornburgh et al. [83] performed parametric studies on model-scale blades in order to determine the variables critical for active twist response and to determine the effect of twist rate on cross-sectional constraints like mass per unit length, chordwise location of shear center and CG and natural frequencies of blade and material stresses. They also looked at the effect of scaling changes on optimal structural design.

1.3.1.3 Active Twist Optimization

Active twist obtained from the active blade is dependent on the cross-sectional properties of the rotor blade. Due to the large number of variables involved, the principle of mathematical optimization provides a reliable way to explore the design space.

Cesnik and co-workers [84-86] developed an optimization framework to design an active blade that maximizes the static twist actuation while satisfying constraints on various blade requirements. The framework included UM/VABS for active cross section analysis, DYMORE for one dimensional geometrically exact beam analysis, a MATLAB based cross-sectional parametric mesh generator and MATLAB's gradient based optimizer. Results showed that the ATR (Active Twist Rotor) blade [68] could exhibit 30% higher twist actuation than the tested one. The same framework was used to design the ATR-A blade for tests in NASA's Transonic Dynamics Tunnel. The ATR-A was based on a scaled model of AH-60D blade [84] that has a more complex geometry and the final design obtained included manufacturing constraints. In the Friendcopter program [87], the objective was to maximize the twist per unit span of a uniform beam section under given constraints on airfoil shape, chordwise location of CG (center of

gravity) and SC (shear center), torsional frequency and beam stiffness. The design variables used were chordwise location, length and thicknesses of piezoelectric layers, ballast mass and four parameters that define the front C spar. Similar framework was used with response surface technique for optimization in [88, 89]. Here approximations of the original functions for constraints and objective function were obtained using a low order polynomial.

1.3.1.4 Hybrid Active/Passive Optimization

In a hybrid active/passive optimization process, an optimal control law is combined with the nonlinear optimization programming. The optimal controller tries to minimize an objective function usually consisting of vibratory hub loads and flap control inputs while the passive structural optimization aims to enhance the effectiveness of controller. Due to the fact that the performance of active control strategies like active flaps or active twist rotors is heavily dependent on the blade dynamics properties, it is useful to perform an active/passive hybrid optimization to take advantage of the structural optimization to enhance the effects of active control. Hybrid optimization technique has been used for active flaps where a trailing edge flap controller design is combined with blade structural optimization [90, 91]. Results obtained in [91] showed that an active-passive hybrid method can outperform an optimal passive blade or an active flap retrofitted to a baseline blade by achieving more vibration reduction with less control effort. This occurs due to the tuning of blade flapwise bending frequencies and first torsional frequency close to actuation frequency of the trailing edge flap. A multi-objective function optimization approach was used in [90] to obtain simultaneous vibration and power reduction. The

results obtained highlighted strong tradeoff between performance enhancement and vibration reduction, and both combined and sequential active/passive approaches led to useful designs.

1.3.2 Passive Optimization

For the purpose of passive optimization, it is very important to perform the analysis of rotor blades using a high fidelity aeroelastic framework. The current state of art with respect to the analysis of rotor blades is discussed in [92] and [93] and the future needs are described in [94]. The most recent reviews of different optimization methods used for helicopter vibration reduction are provided in [15, 95]. Here, the literature review related to recent work done in multidisciplinary optimization is presented.

In [96], Glaz used the efficient global optimization (EGO) algorithm with surrogate models for rotor blade design optimization and a modified version of EGO based on weighted expected improvement function (WEIF) for multi-objective function optimization. The multi-objective optimization problems considered in the study were: 1) vibration reduction through entire flight envelope, 2) noise and vibration reduction at low advance ratio, and 3) vibration reduction and performance enhancement at high advance ratios. The aeroelastic analysis in these studies was performed using high fidelity yet computationally efficient aeroelastic code called AVINOR [97] developed at UCLA and at University of Michigan. Jieun Ku [98] developed a rotor blade multilevel optimization framework by including computationally efficient yet realistic and sufficiently accurate tools like VABS and DYMORE. At the global level, optimization seeks structural configuration that satisfies global constraints and focuses on rotorcraft dynamics. The

goal of the local level optimization is to find specific cross-sectional layout that satisfies constraints obtained from the global level. Li et al. [99] developed a design tool which incorporated manufacturing constraints, fatigue analysis and manufacturing uncertainty. The design tool included VABS for cross section analysis and a parametric geometry generator. A hybrid optimization procedure was developed that could handle a mixed variable (discrete and continuous) problem. Khalid [100] incorporated the effects of vehicle engineering, stability and control, aerodynamics, propulsion, transmission, weight and balance, noise and cost calculations in the rotorcraft design environment using low fidelity techniques. Collins [101] developed an automated high fidelity CFD based simulation framework capable of predicting acoustic noise. A novel method using combination of low fidelity and high fidelity results with statistical analysis was developed and was used for optimization studies. Mustafa [95] used ModelCenter to combine various software tools like: CATIA as the CAD tool, ANSYS as the FEA tool, VABS for obtaining cross-sectional structural properties and DYMORE for frequency and dynamic analysis of the rotor and MATLAB codes for generating input files and reading output files.

1.3.3 Active Flaps

In the case of active flaps, the analysis performed in this thesis focuses on the design of cross section for a composite rotor blade in order to maximize the control authority for vibration reduction. In the next step, design and testing of a flap-actuation mechanism using the X-frame actuator is presented which can be used for actuating flaps on a Mach-scaled rotor blade.

1.3.3.1 Cross-sectional Design for Composite Blade with Active Flaps

There have been very few studies that have focused on the design of a composite rotor blade with active flaps. For the design of a rotor blade with active flap, hybrid active-passive techniques [90, 91] have been proposed. In [91], the optimal cross-sectional stiffness values were determined using an integrated active-passive approach to reduce vibration while minimizing control effort. In [90], simultaneous vibration reduction and performance enhancement were obtained using active/passive optimization for a simplified blade cross section. Ganguli and co-workers [102, 103] have performed optimization using response surface and neural networks metamodels to determine the optimal flap locations and the blade stiffness (torsional) for a rotor blade with multiple trailing edge flaps to achieve minimum hub vibration level. In most of these studies, either the cross-sectional stiffnesses are used as design variables or a simplified cross section is used. Thus, there is a need for an optimization framework which can analyze a "realistic" composite rotor blade with all the cross-sectional details such that the final design obtained at the end of optimization is suitable for fabrication.

1.3.3.2 Dual/Multiple Trailing Edge Active Flaps

Patt et al. [104] used a single 12% long flap and dual 6% flaps for vibration reduction and showed that the dual flap configuration is more effective. The increase in noise level as an adverse effect of vibration reduction is smaller in the case of dual flaps. It was also shown that dual flaps work better than a single flap for BVI noise reduction [105] and for simultaneous vibration reduction and performance enhancement in dynamic stall conditions [106]. Kim [107] used dual flaps to reduce both vibratory hub loads and

bending moments without significant change of control settings. Visvamurthy and Ganguli [108] and Dalli [109] used multiple trailing edge flaps with differential weighting to modify the contribution of second flapwise bending mode at a much lower control power as compared to single and dual flaps. Some of the recent studies have explored the experimental analysis of dual active flaps for BVI noise neduction [110] and vibration reduction [111]. Thus, earlier work has demonstrated the advantages of multiple flaps; however there have been no experimental studies to demonstrate their effectiveness.

1.3.3.3 Piezoelectric Actuator for Active Flaps

Over the last two decades, a variety of actuators have been developed for rotor blades with active flaps. A summary of these actuators is provided in [38] and [112]. More recently, trailing edge flap actuation system using Pneumatic Artificial Muscles (PAM) [113] were tested which can produce required levels of blocked force and free strain without the need for an amplification mechanism. Different types of actuators for oscillating flaps that have been used in the past are given in Table 1-1, Table 1-2 and Table 1-3.

Table 1-1: Active Flaps Implemented on Full Scale Blades

Num	Baseline	Program	Actuator Details	Blade Dim	Flap Dimension
1	BK 117 Helicopter	ONERA/Eurocopter/ DLR [46]	CEDRAT Actuator	5.5m radius 0.325m chord	0.109 R and 0.156 c centered at 0.75, 0.8, 0.85
2	Modified MD900	Boeing [114, 115]	Double X-frame Actuator	5.15 m radius 0.25m chord	0.18R, 0.35c, centered at 0.82R
3	Blade with AK120g and AK100g airfoil sections	JAXA [110]	Two piezo stacks with an amplifying mechanism	5.8 m radius 0.4 m chord	0.1c, 0.1R centered at 0.75R
4	Modified S-434 rotor blades	Sikorsky, UTRC, AATD [116]	Electromechanical Actuator	4.45m radius 0.2 m chord	0.24c, 0.12R centered at 0.72R

Table 1-2: Active Controlled Flaps Tested on a Model Scale Rotor in Whirl Tower or Wind Tunnel

Num	Blade	Program	Actuator Details	Blade Dimension	Flap Dimension
1	2.1 m radius Adv Tech Rotor [117]	ONERA/Eurocopter/ DLR/Eurocopter Deutschland [118]	CEDRAT Actuator	2.1 m R, 0.14m c	0.1R and 0.15c, centered at 0.75R, 0.8R, 0.85R
2	1/6th scaled CH 47D rotor blade	MIT [119]	X-frame Actuator	1.54m span , 0.137m chord	0.12R and 0.2c centered at 0.78R
3	Blade with NACA 0012 airfoil	Univ of Maryland [120, 121]	Piezo bender with mech level	0.914m, 0.0762 c	0.05R and 0.2c
4	Blade with NACA 0015 airfoil	Univ of Maryland Boeing [122, 123]	Cam Follower Assembly	1.848m, 0.1334m	0.25c , 0.18R centered at 0.88R
5	Blade with uniform NACA 0012	AFDD [124]	PZT bimorph bender beam with elevon lever arm mechanism	1.143m,0.0864m	0.1c, 0.12R centered at 0.75R

Table 1-3: Conceptual Designs for Active Flaps

Num	Program	Actuator Description	Results
1	Penn State University [125]	Induced shear Piezoelectric actuator	2.8 deg at 0 RPM 1.4 deg at 400RPM
2	Univ of Michigan [126]	Piezoceramic C Blocks	20 deg flap deflection in wind tunnel tests
3	MIT [127]	Piezoelectric bender with flexure mechanism	flap deflection of 11.5 in no load at 100Hz
4	Boeing [128]	Biaxial piezostack column	Tested in 814g steady and 29g vibratory
5	Univ of Maryland [129]	Double-lever (L-L) Actuator	Amplification of 20 upto 8/rev frequency

1.3.1 Optimization for Composite Structures

Different optimization techniques have been proposed for determining the minimum number of layers in a composite laminate and the best fiber orientation and thickness for each layer. In review papers [130, 131], the main optimization methods are described and their characteristic features are contrasted for constant stiffness design and variable stiffness design. In [132], composite laminate optimization with discrete variables is discussed and issues associated with design of composite laminates are highlighted. In, [133, 134] a novel laminate parameterization technique based on discrete material optimization is used which is well suited for gradient based design optimization to handle problems where ply angles and ply thicknesses are treated as discrete. Most of these studies focus on the design of a simplified composite laminate.

For optimizing complex composite structures where time consuming finite element analysis is required, surrogate modeling and response surface methods are proposed that efficiently explore the design space and limit the number of FEA runs. Surrogate based optimization technique have been used earlier for the design of composite rotor blade [97, 135]. However in these studies, only continuous design variables were considered. Guido et al. [136] presented a mixed continuous-discrete variable optimization for design of composite panel using surrogate modeling. Here, first a solution with continuous design variables is determined and the solution with mixed design variable is obtained by branching into sub-problems.

1.3.2 Camber Actuation

Airfoil camber deformation can potentially be achieved by embedded smart actuators such as piezoelectric materials in the wing structure [137], or through compliant substructures such as airfoils with deformable leading edge [138, 139]. Continuously deformable airfoils have already been considered for performance and handling-quality improvement of fixed-wing aircraft. Kota and co-workers [138, 140], demonstrated the use of compliant mechanism for design of morphing aircraft structures. They suggested the use of passive compliant structures with a generic force actuator to produce static shape control of an airfoil camber. Gandhi and Anusonti-Inthra [141] looked at desirable attributes of a flexible skin on a morphing wing. Parametric study was conducted to determine the required in-plane and out-of-plane stiffness by considering the requirement for actuation force, local and global deformation under aerodynamic loading and local buckling of skin. Santer and Pellegrino [139] introduced network analysis technique to determine an optimized compliant structure that deforms in conjunction with the wing skin in response to a single displacement actuation. Rediniotis et al. [142] demonstrated the use of shape memory alloys as artificial muscles to actuate a biomimetic hydrofoil. Kudva and co-workers [137, 143], as a part of the Defense Advanced Research Projects Agency (DARPA) sponsored Smart Wing program, developed deformable airfoil surfaces using ultrasonic piezoelectric motors and eccentuator to ensure effective transmission of motor torque to deflect control surface and demonstrated that the airfoil could achieve trailing-edge deflections of up to 20 deg at deflection rate of over 80 deg/s.

The use of conformable airfoils in rotorcraft blades has been limited. Anusonti-Inthra et al. [56] conducted research on conformable rotor airfoils using an optimized ground

structure of piezoelectric elements. The predicted trailing-edge deflections were 4 deg, but the structure required a large number of piezoelectric elements. Later, Gandhi et al. [144] proposed a conformable rotor airfoil design consisting of a passive compliant structure coupled with a limited number of piezoelectric actuators to reduce the complexity of the design. In this research, a detailed numerical analysis is performed with different camber deformation shape function to explore the possibility of vibration reduction and performance enhancement in the dynamic stall condition using camber actuation.

In order to analyze morphing-type rotors, an analysis code called UM/NLABS-A (University of Michigan Non-linear Active Beam Solver with Aerodynamics) was developed by Thepvongs et al. [145] where the structural formulation captures plate-like deformation in a geometrically-nonlinear beam-like framework. The aerodynamic model was based on the 2D flexible airfoil theory and it includes 3D dynamic inflow model. This code was also coupled with unstructured Reynolds Averaged Navier Stokes (RANS) computational fluids dynamics (CFD) solver to obtain high fidelity aeroelastic solution [146]. The comparison of aeroelastic loads predicted by the low order model and CFD showed agreement in trimmed control setting, and some aspects of tip deflections and fixed-frame hub loads.

1.4 Objectives of the Dissertation

In this study, further analysis has been done on the various on-blade approaches available for vibration reduction with the aim of gaining further insight into the problem.

The specific areas of vibration reduction methodologies that this research focuses on are highlighted in Figure 1-6.

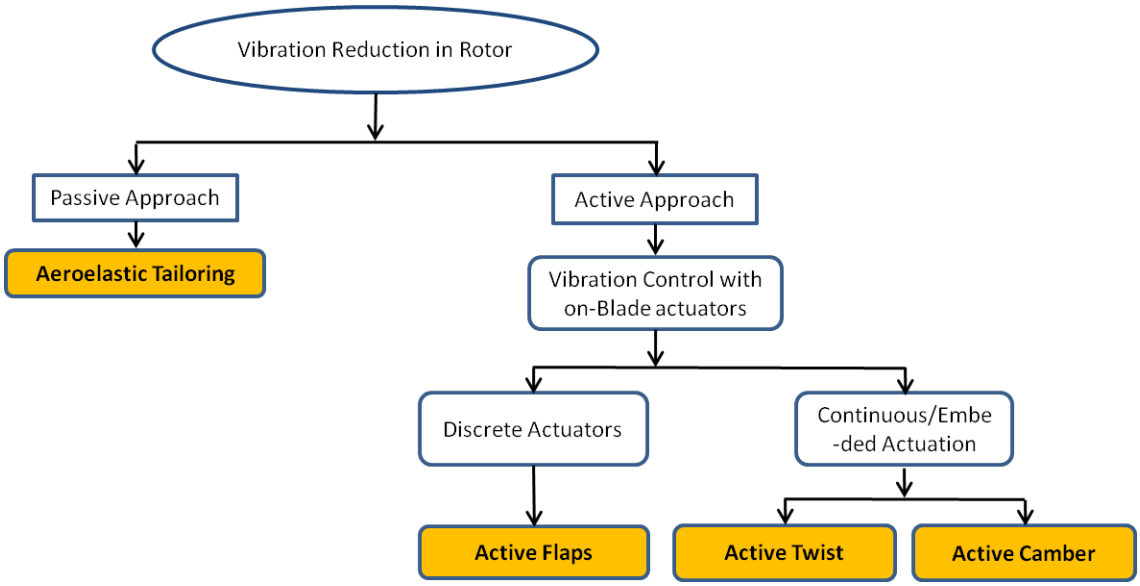

Figure 1-6: Area of Focus for the Thesis

For the case of aeroelastic tailoring, there is a need to develop a high fidelity multidisciplinary analysis framework which can model the structural properties of realistic composite rotor blades. This framework can be used for design and analysis of new rotor blade configuration with isotropic and orthotropic materials in their cross section, which can be either active or passive. The design environment should combine a) computational efficiency and speed of nonlinear 1D beam analysis with unsteady aerodynamics, b) high-fidelity cross sectional analysis, and c) the ability to model complicated topological details of a "realistic" composite rotor blade cross section.

With the use of composite material it is possible to design a rotor blade such that the blade-twist due to active material in the blade is maximized. For the active twist rotor blades, a tip twist of the order of ±2 deg at the actuation frequency is required to obtain

vibration reduction. In the preliminary analysis that was performed, it was observed that the amplitude of dynamic twist is more directly related to the vibration reduction ability of the active twist rotor blade, as compared to the static twist. Thus, the optimization analysis should use dynamic twist as its objective function for optimum active rotor blade design, which has not been done earlier. Also, the optimization framework must be capable of working with both continuous and discrete design variables. This research presents a new optimization strategy and framework for the design of a rotor blade with active twist mechanism to enhance its capability for vibration reduction.

In most of the experimental and numerical studies that have been done till now to analyze active flaps, the rotor blades are designed with low torsional stiffness such that the effect of active flaps is enhanced. However, low torsional stiffness of the blade may lead to detrimental effects like higher baseline vibrations (vibration in the absence of active flap motion) and higher stresses in the blade root. In order to avoid these issues, it is essential to design a blade with sufficient stiffness without compromising on the effectiveness of active flaps for vibration reduction. This can be achieved by dynamically tuning the blade frequencies near the expected actuation frequency. Thus, in the analysis performed here, the amplitude of tip twist obtained due to the flap motion is used as the objective function which is maximized.

The literature review in the previous section has highlighted that very few numerical studies have been performed to explore the full potential of camber actuation for vibration reduction and performance enhancement. Preliminary analysis done with lower order model showed potential for vibration reduction and performance enhancement by varying the amplitude and the phase of camber deformation along the blade span for a

scaled Bo105 rotor used in the HART II experiments. This research presents a detailed study to explore the possibility of vibration reduction and performance enhancement using camber actuation in forward flight conditions.

1.5 Outline of the Thesis

The main objective of this dissertation is to develop design strategies to enhance the capabilities of active/passive rotor blades for vibration reduction. This objective is achieved through the development of a high-fidelity aeromechanic analysis framework and the use of appropriate optimization techniques. The achievements of this thesis and the organization of chapters are given below:

1) Development of an aeromechanic analysis and design framework

Chapter 2 presents the development of an aeromechanic analysis environment for the design of a composite rotor blade such that vibration reduction and performance enhancement at the rotor hub is achieved using *aeroelastic tailoring*. This analysis environment includes an advanced mesh generator for capturing the topological details of a composite rotor blade cross section and for generating the 2D finite element mesh, UM/VABS for the active cross-sectional analysis and comprehensive rotorcraft analysis code for the aeroelastic analysis of rotor blade. The design environment was successfully used to perform detailed parametric and optimization studies on the full scale model of a UH-60 composite rotor blade [147] and on the passive version of ATR blade [148].

2) Optimization strategy for the design of active twist rotor

Chapter 3 introduces an optimization framework for the design and analysis of a composite active twist rotor blade. The aeromechanic analysis environment described in Chapter 2 was enhanced to include the effects of active plies in the cross section and it was augmented with surrogate-based optimization technique to form an optimization framework. In this study, the amplitude of *dynamic twist* has been proposed as the *new* objective function for optimization studies for the design of active composite blade cross section. It has been demonstrated using post-processing analysis that the dynamic twist is a true indicator for vibration reduction capabilities of an active twist rotor. In this framework, surrogate based optimization is included to explore the large design space efficiently and to avoid the issues associated aeroelastic problems. (In these problems, the runtime for each iteration is high (10-20 min) and some of the cases do not complete due to failed convergence within the analysis). The optimum result obtained by maximizing the dynamic twist amplitude is compared with optimum result obtained my maximizing the static twist (the objective function used in all the studies discussed in literature review) and advantages of the new strategy are highlighted [149]. Appendix A provides mathematical expressions related to the development of surrogate models and Efficient Global Optimization (EGO) algorithm used in the thesis.

3) Optimization at a range of actuation frequencies

Vibration reduction studies with the on-board active control devices have shown that actuation frequency of (N_b-1)/rev, N_b/rev and (N_b+1)/rev are required for vibration reduction in a rotor with N_b blades. Hence, the dynamic twist optimization performed in Chapter 3 is carried out at a range of actuation frequencies and the active composite cross

section which is effective at a range of actuation frequencies simultaneously is determined.

4) Active twist optimization with mixed design variables

In Chapter 4, the framework that was developed in Chapter 3 was extended to include *discrete design variables* in the optimization study. The mixed-variable (with discrete and continuous design variables) optimization described here is useful to obtain a realistic optimum design and it highlights the effect of variable discretization on different objective functions considered here. In the optimization studies performed in this chapter, the ply thicknesses and ply angles are treated as discrete design variables. The modified optimization framework includes both a genetic based optimizer and a gradient based optimizer. The solution with mixed design variables is obtained using three different techniques for comparison [150].

5) Design of a composite rotor blade with active flaps

The literature review highlighted that very few studies have been conducted to design a composite rotor blade with active flaps that can be readily manufactured. Chapter 5 presents design studies for a composite rotor blade with active flaps such that the authority of active flaps for vibration reduction is enhanced. In this study, a Mach-scaled rotor blade which can be tested in the University of Michigan spin test stand is used as the baseline rotor blade. In this study also, the mixed-variable surrogate-based optimization framework described in Chapter 4 is used [151]. The aeromechanic analysis was modified to account for the presence of active flaps on the rotor blade. Appendices C

to F present details about the design, fabrication and testing of a composite rotor blade with dual flaps in a hover test stand.

6) Vibration reduction and performance enhancement in dynamics stall condition using camber actuation

In Chapter 6, numerical studies are performed using UM/NLABS-A to study the effect of camber actuation on vibratory loads at the hub and on rotor performance. The rest of the surrogate based optimization framework is the same as in earlier chapters. In the first study, the analysis is performed at an advance ratio of 0.24 where the quadratic camber deformation shape function was used to obtain reduction in vibration and small improvement in performance [63]. In the next step, a modified version of the ONERA dynamic stall model was included in UM/NLABS-A for performing aeroelastic analysis at high forward airspeeds. The vibration reduction and performance enhancement studies in this section are carried out using both quadratic and cubic camber deformation shape function [152] for $\mu = 0.33$. Results obtained at the end show that the cubic camber deformation shape function is more effective at reducing vibration and improving performance of the rotor blade. Appendix B provides detailed description of the unified aerodynamic model used in UM/NLABS-A.

Finally, Chapter 7 summarizes the work done in this thesis and presents recommendations for the future work.

Chapter 2. A Multidisciplinary Design Environment for Passive Composite Rotor Blades

The work presented in this chapter introduces a new design environment that combines the computational efficiency and speed of 1D beam analysis with high-fidelity accuracy approaching that of a 3D FE model for analyzing a composite rotor blade. The environment contains a graphical modeling tool to rapidly define the cross-sectional layup of a rotor blade or wing and a cross section mesh generator, both part of the IXGEN pre-processing tool. It uses a cross-sectional beam analysis code (UM/VABS) to determine the cross-sectional mass and stiffness properties, which it then feeds into a comprehensive rotorcraft analysis code (RCAS). Using Phoenix Integration's ModelCenter as the optimization software, a full multidisciplinary design and optimization environment for the preliminary design of composite rotor blades and wings has been developed. As a test case, structural optimization case studies are presented where the cross-sectional layup of the blade is determined that results in significant vibration reduction at the rotor hub in forward flight condition for a model UH60 rotor blade.

The implementation of the design environment was done in collaboration with Advatech Pacific, Inc (San Bernardino, CA) as part of a SBIR project.

2.1 Introduction

The design of a composite rotor blade in a helicopter is inherently a multidisciplinary problem involving aerodynamics, static and dynamic loads, aeroelasticity, materials, fatigue life, manufacturing aspects, etc. Different stages of a product design and the variation of estimated cost committed, design freedom and knowledge about the design is shown in Figure 2-1 [100]. It also highlights the current design process and future trend in product design. As indicate in the figure (by dark lines), during the preliminary design stage, the knowledge about the design and the cost committed is the least while the design freedom is the highest. As further progress is made in the design, there is an increase in the cost and knowledge about the design and there is a decrease in the design freedom. At the completion point, we have a complete product. The future trend (indicated by gray lines) would be to shift the "knowledge about the design" curve towards conceptual and preliminary design stage such that there is more design freedom at less cost in the early stages. This strategy will help the designers to make better exploration of the design variables in the early stages without significant cost. In order to achieve this target, it is desired to obtain "mature" designs in the preliminary design stage by making use of high-fidelity numerical tools for analysis. Thus, during the conceptual design stage, there is a need to balance the fidelity of different models used in the analysis with computational time requirements. Since making design changes in later stages is far more expensive, it is essential to explore the complete design space in the preliminary design stage itself.

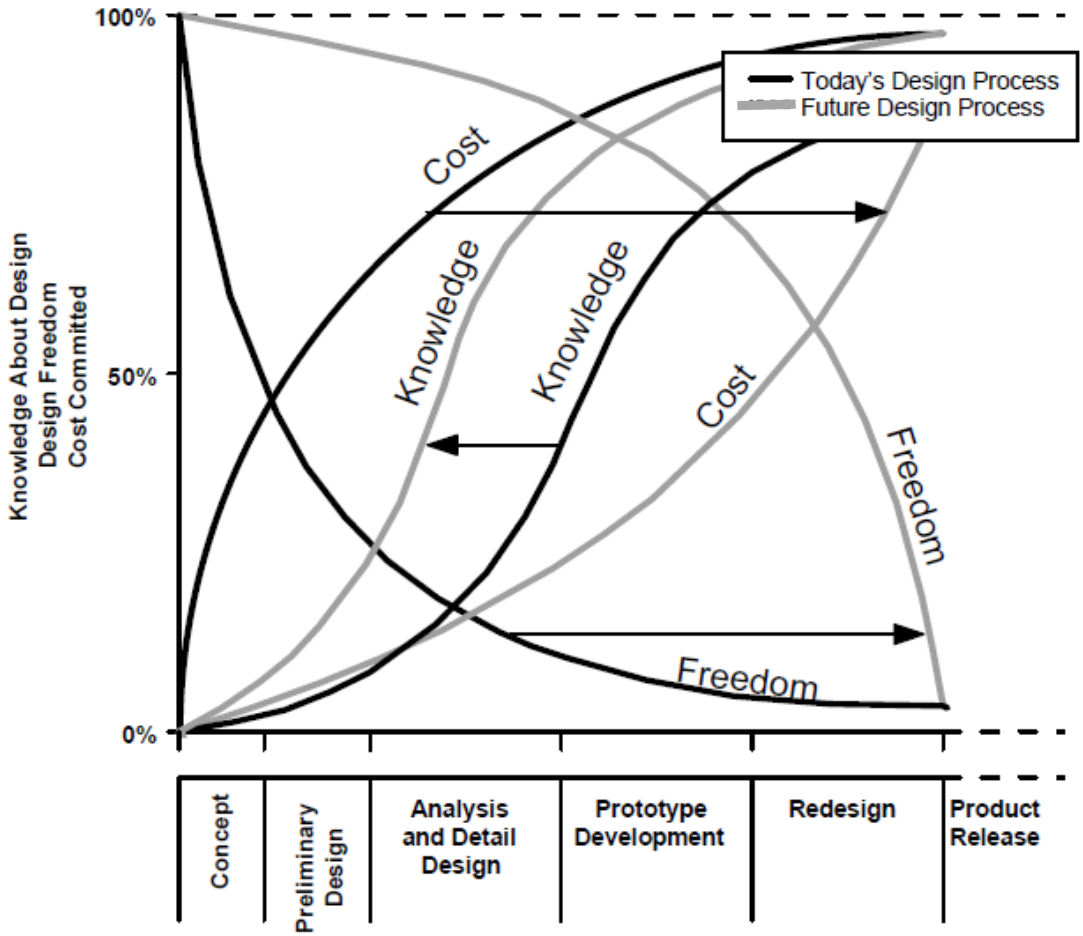

Figure 2-1: Different Stages of Product Design [100]

For the detailed structural analysis of a rotor blade, a 3D Finite Element (FE) analysis is required in order to capture all the topological details. However, the time-consuming FE analysis is not suitable for conceptual design since a large design space needs to be explored. Instead, due to the geometry of rotor blades, a "dimensional reduction" can be performed that takes the original 3-D body and represents it as a 1D beam along a predefined reference line. This can be done because one dimension (along the length) of a rotor blade is much larger than the other two, and the structure is mostly uniform along the span. For accurate dimensional reduction, following features are required:

a) Detailed modeling of the rotor blade cross section which includes isotropic and orthotropic material properties and cross section topology.
b) Accurate representation of 3D blade properties along a reference line.
c) Non-linear aeroelastic analysis of the 1D blade.

The design environment presented here includes these features for rotor blade design through the coupling of the following high-fidelity analysis tools in a design environment:

a) IXGEN, the Intelligent Cross Section generator developed by Advatech Pacific, Inc [153],
b) UM/VABS, the University of Michigan /Variational-Asymptotic Beam Sectional analysis [70], and
c) RCAS, the Rotorcraft Comprehensive Analysis System [154].

2.2 Design Approach

The basic approach to the rotor blade design problem, which is adopted in this thesis, is shown in Figure 2-2. It is based on the approach used for the design of a rotor blade with active twist in [84, 86], however, that framework did not include the aeromechanic analysis. In [84, 86], the failure analysis was done using the worst case loading obtained *a priori*.

In this approach, important sections along the blade span are identified, where geometrical or material properties do not change significantly. For each of these sections, structural topology, layout of composite plies, materials and ply thicknesses are obtained either through a user input or from the optimizer. This information is passed as input for

generating cross-sectional mesh and a UM/VABS input file using IXGEN. In the analysis performed in this thesis, IXGEN is used as a mesh generator, though it has more capabilities which are discussed in [153]. The cross-sectional analysis performed using UM/VABS provides the mass and stiffness matrices which are used as input for 1D nonlinear beam analysis. These matrices can also be used to determine the chordwise location of shear center and center of gravity which act as constraints in the optimization studies. The nonlinear beam finite element analysis of the composite beam is performed in RCAS. It also includes aerodynamic models of different fidelities and various models for determining inflow velocity and for capturing the dynamic stall effects. In a post-processing step, the element loads resulting from the dynamic or aeromechanical analysis are converted to equivalent stress and strain distributions in the individual cross sections.

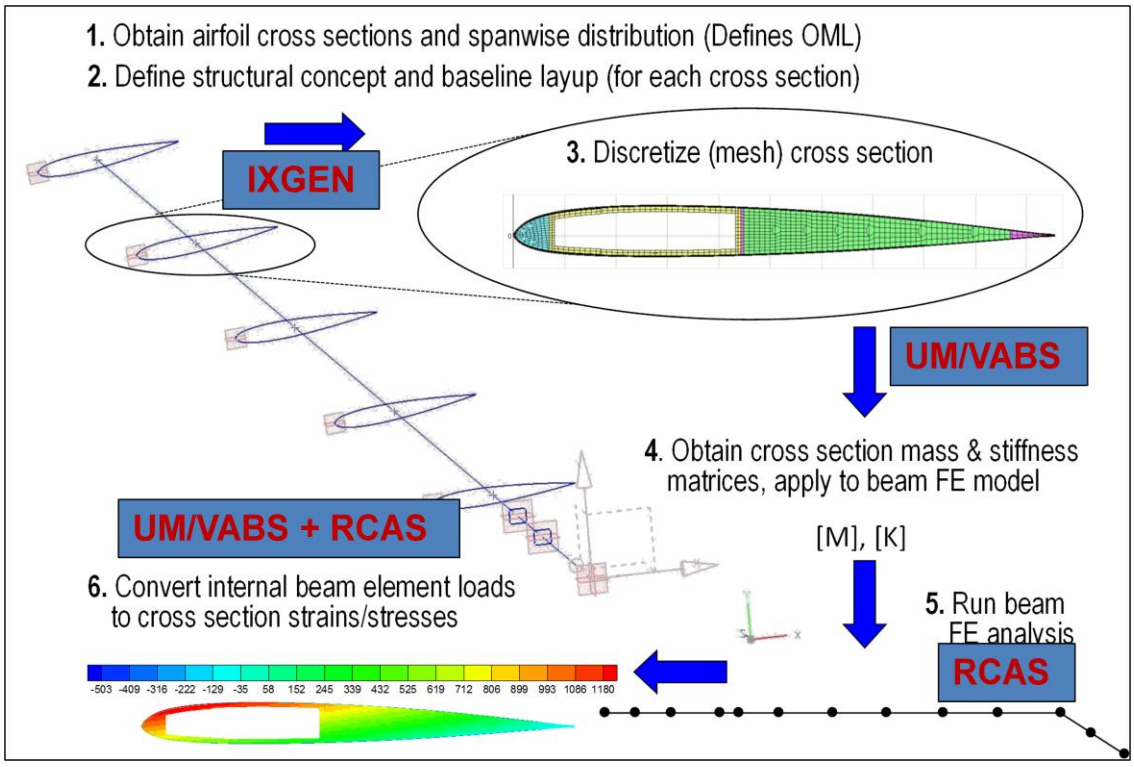

Figure 2-2: 2D - 1D Design Approach.[148]

Figure 2-3 shows the Multidisciplinary Design Optimization (MDO) process that implements the design approach described earlier for the design of a passive composite rotor blade. The main pieces of software/codes used in this analysis are IXGEN, RCAS and UM/VABS

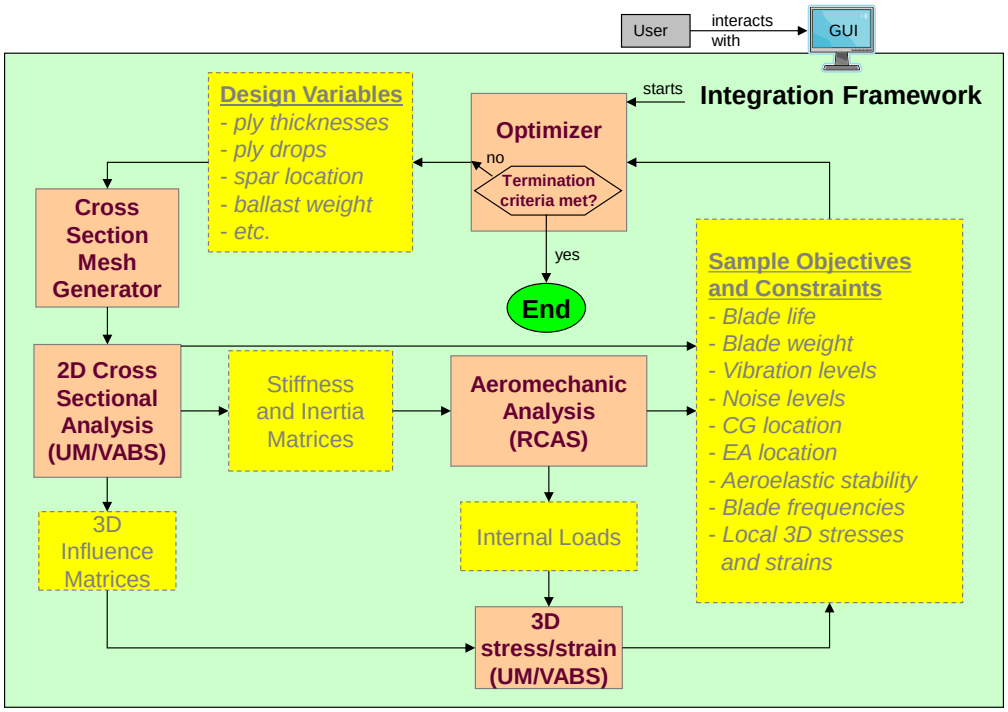

Figure 2-3: Multidisciplinary Optimization Process for Design of Passive Blade.

2.2.1 Blade Modeling Tool IXGEN

IXGEN [147, 148, 153] is a rotor blade and slender wing modeling environment that lets the user quickly and easily define a rotor blade as a sequence of cross sections stacked in the spanwise direction along a user-defined stacking axis. IXGEN has two modes of operation – a GUI-driven mode for the designer to set up the blade, and a batch mode for use in an automated design framework, where an optimizer or other type of programmatic design driver modifies the defining parameters and regenerates the blade.

IXGEN contains a finite element mesh and UM/VABS model generator, and it has the ability to execute UM/VABS directly from the UI. IXGEN has the capability to abstract the definition of a rotor blade and its cross sections to a higher, feature based level. These defining features, such as spar webs, spar caps, wrap layers, etc. are then parameterized, and these parameters, in turn, can then be driven by an optimizer or a similar design driver. IXGEN currently supports box, D and multi-cell spar concepts with spar webs either perpendicular to the defining airfoil chord or at a slant angle off perpendicular. Figure 2-4 shows several representative blade sections that have been modeled with IXGEN. While the tool was developed for helicopter rotor blade design, it has also been used to model typical wind turbine blade geometries.

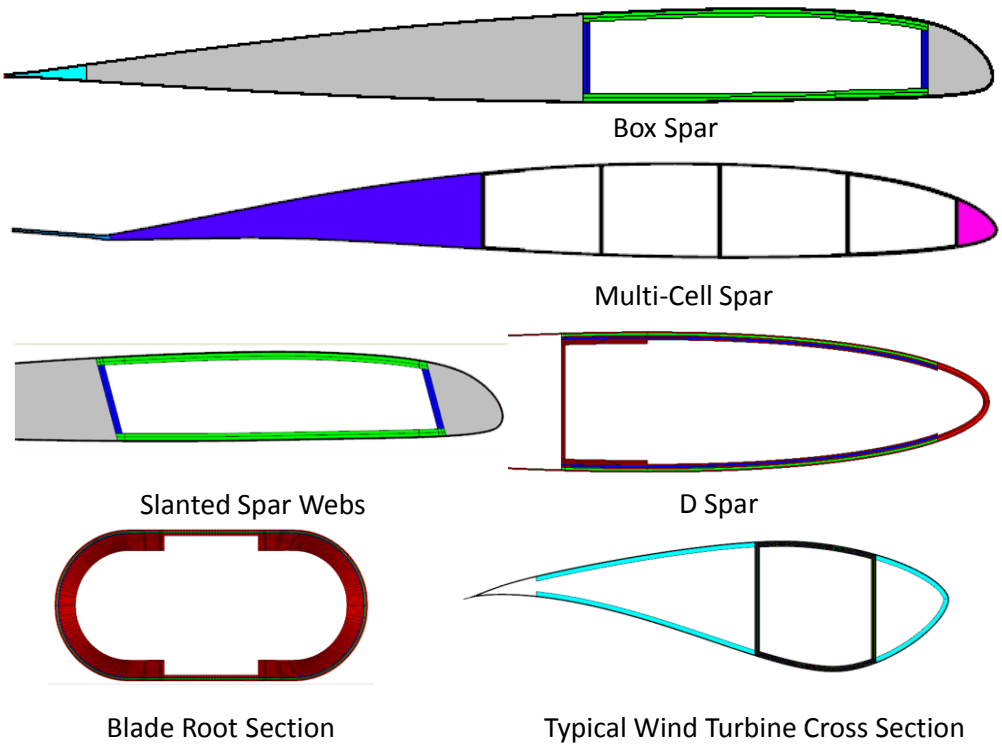

Figure 2-4: Representative Cross Sections Developed using IXGEN [148]

2.2.2 UM/VABS

UM/VABS [71] is a FORTRAN90 code developed at the University of Michigan which solves the coupled equations of electro-thermo-elasticity in the cross section using an asymptotic solution [155]. It includes cross-sectional analysis using different beam theories: Euler-Bernoulli beam theory, Timoshenko beam theory, Vlasov beam theory, and the original extended beam theory with finite section deformation modes. All these models support the actuation effects in case active material is embedded in the cross-sectional layup. As a post processing step, UM/VABS provides strain/stress influence coefficients (SIC) which can be used to recover cross-sectional stress/strain and displacements. The basic process of UM/VABS is shown in Figure 2-5.

In the UM/VABS analysis performed in this thesis, Timoshenko beam theory is used. The analysis performed in Chapter 3 includes the effect of active plies used in the cross section. As a result, the output produced by UM/VABS includes actuation forces and strains in addition to the traditional mass and stiffness matrices. In Chapter 6, finite section modes are used to model the effects of camber deformation and to determine the corresponding higher-order mass and stiffness matrices.

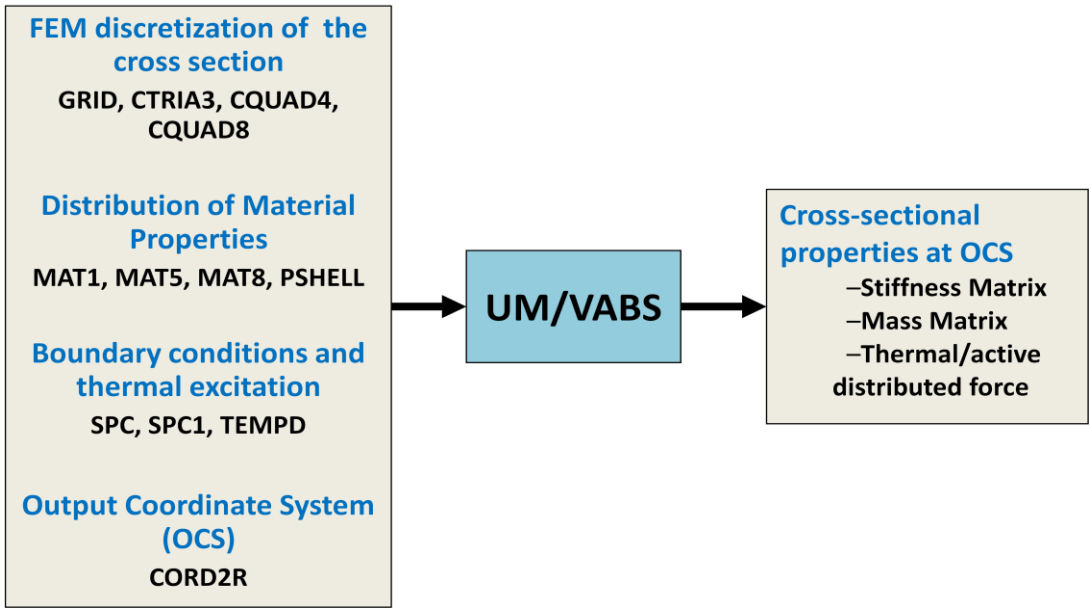

Figure 2-5: Basic Process of UM/VABS [71]

2.2.3 RCAS

The Rotorcraft Comprehensive Analysis System (RCAS) is a software code developed by U.S. Army Aeroflightdynamics Directorate (AFDD) and Advanced Rotorcraft Technology (ART) to provide state-of-the-art rotorcraft modeling and analysis technology for Government, Industry and Academia [156]. The current capabilities of RCAS (RCAS v12.08) include large rigid-body motion, a nonlinear beam element valid for large blade deformation, easier procedures for building complex finite-element rotorcraft models, and various options for modeling unsteady aerodynamics, rotor inflow and dynamic stall effects. RCAS is capable of modeling a complete range of complex aircraft configurations operating in hover, forward flight, and maneuvering flight conditions. RCAS is designed to perform a wide variety of rotorcraft engineering analyses like vehicle performance, aerodynamics, aeroelastic stability, flight dynamics, etc. It uses hierarchical finite-element modeling for the structure and airloads in order to

model complex rotorcraft configurations. In [154], a number of examples are presented to demonstrate the unique and advanced modeling and analysis capabilities from RCAS.

2.2.4 ModelCenter Integration

ModelCenter is used for integrating all the numerical tools described above and for performing parametric and optimization studies in this chapter. Any response parameter produced by either UM/VABS or RCAS which is exposed by the MDO environment is available to the optimizer as either a constraint or objective value. Figure 2-6 shows the ModelCenter components implementing the rotor blade design. Detailed information about each of the modules shown in Figure 2-6 is provided in [148].

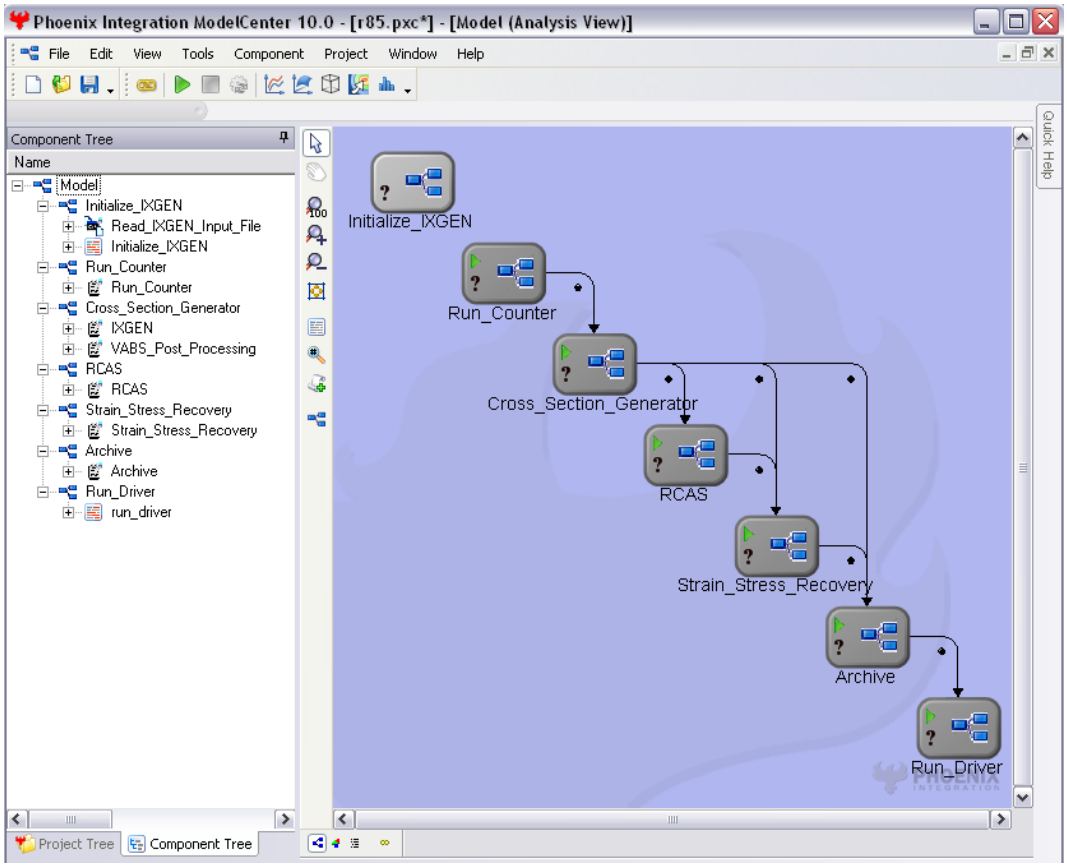

Figure 2-6: ModelCenter-Based Blade Optimization Process.

This implementation of the rotor blade design process in ModelCenter facilitates a wide variety of trade study and optimization scenarios. Design drivers can be wrapped around either the entire process, or individual components, such as IXGEN-UM/VABS-VABS Post-Processing, to optimize the structural properties of an individual cross section without running the aeromechanical analysis, as demonstrated in [153]. ModelCenter's parameter linking functionality can be used to link IXGEN parameters to reduce the number of design variables and enforce continuity or manufacturing constraints.

The development of IXGEN software and the integration of various analysis codes into the ModelCenter were carried out by Advatech Pacific. Detailed analysis for the verification and validation of the design environment and all the design studies presented in this chapter were performed at the University of Michigan.

2.3 Application Example: Vibratory Hub Load Minimization

The MDO environment described in this chapter can be used to solve a variety of optimization and design problems involving metallic and composite rotor blades. Any parameter exposed in ModelCenter can be used as a design variable, part of a response, constraint, or objective function. In order to demonstrate the capability of the design environment described in the previous sections, a full-scale UH-60 rotor model given in the RCAS examples is used as the baseline case for parametric and optimization studies.

2.3.1 Description of the Baseline Rotor Blade

The characteristics of the UH-60 rotor are listed in Table 2-1, and the top view of the rotor blade is shown in Figure 2-7. For the purpose of analysis, the blade was subdivided into three spanwise regions, as shown in Figure 2-7. These regions match with the airfoil breaks existing in the actual UH-60 blade. The rotor blade consists of a SC1095 airfoil in Section 1 and Section 3, while Section 2 has a SC1094R8 airfoil.

Table 2-1: Characteristics of UH-60 Rotor

Rotor Type	Fully Articulated
Number of blades	4
Blade radius (R)	26.83ft (8.18m)
Blade Chord (c)	1.73 ft* (0.527m)
Solidity	0.0826
Airfoil Section	SC1095/SC1094R8
Blade Pretwist	-12 deg
Hinge Offset	1.25ft (0.381m)
Rotor Speed	258 RPM
C_T	0.008
C_Q	0.000354
Air density	0.00237 slugs/ft^3 (1.225 kg/m^3)
Advance ratio (μ)	0.24
Blade tip sweep	20 deg

*** Average chord**

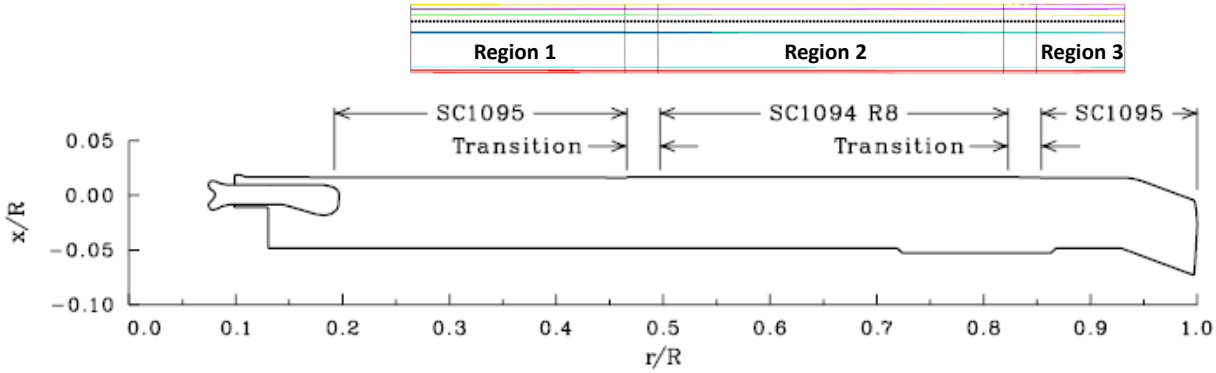

Figure 2-7: Top View of the UH-60 Rotor Blade [157]

The UH-60 rotor blade cross section as modeled in IXGEN is shown in Figure 2-8. It consists of a boxed spar with overwrap plies wrapping around the whole airfoil. It also includes an erosion strip, leading edge wrap, trailing edge tab and trailing edge fill that are commonly observed in a typical rotor blade cross section. Finer details about the cross section and material used in different regions of the airfoil are shown in Figure 2-9. Among the plies used, E-Glass is bidirectional while S-Glass and IM7 plies are unidirectional. The specific material properties for different materials used in the cross section can be found in Table 2-2.

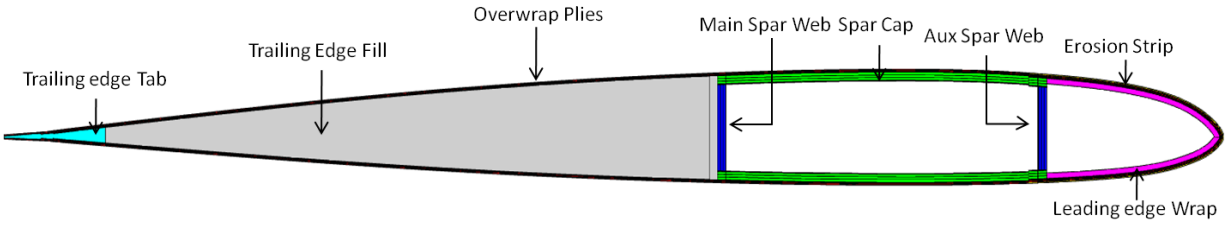

Figure 2-8: Cross Section of the UH-60 Rotor Blade

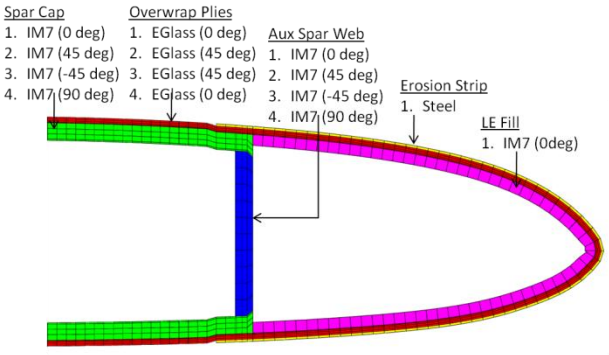

(A) Front Spar

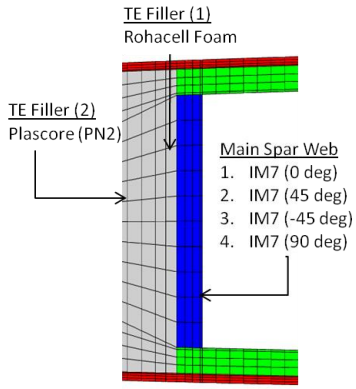

(B) Middle Main Spar Region

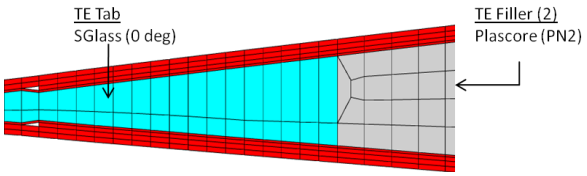

(C) Trailing Edge Region

Figure 2-9: Cross Section Layup

Table 2-2: Material Properties

	E-Glass	IM7	Steel	S-Glass	Plascore
ρ (slugs/ft^3)	3.34	3.01	15.13	3.61	0.09
E_{11} (ksi)	3002	23933	29736	6295	1.00
E_{22} (ksi)	3002	1276	29736	1740	20.02
E_{33}(ksi)	3002	1276	29736	1740	1.00
G_{12} (ksi)	594	710	11169	522	3.48
G_{13} (ksi)	594	710	11169	522	1.00
G_{23} (ksi)	594	710	11169	522	5.80
ν_{12}	0.15	0.34	0.3	0.28	0.01
ν_{13}	0.15	0.34	0.3	0.28	0.3
ν_{23}	0.3	0.3	0.3	0.3	0.01

The thickness of the plies used in the different regions is given in Table 2-3. These thicknesses are the same as those obtained in [153] based on matching the cross-sectional properties of an existing rotor blade. In [153], different sets of ply thicknesses were obtained for Region 1, Region 2 and Region 3. However, for the optimization and parametric studies shown in this chapter, it has been assumed that the cross-sectional layup is the same in all the three regions to reduce the number of design variables, thereby reducing the runtime required for optimization studies. The design environment itself is capable of handling any number of design variables.

Table 2-3: Thickness of Plies used in the Layup

Ply Thickness	Thickness (mil)
Spar Cap Ply 1	4.10
Spar Cap Ply 2	3.72
Spar Cap Ply 3	3.72
Spar Cap Ply 4	1.00
Overwrap Ply 1	0.50
Overwrap Ply 2	0.50
Overwrap Ply 3	0.50
Overwrap Ply 4	0.50
Erosion Strip	1.64
LE Fill	7.71

The structural frequencies of the blade at 100% RPM are listed in Table 2-4 and were obtained using RCAS. The frequencies are slightly different (within ±6%) from those obtained in [153] because of the assumption that cross-sectional layup is the same in all the three regions of the blade. For the rotor aeroelastic analysis, the trim option (*wind tunnel trim*) is used in the RCAS solution. The trim targets used in the analysis are: C_T = 0.008, no longitudinal and lateral flapping angle for tip path plane ($\beta_{1s} = 0$ and $\beta_{1c} = 0$ for the tip path plane), and the blade pitch settings are used as the trim variables. The mean value of the hub loads and the amplitude of the 4/rev component for the baseline blade are given in Table 2-5, where F_x, F_y, and F_z represent components of the hub force in the non-rotating frame, while M_x, M_y, and M_z represent components of the moments at the hub. In all the results shown in this chapter, an advance ratio of 0.24 is used in RCAS.

Table 2-4: Structural Frequencies of the Blade at 100% RPM

Mode Shape	Frequencies (/rev)	(rad/s)
1st chordwise bending	0.27	7.26
1st flapwise bending	1.04	28
2nd flapwise bending	2.68	72.4
1st torsion	4.57	123.5
2nd chordwise bending	4.98	134.4
3rd flapwise bending	5.48	148

Table 2-5: Mean Value and Amplitude of 4/rev Vibratory Loads at the Rotor Hub for μ = 0.24

	Mean Values	4/rev Amplitude
F_x (lbf)	107.8	23.03
F_y (lbf)	559.9	18.74
F_z (lbf)	22586	212.1
M_x (ft-lbf)	3397	6696
M_y (ft-lbf)	1368	5458
M_z (ft-lbf)	26745	377.5

2.3.2 Definition of the Rotor Blade Optimization Problem

A different set of objective functions can be defined depending upon the problem being solved. In principle, any output provided by RCAS or by UM/VABS can be selected as the objective function. For this chapter, the following objective functions are considered:

a) Minimization of 4/rev vertical vibratory load at the hub (min F_{Z4})

b) Minimization of combined vibratory load (from all the hub load components)

Similarly, any combination of outputs from RCAS and UM/VABS can be used to form constraints. For the optimization studies presented herein, the following parameters are constrained:

a) Chordwise location of blade cross-sectional center of gravity

b) Chordwise location of cross-sectional shear center

c) Blade fundamental rotating frequencies

d) Maximum allowable blade strain in the cross section

e) Mass per unit length for each section of the blade

The optimization problem can also include constraints on aeroelastic stability and autorotation, however, these were not considered directly in the problems studied in this thesis. The optimization problem can be solved using gradient based optimizer or non-gradient based methods such as genetic algorithm and surrogate optimization. Finally, the selected design variables for this study are:

- The thickness and lamination angle of spar cap plies in the cross section layup. However, the material properties used in each ply are kept constant.
- The chordwise location of the vertical auxiliary spar web.
- Discrete ballast mass and its chordwise location in each of the sections

From the above discussion it can be seen that a large number of variables could be used as design variables. However, since each run for a complete rotor analysis takes between 15 to 30 minutes on a Windows machine (Intel Core2 QUAD CPU @ 2.39GHz and 1.96GB of RAM), and the number of runs required for optimization increases exponentially with the number of design variables, it is desirable to reduce the number of design variables to the most influential ones. The variables which are most critical for the design can be identified through parametric studies. Thus, as a first step, a parametric study is performed with respect to different design variables.

2.3.3 Preliminary Parametric Study

In the first parametric study, the thickness of the plies used in the spar cap and the fairing were considered independent variables. The thickness of each ply was varied between ±25% of the baseline value, and the variation in blade properties was observed. A total of 300 test cases were set up using the Latin Hypercube Method which spans the whole design space. This example also helped to show the robustness of IXGEN in generating the cross-sectional mesh for different kinds of layups. Table 2-6 shows the variation observed for some of the critical responses during the parametric study with ply thicknesses, where S_{11} is the axial stiffness, S_{44} is the torsional stiffness, S_{55} is the flapwise bending stiffness, SC is the shear center, F_{Z4} is the amplitude of the 4/rev vertical force, and M_{X4} is the amplitude of 4/rev rolling moment at the hub measured in fixed system. Results obtained here show that the cross-sectional stiffness and 4/rev vibratory moments at the hub are very sensitive to variation in ply thickness.

Table 2-6: Variation in Blade Parameters Observed During the Parametric Study with Ply Thickness

Response	Variation
S_{11}	-11.30% to 10.72%
S_{44}	-12.34% to 11.63
S_{55}	-14.76% to 13.88%
SC	-2.73% to 3.26%
1^{st} Tor Freq	-2.53% to 2.53%
F_{Z4}	-11.78% to 9.77%
M_{X4}	-61.17% to 83.97%

Further information about the influence of each design variable can be obtained by observing the contribution of each design variable to the overall variation in the observed response, as shown in Figure 2-10. In these plots, the Y-axis represents the percentage

contribution of each design variable while the X-axis lists each of the design variables considered. (OW1 refers to thickness of Overwrap Ply 1, SC1 refers to thickness of Spar Cap Ply 1, and so on.) The axial stiffness (S_{11}) of the cross section is mainly influenced by the thickness of Ply 1 in the spar cap since it is the unidirectional IM7 ply at 0 deg angle. S_{55} follows the same trend as S_{11}, and the effect of the thickness of the SC1 ply is more apparent here. However, S_{44} is more influenced by the thickness of the SC2 and SC3 plies since they are oriented at $+45^0$ and -45^0 angles, respectively. All plies in the spar cap region and all plies in the overwrap region contribute equally to the variation in mass per unit length, as expected. However, the contribution of the overwrap plies is larger than the contribution of the spar cap plies since overwrap plies occupy a larger fraction of the airfoil contour. The contribution of different ply thickness to the variation in the first torsional frequency and F_{Z4} is less intuitive to predict, and in these cases, the parametric studies are very useful in the overall understanding of the problem.

Similar parametric studies can also be done with respect to other design variables like ballast mass and their chordwise locations, ply angle, and chordwise location of the main and auxiliary spar web.

2.4 Optimization Studies for Vibration Reduction

In this section, results are presented for two optimization studies which were performed to obtain a design with low vibration level using the design environment described in the earlier section. The vertical component of 4/rev vibratory load (F_{Z4}) is used as the objective function for the first optimization study while in the second

optimization study, the combined vibratory load, which includes contribution from all the three force and moment components, is reduced.

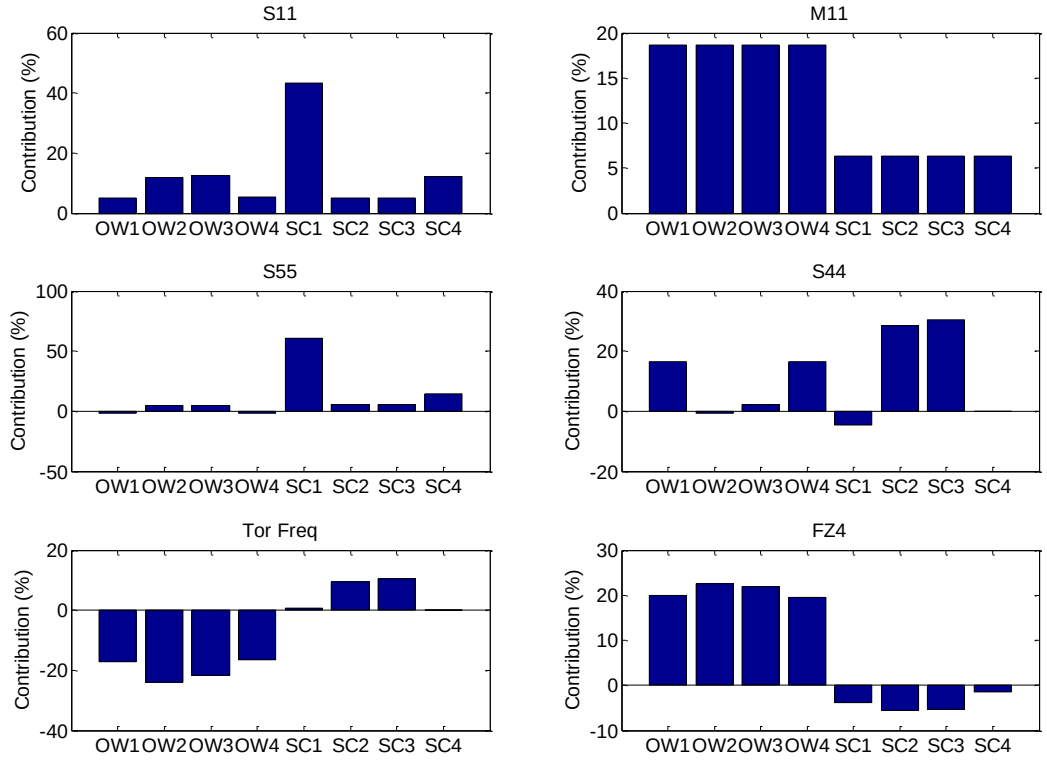

Figure 2-10: Contribution of each Ply Thickness to Overall Variation in the Response

2.4.1 Minimizing Vertical Component of the 4/rev Vibratory Hub Load (min F_{Z4})

In the first optimization study, the amplitude of the 4/rev vertical hub force (F_{Z4}) is used as the objective function to be minimized. The design variables used for this study are ply angles and ply thicknesses for the spar cap plies, chordwise location of the auxiliary spar web and mass, and location of the ballast mass used in Section 1 and Section 2. (Since Section 1 and Section 3 have same airfoil section and layup, the ballast mass used in Section 1 and Section 3 were assumed to be the same.) Upper and lower

limits for these design variables are listed in Table 2-7. The lower limit used for the ply thickness corresponds to $1/4^{th}$ of the baseline ply thickness while the upper limit for the ply thickness corresponds to two times the baseline value. The upper and the lower limit used for the ply angles depend upon the nature of the material, whether it is unidirectional or bidirectional. The ballast mass is allowed to vary between 0.05 slugs/ft and 0.15 slugs/ft while their chordwise location is allowed to vary between the leading edge and the quarter chord of the airfoil section. Constraints used during the optimization are listed in Table 2-8. The shear center (SC) and center of gravity (CG) of the cross section are constrained to lie near the quarter chord of the airfoil to indirectly enforce stability criteria. Mass per unit length of the cross section is allowed to vary between ±15% of the baseline value. Maximum allowable axial strain along the material direction is limited to 6000 microstrain. The 1^{st} torsion frequency is constrained between 3/rev and 6/rev.

Table 2-7: Design Variables used in the Optimization Study for Min F_{Z4}

Design variables	Baseline	Min	Max
Thickness SC Ply 1 (mil)	4.10	0.03	8.20
Thickness SC Ply 2 (mil)	3.72	0.93	7.40
Thickness SC Ply 3 (mil)	3.72	0.93	7.4
Thickness SC Ply 4 (mil)	1.0	0.25	2.0
Angle SC Ply 1 (deg)	0.0	-90.0	90.0
Angle SC Ply 2 (deg)	45.0	-90.0	90.0
Angle SC Ply 3 (deg)	-45.0	-90.0	90.0
Angle SC Ply 4 (deg)	90.0	-90.0	90.0
Aux Web Loc (%c)	6.60	2.5	15.0
Ballast mass 1 (slugs/ft)	0.10	0.05	0.15
Ballast mass 1 Loc (%c)	15.0	0.0	25.0
Ballast mass 2 (slugs/ft)	0.11	0.05	0.15
Ballast mass 2 Loc (%c)	16.0	0.0	25.0

Table 2-8: Constraints used in the Optimization Problem for Min F_{Z4}

Constraints	Baseline	Min	Max
CG Sec 1 (%c)	25.0	20.0	30.0
CG Sec 2 (%c)	25.0	20.0	30.0
M_{11} Sec 1 (slugs/ft)	0.212	0.180	0.244
M_{11} Sec 2 (slugs/ft)	0.223	0.256	0.189
SC Sec 1 (%c)	36.5	25.0	37.0
SC Sec 2 (%c)	35.9	25.0	37.0
Tor Freq (/rev)	4.53	3.0	6.0
Max Strain ε_{11} ($\mu\varepsilon$)	2175.7	0.0	6000.0

For this optimization, the complete rotor blade analysis process is executed at each run, which involves running IXGEN, UM/VABS and RCAS. During the parametric studies, it was observed that some of the cases in RCAS did not reach a converged solution for trim analysis, and hence, there were a few failed cases involved. For the gradient-based optimization, it is required that none of the cases fail during the run. As a result, the gradient-based algorithm was not used for this optimization. Among the various options available in the ModelCenter Release 10 optimization tool package, "Non-dominated Sorting Genetic Algorithm II" (NSGA) [158] was used since it allows for failed runs in the optimization process. Parameters used for NSGA optimization are listed in Table 2-9. The optimization process ran for approximately 48 hours and stopped after exceeding the limit on maximum number of generations allowed. During this time, a total of 236 complete iterations were performed. Although not the global optimum, the result obtained at the end shows 52% reduction in F_{Z4} while satisfying all the constraints. Details for the optimized case are listed in Table 2-10. The variation of the objective function, design variables and constraints with generation are shown in Figure 2-11 to Figure 2-14.

Table 2-9: Parameters used for NSGA II Algorithm

Population	24
Optimization Parameters for Binary Variables	
Binary Crossover Probability	0.7
Binary Mutation Probability	0.5
Optimization Parameters for Real Variables	
Crossover Probability	0.7
η_C (Index for crosssover)	15
η_M (Index for mutation)	20
Mutation Probability	0.167
Stopping Criteria	
Convergence Generations	5
Convergence Threshold	0.001
Max Evaluations	1000
Max Generations	12

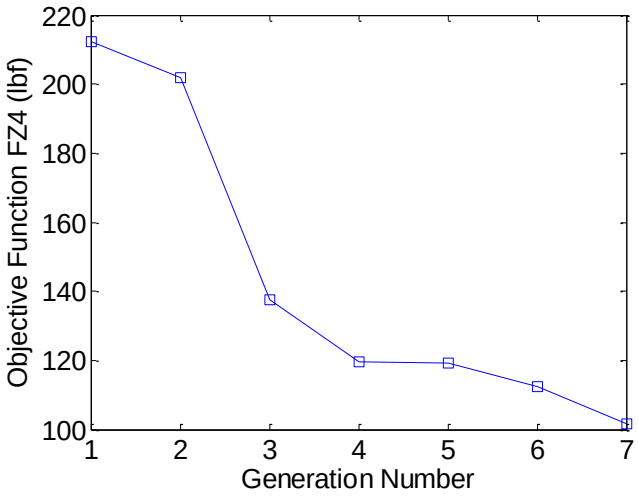

Figure 2-11: Variation of Objective Function (F_{Z4}) with Generation Number

Among the ply thicknesses, Ply 1 which is oriented at 0 deg shows the maximum increase of 34% in ply thickness. As compared to the baseline case, the most significant variation is shown by all the ply angle variables. In the optimized case, all the plies are oriented at approximately 76 deg. This is a direct result of the objective function being purely the minimization of F_{Z4} (more in the next subsection). As a result of this, there is a

48% reduction in the axial stiffness (S_{11}) and more than 60% reduction in torsional (S_{44}) and flapwise bending (S_{55}) stiffness of the blade cross section, as shown in Table 2-11. (The values listed in Table 2-11 are nondimensionalized with respect to the baseline case, that is, $\bar{S}_{ii} = (S_{ii})_{optim}/(S_{ii})_{baseline}$). The reduction in chordwise stiffness is relatively small (11%). As shown in Figure 2-13, the variation in ballast masses and their chordwise location is small, too. Also, the auxiliary spar web has moved back by 0.04c, resulting in a further decrease in cross-sectional stiffness.

Table 2-10: Design Variables and Constraints for the Optimized Case

Design variables	Baseline	Min F_{Z4}
Thickness SC Ply 1 (mil)	4.10	5.49
Thickness SC Ply 2 (mil)	3.72	3.49
Thickness SC Ply 3 (mil)	3.72	4.38
Thickness SC Ply 4 (mil)	1.00	0.89
Angle SC Ply 1 (deg)	0.00	77.37
Angle SC Ply 2 (deg)	45.00	78.76
Angle SC Ply 3 (deg)	-45.00	73.24
Angle SC Ply 4 (deg)	90.00	76.12
Aux Web Loc (%c)	6.60	10.27
Ballast mass 1 (lb/ft)	0.10	0.114
Ballast mass 1 Loc (%c)	15.00	18.50
Ballast mass 2 (lb/ft)	0.11	0.079
Ballast mass 2 Loc (%c)	16.00	0.226

Constraints	Baseline	Min F_{Z4}
CG Sec 1 (%c)	24.14	25.52
CG Sec 2 (%c)	24.1	28.38
M_{11} Sec 1 (lb/ft)	0.207	0.2323
M_{11} Sec 2 (lb/ft)	0.223	0.197
SC Sec 1 (%c)	36.5	34.62
SC Sec 2 (%c)	35.9	34.07
Tor Freq (/rev)	4.53	3.71
Max Strain (με)	2175.7	4901.0

The overall effect of these variations can be seen in the dynamic frequencies for the optimized case, which are shown in Table 2-12, where the first torsion frequency, second chordwise bending frequency, and third flapwise bending frequency have moved further away from each other. Thus, the optimization study indicates that reducing the coupling between these modes has resulted in lower vibration amplitude for F_{Z4}.

Table 2-11: Ratio of Cross-Sectional Properties for the Optimized Case

Ratio	Min F_{Z4}
$\bar{S}_{11}$	0.523
$\bar{S}_{44}$	0.377
$\bar{S}_{55}$	0.379
$\bar{S}_{66}$	0.889

Ratio	Sec 1	Sec 2
$\bar{M}_{11}$	1.096	0.882
$\bar{M}_{44}$	0.947	0.913
$\bar{M}_{55}$	1.056	1.059
$\bar{M}_{66}$	0.945	0.91

Table 2-12: Blade Structural Frequencies for the Optimized Case

Mode Shape	Frequencies (/rev)	
	Baseline	Optimized
1st chordwise bending	0.269	0.269
1st flapwise bending	1.0356	1.0356
2nd flapwise bending	2.679	2.59
1st torsion	4.57	3.72
2nd chordwise bending	4.979	5.019
3rd flapwise bending	5.48	4.44

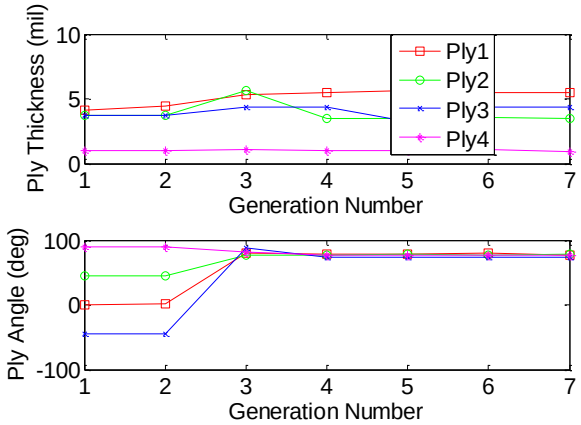

Figure 2-12: Variation of Ply Thickness and Ply Angle with Generation Number

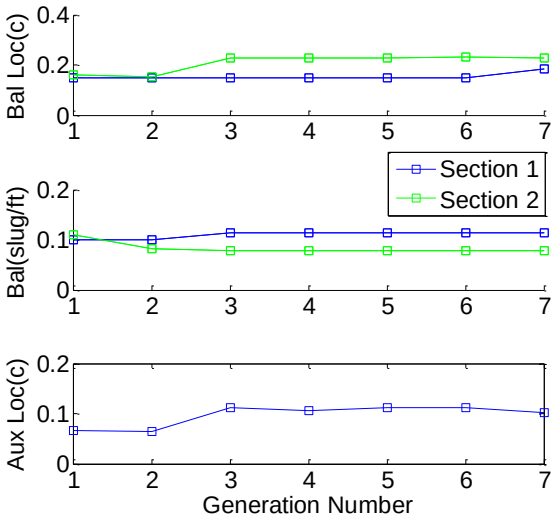

Figure 2-13: Variation of Ballast Mass and Auxiliary Spar Web with Generation Number

All the constraints used in the optimization problem are shown in Figure 2-14. The constraints are non-dimensionalized using their maximum and minimum values such that "0" represents the minimum value of the constraint while "1" represents the maximum value of the constraints. The limits for the constraints are represented by solid red lines in the plot. The results obtained indicate that only the constraint on mass per unit length for Section 2 (M_{11}-Sec 2) is closer to its lower limit while the rest of the constraints are well within the boundaries. Besides this, an increase is observed in the maximum strain for the cross section. This also indicates that the optimized solution obtained here may not be the optimum solution, and there is a possibility of finding a better solution by increasing the maximum number of generations allowed in the stopping criteria listed in Table 2-9. Since, the aim of this study was to demonstrate the robustness of the aeroelastic design environment for passive optimization studies, further iterations were not carried out.

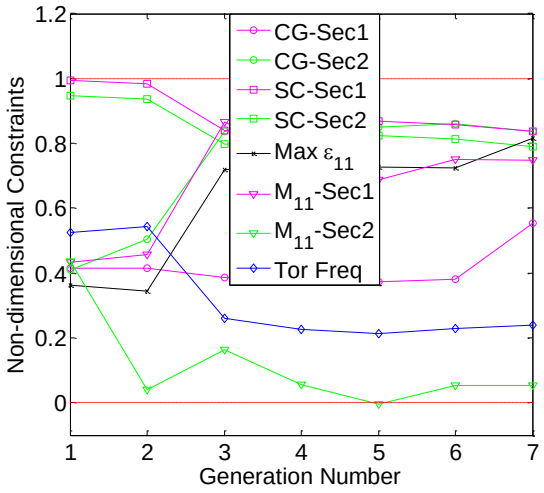

Figure 2-14: Variation of Constraints with Generation Number

In the first optimization study, only the vertical component of the 4/rev vibratory force at the rotor hub was minimized. As shown in Figure 2-15, vibration reduction in F_{Z4} is accompanied by an increase in amplitude for F_{X4}, F_{Y4}, M_{X4} and M_{Z4}. In order to reduce the vibratory loads for all the hub load components simultaneously, a different objective function was selected in the second optimization study.

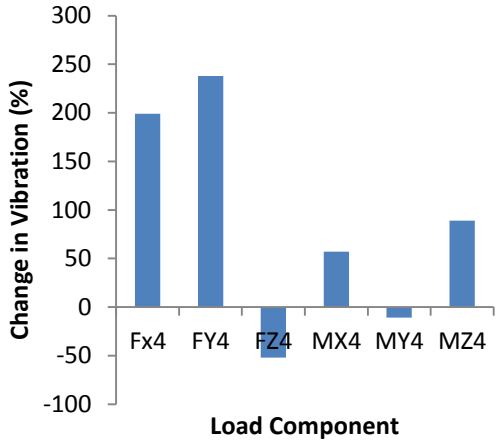

Figure 2-15: Percentage Change in Amplitude of 4/rev Vibratory Hub Load Components for the Optimized Case (min F_{Z4}) with respect to the Baseline Case

2.4.2 Minimizing Combined Vibratory Hub Load (min F_{H4})

In this case, the contributions from all the load components at the hub are included in the objective function (F_{H4}). The new objective function is defined as:

$$F_{H4} = \sqrt{{F_{X4}}^2 + {F_{Y4}}^2 + {F_{Z4}}^2} + \frac{1}{R}\sqrt{{M_{X4}}^2 + {M_{Y4}}^2 + {M_{Z4}}^2}$$

where, *R* is the radius of the rotor blade.

The optimization problem is solved using the design variables, constraints, and optimization parameters described in Table 2-7, Table 2-8 and Table 2-9, respectively. In this case, as before, the optimization process stopped after exceeding the limit on the maximum number of generations allowed. The final results show a 27% reduction in F_{H4}, as indicated in Figure 2-16. Table 2-13 shows the final optimized design for this case along with the results obtained from the "min F_{Z4}" case.

Among all the design variables, the most significant variation occurs in the thickness of Ply 2, which has almost doubled. The effect of this can be seen in the cross-sectional properties listed in Table 2-14 where the torsional stiffness of the cross section has increased by almost 24%. In spite of the increase in ply thickness, the bending and axial stiffness of the blade section has decreased due to a 15 deg change in ply angle for Ply 1. Also, there is an approximately 15% increase in the flapwise-bending inertia.

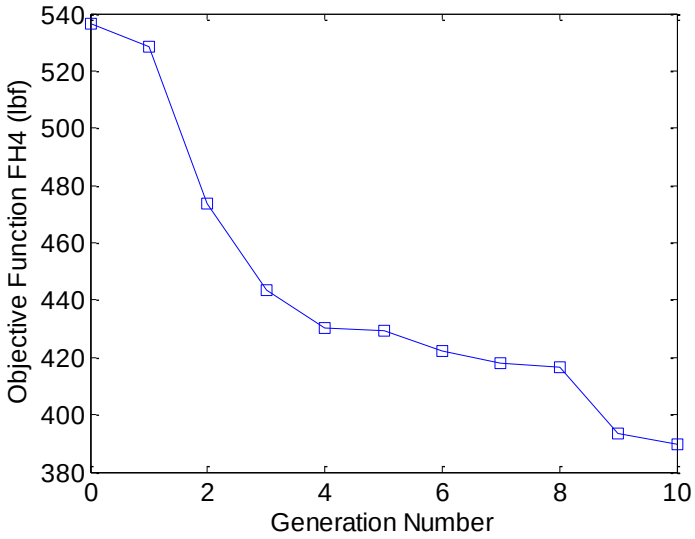

Figure 2-16: Variation of F_{H4} with Generation Number

Unlike the variation observed in the "min F_{Z4}" case for the blade structural frequencies, the dynamic frequencies for "min F_{H4}" are very close to the baseline case. As shown in Table 2-14 and Table 2-15 the increase in cross-sectional torsional stiffness is accompanied by an increase in torsional inertia, due to which the resultant increase in torsional frequency for the blade is very small. Thus, from the second optimization study, it appears that a decrease in combined vibratory load at the rotor hub can be obtained by increasing the torsional stiffness of the blade section without making any significant changes in blade dynamic properties.

The percentage reduction in 4/rev vibratory loads at the rotor hub for the "min F_{Z4}" case and "min F_{H4}" case are shown in Figure 2-17. For the "min F_{H4}" case, lower vibrations are observed for four of the six hub load components. The baseline vibration shown in Table 2-4 clearly indicates that F_{Z4}, M_{X4} and M_{Y4} have the largest contribution to the overall vibratory loads at the hub, and thus in order to reduce combined vibratory loads, it is important to reduce vibration in these components.

Table 2-13: Design Variables and Constraints for Min F_{H4}

Design variables	Baseline	Min F_{H4}	Min F_{Z4}
Thickness SC Ply 1 (mil)	4.10	4.32	5.49
Thickness SC Ply 2 (mil)	3.72	7.14	3.49
Thickness SC Ply 3 (mil)	3.72	3.89	4.38
Thickness SC Ply 4 (mil)	1.00	1.00	0.89
Angle SC Ply 1 (deg)	0.00	15.86	77.37
Angle SC Ply 2 (deg)	45.00	50.57	78.76
Angle SC Ply 3 (deg)	-45.00	-45.00	73.24
Angle SC Ply 4 (deg)	90.00	90.00	76.12
Aux Web Loc (%c)	6.60	6.60	10.27
Bal Mass 1 (slugs/ft)	0.10	0.11	0.11
Bal Mass 1 Loc (%c)	15.00	12.30	18.50
Bal Mass 2 (kg/m)	0.11	0.10	0.08
Bal Mass 2 Loc (%c)	16.00	16.03	0.23

Constraints	Baseline	Min F_{H4}	Min F_{Z4}
CG Sec 1 (%c)	24.14	22.39	25.52
CG Sec 2 (%c)	24.1	24.42	28.38
M_{11} Sec 1 (lb/ft)	0.207	0.236	0.232
M_{11} Sec 2 (lb/ft)	0.223	0.226	0.197
SC Sec 1 (%c)	36.5	36.23	34.62
SC Sec 2 (%c)	35.9	35.72	34.07
Tor Freq (/rev)	4.53	4.58	3.71
Max Strain (με)	2175.7	2471.0	4901

Table 2-14: Cross-sectional Properties for the Optimized Case (min F_{H4})

	Sec 1	Sec 2
$\bar{M}_{11}$	1.138	1.034
$\bar{M}_{44}$	1.103	1.015
$\bar{M}_{55}$	1.147	1.150
$\bar{M}_{66}$	1.102	1.012

	Sec 1
$\bar{S}_{11}$	0.934
$\bar{S}_{44}$	1.247
$\bar{S}_{55}$	0.88
$\bar{S}_{66}$	0.974

Table 2-15: Structural Frequencies for the Optimized Case

Mode Shape	Frequencies (/rev)		
	Baseline	Min F_{H4}	Min F_{Z4}
1st Chordwise bending	0.269	0.269	0.269
1st Flapwise bending	1.0356	1.036	1.0356
2nd Flapwise bending	2.679	2.650	2.59
1st Torsion	4.57	4.584	3.72
2nd Chordwise bending	4.979	4.866	5.019
3rd Flapwise bending	5.48	5.352	4.44

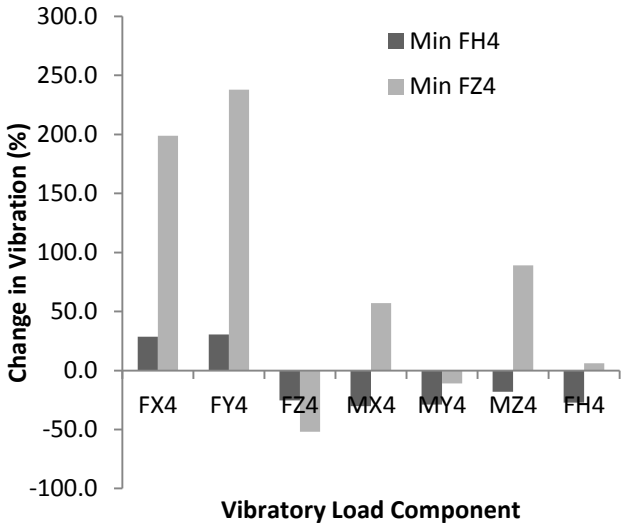

Figure 2-17: Percentage Change in Vibratory 4/rev Hub Loads for the Optimized Cases

2.5 Concluding Remarks

A powerful, easy-to-use design environment has been developed to support conceptual and preliminary rotor blade design. It integrates several well-established analysis codes from different sources: UM/VABS for cross sectional analysis, RCAS for rotorcraft simulation and ModelCenter for optimization. This design environment enables conceptual/early preliminary multidisciplinary rotor blade design, allowing rapid design

trade studies early in the design process with realistic structural properties for modern composite rotor blades. The tool supports multiple design scenarios. It can be used in a cross-section-focused structural design problem in which one might want to find a feasible structural concept and layup resulting in particular blade stiffness and mass properties or location of the elastic axis. It can also be used in a more comprehensive multidisciplinary environment including a full rotorcraft aeromechanical analysis, where the entire rotor system can be optimized with respect to objectives such as rotor performance, vibratory loads, etc. subject to aeroelastic and dynamic stability and other design constraints.

The design environment was successfully used to perform detailed parametric and optimization studies on the full scale model of a UH-60 composite rotor blade. The cross-sectional design variables which can be easily modified during the composite rotor blade manufacturing process were identified and a parametric study was conducted with each of them. This study was useful in determining the influence of each design variable on different objective functions and blade dynamic properties. Based on these studies, two different optimization cases were set up to reduce 4/rev vibratory loads at the rotor hub in the forward flight condition ($\mu = 0.24$). These optimization problems required complete cross-sectional and aeromechanic analysis of the rotor blade. The results obtained from these studies showed:

a) 52% vibration reduction in F_{Z4} (Objective function: min F_{Z4})

b) 28% vibration reduction in F_{H4} (Objective function: min F_{H4})

where, F_{Z4} is the amplitude of the 4/rev vibratory vertical force at the hub and F_{H4} is the amplitude of the combined 4/rev vibratory load at the hub.

Chapter 3. Optimization Framework for the Dynamic Analysis and Design of Active Twist Rotors

This chapter presents the development of an optimization strategy/framework for the aeroelastic analysis and design of active twist rotors. The active twist is generated by piezoelectric material in the form of Active Fiber Composite (AFC) or Macro Fiber Composite (MFC) embedded in the blade cross section. Proper tailoring of the blade properties can lead to the maximization of the active twist authority under operating conditions. Thus, using mathematical optimization, the cross-sectional layout is designed for an active composite rotor blade to maximize the dynamic active twist while satisfying a series of constraints on blade cross section parameters, stiffness and strength. The dynamic twist is defined as the amplitude of twist obtained at the blade tip when the active plies are actuated in rotating conditions. The optimization problem is solved using a surrogate-based approach in which the "true" objective function and constraints are replaced with computationally efficient functional relationships. Since approximation errors can lead to sub-optimal solutions, the Efficient Global Optimization (EGO) algorithm, which accounts for uncertainty in surrogate predictions, is employed.

The objectives of the work presented here are:

1) Develop the optimization strategy and framework for the dynamic analysis and design of active twist rotor blades;
2) Demonstrate the impact of the new design strategy using existing results available in literature for maximizing static twist per unit length;

3) Exemplify the optimization framework by maximizing the amplitude of tip twist for 4/rev actuation in hover conditions; and

4) Perform optimization at a range of actuation frequencies.

3.1 Optimization Framework

The basic flow diagram of the new optimization framework that implements the strategy described above is shown in Figure 3-1. It consists of two main parts: a) the ModelCenter-based structural/aeromechanical analysis of active twist rotors, and b) the surrogate-based optimization with the Efficient Global Optimization (EGO) algorithm [159]. By replacing the high-fidelity analyses with surrogates, a significant increase in the robustness of the process is achieved. A description of each of these two main parts is presented below.

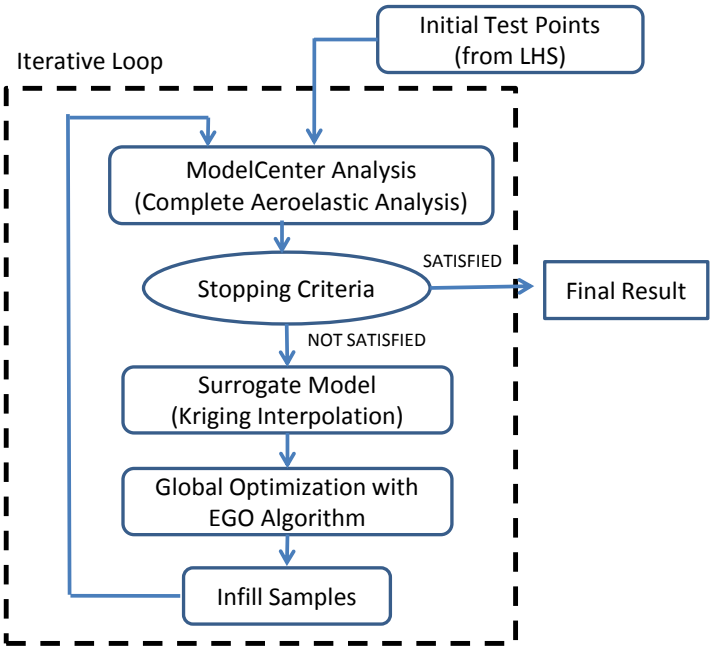

Figure 3-1: Optimization Framework for Designing Active Twist Rotor Blades

3.1.1 High-Fidelity Analysis Framework

The aeromechanic analysis approach described in Figure 3-2 is a modified version of the work presented Chapter 2 (in Figure 2-3), but now accounting for the presence of active materials embedded in the blades. In the current analysis, UM/VABS also provides actuation forces/moments produced by embedded active material to be used in blade (beam) analysis. The magnitude of the active twisting moment determined using UM/VABS is used as the amplitude of the external twisting moment applied to nodes of the blade in the RCAS beam model. Although the active plies generate all the components of forces and moments [70], it was observed during the preliminary analysis that only twisting moment is the critical one. The frequency and phase of the twisting moment are provided by the user or the optimizer. In turn, RCAS evaluates the blade dynamic twist response for the prescribed frequency range, which will be used as the objective function.

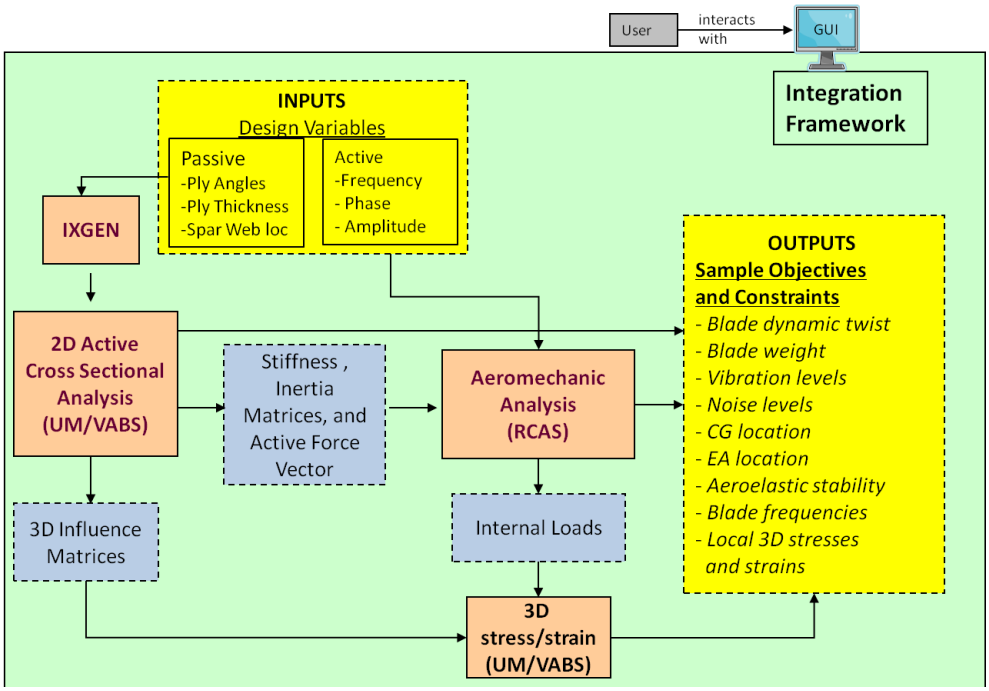

Figure 3-2: Analysis Framework for Active Twist Rotors

3.1.2 Surrogate-based Optimization

The goal of using surrogate method [160, 161] is to replace the true objective function and constraints with smooth functional relationships of acceptable fidelity that can be evaluated quickly. To form the surrogate, the objective function must first be evaluated over an initial set of design points. The surrogate is then generated by interpolating the initial design points. Although function evaluations coming from the expensive aeroelastic simulation are needed to form the approximation, this initial investment of computer time is significantly less than that needed in a global search using non-surrogate based optimization methods. Once the surrogates have been created, they can be used to replace the more expensive "true" objective function in the search process for the global optimum. Moreover, experience shows that for some parameter combinations of design variables, RCAS analysis does not converge. Therefore, few missing points in the construction of the surrogates due to failed RCAS runs do not significantly impact accuracy of the surrogates and the ability of the surrogate-based optimization process to determine the optimum solution. The increased robustness of the process has a direct impact on the ability to completely explore the entire design space. In this study, the objective function and constraints used in the optimization are replaced by surrogates. Detailed description of the surrogate based modeling technique used in this thesis is provided in Appendix A.

The MATLAB's Latin hypercube sampling function "*lhsdesign"* was used to generate the space-filling design of experiments used in this study. The points in the Latin hypercube represent design points at which complete aeroelastic helicopter simulations are to be conducted. Once an initial set of fitting points has been produced, kriging

interpolation [162] is used to create the surrogate for the objective function and constraints. Kriging interpolation is well suited to approximating nonlinear functions, and does not require a priori assumptions on the form of the function that is to be approximated. In kriging, the unknown function of interest, *y(x)*, is assumed to be a random variable of the form:

$$y(x) = g(x) + Z(x)$$

where *g(x)* is an assumed function (usually a low-order polynomial) and *Z(x)* is a stochastic (random) process. The kriging surrogates were created with an available MATLAB toolbox [163].

Once the surrogate objective function is created using kriging, a potential method for finding the optimum is to optimize the surrogate directly, that is, the "one-shot" approach. However, if the surrogate is not accurate everywhere in the design space, the optimization may lead to local optima. Therefore, it is desirable to account for the uncertainty in the surrogate model since promising designs could lie in regions where the surrogate is inaccurate. After the first few iterations (2 to 4 iterations) during the optimization process, it was observed that the EGO algorithm was not able to provide further improvement to the objective function, and hence, the objective function predicted by the surrogate model was maximized directly for the next two iterations.

3.1.3 EGO Algorithm

The Efficient Global Optimization (EGO) algorithm [159] is an alternative to the "one-shot" approach which accounts for uncertainty in the surrogate and is more efficient. The effectiveness of the EGO algorithm for passive design of helicopter rotors

for vibration reduction was demonstrated in [164]. In EGO, a small number of initial design points are used to fit a kriging approximation. Based on the stochastic nature of kriging, an expected improvement function (EIF) is created in order to facilitate the selection of additional sample points (infill samples) where expensive computer simulations are to be conducted. These sample points are chosen where there is a high probability of producing a superior design over the current best design and/or where the predictions of the surrogate are unreliable due to a high amount of uncertainty. These infill samples represent a balance between the local consideration of finding an optimal design based on the information in the surrogate, and the global consideration of sampling in the design space where there is much uncertainty in the surrogate's predictions. Therefore, the EGO algorithm is able to adapt to potential errors in the approximate objective function by sampling at points at which there is much uncertainty in the surrogate's predictions. The kriging model is revised after the additional sample data is added to the initial data set, and the process of choosing additional sample points is repeated until a user defined criterion is satisfied. In summary, the advantages of such a method over the "one-shot" approach are: (1) a global search is conducted by sampling in regions with high uncertainty in the surrogate, and (2) fewer expensive function evaluations are required since a smaller initial sample set is used and additional sample points are selected in a more "intelligent" manner, as opposed to starting with a larger initial data set.

3.2 Numerical Studies

In the following sections, numerical studies of the new design strategy and framework are presented. They are exercised using the original NASA/Army/MIT Active Twist Rotor blade as the baseline case as described next.

The NASA/Army/MIT Active Twist Rotor (ATR) [65, 165] was originally designed to study the effects of twist actuation on vibration and noise reduction and performance improvement in helicopter rotors. The 9-ft-diameter, four-bladed rotor was tested at NASA LaRC's Transonic Dynamics Tunnel and was the first-of-a-kind system to demonstrate vibration reduction using embedded AFC in open and closed loop forward flight conditions [69]. This particular rotor blade was chosen for this study due to its known properties and available experimental and computational results [68]. Figure 3-3 shows the planform view of the blade and its corresponding dimensions. The airfoil for this blade is the NACA 0012 and it is uniform along the blade radius. The reference cross-sectional layup is shown in Figure 3-4, while Table 3-1 lists the ply angles for all the plies used in the cross section of the rotor blade. Among the plies used, E-Glass is bidirectional while, S-Glass and AFC plies are unidirectional. The specific material properties can be found in Table 3-2.

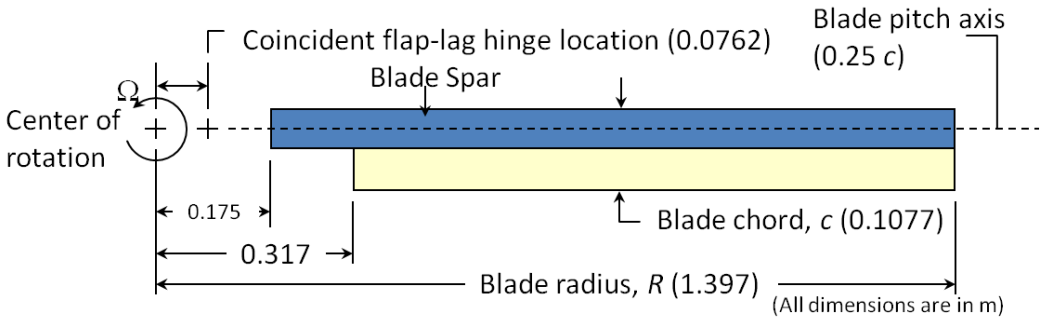

Figure 3-3: Planform View of the ATR Rotor Blade (Dimensions in Meters) [62]

The characteristic properties of the baseline ATR blade and its structural frequencies at 100% RPM are listed in Table 3-3. Blade structural frequencies in vacuum were obtained using RCAS. For the rotor dynamic analysis, the trim option (wind tunnel trim) is included in the RCAS model. The trim targets used in the analysis are: $C_T = 0.0066$, no cyclic moments ($M_x = 0$ and $M_y = 0$), and the blade pitch settings are used as the trim variables. (Note that the value of C_T used in the numerical analyses performed here is the same as that obtained in the experimental analysis presented in [69].) The mean value of the hub loads and the amplitude of the 4/rev component of the hub loads in the fixed system for the baseline blade (with no twist actuation) at an advance ratio of 0.24 are given in Table 3-4 where F_x, F_y, and F_z represent the components of the hub force in the non-rotating frame, while M_x, M_y, and M_z represent the components of the moments at the hub.

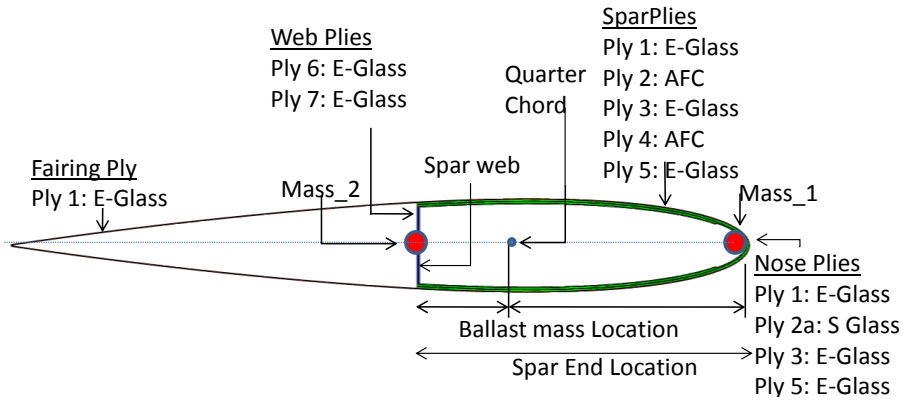

Figure 3-4: Cross-Sectional Shape of the Rotor Blade (NACA 0012 Airfoil)

Table 3-1: Baseline ATR Cross Section Ply Angles

Ply #	Angle	Ply #	Angle
Ply 1	0/90	Ply 6	0/90
Ply 2	45	Ply 7	0/90
Ply 2a	0		
Ply 3	±45		
Ply 4	-45		
Ply 5	0/90		

Table 3-2: Material Properties

	E-Glass	S-Glass	AFC
Thickness (μm)	114.3	230	200
Density (kg/m^3)	1720	1860	4060
E_{11} (GPa)	20.7	43.4	30.2
E_{22} (GPa)	20.7	12	14.9
E_{33} (GPa)	20.7	12	14.9
G_{12} (GPa)	4.1	3.6	5.13
G_{13} (GPa)	4.1	3.6	5.13
G_{23} (GPa)	4.1	3.6	5.13
ν_{12}	0.13	0.28	0.454
ν_{13}	0.13	0.28	0.454
ν_{23}	0.3	0.3	0.3

Table 3-3: Characteristics of the Baseline ATR

Rotor Type	Fully Articulated
Number of blades	4
Blade radius (R)	1.397 m
Blade Chord (c)	0.1077 m
Airfoil Section	NACA 0012
Blade Pretwist	-10 deg
Hinge Offset	0.0762 m
Rotor Speed	687.5 RPM
C_T	0.0066
Air density	2.42 kg/m^3

Mode Shape	Frequency (/rev)
1st Chordwise bending	0.29
1st Flapwise bending	1.04
2nd Flapwise bending	2.78
3rd Flapwise bending	5.34
2nd Chordwise bending	5.76
1st Torsion	6.51

Table 3-4: Hub Loads for the Baseline ATR Case (μ = 0.24)

	Mean Values	4/rev Amp
F_x (N)	8.85	1.38
F_y (N)	13.39	2.04
F_z (N)	990.7	23.56
M_x (Nm)	0.44	40.52
M_y (Nm)	1.19	36.24
M_z (Nm)	47.41	1.06

3.3 Optimization Results

Optimization studies were conducted to maximize the static twist per unit length (twist rate obtained when a constant DC voltage is given to active plies) and to maximize the dynamic tip twist amplitude (amplitude of tip twist obtained when a sinusoidal input voltage is given to active plies at a fixed actuation frequency) in hover conditions (μ = 0.0) with wind tunnel trim. The cases considered in this chapter are similar to the static twist optimization cases presented in [86]. This was done to verify the results obtained for static case using the current framework. For all the active twist optimization studies presented in this thesis, the amplitude of actuation voltage was fixed at 1000V.

For the results presented in this chapter, only six design variables were used, namely, the chordwise location of the main spar web, the chordwise ending location of the spar/AFC plies, and the magnitude (m_1,m_2) and location (x_1,x_2) of the ballast masses. The design variables used in the current study and their upper and lower bounds are listed in Table 3-5, while the constraints used are given in Table 3-6. For all the variables, the initial value and the bounds used were the same as in [86], whenever they were available. For the remaining cases, reasonable values were used for bounds such that the optimization process was not affected.

Table 3-5: Design Variable Used for Optimization Study

Design variables	Baseline	Min	Max
Main Spar Loc (c)	0.443	0.2	0.85
Spar End (c)	0.443	0.2	0.85
Ballast Mass 1 (m_1) (kg/m)	0.222	0	0.5
Ballast Mass 1 Loc (x_1) (c)	0.443	0	0.8
Ballast Mass 2 (m_2) (kg/m)	0.23	0	0.5
Ballast Mass 2 Loc (x_2) (c)	0.02	0	0.8

Table 3-6: Constraints used in Optimization

Constraints	Baseline	Max	Min
SC (%c)	20.95	25	17
CG (%c)	24.3	28	20
M_{11} (kg/m)	0.677	0.65	0.72
1^{st} Tor Freq (/rev)	6.51	4.5	8
Max $\|\varepsilon_{11}\|$ ($\mu\varepsilon$)	2747	6000	0
Max $\|\varepsilon_{12}\|$ ($\mu\varepsilon$)	3807	6000	0

3.3.1 Construction and Verification of the Surrogate Models

For each of the constraints and objective function considered, a surrogate model was developed using MATLAB's kriging toolbox described above. To test the surrogate model, a sample of 30 test points (different from those used to construct the surrogate) was generated. The complete aeroelastic simulation was performed for those 30 cases and the results obtained were compared with those obtained from the surrogate model. The values of average error, maximum error and standard deviation of the error obtained from this analysis are shown in Table 3-7. Results show that the surrogate model prediction for static twist, CG location, and mass per unit length are very accurate. For other cases, the mean value of the error is less than 12%. However, for all the cases, it was observed that the surrogate model was able to capture well the qualitative trends of the problem.

Table 3-7: Error Obtained in the Prediction of Design Variable and Constraints for Surrogate models

Percentage Error (%)

Variable	Mean	Max	Std Dev
$\theta_{dyn,4/rev}$	11.77	43.06	9.34
θ_{stat}	0.93	2.01	0.55
CG	0.39	0.81	0.22
SC	8.65	46.78	10.67
1^{st} Tor Freq	9.54	19.35	5.47
ε_{11}	6.83	26.72	5.82
M_{11}	0.01	0.05	0.03
ε_{12}	10.17	34.78	9.41

3.3.2 Optimization Cases

3.3.2.1 Static Twist Optimization (Max θ_{stat})

To verify the framework, one of the cases presented in [86] is studied first. In this case, the static twist per unit length (θ_{stat}) obtained from the cross-sectional analysis was defined as the objective function. Final results are compared with those in [86] and are summarized in Table 3-8. It should be noted that the constraints shown in Table 3-8 are non-dimensionalized such that a value of "0" represents their lower bound while a value of "1" represents their upper bound.

The final result obtained for the "Max θ_{stat}" case is very close to that obtained in [86]. It can be seen that in both the cases, there is an increase in mass per unit length due to the increase in length of the active plies used in the cross section. This is also accompanied by a simultaneous increase in torsional stiffness of the cross section. However, the increase in torsional stiffness is less when compared to the increase in torsional inertia that occurs due to addition of the plies and the relocation of the ballast masses further

away from the reference axis (quarter chord). Thus, the optimized results in both cases show an overall decrease in torsional frequency. The vertical spar web in both results is located very close to the half chord. The only dissimilarity between the two sets of results lies in the location of ballast masses and the chordwise location of the CG.

Table 3-8: Static Twist Optimization Result

	Max θ_{stat}	Ref. [86]	Baseline
θ_{stat} (deg/m)	1.59	NA	1.34
% Increase	**18.6**	**19.0**	-
Non-Dimensional Constraints			
1^{st} Tor Freq	0.349	0.353	0.738
M_{11}	0.965	0.714	0.486
SC	0.32	0.25	0.21
Max ε_{11}	0.516	NA	0.458
Max ε_{12}	0.690	NA	0.635
CG	0.655	0.475	0.493
Design Variables			
m_1 (kg/m)	0.001	NA	0.222
x_1 (c)	0.793	0.418	0.443
m_2 (kg/m)	0.311	NA	0.23
x_2 (c)	0.006	0.045	0.02
Spar Web (c)	0.521	0.49	0.443
Spar End (c)	0.838	0.85	0.443

NA: Not Available

3.3.2.2 Dynamic Twist Optimization (Max $\theta_{dyn,4/rev}$)

In this case, the amplitude of dynamic twist at the blade tip ($\theta_{dyn,4/rev}$) was maximized for a 4/rev actuation frequency. In the preliminary analysis that was carried out with the baseline case, it was observed that the amplitude of dynamic twist does not vary significantly with advance ratio. Thus to avoid unnecessary calculations, the flow was set for hover conditions ($\mu = 0.0$). In order to make sure that this is indeed the cases for the optimized cases, aeroelastic analysis was performed in forward flight condition in Section

3.7. In the results shown in Table 3-9, it can be seen that the case with maximum static twist does not coincide with the case with maximum dynamic twist. The case with maximum static twist shows an increase of 57% in dynamic twist, while the case optimized for maximum dynamic twist shows an increase of 63%. Also, the amount of active material used in "Max $\theta_{dyn,4/rev}$" case is 20% less than that used in "Max θ_{stat}" case. In the "Max $\theta_{dyn,4/rev}$" case, the spar plies (which includes AFC plies) end at 0.68c while in case of "Max θ_{stat}", spar plies extend to 0.85c. In both "Max θ_{stat}" and "Max $\theta_{dyn,4/rev}$" cases, there is a decrease in torsional frequency; however, the decrease is more pronounced in "Max $\theta_{dyn,4/rev}$" case. The shear center for "Max $\theta_{dyn,4/rev}$" case is very close to its lower limit, implying that it is a critical constraint for dynamic twist optimization. The total ballast mass used in "Max $\theta_{dyn,4/rev}$" case is more than that used in "Max θ_{stat}" case and it is distributed further away from the reference axis, resulting in higher torsional inertia.

Thus, in the "Max $\theta_{dyn,4/rev}$" case, higher dynamic tip twist is obtained when compared to the baseline ATR design due to increase in active ply coverage used in the cross section and dynamic tuning of the blade properties. The shape of the blade cross section for the baseline case and the optimized cases are shown in Figure 3-5. The ballast masses used in the cross section are represented by "blue" and "red" circles.

Table 3-9: Dynamic Optimization Results

	Max θ_{stat}	Max $\theta_{dyn,4/rev}$	Baseline
θ_{stat} (deg/m)	1.59	1.46	1.34
% Increase	18.6	8.94	-
$\theta_{dyn,4/rev}$ (deg)	3.45	3.58	2.19
% increase	**57.6**	**63.6**	-
Non-Dimensional Constraints			
1st Tor Freq	0.349	0.253	0.738
M_{11}	0.965	0.513	0.486
SC	0.320	0.127	0.214
Max ε_{11}	0.516	0.485	0.458
Max ε_{12}	0.690	0.657	0.635
CG	0.655	0.976	0.493
Design Variables			
m_1 (kg/m)	0.001	0.066	0.222
x_1 (c)	0.793	0.764	0.443
m_2 (kg/m)	0.311	0.282	0.23
x_2 (c)	0.006	0.005	0.02
Spar Web (c)	0.520	0.488	0.443
Spar End (c)	0.838	0.682	0.443

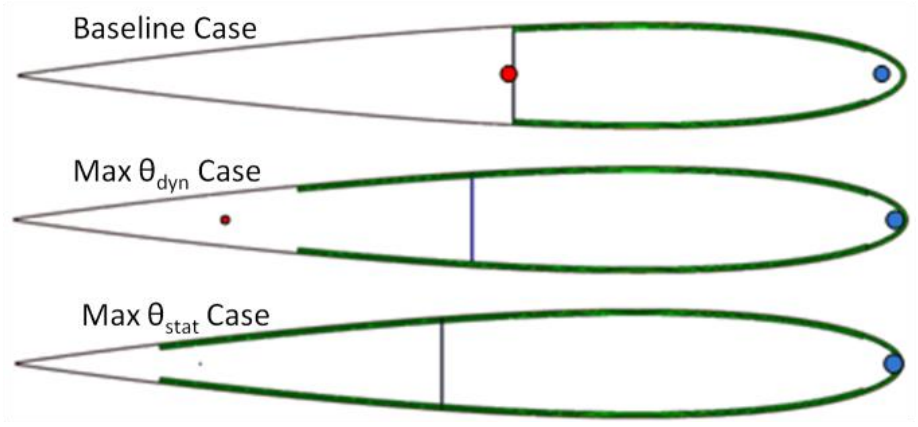

Figure 3-5: Baseline and the Optimized Cross Sections

3.3.3 Analysis of Optimized Results

3.3.3.1 Relation between blade twist and induced F_{Z4}

To determine the relation between static tip twist, dynamic tip twist, and 4/rev vertical hub shear (F_{Z4}) induced by the twist actuation in hover condition, results obtained for all the iterations (during the optimization process) that satisfy all the constraints were plotted in order of increasing static twist in Figure 3-6, and in order of increasing dynamic twist in Figure 3-7. Note that for the hover condition, "Induced F_{Z4}" is a measure of control authority of the active twist actuation. Hence, in order to maximize the control authority, it is desired to maximize induced F_{Z4}. The dashed black lines in both the figures correspond to the baseline results. Here, it can be clearly seen that an increase in static tip twist may not always result in an increase in dynamic tip twist and induced F_{Z4}. However, an increase in dynamic tip twist amplitude results in a proportional increase in F_{Z4} amplitude. Thus, the F_{Z4} induced at the rotor hub by actuation of the embedded active material inside the blade cross section is proportional to the dynamic tip twist amplitude of the blade.

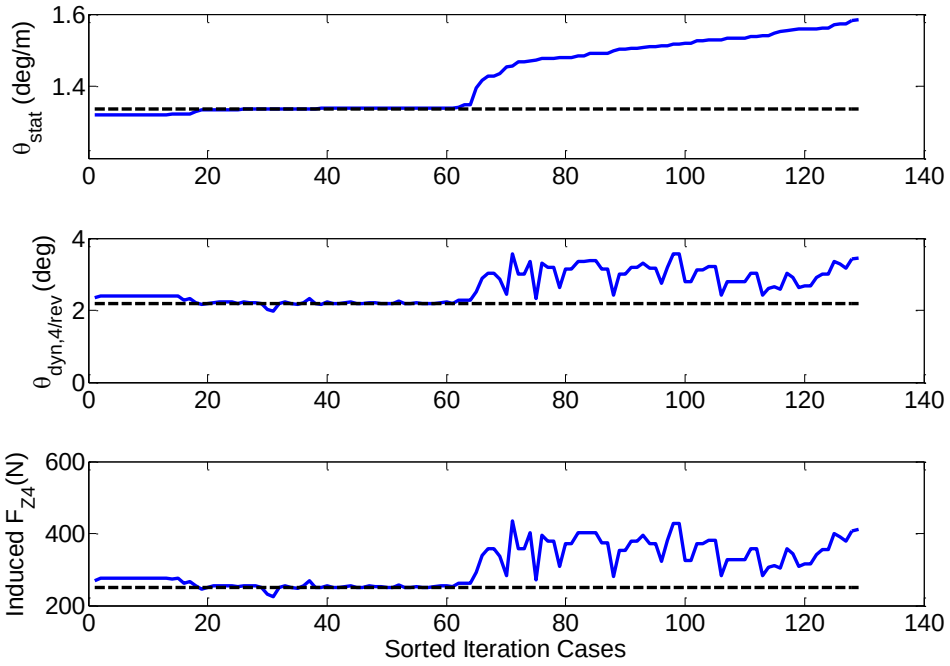

Figure 3-6: Objective Function Results in Order of Increasing Static Twist

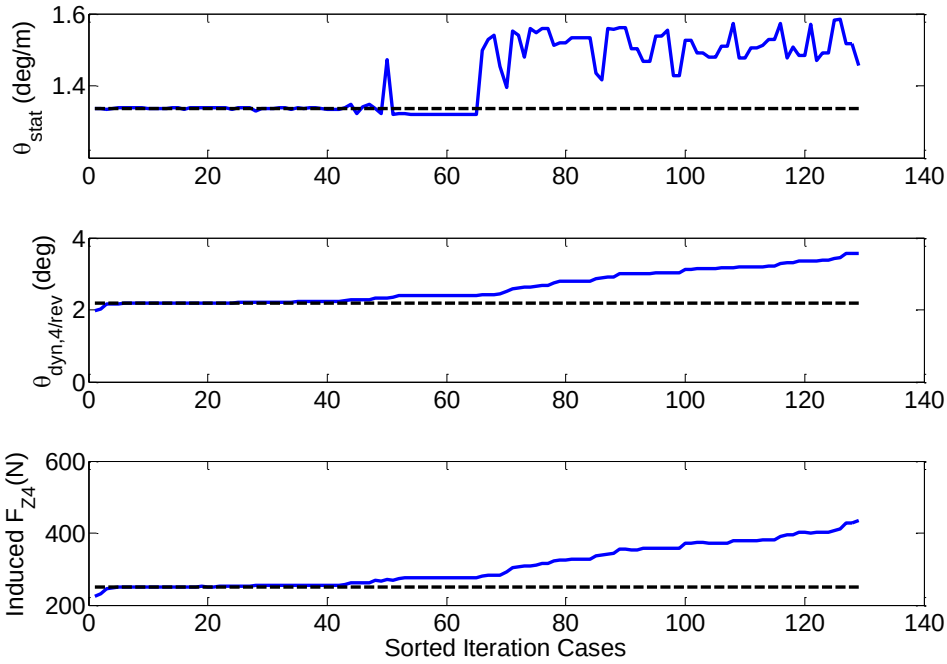

Figure 3-7: Objective Function Results in Order of Increasing Dynamic Twist

3.3.3.2 Effect of Frequency of Actuation

In the next step, frequency of actuation was varied for all three cases, namely, baseline case, maximum static twist case (Max θ_{stat}), and maximum dynamic twist case (Max $\theta_{dyn,4/rev}$) at $\mu = 0.0$. Results described in Figure 3-8 show that the "Max $\theta_{dyn,4/rev}$" case consistently provides maximum dynamic tip twist as compared to the other two cases, except at the 5/rev actuation case. This is due to the fact that "Max $\theta_{dyn,4/rev}$" case is optimized for 4/rev twist actuation frequency. Figure 3-9 shows effect of frequency of actuation on amplitude of vertical displacement at the blade tip, which shows similar behavior as was observed for tip twist. The only difference is that all the cases here show a peak close to 3/rev frequency that coincides with the blade second flapwise bending frequency.

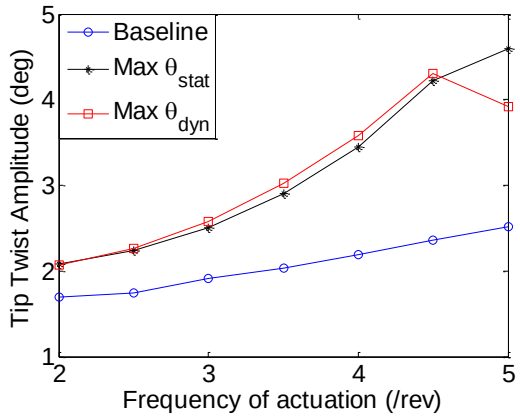

Figure 3-8: Effect of Frequency on Dynamic Twist

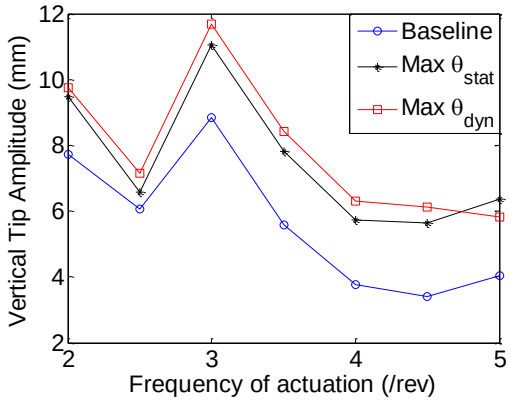

Figure 3-9: Effect of Frequency on Amplitude of Vertical Tip Displacement

3.3.3.3 Effect on Vibratory Loads in Forward Flight Conditions for Zero Twist Actuation

The blade designs obtained from the surrogate optimization for "Max $\theta_{dyn,4/rev}$" and "Max θ_{stat}" cases have different dynamic properties as compared to the baseline one. Even though the optimized cases have higher twist actuation and, therefore, higher control authority for vibration reduction using active twist actuation, it is desired to know the vibratory characteristics of each design in the absence of any twist actuation. Thus, in order to determine the baseline vibratory loads in forward flight conditions, all three cases were run at an advance ratio of 0.24 with wind tunnel trim, and 4/rev vibratory loads at the hub were determined. The percentage increase in vibratory loads for "Max $\theta_{dyn,4/rev}$" and "Max θ_{stat}" cases is shown in Figure 3-10. (Since the RCAS model used in *this* analysis did not include the free wake mode for capturing BVI effects and a dynamic stall model to account for the dynamic stall effects, an advance ratio of 0.24 was used to minimize contribution from BVI and dynamic stall effects).

Results show a 10% increase in F_{Z4} and a 15% increase in M_{Y4} for "Max $\theta_{dyn,4/rev}$" case and a 7-8% increase in F_{Z4} and M_{Y4} for "Max θ_{stat}" case. Although the F_{Y4} component

shows a higher percentage increase, results presented in Table 3-4 show that the amplitude of vibration for the F_{Y4} component is very small. The increase in vibration for the optimized cases can be attributed to the decrease in torsional frequency.

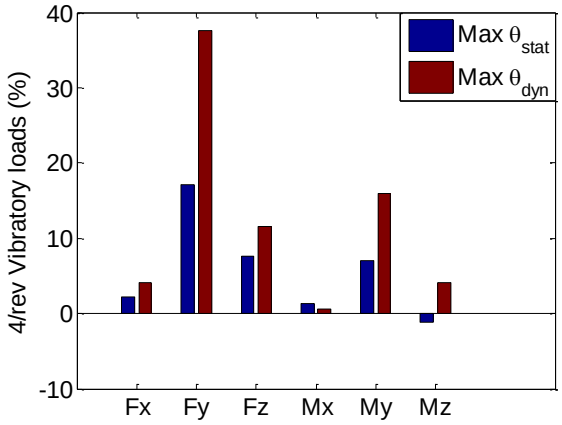

Figure 3-10: Percentage Increase in 4/rev Vibratory Loads at the Rotor Hub with no Actuation at μ = 0.24

3.3.3.4 Circle Plot for the Optimized Results

The circle plots for 4/rev vibratory loads at the rotor hub at μ=0.24 were obtained for all the hub load components. In this analysis, the phase angle of actuation was varied, while the frequency of actuation was kept constant at 4/rev. Figure 3-11 and Figure 3-12 show circle plots obtained for F_{Z4} and M_{Y4} (4/rev component of the shear force and lateral cyclic moment at the rotor hub, respectively). In these figures, non-actuated vibratory loads (loads in the absence of twist actuation) for each of the cases are represented by "x" while the origin is represented by "*". The straight line drawn in these plots joins the non-actuated vibratory load to vibratory load corresponding to 0-deg phase actuation for each of the cases.

As it is shown in Figure 3-10, baseline vibratory loads for each of the cases considered are very close to each other. From the obtained circle plots, it can be concluded that the "Max $\theta_{dyn,4/rev}$" case provides maximum control authority for vibration reduction. Since the current analysis is done for μ =0.24, the baseline F_{Z4} load is small and very small twist actuation is required to reduce F_{Z4} to zero. However, in case of the M_{Y4} component, larger twist actuation is required to minimize the vibratory loads. Similar analysis can be conducted at different advance ratios.

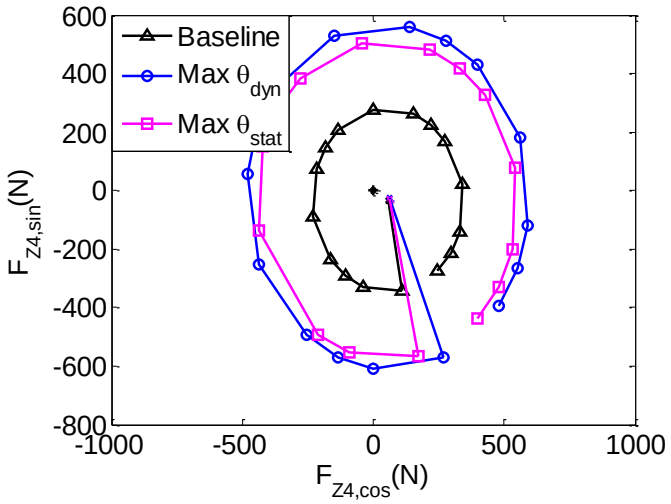

Figure 3-11: Vibratory Hub Vertical Shear Force (μ = 0.24)

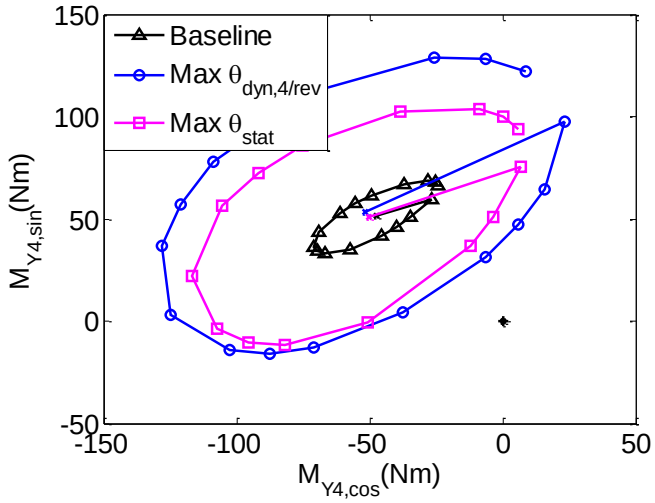

Figure 3-12: Vibratory Hub Lateral Cyclic Moment (μ = 0.24)

3.3.3.5 Effect of Aeromechanic Analysis on Optimized Results

The analysis performed until now for dynamic twist optimization included trim option (wind tunnel trim) for aeroelastic analysis. This was done so that the blade experiences accurate aerodynamic loads. However, the trim analysis is very time consuming and each run in RCAS takes 15-20 min for a complete aeroelastic analysis. As a result, following two simplifications were considered to the analysis:

Case 1: Periodic Analysis: In this case, the pitch settings are kept constant and a periodic solution is obtained. The rest of the analysis variables are kept the same. Thus, the blade experiences similar aerodynamic stiffness (aerodynamic forces per unit blade twist) as in the trim cases but the magnitude of aerodynamic loads is small since the initial pitch settings used are very close to zero. The computation time (on an Intel Core 2 Quad CPU@2.40 GHz) required for a "Periodic Analysis" (~ 1 min) is an order of magnitude less than the computational time required for the "Trim Analysis" (~15 min). The "Periodic Analysis" can only be used to approximate the amplitude of blade deformation due to actuation of on-blade active devices. The amplitude and mean value of tip twist for active twist actuation at 3, 4 and 5/rev actuation frequencies for the baseline ATR blade at $\mu = 0.0$ are shown in Figure 3-13. As show in Figure 3-13, the amplitude of tip twist predicted by "Trim Analysis" and "Periodic Analysis" are very close to each other, however there is a significant difference in the mean value of tip twist predicted by the two analyses.

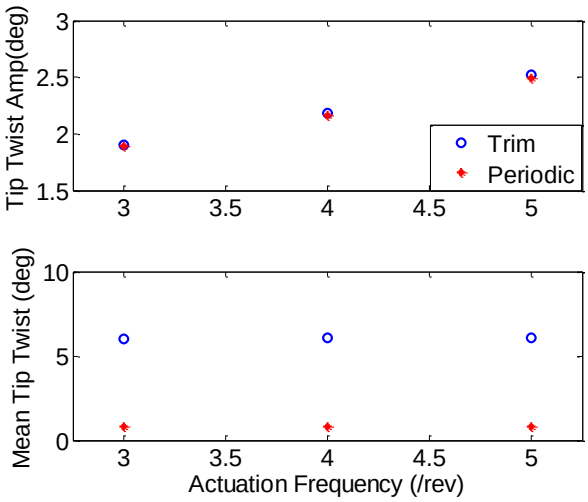

Figure 3-13: Variation of Mean Value and Amplitude of Tip Twist for twist actuation at μ=0.0

Case 2: Low density analysis: In this case, a periodic solution is obtained, as in Case 1, but the density of the medium is reduced significantly (from 2.42kg/m^3 to 0.3kg/m^3). Thus, the aerodynamic stiffness is much smaller (almost an order of magnitude reduction) in this case. This analysis was done to check if the optimization study can be done in vacuum (without aerodynamic loads).

The design variables and the constraints used in the optimization are the same as in the earlier study. In both these cases, the blade does not experience complete aerodynamic loads as it would experience in a trim analysis. As a result, the constraints on the cross-sectional strains were removed. As expected, the strains observed during these studies were well below their upper bound for all the cases.

The values of dynamic twist obtained for each of the cases are shown in Table 3-10. At the end of optimization process, it was observed that the optimized case obtained from trim analysis and the optimized case obtained from periodic analysis is the same and is referred as "Max $\theta_{dyn,4/rev,T/P}$" case. The optimized result obtained from analysis at low

density medium is referred as "Max $\theta_{dyn,4/rev,low\ \rho}$" case, while the case corresponding to maximum static twist per unit length is denoted "Max θ_{stat}" as before. Results also show how each case performs in different analysis conditions. (Note that the optimized solution obtained for "Max $\theta_{dyn,4/rev,T/P}$" and "Max θ_{stat}" cases in the current analysis are slightly better than the optimized solution obtained for the Max θ_{stat} and Max $\theta_{dyn,4/rev}$ case in Section 3.3.2.1 and Section 3.3.2.2, respectively.)

Table 3-10: Optimized Results

	Static Twist	Dynamic Twist		
	(deg)	Trim Analysis (deg)	Periodic Analysis (deg)	Low ρ Analysis (deg)
Baseline Case	1.34	2.19	2.17	2.37
Max $\theta_{dyn,4/rev,T/P}$ Case	1.42	4.16	4.00	5.90
Percentage Increase (%)	5.82	**90.20**	**84.42**	148.97
Max $\theta_{dyn,4/rev,low\ \rho}$ Case	1.40	3.99	3.89	6.98
Percentage Increase (%)	4.89	82.55	79.33	**194.74**
Max θ_{stat} Case	1.61	3.91	3.80	4.18
Percentage Increase (%)	**20.02**	78.99	75.51	76.43

The maximum increase obtained in static twist per unit length is 20%. For this case, the increase in dynamic twist is significant but less than the optimal. The "Max $\theta_{dyn,4rev,T/P}$" case shows a maximum increase of 90% in dynamic twist in aerodynamic conditions with trim. Although the trim analysis and periodic analysis have the same optimized result, the dynamic twist corresponding to these analyses are slightly different (~4%). During the optimization, it was observed that the dynamic twist obtained from trim analysis was consistently higher than that obtained from periodic analysis, but the difference between them is small. The "Max $\theta_{dyn,4rev,\ low\ \rho}$" case shows an increase of 194% in tip twist amplitude in low density analysis, which corresponds to approximately

80% increase in twist amplitude in trim and periodic analysis. Also, it should be noted that the dynamically optimized cases have only 5-6% higher static twist per unit length as compared to the baseline case. Thus, the increase in dynamic twist is due to tailoring of the dynamic properties of the rotor blade.

Table 3-11: Optimization Constraints and Other Parameters

Constraints	Baseline Case	Max $\theta_{dyn,4rev,T/P}$ Case	Max $\theta_{dyn,4rev,low\ \rho}$ Case	Max θ_{stat} Case
1st Tor Freq (/rev)	6.34	4.60	4.51	5.199
M_{11} (kg/m)	0.68	0.70	0.712	0.710
SC (%c)	18.71	20.75	17.49	17.01
CG (%c)	23.95	27.47	25.06	27.06
Other parameters				
S_{44} (Nm^2)	37.71	44.32	41.46	50.47
Act Mom M_x (Nm)	0.91	1.12	1.07	1.48
2nd Flap Freq (/rev)	2.76	2.79	2.79	2.82

The values of the constraints for the optimized cases are shown in Table 3-11. All the cases show a decrease in the torsional frequency in spite of an increase in the cross-sectional torsional stiffness. This occurs due to the redistribution of ballast masses such that there is a net increase in the torsional inertia for the blade cross section. Also, for the dynamically optimized cases, the first torsional frequency is very close to the lower bound of the 1st torsion frequency and the actuation frequency of 4/rev. For the Max $\theta_{dyn,4/rev,low\rho}$ case, the torsion frequency is exactly at the lower bound, implying that the optimization at low density is driven mainly by the constraint on the 1st torsion frequency and the optimizer tries to get the torsion frequency as close as possible to the actuation frequency of 4/rev. All the cases show an increase in mass per unit length, which happens due to the increase in the active plies used in the cross section. The chordwise location of

SC and CG for the optimized sections is close to its lower bound and upper bound, respectively.

The optimized cases have higher cross-sectional torsional stiffness and they also produce higher active twisting moment as compared to the baseline case. This occurs due to the increase in the coverage of plies used in the cross section. The torsional stiffness and active moment is highest for the Max θ_{stat} case, as expected, since it has the maximum amount of active ply in the cross section.

Table 3-12: Design Variables for the Optimized Cases

	Baseline Case	Max $\theta_{dyn,4rev,T/P}$ Case	Max $\theta_{dyn,4rev,low\ \rho}$ Case	Max θ_{stat} Case
Spar End (c)	0.443	0.556	0.590	**0.850**
Spar Web Loc (c)	0.443	0.501	0.460	0.481
Mass (m_1) (kg/m)	0.23	0.109	0.095	0.075
Mass 1 Loc (x_1) (c)	0.02	0.831	0.830	0.002
Mass 2 (m_2) (kg/m)	0.222	0.313	0.321	0.224
Mass 2 Loc (x_2) (c)	0.443	0.000	0.001	0.001

The design variables for the optimized cases are listed in Table 3-12. The chordwise ending location of active plies is at its upper limit for the Max θ_{stat} case. As a result of this, both the ballast masses for the Max θ_{stat} case are close to the leading edge. In the case of dynamically optimized cases, the ballast masses are located on either side of the quarter chord which results in an increase in torsional inertia. The optimum result obtained from trim analysis and low density analyses are close to each other. The difference lies in the fact that in the case of low density analysis, the torsional frequency is the only driving factor whereas in the case of periodic/trim analysis, active moment generated by active plies and aerodynamic stiffness also influence the results.

3.3.4 Trend Analysis

In order to observe the trends in the variation of the objective function and other response variables, a set of 40 design points was created using the results obtained from all the optimization studies. For these 40 points, all three of the analyses, namely: the trim analysis, the periodic analysis, and the low density analysis was carried out. Figure 3-14 shows the variation of tip twist amplitude, torsional stiffness, and first torsion frequency with iteration number when the data is sorted in order of increasing dynamic twist obtained from low density analysis. Results show that the amplitude of dynamic twist obtained from the low density analysis is directly related to the torsional frequency of the blade. The amplitude of tip twist increase as the torsion frequency approaches actuation frequency. The dynamic twist obtained from the trim analysis and periodic analysis does increase with decrease in torsion frequency, however, the variation is not uniform and thus, the torsion frequency is not the only critical parameter. Other variables shown in Figure 3-15 do not show any consistent trend. It should be noted that the amplitude of vertical displacement at the blade tip is highest for trim analysis for all the cases considered since the trim analysis case experiences higher aerodynamic loads.

The results presented in this section can be used to conclude that it is sufficient to carry out "periodic analysis" instead of the more time consuming "trim analysis" for active twist optimization studies. However, a purely structural dynamic solution is not sufficient and would not lead to an optimal solution as observed in the "Low ρ Analysis".

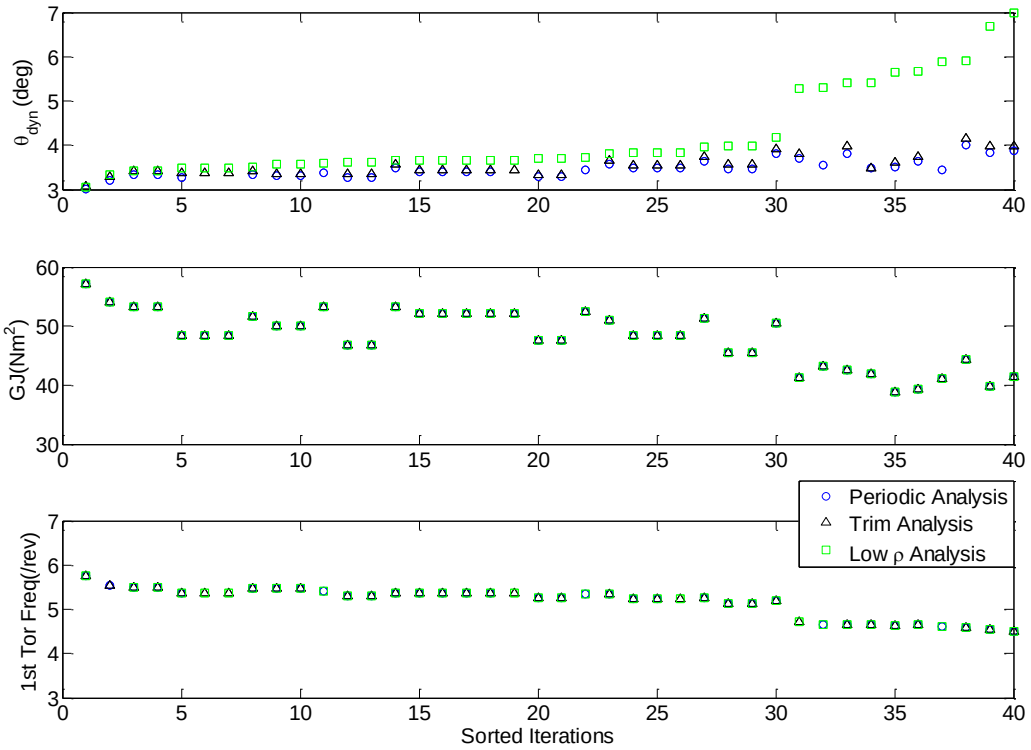

Figure 3-14: Variation of Amplitude with Torsional Stiffness and 1st Torsion Frequency (sorted with respect to amplitude obtained from **low density analysis**)

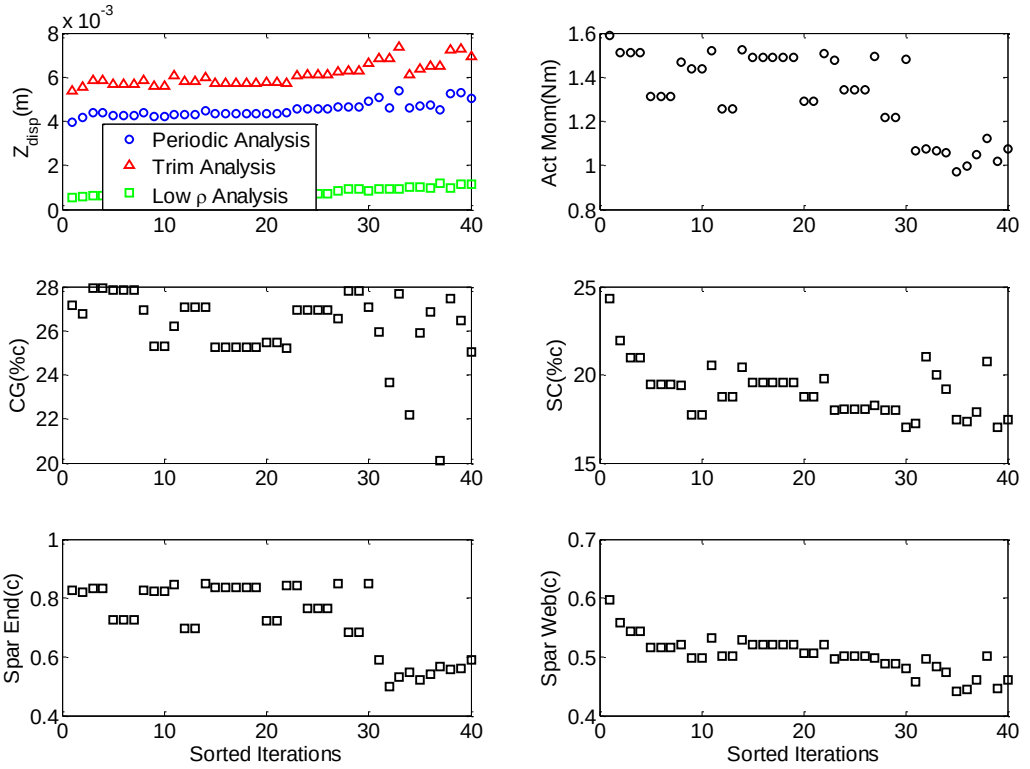

Figure 3-15: Variation with Iteration Number for Other Parameters (sorted with respect to amplitude obtained from **low density analysis**)

3.4 Optimization at 3/rev Actuation Frequency (Max $\theta_{3/rev}$)

After completion of the optimization at 4/rev actuation frequency, optimization was done at 3/rev actuation frequency. The constraints and design variables used were kept the same as in the earlier optimization problems. The final results obtained are shown in Table 3-13 and compared with results obtained with Max θ_{stat} and Max $\theta_{dyn,4/rev}$ (now referred as $\theta_{4/rev}$) cases (optimized result corresponding to 4/rev actuation frequency). Based on the observation made in the previous section, the "Periodic Analysis" is used here.

Table 3-13: Optimized Results for 3/rev Actuation Frequency

Cases	Max θ_{stat}	Max $\theta_{3/rev}$	Max $\theta_{4/rev}$	Baseline
θ_{stat} (deg/m)	1.61	1.40	1.42	1.34
% Increase	20.02	4.75	5.82	-
$\theta_{3/rev}$ (deg)	2.81	2.96	2.72	1.94
% Increase	44.97	**52.59**	40.18	-
Constraints				
1st Tor Freq (/rev)	5.20	**4.51**	4.60	6.34
M_{11} (kg/m)	0.710	0.711	0.703	0.684
SC (%c)	17.00	17.03	20.75	18.71
CG (%c)	27.05	27.97	27.47	23.94
Design Variables				
Spar End (c)	0.850	0.593	0.556	0.443
Spar Web Loc (c)	0.481	0.455	0.501	0.443
Mass m_1 (kg/m)	0.224	0.098	0.109	0.222
Mass 1 Loc (x_1) (c)	0.001	0.826	0.831	0.443
Mass m_2 (kg/m)	0.075	0.315	0.313	0.230
Mass 2 Loc (x_2) (c)	0.002	0.010	0.000	0.020
Other parameters				
S_{44} (Nm^2)	50.47	41.16	44.32	37.71
Active Moment (Nm)	1.48	1.07	1.12	0.91
2nd Flap Freq (/rev)	2.82	2.80	2.79	2.76

The optimized result shows a 52% increase in the dynamic twist at 3/rev actuation frequency. The Max θ_{stat} and the Max $\theta_{4/rev}$ cases show a 44% and 40% increase in dynamic twist, respectively. As observed earlier for optimization at 4/rev frequency, the increase in static twist for Max $\theta_{3/rev}$ is only 4.75%. The Max $\theta_{3/rev}$ and Max $\theta_{4/rev}$ cases show similar behavior for ballast masses and CG location. There are small variation in location of SC, torsional stiffness, length of active plies, and location of vertical spar web. As a result of this, the torsional frequency of the optimized blade is at its lower bound of 4.5/rev. The trend observed for Spar End (chordwise location where the spar/active plies end) shows that a higher twist amplitude can be obtained either through an increase in the amount of active material in the cross section or by dynamic tuning of the blade stiffness properties with significantly less active material. The vertical spar web is located near the mid chord in the optimum cases. Between the ballast masses used, ballast mass m_2 is higher in magnitude and is located very close to the leading edge of the blade cross section to get the CG close to the quarter chord. The ballast mass m_1 is much lower in magnitude and its location varies. For the dynamically optimized case, where the higher dynamic twist is obtained by dynamic tuning, the ballast mass m_1 is located aft of mid chord.

3.5 Optimization at 5/rev Actuation Frequency (Max $\theta_{5/rev}$)

In the next step, the optimization was done at 5/rev actuation frequency. The design variables and constraints used in the optimization were kept the same as in earlier studies. Final results obtained are shown Table 3-14. The table also includes optimized results corresponding to 3/rev and 4/rev actuation frequency and the dynamic twist obtained for these cases at 5/rev actuation frequency.

Table 3-14: Optimization Results for 5/rev Actuation Frequency

Cases	Max $\theta_{5/rev}$	Max $\theta_{4/rev}$	Max $\theta_{3/rev}$	Max θ_{stat}	Base
θ_{stat} (deg/m)	1.6	1.42	1.4	1.61	1.34
% Increase	19.48	5.82	4.75	**20.02**	-
$\theta_{5/rev}$ (deg)	5.17	2.57	2.35	4.85	2.56
% Increase	**101.83**	0.24	-8.22	89.44	-
Design Variables					
Spar End (c)	0.848	0.556	0.593	0.85	0.443
Spar Web Loc (c)	0.561	0.501	0.455	0.481	0.443
Mass 1 (m_1) (kg/m)	0.01	0.109	0.098	0.075	0.222
Mass 1 Loc (x_1) (c)	0.447	0.831	0.826	0.002	0.443
Mass 2 (m_2) (kg/m)	0.299	0.313	0.315	0.224	0.23
Mass 2 Loc (x_2) (c)	0.002	0	0.01	0.001	0.02
Constraints					
1st Tor Freq (/rev)	5.47	4.6	4.51	5.2	6.34
M_{11} (kg/m)	0.718	0.703	0.711	0.71	0.684
SC (%c)	22.5	20.75	17.03	17	18.71
CG (%c)	27.9	27.47	27.97	27.05	23.94
Other parameters					
S_{44} (Nm^2)	55.43	44.32	41.16	50.47	37.71
Active Moment (Nm)	1.57	1.12	1.07	1.48	0.91
2^{nd} Flap Freq(/rev)	2.82	2.79	2.8	2.82	2.76

The final optimized result shows a 101% increase in amplitude of dynamic tip twist for 5/rev actuation frequency. Also, it is interesting to note that Max $\theta_{4/rev}$ and Max $\theta_{3/rev}$ cases have poor twist amplitude at 5/rev actuation frequency, whereas Max θ_{stat} case performs well even at 5/rev actuation frequency. This is due to the placement of 1^{st} torsion frequency for the Max θ_{stat} case. For the Max $\theta_{5/rev}$ case, higher twist amplitude is obtained due to the combination of both: higher amplitude of active twisting moment and dynamic tuning. In the 3/rev and 4/rev actuation cases, the 1^{st} torsion frequency of the

blade could not get very close to the twist actuation frequency due to the constraint on the minimum value for the first torsion frequency. However, for 5/rev actuation case, the actuation frequency is in the range of allowable torsional frequencies. As a result, the percentage increase in dynamic twist amplitude for 5/rev actuation frequency is larger than that obtained for 3/rev and 4/rev actuation cases. Another important observation from the analysis is that the torsion frequency for the optimized cases is not exactly at 5/rev frequency. This can be attributed to aerodynamic forces which act against the motion of the rotor blades.

Among the design variables, the value of 0.848c for design variable "Spar End" implies that the coverage of the active region is close to the maximum allowable value, indicating that the optimizer is trying to maximize the active twisting moment. It should be noted that in Max $\theta_{5/rev}$ case, both active twisting moment and torsional stiffness are higher than that for Max θ_{stat} case even though the amount of active material used in the cross section is the same in both cases. This is due to the difference in the location of the vertical spar web for these cases. The increase in active twisting moment for the Max $\theta_{5/rev}$ case is offset by an even larger increase in torsional stiffness of the blade. As a result, the static twist for Max $\theta_{5/rev}$ case is smaller than that obtained for Max θ_{stat} case. For optimization at 5/rev frequency, the mass per unit length and the chordwise location of the CG are critical constraints and they both are closer to their upper limit.

3.6 Optimization at a Range of Actuation Frequencies (Max $\theta_{345/rev}$)

In this case, the objective is to maximize the amplitude of tip twist at a range of actuation frequencies, which maybe required for vibration and noise reductions. In this

particular case, the objective function includes amplitude of dynamic twist at 3/rev, 4/rev and 5/rev actuation frequencies since this a four-bladed rotor. During the optimization studies at these actuation frequencies, it was observed that the amplitude of tip twist for the optimized design for each of the cases was different. Thus, in order to remove the bias towards a particular frequency, the amplitude corresponding to each frequency was non-dimensionalized by the maximum amplitude obtained when the optimization was done at that particular frequency. The objective function used is given by:

$$maximize\ \theta_{345/rev} = \frac{1}{3}\left[\frac{\theta_{3/rev}}{\theta_{3/rev,max}} + \frac{\theta_{4/rev}}{\theta_{4/rev,max}} + \frac{\theta_{5/rev}}{\theta_{5/rev,max}}\right]$$

where, $\theta_{3/rev,max}$ is the maximum amplitude of tip twist obtained from optimization at **3/rev** actuation frequency, $\theta_{4/rev,max}$ is the maximum amplitude of tip twist obtained from optimization at **4/rev** actuation frequency, and $\theta_{5/rev,max}$ is the maximum amplitude of tip twist obtained from optimization at **5/rev** actuation frequency. The design variables and constraints used in the optimization were kept the same as in the earlier studies.

The final result obtained from all the cases considered are shown in Table 3-15. The columns in Table 3-15 show the value of non-dimensionalized tip twist amplitude for different frequencies and the value of $\theta_{345/rev}$ for all the optimum cases. As expected, the Max $\theta_{345/rev}$ case shows high twist amplitude at all the actuation frequencies. Max $\theta_{3/rev}$ and Max $\theta_{4/rev}$ cases show high amplitude of twist for 3/rev and 4/rev actuation frequencies, respectively, however their performance deteriorates at 5/rev actuation frequency since the 1st torsional frequency for both these cases lies close to 4.5/rev (lower bound for allowable torsion frequency). Also, results shown in Table 3-15 indicate that

Max $\theta_{345/rev}$ case and Max θ_{stat} case are very close to each other and maximizing static twist would have been sufficient to maximize the twist amplitude over a range of actuation frequencies. However, this is only partially true, since the increase in dynamic twist amplitude occurs due to both dynamic tuning and higher active twisting moment. For the particular case being analyzed, the first torsion frequency for the Max θ_{stat} case lies very close to the first torsion frequency obtained for Max $\theta_{345/rev}$ case as seen in the results shown in Table 3-16.

Table 3-15: Results obtained from all the Optimization Cases

Cases	$\bar{\theta}_{3/rev}$	$\bar{\theta}_{4/rev}$	$\bar{\theta}_{5/rev}$	$\theta_{345/rev}$
Max $\theta_{345/rev}$	0.95	0.94	0.97	**0.96**
Max $\theta_{5/rev}$	0.86	0.84	**1.00**	0.90
Max $\theta_{4/rev}$	0.92	**1.00**	0.50	0.80
Max $\theta_{3/rev}$	**1.00**	1.02	0.45	0.83
Max θ_{stat}	0.95	0.95	0.94	0.95
Baseline	0.65	0.54	0.50	0.56

where $\bar{\theta}_{3/rev} = \frac{\theta_{3/rev}}{\theta_{3/rev,\max}}$, $\bar{\theta}_{4/rev} = \frac{\theta_{4/rev}}{\theta_{4/rev,\max}}$, and $\bar{\theta}_{5/rev} = \frac{\theta_{5/rev}}{\theta_{5/rev,\max}}$.

The final values of the objective function, constraints, and design variables for the optimized case are shown in Table 3-16. As observed earlier, the Max θ_{stat} and Max $\theta_{345/rev}$ cases are very close to each other. Among the dynamically optimized cases, Max $\theta_{5/rev}$ case is the closest to optimum due to the location of the first torsional frequency.

The critical parameters for the optimization conducted at 3, 4 and 5/rev actuation frequencies are mass per unit length and chordwise location of CG. Both these constraints are close to their upper limit. The first torsion frequency of the blade approaches a value

between 5/rev and 5.5/rev. Also, the chordwise location of SC tends to be closer to its lower limit.

Table 3-16: Optimization Results for 3, 4 and 5/rev Actuation Frequencies

Cases	Max $\theta_{345/rev}$	Max $\theta_{5/rev}$	Max $\theta_{4/rev}$	Max $\theta_{3/rev}$	Max θ_{stat}	Base
θ_{stat} (deg/m)	1.6	1.6	1.42	1.4	1.61	1.34
% Increase	19.96	19.48	5.82	4.75	**20.02**	-
$\theta_{345/rev}$	0.956	0.901	0.804	0.826	0.946	0.564
% Increase	**69.49**	59.82	42.65	46.45	67.78	-
Design variables						
Spar End (c)	0.849	0.848	0.556	0.593	0.85	0.443
Spar Web Loc (c)	0.482	0.561	0.501	0.455	0.481	0.443
Mass 1 (m_1) (kg/m)	0.165	0.01	0.109	0.098	0.075	0.222
Mass 1 Loc (x_1) (c)	0.017	0.447	0.831	0.826	0.002	0.443
Mass 2 (m_2) (kg/m)	0.136	0.299	0.313	0.315	0.224	0.23
Mass 2 Loc (x_2) (c)	0.001	0.002	0	0.01	0.001	0.02
Constraints						
1st Tor Freq (/rev)	5.25	5.47	4.6	4.51	5.2	6.34
M_{11} (kg/m)	0.71	0.718	0.703	0.711	0.71	0.684
SC (%c)	17.07	22.5	20.75	17.03	17	18.71
CG (%c)	27.96	27.9	27.47	27.97	27.05	23.94
Other parameters						
S_{44} (Nm^2)	50.51	55.43	44.32	41.16	50.47	37.71
Active Moment (Nm)	1.48	1.57	1.12	1.07	1.48	0.91
2nd Flap Freq(/rev)	2.82	2.82	2.79	2.8	2.82	2.76

During the optimization studies, it was observed that the 1st torsion frequency is the main driving parameter for optimization in dynamic conditions. In order to understand it further, the amplitude of dynamic twist for different actuation frequencies is plotted as a function of the first torsion frequency (see Figure 3-16). Results shown in Figure 3-16 are non-dimensionalized as described in Table 3-15. The amplitude of tip twist for 3/rev and 4/rev actuations is high near the torsion frequency of 5.2/rev (due to large active twisting

moment) and near 4.5/rev frequency (due to the location of the first torsion frequency near the actuation frequency). In the case of 5/rev actuation frequency, torsion frequencies ranging from 5.2/rev to 5.6/rev provide high dynamic twist. In all the cases, the amplitude of tip twist decreases significantly as the first torsion frequency moves away from the actuation frequency. Since dynamically optimized cases are very sensitive to the first torsion frequency, the optimum case at one frequency may not be optimum at a different actuation frequency.

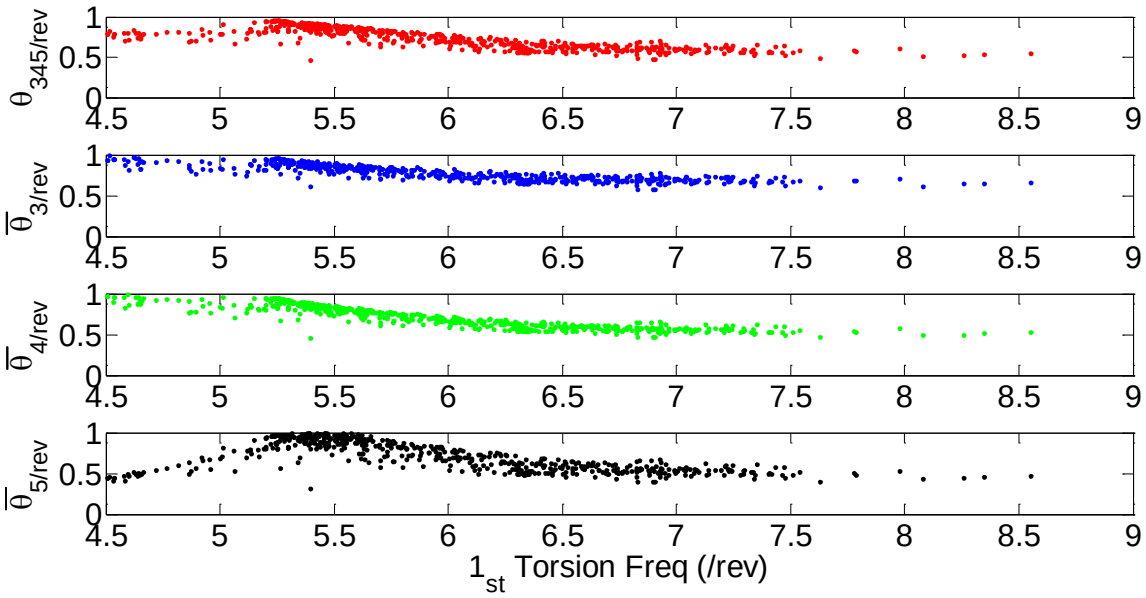

Figure 3-16: Variation of Dynamic Twist Amplitude with Torsion Frequency

3.7 Effect of Advance Ratio

The optimization studies for determining the optimum active cross section at different actuation frequencies was performed in hover condition to simplify the analysis. Also, preliminary analysis performed showed that the amplitude of dynamic twist does not vary significantly with forward airspeed. In order to verify this for the optimized cases, the aeroelastic analysis of the active twist blade was performed in forward flight condition at different actuation frequencies and the variation in the amplitude of dynamic twist was

determined. Note that for the results presented in this section, the "Trim Analysis" option was selected and hence the dynamic twist obtained for μ=0 in this section might not be the same as that obtained in the earlier sections, however, their values are close to each other. For each of the actuation frequencies, the result obtained for the dynamically optimized case are compared with the result obtained by maximizing the static twist and the result obtained for the baseline case.

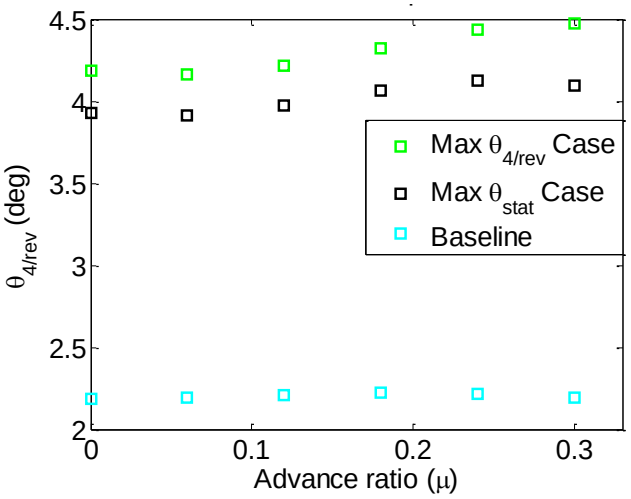

a) Results obtained for 4/rev actuation frequency

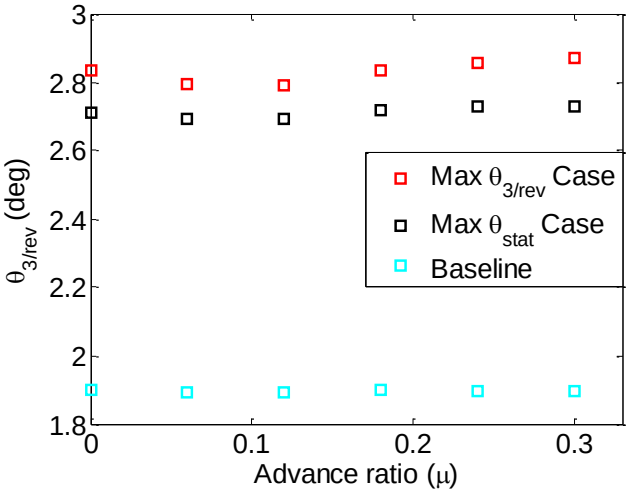

b) Results obtained for 3/rev actuation frequency

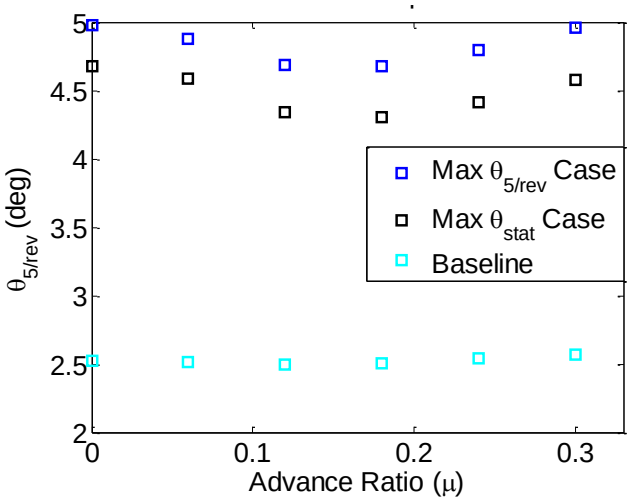

c) Result obtained for 5/rev actuation frequency

Figure 3-17: Effect of Advance ratio on Dynamic Twist Amplitude

The results obtained for the variation of dynamic twist amplitude with advance ratio are shown in Figure 3-17. It can be seen that, although there is a small variation in the twist amplitude with advance ratio, the dynamically optimized cases consistently provides higher dynamic twist than the Max θ_{stat} case and the baseline case. Also, all the three cases follow similar trend in the variation with advance ratio. Thus, these results justify the original assumption that the optimization studies for maximizing the amplitude of dynamic twist can be performed in hover condition.

3.8 Concluding Remarks

This chapter presented a new strategy and the corresponding framework for the optimum design of active twist rotor blades. The design framework integrates different codes: IXGEN for meshing composite rotor blade cross section, UM/VABS for the analysis of active cross sections, RCAS for rotorcraft simulation, and ModelCenter for integration. The optimization problem in the framework is solved using a surrogate-based approach in which the "true" objective function and constraints are replaced with

computationally efficient functional relationships. The surrogate-based optimization problem is solved in combination with the Efficient Global Optimization (EGO) algorithm, which accounts for uncertainty in surrogate predictions. To demonstrate the capability of the framework, three different optimization problems have been considered, namely, a) maximizing static active twist per unit length, b) maximizing amplitude of dynamic active twist at the blade tip at a fixed actuation frequency, and c) maximizing dynamic twist at a range of actuation frequencies. In this chapter, 3, 4 and 5/rev actuation frequencies were considered for optimization studies since these are most effective for reduction of 4/rev vibratory loads at the hub in fixed frame. All the studies were conducted using the same set of design variables and constraints. The design variables considered in this study were: the chordwise location of the main spar web, the chordwise ending location of the spar/AFC plies, and ballast masses and their chordwise location.

Departing from the NASA/Army/MIT Active Twist Rotor design, it was found that:

1) The optimized results for the blade cross section showed:
   - 18.5% increase in static twist per unit length
   - 63.6% increase in tip twist amplitude for 4/rev twist actuation.
   - 52.6% increase in tip twist amplitude for 3/rev twist actuation
   - 101% increase in tip twist amplitude for 5/rev twist actuation
   - 71% increase in twist amplitude for actuation at a range of frequencies (3, 4 and 5/rev).
2) The optimum design corresponding to maximum dynamic active twist and the one corresponding to the maximum static active twist are different from each other. Also, the dynamic active twist amplitude is a direct measure of control authority associated

with twist actuation mechanism, while the same may not hold for the static active twist.

3) When no twist actuation is used, the dynamically optimized case may result in a small increase in vibratory loads in forward flight conditions as compared to the baseline case

4) The circle plots show that the optimized design for maximum dynamic active twist provides higher control authority for reducing vibrations in all the hub load components when compared to the other designs.

5) Optimization studies for design of cross section with maximum dynamic twist can be performed in hover condition using periodic analysis to reduce the computational time and to improve efficiency.

6) The optimum design obtained by maximizing dynamic twist at a range of frequencies is better for vibration reduction as compared to designs obtained by maximizing static twist or dynamic twist a fixed actuation frequency.

7) Based on the optimization studies conducted, important factors that can be identified for maximizing dynamic twist are: a) first torsional frequency of the rotor blade, b) active moment generated by active material, and c) aerodynamic loads acting on the rotor blade.

Chapter 4. Mixed-Variable Optimization for Design of Active Twist Rotor Blades

In the previous chapter, preliminary optimization for maximizing the dynamic twist amplitude was performed with a limited number of (six) design variables and it was demonstrated that the dynamic twist obtained from twist actuation is the true measure of control authority for vibration reduction. Optimization approaches suitable to deal with a larger number and different types of design variables are needed to fully explore the active blade design space and to obtain realistic designs. In addition to the design variables used in the previous study, the thickness and ply angle of different plies used in the cross section also need to be considered as design variables. The plies used in the fabrication of composite rotor blades are made up of discrete layers, each with a prescribed thickness (pre-preg composites). Therefore, the mixed-variable optimization needs to be performed in order to design a manufacturable rotor blade.

In the case of optimization with (m + n) mixed design variables, some (m) of the variables are continuous while the (n) remaining ones can take discrete values only. A typical vector of (m+n) design variables is shown below:

$$X_{DV} = [x_{c,1}\ x_{c,2}\ \ldots..\ x_{c,n}\ x_{d,1}\ x_{d,2}\ \ldots\ldots\ x_{d,m}]$$

where $x_{c,i}$ ($1 \leq i \leq$ n) are n continuous design variables and $x_{d,j}$ ($1 \leq j \leq$ m) are m discrete design variables. In the optimization problem considered here, the ply thicknesses and ply

angles are treated as discrete design variables while the ballast masses, the chordwise location of vertical spar web, and the chordwise location where the active plies end are treated as continuous design variables. The ply thickness used in this chapter is the multiple of the nominal prepreg ply thickness and it is referred to as "normalized ply thickness" in rest of the thesis. The basic mixed-variable optimization problem in this chapter is solved using the genetic algorithm in MATLAB 2012's Global Optimization Toolbox. It is based on special creation, crossover, and mutation functions which enforce the variables to be integers, as described in [166]. In this chapter, the genetic optimization process is combined with the gradient based optimization to obtain an optimum design with continuous design variables and an optimum design with mixed design variables in an efficient manner.

4.1 Architecture for New Mixed-variable Optimization Framework

The architecture of the framework used to obtain solution for a mixed-variable optimization problem is shown in Figure 4-1. It is a modified version of the framework described in the earlier chapter which efficiently accounts for:

a) Discrete design variables; and

b) Increased number of design variables in the optimization problem.

All the steps involved in the new mixed-variable optimization framework are described below.

ModelCenter Analysis: In this part, the complete aeroelastic analysis of the active twist rotor is performed as described in Section 3.1.1. In order to reduce the computational time for the aeroelastic analyses required for optimization studies, the "Periodic

Analysis" is performed instead of using the "Trim Analysis". All the cases are run in hover condition, as explained earlier.

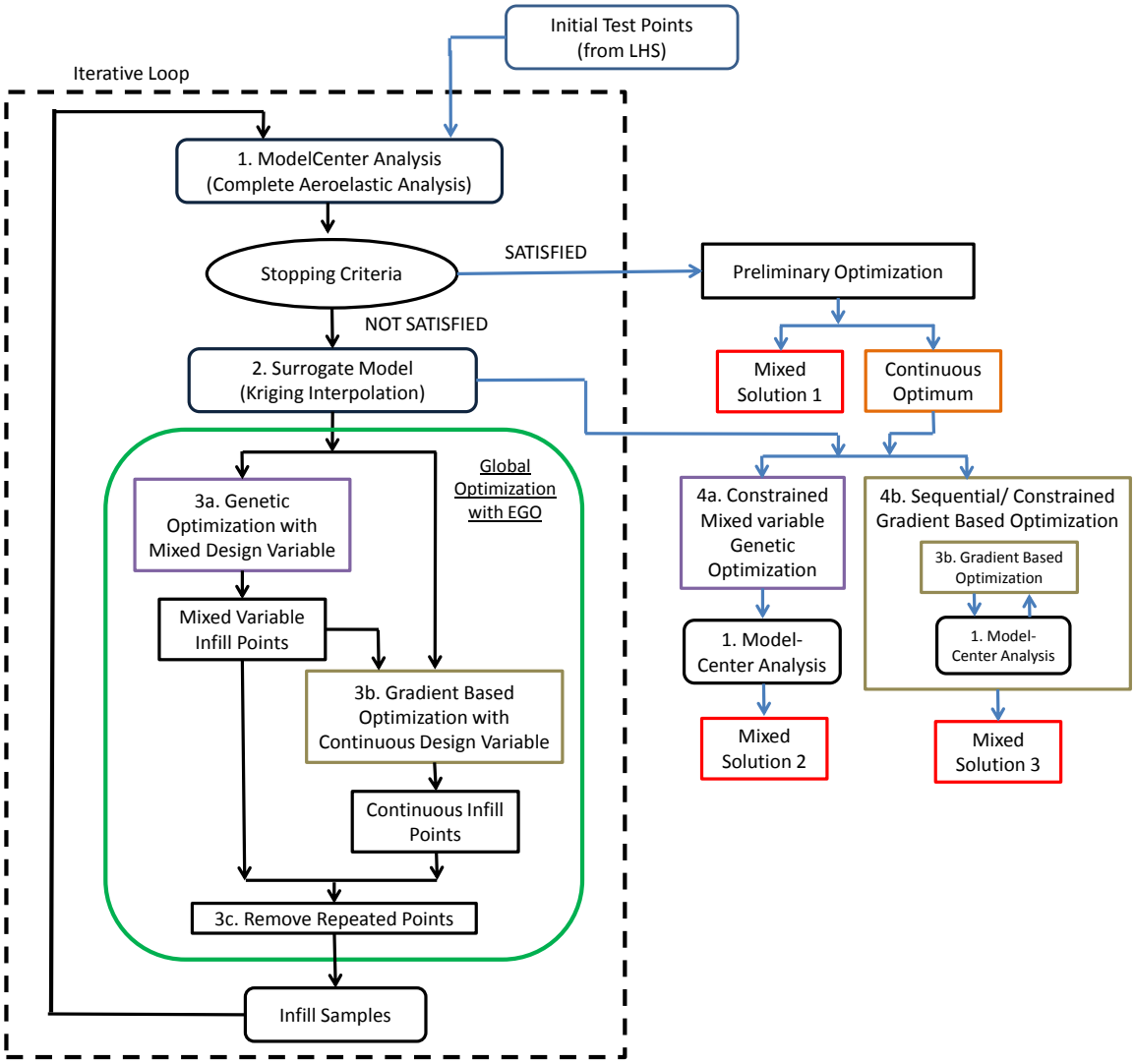

Figure 4-1: Augmented Optimization Framework for Continuous/Discrete Design Variables

Stopping Criteria: The stopping criteria can either be based on the maximum number of iterations allowed or on the difference between the optimal value of the objective function obtained from successive iterations. In the analysis performed here, the optimization process was stopped after 4-6 iterations. It was observed during the

optimization process that the difference between the successive optimal point reduced and the accuracy of the surrogate models improved with each iteration.

Surrogate Modeling: The surrogate modeling was performed using the DACE toolbox in MATLAB as described in Section 3.1.2. Different correlation functions available in the toolbox were used for different variables in order to reduce the error. The error was calculated based on the process described in Section 3.3.1.

Global Optimization with EGO Algorithm: Global Optimization with EGO algorithm was performed in multiple steps to account for: the mixed design variables and to reduce the computational time.

In the first step, *genetic optimization is performed with mixed design variables* where some of the design variables are continuous while the remaining ones are discrete. It was observed that the genetic algorithm works faster when some of the variables are treated as discrete instead of the case when all the design variables are continuous. Hence, the genetic optimization process was used to obtain optimum results with mixed design variables only. The results obtained from this analysis are referred to as "Mixed-variable Infill Points." It should be noted that multiple points (a set of best 5-10 points) are selected at the end of each optimization and not just the one optimum point. These multiple points represent different local minima in the design space and form a part of the Infill Samples for the next round of iteration. These "Mixed-variable Infill Points" are also used as the starting points for the *gradient based optimization* performed on the surrogate models. The gradient based optimizer provides a set of continuous optimum points. The gradient based optimization is performed using the "*fmincon*" function in

MATLAB. The set of points obtained at the end of the continuous optimization are referred as “Continuous Infill Points.”

The set of best points obtained from genetic optimization and gradient based optimization are used as Infill Samples. Before transferring these points to the next stage, *repeated points are removed* from the analysis by checking the absolute distance between the design points.

Iterative Loop: The complete aeroelastic analysis is performed again at the Infill Sample points using the ModelCenter environment. The results obtained from new points are used to update the surrogate models for all the constraints and the objective function. The process of global optimization with genetic algorithm and gradient based optimization is performed again. The iterative loop is repeated multiple times depending upon the stopping criteria and each iteration is referred to as “SBO Iteration.”

Preliminary results: At the end of the iterative loop, the set of points which satisfy all the constraints are sorted in the order of increasing objective function. The best point obtained is referred as “Continuous Optimum” and it represents the best design point with continuous design variables. Next, the points where the ply thicknesses (or ply angles) have discrete values are sorted out of the group. The point with the best objective function in this group is referred to as “Mixed Solution 1.” This point is the most optimum solution obtained at the end of the iterative loop when the discrete design variables have integer values only.

The mixed-variable solution can also be obtained in two other different ways using the “Continuous Optimum” point obtained earlier. In the first method, the genetic

optimization for mixed design variable is used, while the second method involves the usage of a gradient based method. These two methods are described in detail here.

a) Constrained Mixed-variable Genetic Optimization

This optimization is similar to what was performed in "Optimization with EGO algorithm", except that the bounds for discrete design variables are modified such that a discrete solution is determined *near* the "Continuous Optimum" point. For example, if the "Continuous Optimum" point gives a value of 1.36 for the normalized ply thickness, then a lower bound of "1" and an upper bound of "2" are used for this normalized ply thickness in the genetic optimization. The bounds for a continuous design variable are kept unchanged during this process. A sample case is shown in Table 4-1 where the optimization is performed with 12 design variables. Of these 12 design variables, four are continuous while the remaining eight can take discrete values only. The initial upper and lower bound for these design variables (as used in "Optimization with EGO algorithm") are shown by the rows corresponding to X_{upper} and X_{lower} , respectively. The "Continuous Optimum" solution obtained at the end of Preliminary Optimization is shown by X_{opt}. Based on the optimum result obtained, the upper and lower bounds on the design variables are modified to X'_{upper} and X'_{lower}, respectively. Note that in this step, only the bounds for discrete design variables are modified while the bounds on continuous design variables remain unchanged. The mixed-variable solution obtained at the end of this optimization process is referred as "Mixed Solution 2."

Table 4-1: Modified Bounds for Constrained Mixed-variable Genetic Optimization

	x_{c1}	x_{c2}	x_{c3}	x_{c4}	x_{d1}	x_{d2}	x_{d3}	x_{d4}	x_{d5}	x_{d6}	x_{d7}	x_{d8}
Bounds for Original Mixed-variable Genetic Optimization												
X_{upper}	0.85	0.85	0.5	0.5	5	5	5	5	5	5	5	5
X_{lower}	0.2	0.2	0	0	0	0	0	0	0	0	0	0
Solution Obtained from Continuous Gradient-Based Optimization												
X_{opt}	0.85	0.84	0.29	0.012	0.10	4.93	1.16	0.10	1.31	0.10	0.54	0.64
Modified Bounds for Constrained Mixed-variable Optimization												
X'_{upper}	0.85	0.85	0.5	0.5	1	5	2	1	2	1	1	1
X'_{lower}	0.2	0.2	0	0	0	4	1	0	1	0	0	0

b) Sequential Constrained Gradient-based optimization

Another approach for obtaining a mixed-variable solution using the "Continuous Optimum" design is the classical sequential optimization approach which can be performed using a gradient based optimizer. In this approach, if any of the discrete design variables in X_{opt} has a value close to an integer, then the value for that particular design variable is fixed to that integer value and it is not considered a design variable anymore. For example, in the results shown in Table 4-1, the value corresponding to x_{d2} is 4.93 in X_{opt}. Since this value is very close "5", the value for this design variable is fixed to "5" and it is not considered a design variable. Similarly, the value of design variables x_{d1}, x_{d4} and x_{d6} is fixed to "0". The modified vector of design variables and their upper and lower bounds for the next gradient-based optimization study are shown in Table 4-2. In the next step, the value of one more discrete design variable is fixed to an integer value and the process repeated till all the discrete design variables have been assigned an integer value. In this particular case, the gradient based optimization had to be performed

four more times in order to get the final mixed-variable solution. The solution obtained at the end of this method is referred as "Mixed Solution 3."

Table 4-2: Modified Set of Design Variables for Sequential Gradient-Based Optimization

	x_{c1}	x_{c2}	x_{c3}	x_{c4}	x_{d3}	x_{d5}	x_{d7}	x_{d8}
X_{upper}	0.85	0.85	0.5	0.5	5	5	5	5
X_{lower}	0.2	0.2	0	0	0	0	0	0

This optimization technique has the advantage that it provides a mixed-variable solution using a gradient-based optimizer. However, the optimization needs to be performed multiples times depending upon the number of discrete design variable in the problem. Every time, the time to convergence decreases as the size of the problem decreases and the starting condition are very close to the optimum. Hence, the Sequential Gradient Based Optimization approach may be time-consuming.

Optimization Parameters: The optimization parameters used for the GA optimization performed in steps 3a and 4a using the MATLAB's Global Optimization Toolbox are listed in Table 4-3. In most of the optimizations performed using GA, it was observed that the process stopped after exceeding the limit on the maximum number of generations allowed. Similarly, the optimization parameters used for GBO performed using the *fmincon* function in MATLAB in steps 3b and 4b are listed in Table 4-4. It should be noted that in the framework presented here (used in Chapter 4 and Chapter 5), both GA and GBO optimizations are performed on the surrogate models for objective function and constraints and thus, it is possible to perform a large number of iterations.

Table 4-3: Parameters used in GA Optimization

Parameter	Value
Function Tolerance (def)	1.0e-06
Population Size	400
EliteCount	20
Generations	150
Crossover Fraction	0.6

Table 4-4: Optimization Parameters for GBO

Parameter	Value
Tolerance (def)	1.0e-08
Maximum Fun Eval	10000
Maximum Iterations	500

4.2 Optimization with Normalized Ply Thickness

The baseline rotor blade used for the optimization studies in this chapter is the same NASA/Army/MIT Active Twist Rotor (ATR), as described in Chapter 3. The cross section shape and composite layup, planform of the rotor blade and rotor characteristics are all described in Chapter 3. In the first study, the normalized ply thicknesses of different plies used in the cross section are considered as design variables, along with the variables described in Chapter 3. In order to make the rotor blade design more realistic, the location of first ballast mass is fixed near the leading edge at x = 0.02c while the second ballast mass is located just in front of the vertical spar web. (This is done to ensure that the ballast mass is added in the region where passive plies can be used to support it and thus prevent the ballast mass from flying out during the operation). Due to these changes, there were small changes in the dynamic properties of the baseline case. The set of design variables and their upper and lower bounds are given in Table 4-5. In order to prevent the mesh generator from crashing, the lower bound on normalized ply

thickness is fixed at 0.1 instead of zero. A value of 0.1 for normalized ply thickness in an optimum design implies that that particular ply is not required in the cross section and should be removed in the next optimization. The constraints used in the optimization are the same as those used in Chapter 3, except the lower bound on first torsional frequency. As listed in Table 4-6, the lower bound for first torsional frequency was lowered to 3/rev instead of 4.5/rev used earlier.

Table 4-5: Design Variables and their Bounds

	Design variables	Baseline	Lower	Upper	Ply Type
1	Spar Web Loc (c)	0.443	0.2	0.85	
2	Spar End (c)	0.443	0.2	0.85	
3	Ballast Mass 1 (m_1) (kg/m)	0.23	0	0.5	
4	Ballast Mass 2 (m_2) (kg/m)	0.22	0	0.5	
5	Nor Thickness of Ply 1	1	0.1	5	E-Glass
6	Nor Thickness of Ply 2a	1	0.1	5	S-Glass
7	Nor Thickness of Ply 2	1	0.1	5	AFC
8	Nor Thickness of Ply 3	1	0.1	5	E-Glass
9	Nor Thickness of Ply 4	1	0.1	5	AFC
10	Nor Thickness of Ply 5	1	0.1	5	E-Glass
11	Nor Thickness of Ply 6	1	0.1	5	E-Glass
12	Nor Thickness of Ply 7	1	0.1	5	E-Glass

Table 4-6: Constraints for Optimization Problem

Constraints	Min	Max
SC (%c)	17	25
CG (%c)	20	28
M_{11} (kg/m)	0.65	0.72
1^{st} Tor Freq (/rev)	**3.0**	7

Objective functions which are considered for optimization studies are listed below:

1) Maximize static twist per unit length (Max θ_{stat})
2) Maximize amplitude of twist for 3/rev actuation (Max $\theta_{3/rev}$)
3) Maximize amplitude of twist for 4/rev actuation (Max $\theta_{4/rev}$)

4) Maximize amplitude of twist for 5/rev actuation (Max $\theta_{5/rev}$)

5) Maximize amplitude of twist at 3,4 and 5/rev actuation simultaneously (Max $\theta_{345/rev}$)

. For all the active twist optimization studies presented in this chapter, the amplitude of actuation voltage was fixed at 1000V. Final results obtained for the objective functions at the end of optimization are shown in Table 4-7. The results show the optimum value of objective function when all the design variables are treated as continuous and when the normalized ply thicknesses are treated as discrete (obtained from all the three mixed-variable optimization techniques described in Figure 4-1).

Table 4-7: Final Result obtained from Optimization Studies

	Max θ_{stat} (deg/m)	Max $\theta_{3/rev}$ (deg)	Max $\theta_{4/rev}$ (deg)	Max $\theta_{5/rev}$ (deg)	Max $\theta_{345/rev}$
Continuous Optimum	2.59	5.69	6.56	7.97	0.89
Mixed Solution 1	2.56	4.24	5.88	7.79	0.87
Mixed Solution 2	2.55	4.19	6.01	7.93	0.89
Mixed Solution 3	2.55	4.18	5.85	7.98	0.89
Baseline	1.34	1.85	2.06	2.34	0.31

The results show that the value of objective function corresponding to optimization with continuous design variables is always better than those obtained for the cases with mixed design variables. In general, the results obtained from the three mixed-variable optimization techniques are close to each other. The most interesting aspect of these results is the difference between the value of the objective function when all the variables are treated as continuous and when the variables are of mixed type. The percentage difference between the value of objective function for the continuous variable case and the average value of objective function for the mixed-variable cases is shown in Table

4-8. The percentage difference is less than 1.5% for Max θ_{stat}, Max $\theta_{5/rev}$ and Max $\theta_{345/rev}$ cases, while it is highest for the Max $\theta_{3/rev}$ case.

Table 4-8: Percentage Difference between the Objective Function for Continuous Variable Optimization and Mixed-variable Optimization

	Max θ_{stat}	Max $\theta_{3/rev}$	Max $\theta_{4/rev}$	Max $\theta_{5/rev}$	Max $\theta_{345/rev}$
Difference (%)	1.42	26.13	9.86	0.88	1.20

4.2.1 Optimization with Continuous Design Variables

The value of design variables and constraints for the optimization cases with continuous design variables and for the baseline case is shown in Table 4-9. As observed earlier, the most critical parameter for maximizing the dynamic twist is the first torsion frequency of the blade. The optimizer tries to bring the first torsion frequency of the blade closer to the actuation frequency. The chordwise location of CG for all the cases is closer to the aft constraint limit on CG location. This can be attributed to the increase in the value of design variable "Spar End" which is at its upper limit. By increasing the chordwise coverage of the spar/active plies, higher active twisting moment can be obtained, which would also result in an increase in the dynamic twist. The chordwise location of the vertical spar web is very close to the "Spar End" value for all the optimized cases. This results in a *box-type spar* for all the optimized cases. The increase in the chordwise coverage of plies in the cross section leads to an increase in the torsional stiffness. For all the optimized cases (except the Max $\theta_{3/rev}$ case), the torsional stiffness of the optimum blade is higher than that for the baseline case, even though the first torsion frequency is lower. The placement of the first torsion frequency for the optimized cases is

controlled by manipulating the values of two ballast masses. The amount of ballast mass used in the cross section is highest for the Max $\theta_{3/rev}$ case and it is least for the Max θ_{stat} case. Thus, the two ballast masses play an important role in varying the first torsional frequency of the blade.

Table 4-9: Constraints and Design Variables for Optimization with Continuous Design Variables

	Baseline	Max θ_{stat}	Max $\theta_{3/rev}$	Max $\theta_{4/rev}$	Max $\theta_{5/rev}$	Max $\theta_{345/rev}$
Constraints						
1st Tor Freq (/rev)	6.53	5.9	3.71	4.86	5.6	5.09
M_{11} (kg/m)	0.682	0.701	0.7	0.719	0.717	0.719
SC (%c)	18.71	23.5	17.07	19.12	24.82	18.98
CG (%c)	21.64	27.22	26.46	27.92	27.41	27.8
Continuous Variables						
Spar End (c)	0.443	0.85	0.818	0.85	0.842	0.85
Spar Web (c)	0.443	0.84	0.813	0.85	0.834	0.85
m_1 (kg/m)	0.23	0.299	0.397	0.346	0.32	0.334
m_2 (kg/m)	0.22	0.012	0.123	0.06	0.034	0.047
Discrete Variables (Normalized Ply Thickness)						
Ply 1	1	0.1	0.16	0.1	0.11	0.1
Ply 2a	1	4.93	2.40	5	4.84	5
Ply 2 (AFC)	1	1.16	0.41	0.84	1.03	0.98
Ply 3	1	0.1	0.10	0.1	0.10	0.1
Ply 4 (AFC)	1	1.31	0.68	1.09	1.27	1.12
Ply 5	1	0.1	0.17	0.1	0.1	0.1
Ply 6	1	0.59	0.26	0.43	0.54	0.59
Ply 7	1	0.64	0.10	0.25	0.82	0.1
Other Parameters						
S_{44} (Nm^2)	37.7	62.4	28.8	49.2	60.1	52.3
Act Mom (Nm)	0.91	2.83	1.16	2.21	2.70	2.37
2nd Flap Freq (/rev)	2.76	2.75	2.67	2.72	2.74	2.73
3rd Flap Freq (/rev)	5.26	5.33	4.80	5.14	5.26	5.19

Among the ply thickness design variables, the normalized ply thickness of all passive plies (Ply 1, Ply 3 and Ply 5) in the spar region have been reduced to their minimum allowable value. This was expected since they do not contribute to the active twist. However, the nose ply (Ply 2a) is very important for obtaining higher active twisting moment and hence all the optimized cases show an increase in the normalized thickness of nose ply. The plies in the vertical spar web (Ply 6 and Ply 7) need to have sufficient thickness in order to control the chordwise location of the shear center. Hence, even though these are passive plies, the normalized ply thickness for the spar web plies is not close to zero.

An increase in the normalized thickness of active plies is also accompanied by a corresponding increase in the torsional stiffness for the cross section. Hence, the optimized cases have different values for the normalized thickness of active plies (Ply 2 and Ply 4), depending upon the actuation frequency. The thickness of active plies is highest for the Max θ_{stat} case while it is the least for the Max $\theta_{3/rev}$ case. The results obtained for normalized ply thickness also demonstrate that, for the fixed amount of active material available, it is preferable to increase the chordwise coverage of active material as compared to increasing the thickness of active plies in order to get a higher dynamic twist amplitude. Another important trend observed is the direct correlation between torsional stiffness (GJ) of the cross section and the active twisting moment generated by the embedded active plies. For all the optimized cases, the normalized thickness of the inner active ply (Ply 4) is higher than that of the outer active ply (Ply 2).

The convergence of the optimum results obtained with continuous design variables is shown in Figure 4-2. The X-axis in the plot represents the number of Surrogate Based

Optimization (SBO) iterations, as described in Section 4.1. Results show that for some of the cases, the optimized result is obtained in the first 1-2 iterations. The variation of constraints and design variables for the Max $\theta_{4/rev}$ case with SBO iterations is shown in Figure 4-3 and Figure 4-4, respectively. Results presented here show that a local optimum results is obtained in the 1st iteration where the first torsion frequency of the blade is very close to the actuation frequency of 4/rev. For this case, the chordwise location of vertical spar web and spar end are close to each other and near the maximum value allowed for these two design variables. Also, the normalized thickness of both the active plies is less than "1". Thus, the optimizer is trying to tune the first torsion frequency to obtain higher amplitude. However, the best result obtained in Iteration 5 shows an increase in the thickness of active plies and a corresponding increase in torsional frequency. Thus, the best case tries to maximize the active twisting moment generated at the cost of higher torsional frequency. The increase in cross-sectional mass due to the increase in thickness of active plies is balanced by reducing the ballast masses used. This also shifts the CG of the cross section closer to its upper bound.

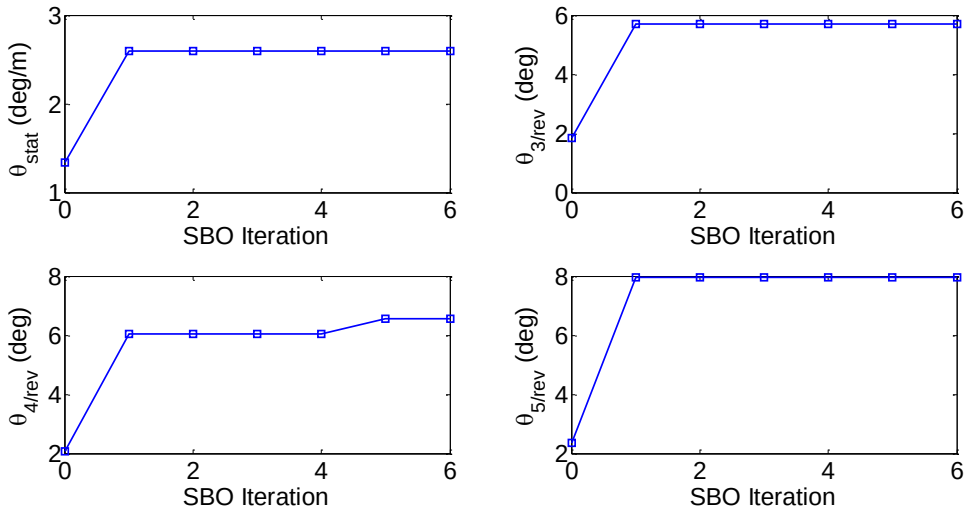

Figure 4-2: Variation of objective function with Iteration number for optimization with Continuous Design Variables

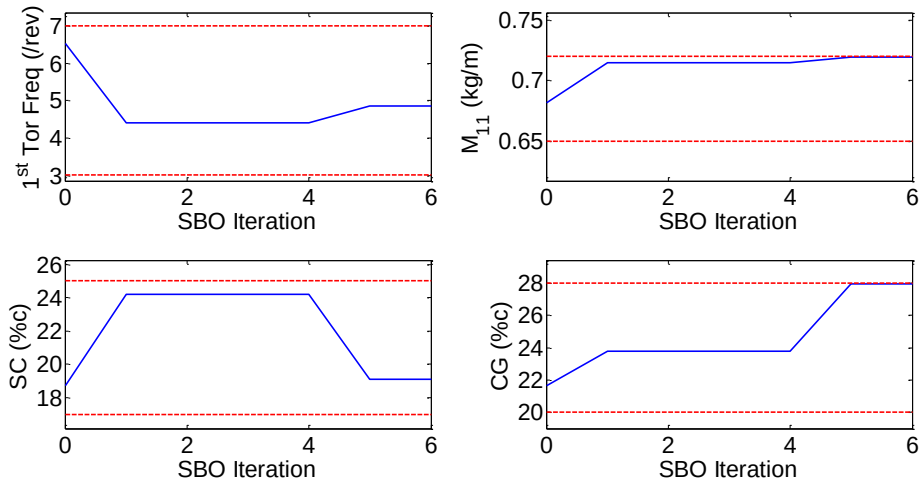

Figure 4-3: Variation of Constraints for Max $\theta_{4/rev}$ Optimization

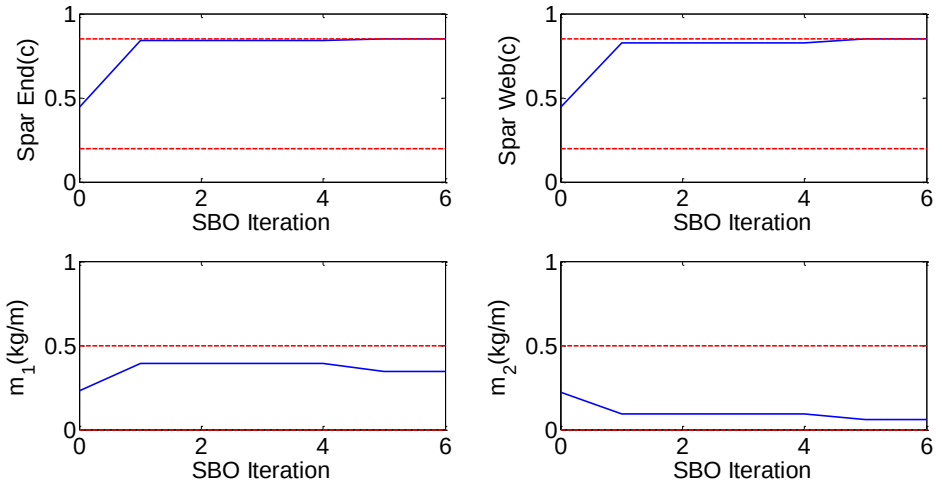

Design Variables (A)

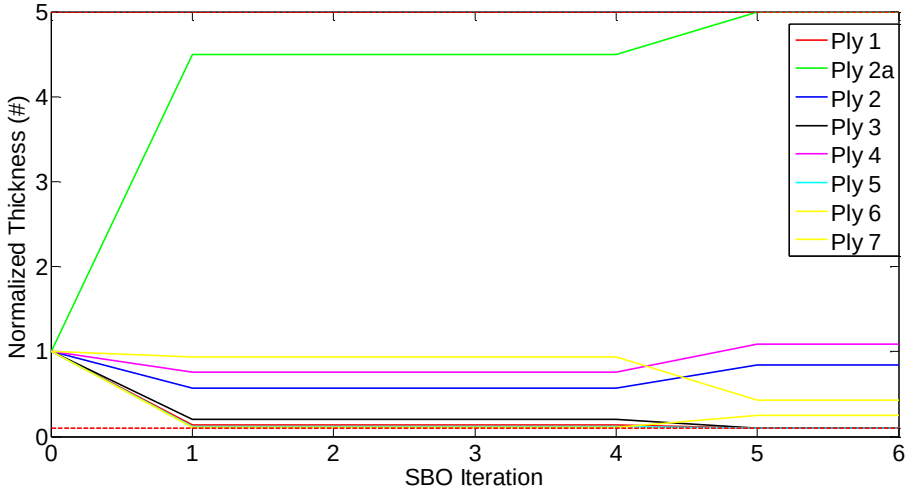

Design Variables (B)

Figure 4-4: Variation of Design Variables for Max $\theta_{4/rev}$ Optimization

The performance of the optimized cases at different actuation frequencies is shown in Table 4-10. Each column represents one of the optimized cases as listed in Table 4-9. The tip-twist values listed in Table 4-10 are non-dimensionalized by the maximum value obtained for that objective function during the optimization study (except for $\theta_{345/rev}$). The results show that the value of static twist is very close to the maximum value that can be obtained for Max $\theta_{4/rev}$, Max $\theta_{5/rev}$ and Max $\theta_{345/rev}$ cases. This table also highlights that the optimum solution obtained at one actuation frequency may not be optimum at a different actuation frequency, and hence the optimization needs to be performed at a range of actuation frequencies. The solution obtained by maximizing $\theta_{345/rev}$ shows high values of dynamic twist for all the actuation frequencies considered.

Table 4-10: Performance of Optimized Cases at other Actuation Frequencies

Cases	Baseline	Max θ_{stat}	Max $\theta_{3/rev}$	Max $\theta_{4/rev}$	Max $\theta_{5/rev}$	Max $\theta_{345/rev}$
$\bar{\theta}_{stat}$	0.52	1	0.87	0.98	0.99	0.99
$\bar{\theta}_{3/rev}$	0.33	0.68	1	0.81	0.69	0.77
$\bar{\theta}_{4/rev}$	0.31	0.73	0.55	1	0.78	0.93
$\bar{\theta}_{5/rev}$	0.29	0.91	0.16	0.81	1	0.97
$\theta_{345/rev}$	0.31	0.77	0.57	0.87	0.82	0.89

where, $\bar{\theta}_{stat} = \frac{\theta_{stat}}{\theta_{stat,\max}}$, $\bar{\theta}_{3/rev} = \frac{\theta_{3/rev}}{\theta_{3/rev,\max}}$, $\bar{\theta}_{4/rev} = \frac{\theta_{4/rev}}{\theta_{4/rev,\max}}$ and $\bar{\theta}_{5/rev} = \frac{\theta_{5/rev}}{\theta_{5/rev,\max}}$;

and $\theta_{stat,max}$ = 2.59, $\theta_{3/rev,max}$ = 5.69, $\theta_{4/rev,max}$ = 6.56, and $\theta_{5/rev,max}$ = 7.97

4.2.2 Optimization with Mixed Design Variables

In this section, the results obtained from the optimization with continuous design variables are compared with those obtained using mixed-variable for each of the objective function described above. As discussed earlier, in the case of mixed design

variable optimization, four of the twelve design variables are as continuous while the remaining eight are discrete and can take integer values only. In this case also, the lower bound on the normalized ply thickness was fixed at 0.1 instead of zero to prevent the mesh generator from crashing.

4.2.2.1 Maximizing θ_{stat}

The final results obtained from maximizing θ_{stat} using the optimization process described in Section 4.1 are shown in Table 4-11. For this objective function, the difference in the value of objective function between the optimization with continuous design variables and the optimization with mixed design variables is less than 1.5%. Although, the final values of the objective function for the optimized cases are close, there is a noticeable difference between the optimum designs. Also, the difference between the results obtained from the three different techniques used for optimization with mixed design variables is small.

The biggest difference between the continuous variable and mixed-variable optimization lies in the value of first torsion frequency for the optimized cases. In the continuous variable case, the active plies, Ply 2 and Ply 4, have thickness 16% and 30% higher than those for the mixed-variable case, respectively. Due to this, the optimum design with mixed design variables has less torsional stiffness and the embedded active plies generate less active twisting moment. This also highlights that multiples local minima exist in the design space being considered. The mixed-variable cases also show an increase in the magnitude of leading edge ballast mass and a corresponding increase in the mass per unit length for the cross section.

Table 4-11: Optimization Results for Maximizing θ_{stat}

Objective Function	Continuous Optimum	Mixed Solution 1	Mixed Solution 2	Mixed Solution 3
θ_{stat} (deg/m)	2.59	2.56	2.57	2.57
Constraints				
Tor Freq (/rev)	5.90	5.14	5.33	5.11
M_{11} (kg/m)	0.701	0.712	0.720	0.719
SC (%c)	23.50	24.52	23.43	23.43
CG (%c)	27.22	27.28	20.55	27.72
Continuous Variables				
Spar End (c)	0.850	0.847	0.850	0.850
Spar Web (c)	0.840	0.844	0.850	0.850
m_1 (kg/m)	0.299	0.342	0.361	0.342
m_2 (kg/m)	0.012	0.052	0.035	0.054
Discrete Variables (Normalized Ply Thickness)				
Ply 1	0.10	0.1	0.1	0.1
Ply 2a	4.93	4	5	5
Ply 2 (AFC)	1.16	1	1	1
Ply 3	0.10	0.1	0.1	0.1
Ply 4 (AFC)	1.31	1	1	1
Ply 5	0.10	0.1	0.1	0.1
Ply 6	0.54	0.1	1	0.1
Ply 7	0.64	1	0.1	1

4.2.2.2 Maximizing $\theta_{3/rev}$

The results obtained by maximizing $\theta_{3/rev}$ using continuous and mixed design variables are shown in Table 4-12. For this case, while the three results obtained with mixed design variables are close to each other, there is a 26% difference between the optimum values of objective function as compared to the continuous variable case. The main reason for this is the discretization of normalized thickness for the active plies. In order to reduce the torsional frequency (and torsional stiffness) of the blade, the normalized thickness of active plies in the cross section is well below "one" for the continuous

design variable case. But when the normalized thickness of active plies is rounded to "one" for the mixed-variable cases, there is a significant increase in the torsional stiffness of the cross section which could not be completely offset by adding more ballast masses. As a result, all the cases with mixed design variables show a higher torsional frequency and thus lower amplitude for the dynamic twist.

Table 4-12: Optimization Results for Maximizing $\theta_{3/rev}$

Objective Function	Continuous Optimum	Mixed Solution 1	Mixed Solution 2	Mixed Solution 3
$\theta_{3/rev}$ (deg)	5.69	4.24	4.19	4.18
Constraints				
1st Tor Freq (/rev)	3.71	5.15	4.81	5.11
M_{11} (kg/m)	0.700	0.694	0.683	0.718
SC (%c)	17.07	19.91	17.27	23.74
CG (%c)	26.46	26.93	27.35	27.61
Continuous Variables				
Spar End (c)	0.818	0.845	0.828	0.816
Spar Web (c)	0.813	0.846	0.599	0.816
m_1 (kg/m)	0.397	0.326	0.309	0.343
m_2 (kg/m)	0.123	0.046	0.072	0.068
Discrete Variables (Normalized Ply Thickness)				
Ply 1	0.16	0.1	0.1	0.1
Ply 2a	2.40	5	2	4
Ply 2 (AFC)	0.41	1	1	1
Ply 3	0.10	0.1	0.1	0.1
Ply 4 (AFC)	0.68	1	1	1
Ply 5	0.17	0.1	0.1	0.1
Ply 6	0.26	1	0.1	0.1
Ply 7	0.10	0.1	1	1

Small differences can be observed among the three results obtained with mixed design variables. In the "Mixed Solution 1", five plies are used in the nose region which gives higher active twisting moment. Thus, the "Mixed Solution 1" provides the maximum

dynamic twist amplitude inspite of having the highest torsional frequency. In the case of "Mixed Solution 2", the vertical spar web is located near mid chord and the first torsional frequency is closer to the actuation frequency of 3/rev. Thus, the optimizer is trying to increase the amplitude of dynamic twist by reducing the first torsion frequency.

4.2.2.3 Maximizing $\theta_{4/rev}$

The optimization results obtained by maximizing $\theta_{4/rev}$ with continuous and mixed design variables are shown in Table 4-13.

Table 4-13: Optimization Results for Maximizing $\theta_{4/rev}$

Objective Function	Continuous Optimum	Mixed Solution 1	Mixed Solution 2	Mixed Solution 3
$\theta_{4/rev}$ (deg)	6.56	5.88	6.01	5.85
Constraints				
1st Tor Freq (/rev)	4.86	5.13	5.11	5.10
M_{11} (kg/m)	0.719	0.714	0.719	0.719
SC (%c)	19.12	24.50	23.43	23.80
CG (%c)	27.92	27.54	27.79	27.81
Continuous Variables				
Spar End (c)	0.850	0.849	0.850	0.819
Main web (c)	0.850	0.842	0.850	0.819
m_1 (kg/m)	0.346	0.342	0.341	0.343
m_2 (kg/m)	0.060	0.053	0.054	0.068
Discrete Variables (Normalized Ply Thickness)				
Ply 1	0.10	0.10	0.10	0.10
Ply 2a	5.00	4	5	4
Ply 2 (AFC)	0.84	1	1	1
Ply 3	0.10	0.10	0.10	0.10
Ply 4 (AFC)	1.09	1	1	1
Ply 5	0.10	0.10	0.10	0.10
Ply 6	0.43	1	1	0.10
Ply 7	0.25	0.10	0.10	1

In this case, the difference between the optimum value of the objective function obtained using continuous design variables and mixed design variables is 9.9%. Here, the normalized thickness of active plies is closer to their discrete value, than they were in the case of "*Maximizing $\theta_{3/rev.}$"* Besides the thickness of active plies and vertical spar web plies, there is very small difference in the optimum design obtained with continuous design variables and mixed design variables. Among the different results with mixed design variables, the "Mixed Solution 2" gives the best result since it has more plies in the nose region that result in a higher active twisting moment.

4.2.2.4 Maximizing $\theta_{5/rev}$

The results obtained for maximizing the amplitude of dynamic twist at 5/rev actuation frequency with continuous and mixed design variables are shown in Table 4-14. Unlike the results obtained for "Maximizing $\theta_{3/rev}$" and "Maximizing $\theta_{4/rev}$" cases, the difference between the optimum value of the objective function obtained using continuous design variables and mixed design variables is very small. In the optimization with continuous design variable, the normalized thickness of active plies is more than 1 in order to obtain higher active twisting moment. However, in the case of mixed design variables, the dynamic twist is maximized by placing the first torsion frequency closer to the actuation frequency. Also, the results with mixed design variables show slightly heavier ballast mass in the spar region to increase the torsional inertia for the cross section and to further reduce the torsion frequency as compared to the continuous design variable case.

Table 4-14 Optimization Results for Maximizing $\theta_{5/rev}$

Objective Function	Continuous Optimum	Mixed Solution 1	Mixed Solution 2	Mixed Solution 3
$\theta_{5/rev}$ (deg)	7.97	7.79	7.93	7.98
Constraints				
1st Tor Freq (/rev)	5.60	5.20	5.10	5.22
M_{11} (kg/m)	0.717	0.704	0.720	0.698
SC (%c)	24.8	23.2	23.5	23.4
CG (%c)	27.4	27.4	28.0	27.9
Continuous Variables				
Spar End (c)	0.842	0.850	0.850	0.848
Spar Web (c)	0.834	0.833	0.850	0.841
m_1 (kg/m)	0.320	0.331	0.342	0.326
m_2 (kg/m)	0.034	0.050	0.055	0.050
Discrete Variables (Normalized Ply Thickness)				
Ply 1	0.11	0.1	0.1	0.1
Ply 2a	4.84	5	5	5
Ply 2 (AFC)	1.03	1	1	1
Ply 3	0.10	0.1	0.1	0.1
Ply 4 (AFC)	1.27	1	1	1
Ply 5	0.10	0.1	0.1	0.1
Ply 6	0.54	0.1	0.1	0.1
Ply 7	0.82	1	1	1

For this particular optimization study, the optimum design shown in "Mixed Solution 3" is slightly better than that obtained for Continuous Optimum, which contrary to the expected trend. This implies that the result obtained with continuous design variables is not optimum solution and it should be possible to find a better solution. However, the difference between optimum values predicted by "Continuous Optimum" and "Mixed Solution 3" is very small and is within the error in the prediction of $\theta_{5/rev}$ by the surrogate model.

4.2.2.5 Maximizing $\theta_{345/rev}$

Table 4-15: Optimization Results for Maximizing $\theta_{345/rev}$

Objective Function	Continuous Optimum	Mixed Solution 1	Mixed Solution 2	Mixed Solution 3
$\theta_{345/rev}$	0.89	0.87	0.88	0.89
Constraints				
1st Tor Freq (/rev)	5.09	5.13	5.08	5.11
M_{11} (kg/m)	0.719	0.714	0.719	0.719
SC (%c)	18.98	24.50	24.51	23.43
CG (%c)	27.80	27.54	27.99	27.82
Continuous Variables				
Spar End (c)	0.850	0.849	0.848	0.850
Spar Web (c)	0.850	0.842	0.848	0.850
m_1 (kg/m)	0.334	0.342	0.346	0.341
m_2 (kg/m)	0.047	0.053	0.056	0.054
Discrete Variables (Normalized Ply Thickness**)**				
Ply 1	0.10	0.1	0.1	0.1
Ply 2a	5.00	4	4	5
Ply 2 (AFC)	0.98	1	1	1
Ply 3	0.10	0.1	0.1	0.1
Ply 4 (AFC)	1.12	1	1	1
Ply 5	0.10	0.1	0.1	0.1
Ply 6	0.59	1	0.1	0.1
Ply 7	0.10	0.1	1	1

Finally, the result obtained for maximizing $\theta_{345/rev}$ using continuous and mixed design variables are shown in Table 4-15. In this case also, the optimum result obtained from optimization with mixed design variables is very close to that obtained using continuous design variables.

In this section, the optimization studies were conducted with twelve design variables, where four of the design variables were continuous while the remaining eight were discrete. Here, the optimum solution was obtained using continuous design variables and

mixed design variables in order to compare the two results and obtain a feasible design, which can be readily manufactured. The results showed that in some cases it is possible to get results with mixed design variables very close to those obtained with continuous design variables, depending upon the objective function.

4.3 Optimization Study with 8 Design Variables

In order to prevent the mesh generator from crashing, the minimum allowable normalized ply thickness was fixed to "0.1" instead of using "0" for the optimization studies performed in Section 4.2. The optimization results obtained showed that the optimizer tried to reduce the normalized thickness of all passive plies in the spar region (Ply 1, Ply 3 and Ply 5) to 0.1 indicating that these plies do not contribute to the dynamic twist amplitude and hence, these plies should be removed from the cross section. Therefore, in the optimization study presented in this section, Ply 3 and Ply 5 are removed from the analysis. Since Ply 1 is the outermost ply, it cannot be removed from the cross section. Thus, the normalized thickness of Ply 1 is fixed to minimum possible thickness, which is "one", for all the studies presented in this section. Also, in order to reduce the number of design variables, both the plies in the vertical spar web region (Ply 6 and Ply 7) are grouped and it is treated as one equivalent ply (Ply 6) whose thickness is a design variable. The modified cross section which is used as the baseline case is shown in Figure 4-5 and is referred to as "Baseline 2" in rest of the thesis. The final set of design variables used in this study and their upper and lower bounds are listed in Table 4-16. The constraints used in this study are the same as those listed in Table 4-6.

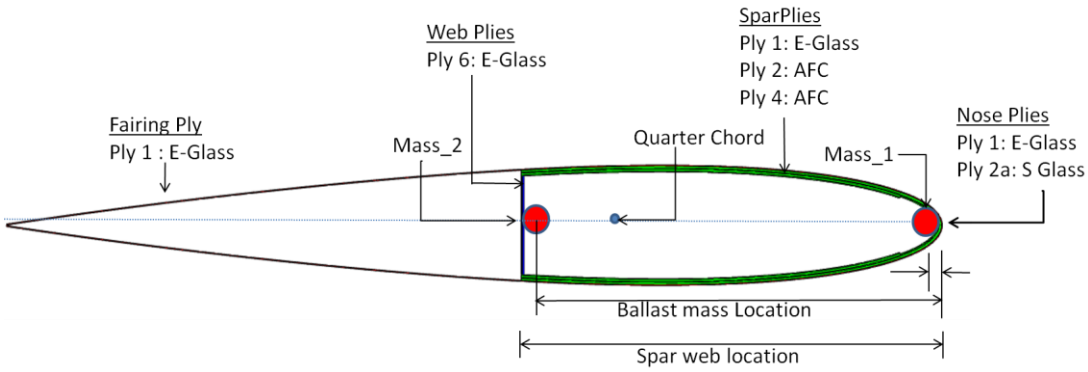

Figure 4-5: Modified Baseline Case (Baseline 2)

Table 4-16: Design Variable and their Bounds

	Design variables	Baseline	Lower	Upper	Ply Type
1	Main Spar Web Loc (c)	0.443	0.2	0.85	
2	Spar End (c)	0.443	0.2	0.85	
3	Ballast Mass 1 (m_1) (kg/m)	0.23	0	0.5	
4	Ballast Mass 2 (m_2) (kg/m)	0.22	0	0.5	
Normalized Ply Thickness					
5	Ply 2a Thickness	1	1	5	S-Glass
6	Ply 2 Thickness	1	1	5	AFC
7	Ply 4 Thickness	1	1	5	AFC
8	Spar Web Ply 6 Thickness	1	1	10	E-Glass

The summary of the results obtained for objective function at the end of optimization with continuous design variables and mixed design variables is shown in Table 4-17. Comparing the results obtained for the optimized cases with those obtained earlier in Table 4-7 and Table 4-9, it can be seen that the final value of objective function is smaller in this optimization study, for all the objective functions considered. The main reason for this is the fact that the normalized thickness of the outermost passive ply (Ply 1) in the cross section is fixed to "1" whereas, in the previous case, the optimizer had the freedom to reduce the normalized thickness of this passive ply to the minimum allowable value

which was fixed at "0.1." Also, the percentage difference in the optimum result obtained with continuous design variables and optimum results obtained with mixed design variables is different in this optimization (as compared to the percentage differences observed in Table 4-8).

Table 4-17: Results obtained for Optimization with 8 Design Variables

	Max θ_{stat} (deg/m)	Max $\theta_{3/rev}$ (deg)	Max $\theta_{4/rev}$ (deg)	Max $\theta_{5/rev}$ (deg)	Max $\theta_{345/rev}$
Continuous Optimum	2.49	4.9	5.94	7.77	0.894
Best Mixed Solution	2.41	4.6	5.41	7.63	0.889
% Difference	3.21	6.12	8.92	1.80	0.56

4.3.1 Optimization Results with Continuous Design Variables

The results obtained for all the cases with continuous design variables using the framework described in Section 4.1 are shown in Table 4-18. For the Max θ_{stat} case, three of the constraints namely, mass per unit length and chordwise location of CG and SC are close to their upper bound. This occurs, because there is an increase in the thickness of all the plies used in the cross section and the chordwise coverage of active plies is at the maximum allowable value. Here, only the leading-edge ballast mass is used to get the chordwise location of CG within the bounds required. Among the ply thicknesses, the thickness of the nose ply is very close to the maximum allowable value since it results in a higher active twisting moment. There is an increase of 23% in the normalized thickness of active plies, namely, Ply 2 and Ply 4. Among all the optimized cases, the Max θ_{stat} case has the highest cross-sectional stiffness.

Table 4-18: Results Obtained with Continuous Design Variables

Cases	Max θ_{stat}	Max $\theta_{3/rev}$	Max $\theta_{4/rev}$	Max $\theta_{5/rev}$	Max $\theta_{345/rev}$	Baseline 2
Objective Function						
θ_{stat} (deg/m)	**2.49**	2.25	2.24	2.42	2.41	1.67
$\theta_{3/rev}$ (deg)	3.67	**4.9**	4.66	3.86	3.91	2.4
$\theta_{4/rev}$ (deg)	4.48	5.92	**5.94**	5.21	5.34	2.54
$\theta_{5/rev}$ (deg)	6.81	3.6	4.31	**7.77**	7.67	2.38
$\theta_{345/rev}$	0.794	0.82	0.835	0.888	**0.894**	0.408
Constraints						
1st Tor Freq (/rev)	6.01	4.53	4.69	5.37	5.29	5.48
M_{11} (kg/m)	0.72	0.719	0.719	0.72	0.72	0.642
SC (%c)	24.8	17.17	17.14	24.95	23.93	19.01
CG (%c)	27.75	27.79	27.75	28	28	21.87
Design Variables						
Spar End (c)	0.85	0.85	0.85	0.85	0.85	0.443
Spar Web (c)	0.85	0.309	0.319	0.85	0.85	0.443
m_1 (kg/m)	0.299	0.309	0.307	0.328	0.33	0.23
m_2 (kg/m)	0	0	0	0.033	0.036	0.22
Normalized Ply Thickness						
Ply 2a (E-Glass)	4.88	1	1.54	4.75	4.85	1
Ply 2 (AFC)	1.23	1.37	1	1.04	1	1
Ply 4 (AFC)	1.24	1	1.36	1	1	1
Ply 6 (E-Glass)	1.2	10	10	1.15	1	1
Other Parameters						
S_{44} (Nm^2)	66.2	35	37.9	57.9	56.4	25.1
Act Mom (Nm)	2.87	1.5	1.61	2.45	2.38	0.76
2nd Flap Freq(/rev)	2.79	2.79	2.79	2.76	2.76	2.72
3rd Flap Freq (/rev)	5.51	5.49	5.51	9.42	5.37	5.07
Max ε_{11} ($\mu\varepsilon$)	2478	3872	3547	2658	2646	3935
Max ε_{12} ($\mu\varepsilon$)	4347	5482	4968	4288	4816	5591

In the Max $\theta_{3/rev}$ case, the presence of the outermost passive ply does not permit significant reduction in the first torsional frequency, as it was possible in the previous optimization study presented in Section 4.2. Thus, the first torsion frequency and cross-sectional torsional stiffness obtained for the Max $\theta_{3/rev}$ case in Table 4-18 is higher than

that obtained for the Max $\theta_{3/rev}$ case in Table 4-9. As a consequence of this, the value of objective function for the optimized case in Table 4-18 is significantly lower than that obtained in Table 4-9. The vertical spar web is located near the quarter chord due to which the chordwise location of shear center is closer to its lower limit. Unlike the Max θ_{stat} case, the normalized thickness of the nose ply, Ply 2a, is at its minimum value while the normalized thickness of vertical spar web ply, Ply 6, is at the maximum allowable value. Thus, in the Max $\theta_{3/rev}$ case, the optimizer is trying to lower the torsional stiffness as much as possible in order to get the first torsion frequency closer to the actuation frequency.

The results obtained for Max $\theta_{4/rev}$ and Max $\theta_{3/rev}$ cases are very close to each other. This is specific to this problem and it can be attributed to the bounds used for constraints and design variables in the optimization problem definition. The only noticeable difference between the Max $\theta_{4/rev}$ case and Max $\theta_{3/rev}$ case is in the thickness of active plies.

As observed in Section 4.2, the result for Max $\theta_{5/rev}$ case is similar to the result obtained for Max θ_{stat} case since their first torsion frequencies are close to each other. In this case, the second ballast mass is also used to tune the first torsion frequency of the blade. The total ballast mass used in the Max $\theta_{5/rev}$ case is higher than that used in the cases discussed above. Thus, for the Max $\theta_{5/rev}$ case, the optimizer takes advantage of both, the higher active twisting moment and dynamic tuning, to obtain large amplitude of oscillation at the blade tip. The result obtained for the Max $\theta_{345/rev}$ case is close to the result for Max $\theta_{5/rev}$ case, but with a slightly lower first torsion frequency to improve the amplitude of twist oscillation for all the actuation frequencies.

In the optimization studies presented in this section, the cross-sectional strains are not included as part of the constraints. The results obtained here show that the maximum value of ε_{11} and ε_{12} in the cross section for all the optimized cases is approximately equal to or less than that obtained for the baseline case. Thus, the blade designs obtained from these optimization studies have sufficient strength to withstand the large centrifugal loads.

4.3.2 Optimization Results with Mixed Design Variables

For the results presented in this section, the normalized ply thicknesses are treated as discrete design variables. In the previous section, it was shown that the optimization with mixed design variables can be performed in three different ways. The mixed solutions, "Mixed Solution 1" and "Mixed Solution 2", are obtained using the genetic mixed-variable optimization while the "Mixed Solution 3" is obtained using a gradient based optimizer only. The results obtained in Section 4.2 showed that the final results obtained for the objective function with different mixed design variables optimization techniques are close to each other. Also, it was observed that obtaining the "Mixed Solution 3" required significant computational time since the optimization is performed in a recursive manner. Hence, in this section, the mixed-variable optimization is performed to obtain "Mixed Solution 1" and "Mixed Solution 2" only. The final results presented here in Table 4-19 show only the best result obtained with mixed design variables.

Table 4-19: Optimization Results with Mixed Design Variables

Cases	Max θ_{stat}	Max $\theta_{3/rev}$	Max $\theta_{4/rev}$	Max $\theta_{5/rev}$	Max $\theta_{345/rev}$	Baseline 2
Objective Function						
θ_{stat} (deg/m)	**2.41**	2.22	2.21	2.41	2.39	1.67
$\theta_{3/rev}$ (deg)	3.36	**4.6**	4.34	3.89	3.88	2.4
$\theta_{4/rev}$ (deg)	4.3	5.28	**5.41**	5.3	5.31	2.54
$\theta_{5/rev}$ (deg)	5.73	3.86	4.81	**7.63**	7.62	2.38
$\theta_{345/rev}$	0.716	0.775	0.806	0.889	**0.889**	0.408
Constraints						
1st Tor Freq (/rev)	5.71	4.71	4.93	5.31	5.28	5.48
M_{11} (kg/m)	0.694	0.688	0.697	0.718	0.72	0.642
SC (%c)	23.81	17.05	17.19	23.81	24.77	19.01
CG (%c)	20.33	27.92	27.79	27.9	28	21.87
Design Variables						
Spar End (c)	0.85	0.849	0.85	0.849	0.846	0.443
Spar Web (c)	0.85	0.303	0.318	0.849	0.843	0.443
m_1 (kg/m)	0.332	0.271	0.273	0.328	0.334	0.23
m_2 (kg/m)	0.009	0.063	0.06	0.036	0.038	0.22
Normalized Ply Thickness						
Ply 2a (S-Glass)	5	1	2	5	4	1
Ply 2 (AFC)	1	1	1	1	1	1
Ply 4 (AFC)	1	1	1	1	1	1
Ply 6-7 (E-Glass)	1	9	10	1	1	1
Other Parameters						
S_{44} (Nm2)	56.5	32.9	37	56.5	55.8	25.1
Act Mom (Nm)	2.38	1.37	1.54	2.38	2.33	0.76
2nd Flap Freq (/rev)	2.77	2.77	2.78	2.76	2.76	2.72
3rd Flap Freq (/rev)	5.4	5.42	5.44	5.38	5.36	5.07
Max ε_{11}	2489	3994	3364	2601	2896	3935
Max ε_{12}	4220	5600	4748	4798	4711	5591

The results obtained with mixed designs variables show the similar trend as it was observed in the results with continuous design variables. The optimum value of the objective function for the optimized cases obtained using mixed design variables is

always lower than that obtained with continuous design variables, however the difference between the results depends on the objective function.

4.4 Optimization Studies with Ply Angles and Ply Thicknesses

In the results presented in this section, the ply angles are also included as the design variables. The "Baseline 2" case, shown in Figure 4-5 and described in Section 4.3, is used as the baseline case. The bounds for design variables and their baseline values are listed in Table 4-20. The bounds for normalized ply thicknesses are the same as that shown in Table 4-16. The bounds used for ply angle depends on the nature of the prepreg. For the unidirectional plies, the ply angle varies from -90 to +90 degrees, whereas for the bidirectional plies, the ply angle varies from 0 to 90 degrees. Even though the ply angle can be treated as a continuous design variable, it is difficult to accurately manufacture a composite structure where the ply angle has a real value. Hence, in the mixed-variable optimization performed here, the ply angles are treated as discrete design variables for the ease of manufacturing. In some of the earlier work [99], ply angles are discretized in multiples of 5 or 10 degree. The framework presented here is also capable of working with this discretization, however for the analysis presented in this section; the ply angle is allowed to take any integer value within the bounds specified. The constraints used in the analysis are the same as those described in Table 4-6.

Table 4-20: Design Variables for Optimization with Ply Thicknesses and Ply Angles

	Design variables	Baseline2	Lower	Upper	Ply Type
1	Main Spar Web Loc (c)	0.443	0.2	0.85	
2	Spar End (c)	0.443	0.2	0.85	
3	Ballast Mass 1 (m_1) (kg/m)	0.23	0	0.5	
4	Ballast Mass 2 (m_2) (kg/m)	0.22	0	0.5	
Normalized Ply Thickness					
5	Ply 2a Thickness	1	1	5	S-Glass
6	Ply 2 Thickness	1	1	5	AFC
7	Ply 4 Thickness	1	1	5	AFC
8	Spar Web Ply 6 Thickness	1	1	10	E-Glass
Ply Angles					
9	Ply 1 Angle	0	0	90	E-Glass
10	Ply 2a Angle	0	-90	90	S-Glass
11	Ply 2 Angle	45	-90	90	AFC
12	Ply 4 Angle	-45	0	90	AFC
13	Spar Web Ply 6 Angle	0	0	90	E-Glass

4.4.1 Optimization Results with Continuous Design Variables

The results obtained, when all the design variables listed in Table 4-20 are treated as continuous design variables, are shown in Table 4-21. The optimization study performed in Section 4.3 is a subset of the analysis performed in this section. For some of the objective functions, it was observed that the results obtained in Section 4.3 are the optimal results and it is not possible to obtain further improvement in the optimum value of the objective function by including ply angles as the additional design variables. This is true for the Max θ_{stat} and Max $\theta_{4/rev}$ cases shown in Table 4-21 and Table 4-18.

Table 4-21: Results for Optimization with Continuous Design Variables

Cases	Max θ_{stat}	Max $\theta_{3/rev}$	Max $\theta_{4/rev}$	Max $\theta_{5/rev}$	Max $\theta_{345/rev}$	Baseline 2
Objective Function						
θ_{stat} (deg/m)	**2.49**	-2.22	-2.24	2.4	2.4	1.67
$\theta_{3/rev}$ (deg)	3.67	**4.91**	4.66	3.9	3.9	2.4
$\theta_{4/rev}$ (deg)	4.48	5.89	**5.94**	5.29	5.29	2.54
$\theta_{5/rev}$ (deg)	6.81	3.53	4.31	**8.02**	8.02	2.38
$\theta_{345/rev}$	0.784	0.811	0.828	0.895	**0.895**	0.408
Constraints						
1st Tor Freq(/rev)	6.01	4.51	4.69	5.32	5.32	5.48
M_{11} (kg/m)	0.72	0.719	0.719	0.72	0.72	0.642
SC (%c)	24.8	17.29	17.14	22.16	22.16	19.01
CG (%c)	27.75	27.79	27.75	27.99	27.99	21.87
Design Variables						
Spar End (c)	0.85	0.85	0.85	0.85	0.85	0.443
Spar Web (c)	0.85	0.309	0.319	0.85	0.85	0.443
m_1 (kg/m)	0.299	0.309	0.307	0.33	0.33	0.23
m_2 (kg/m)	0	0	0	0.036	0.036	0.22
Normalized Ply Thicknesses						
Ply 2a (S-Glass)	4.88	1	1.54	4.91	4.91	1
Ply 2 (AFC)	1.23	1.37	1	1	1	1
Ply 4 (AFC)	1.24	1	1.36	1	1	1
Ply 6-7 (E-Glass)	1.2	10	10	1	1	1
Ply Angles						
Ply 1 (E-Glass)	0	0	0	0	0	0
Ply 2a (S-Glass)	0	1.9	0	62.2	62.2	0
Ply 2 (AFC)	45	43.5	45	-42	-42	45
Ply 4 (AFC)	-45	-54.9	-45	47.1	47.1	-45
Ply 6-7 (E-Glass)	0	0	0	0	0	0
Other Parameters						
S_{44} (Nm^2)	66.2	34.8	37.9	57.4	57.4	25.1
Act Mom (Nm)	2.87	1.48	1.61	2.42	2.42	0.76
2nd Flap Freq (/rev)	2.79	2.78	2.79	2.76	2.76	2.72
3rd Flap Freq (/rev)	5.51	5.47	5.51	9.31	9.31	5.07
Max ε_{11} ($\mu\varepsilon$)	2478	3906	3547	4508	4508	3935
Max ε_{12} ($\mu\varepsilon$)	4347	5263	4968	6201	6201	5591

The results for Max $\theta_{3/rev}$ case show a very small improvement with ply angles, as compared to the results shown in Table 4-18. The improvement is obtained by changing the ply angle for active plies away from ±45 degrees. Although the active twisting moment generated is reduced due to the ply angle changes, the lowering of the torsional frequency results in a higher dynamic twist at the blade tip. In the Max $\theta_{5/rev}$ case also, small changes are observed in the ply angle for active ply. But the most noticeable change occurs in the ply angle for nose ply, which changes to 62.2 degrees. Similar to the Max $\theta_{3/rev}$ case, the changes in ply angle result in lower active twisting and also lower torsional stiffness and first torsion frequency. The result obtained for Max $\theta_{345/rev}$ case is the same as that obtained for Max $\theta_{5/rev}$ case.

4.4.2 Optimization with Mixed Design Variables

The results obtained, when the normalized ply thicknesses and ply angles listed in Table 4-20 are treated as discrete design variables, are shown in Table 4-22. As observed in the results with continuous optimization, for some of the objective functions considered, it was not possible to find a better solution by including ply angles as the design variables. For the mixed-variable optimization performed here, the results obtained for Max θ_{stat}, Max $\theta_{3/rev}$, Max $\theta_{4/rev}$, Max $\theta_{345/rev}$ could not be improved further.

For the Max $\theta_{5/rev}$ case, the changes in ply angle for the nose ply (Ply 2a) and the outermost ply (Ply 1) result in higher twisting moment, and thus larger dynamic twist as compared to the optimum design shown in Table 4-19.

Table 4-22: Results Obtained for Optimization with Mixed Design Variables

Cases	Max θ_{stat}	Max $\theta_{3/rev}$	Max $\theta_{4/rev}$	Max $\theta_{5/rev}$	Max $\theta_{345/rev}$	Baseline 2
Objective Function						
θ_{stat} (deg/m)	**2.41**	-2.22	-2.21	2.39	-2.39	1.67
$\theta_{3/rev}$ (deg)	3.36	**4.6**	4.34	3.81	3.88	2.4
$\theta_{4/rev}$ (deg)	4.3	5.28	**5.41**	5.01	5.31	2.54
$\theta_{5/rev}$ (deg)	5.73	3.86	4.81	**7.87**	7.62	2.38
$\theta_{345/rev}$	0.708	0.769	0.798	0.867	**0.878**	0.408
Constraints						
1st Tor Freq (/rev)	5.71	4.71	4.93	5.48	5.28	5.48
M_{11} (kg/m)	0.694	0.688	0.697	0.697	0.72	0.642
SC (%c)	23.81	17.05	17.19	21.51	24.77	19.01
CG (%c)	20.33	27.92	27.79	27.95	28	21.87
Design Variables						
Spar End (c)	0.85	0.849	0.85	0.839	0.846	0.443
Spar Web (c)	0.85	0.303	0.318	0.839	0.843	0.443
m_1 (kg/m)	0.332	0.271	0.273	0.313	0.334	0.23
m_2 (kg/m)	0.009	0.063	0.06	0.034	0.038	0.22
Normalized Ply Thicknesses						
Ply 2a (E-Glass)	5	1	2	5	4	1
Ply 2 (AFC)	1	1	1	1	1	1
Ply 4 (AFC)	1	1	1	1	1	1
Ply 6-7 (E-Glass)	1	9	10	1	1	1
Ply Angles						
Ply 1 (E-Glass)	0	0	0	87	0	0
Ply 2a (S-Glass)	0	0	0	-28	0	0
Ply 2 (AFC)	45	45	45	-45	45	45
Ply 4 (AFC)	-45	-45	-45	45	-45	-45
Ply 6-7 (E-Glass)	0	0	0	1	0	0
Other Parameters						
S_{44} (Nm^2)	56.5	32.9	37	58.1	55.8	25.1
Act Mom (Nm)	2.38	1.37	1.54	2.44	2.33	0.76
2nd Flap Freq (/rev)	2.77	2.77	2.78	2.76	2.76	2.72
3rd Flap Freq (/rev)	5.4	5.42	5.44	5.35	5.36	5.07
Max ε_{11} ($\mu\varepsilon$)	2489	3994	3364	1340	2896	3935
Max ε_{12} ($\mu\varepsilon$)	4220	5600	4748	6765	4711	5591

The shape of the cross section for the optimized cases is shown in Figure 4-6. In these section, the leading edge ballast mass is presented by a red circle while the ballast mass used near the vertical spar web is represented by a blue circle.

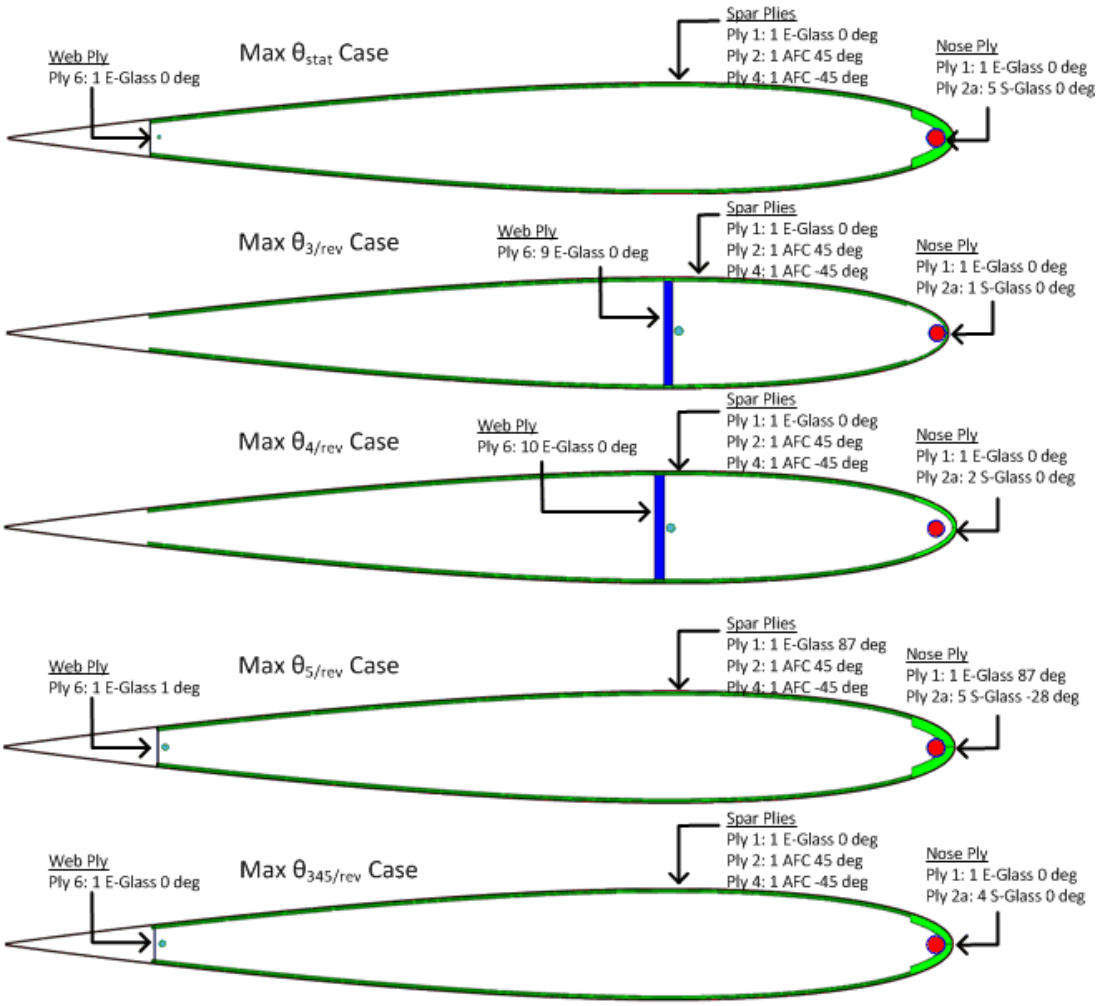

Figure 4-6: Cross Section for the Optimized Cases obtained with Mixed Design Variables

4.5 Post Processing of Optimization Results

The final results obtained at the end of optimization process with mixed design variables, as shown in Table 4-22, are analyzed further in order to check their validity.

Here three different kinds of analyses are performed. In the first check, the variation of vibratory loads in forward flight condition is analyzed when no flap actuation is applied in order to make sure that the optimized designs do not lead to higher baseline vibration (vibration level in the absence of twist actuation). In the second analysis, variation of the amplitude of dynamic twist with advance ratio is determined for different actuation frequencies. And finally, circle plots are generated for each of the optimized cases in forward flight condition at different actuation frequencies in order make sure that the optimized results do provide higher authority for vibration reduction at the hub.

4.5.1 Effect on Baseline Vibration

In this case, the aeroelastic analysis for each of the optimized cases and baseline case is performed at $\mu = 0.24$ using the "Trim Analysis" (wind tunnel trim). When the trim condition is reached, the amplitude of 4/rev vibratory load at the hub in fixed system is recorded. The percentage difference in the vibratory loads for F_z, M_x and M_y components with respect to the baseline case is shown in Figure 4-7. The results obtained show that the increase in baseline vibration is less than 13% for all the optimized cases. Among all the cases, the "Max $\theta_{5/rev}$" case shows maximum vibration.

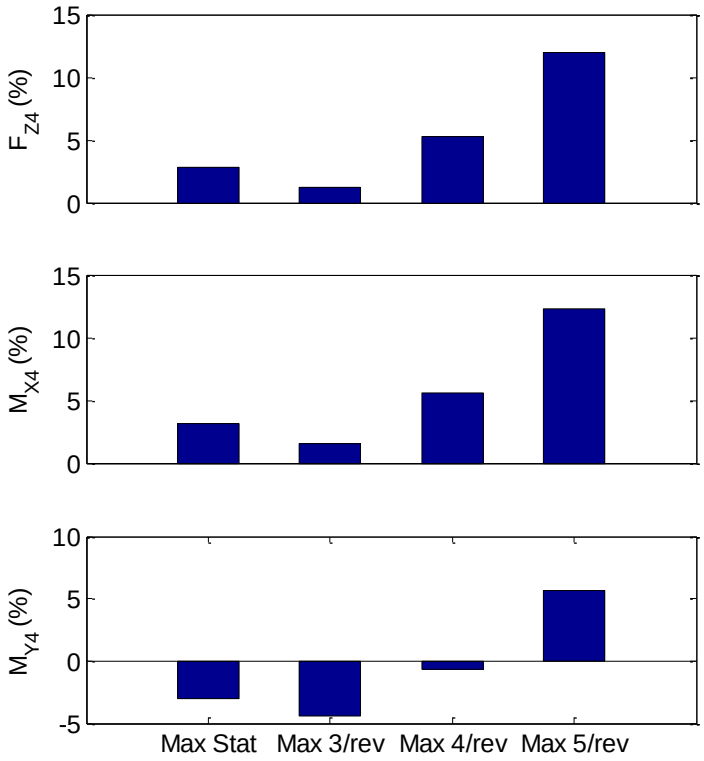

Figure 4-7: Percentage Increase in Vibratory Loads

4.5.2 Effect of Advance Ratio

In this section, aeroelastic studies with "Trim Analysis" were performed for each of the optimized cases at different forward flight speeds. This study was performed to verify the original assumption that there is no significant change in the amplitude of tip twist with forward flight speed. The results obtained for actuation frequencies of 3, 4 and 5/rev are shown in Figure 4-8, Figure 4-9 and Figure 4-10, respectively. The results obtained show that the variation in the amplitude of dynamic tip twist with advance ratio is small. Since the results presented here include "Trim Analysis", they do not match exactly the results shown in Table 4-22 where "Periodic Analysis" is used. For each of the actuation frequency, the corresponding case provides maximum dynamic twist at all the advance ratios considered.

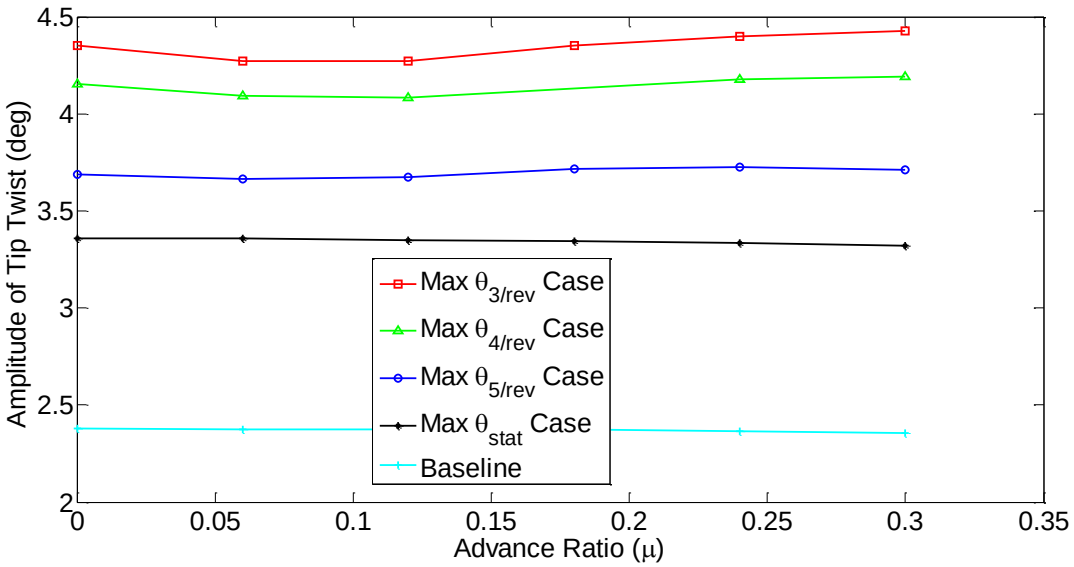

Figure 4-8: Effect of advance ratio at 3/rev actuation frequency

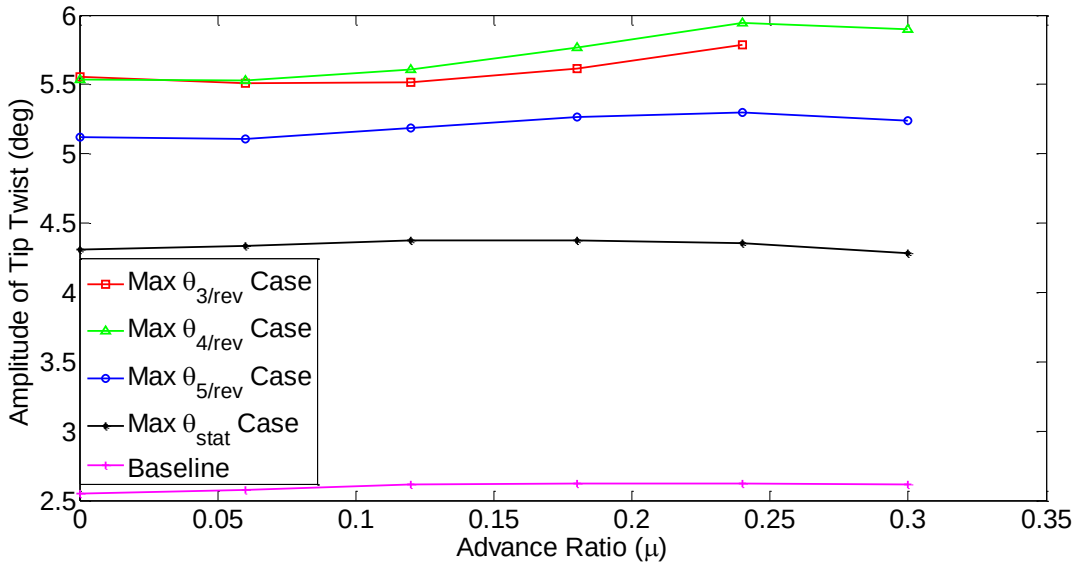

Figure 4-9: Effect of Advance Ratio at 4/rev Actuation Frequency

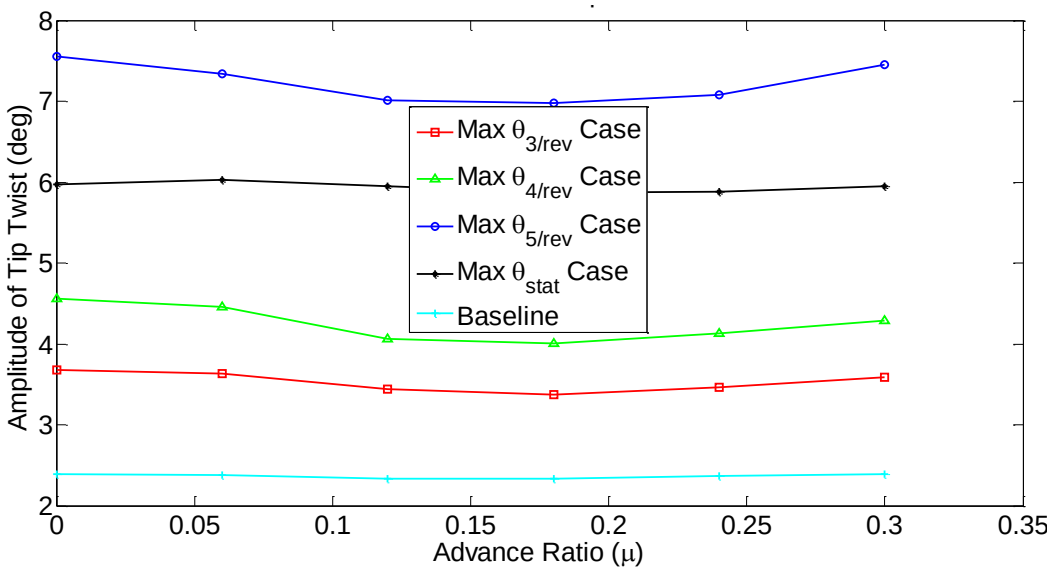

Figure 4-10: Effect of Advance Ratio at 5/rev Actuation Frequency

4.5.3 Circle Plot for Optimized Cases

In order to generate the circle plot for each of the optimized cases and the baseline case, the twist actuation is provided at a fixed frequency and the phase of actuation is varied from 0 to 360 degree in the intervals of 30 degree. Once the response for each of the hub loads in the fixed system is obtained, FFT is used to determine the sine and cosine component of the response corresponding to 4/rev frequency. The circle plots generated for 3/rev, 4/rev and 5/rev actuation frequencies for vertical component of the force at the hub (F_z) are shown in Figure 4-11, Figure 4-12 and Figure 4-13, respectively.

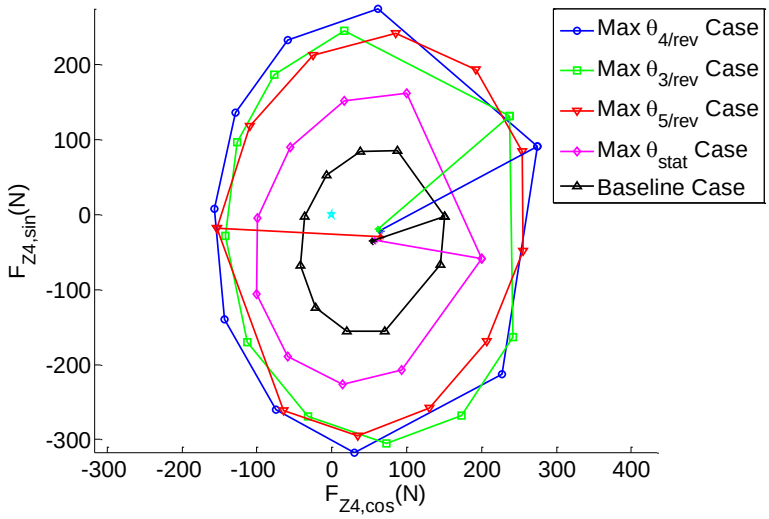

Figure 4-11: Circle Plot for 3/rev Actuation Frequency

Since the optimum result obtained for the "Max $\theta_{3/rev}$" and "Max $\theta_{4/rev}$" cases are close to each other, the circle plots corresponding to these cases for 3/rev and 4/rev actuation frequencies are close to each other. As shown in Figure 4-11 and Figure 4-12, the circle plot corresponding to "Max $\theta_{5/rev}$" case has larger size than that corresponding to "Max θ_{stat}" case. Thus, each of the dynamically optimized cases performs better that statically optimized case for 3/rev and 4/rev actuation frequency.

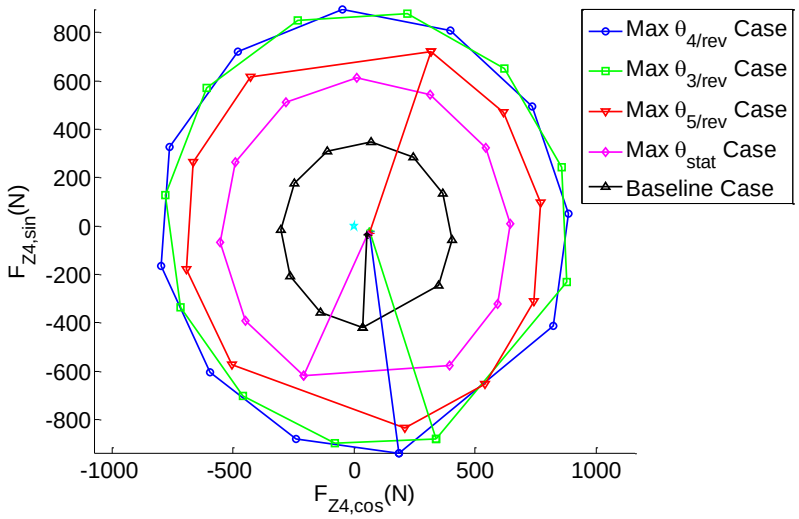

Figure 4-12: Circle Plot for 4/rev Actuation Frequency

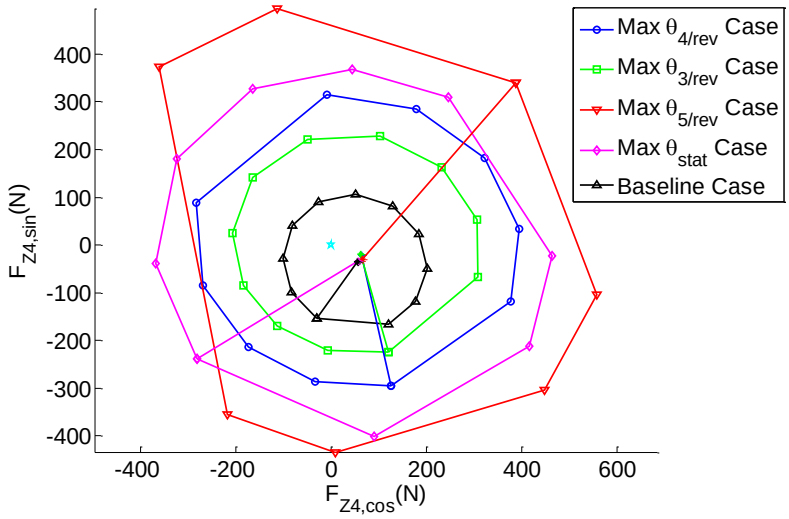

Figure 4-13: Circle Plot for 5/rev Actuation Frequency

In case of the circle plot obtained at 5/rev actuation frequency, the "Max $\theta_{5/rev}$" case is the most effective for vibration reduction as shown in Figure 4-13. Since, the optimum design for "Max θ_{stat}" case is close to that for "Max $\theta_{5/rev}$" case, the "Max θ_{stat}" case outperforms the "Max $\theta_{3/rev}$" and "Max $\theta_{4/rev}$" cases for vibration reduction at 5/rev actuation frequency.

The results presented in this section highlight the original assumption that authority of an active twist rotor to reduce vibratory loads at the hub can be increased by maximizing the amplitude of dynamic twist obtained from twist actuation.

4.6 Concluding Remarks

The use of prepreg material for manufacturing composite aerospace structures leads to discrete design variables in the design and optimization studies. In order to obtain a realistic and manufacturable design at the end of optimization, the ply thicknesses and ply angles should be treated as discrete design variables. This chapter presented the

architecture of a design framework which can be used to perform optimization studies with mixed design variables for designing a composite active twist rotor blade. In the proposed framework, the optimum solution with mixed design variables is obtained using three different methods, in addition to the optimum design when all the variables are treated as continuous. This facilitates the designer to estimate *the loss* due to "discretization" and make necessary changes to improve the design.

The mixed design variable optimization framework was successfully used to design the cross section of a composite rotor blade with embedded active material. In the first case, ply thicknesses were considered as discrete design variables, in addition to the continuous design variables like the chordwise location of vertical spar web, ballast masses and chordwise location where the active plies end. In this case, the minimum allowable normalized thickness of prepreg plies was fixed at "0.1" instead of "0" to prevent the mesh generator from crashing. The results obtained from these studies showed that some of the plies had normalized ply thickness as "0.1" in the optimum results, indicating that these plies should be removed from the analysis. In the next step, these passive plies were not considered as design variable and the minimum allowable normalized thickness was fixed to "1". And the third case considered included the ply angles as discrete design variables in addition to the ply thicknesses.

The final results obtained showed that:

1) The difference between the results obtained from continuous and mixed-variable optimization depends on the objective function being considered.

2) The mixed design variable results obtained using three methods are close to each other. And it is sufficient to obtain only the "Mixed Solution 1" and "Mixed Solution 2" to predict the optimum solution with mixed design variables since the "Mixed Solution 3" is very time consuming.

3) While maximizing the static and dynamic twist, the optimum design obtained always led to a stiffer cross section and thus most of the optimum designs had lower cross sectional strains.

4) A thick prepreg layer is required near the leading edge (Ply 2a) to obtain higher active twisting moment, but it may increase the torsional stiffness which may cause the dynamic twist performance to deteriorate.

5) Increasing the chordwise coverage of active plies is better than increasing the thickness of active plies, in order to get higher static and dynamic twist. Also, boxed-shaped spar design, in which the chordwise location where the spar plies end and the chordwise location of vertical spar web are close to each other, is suitable for maximizing the dynamic twist amplitude.

6) There is a significant difference in the optimum design obtained for different actuation frequencies.

7) For the results obtained for this particular case, the optimum design obtained by maximizing amplitude of dynamic twist at 3, 4 and 5/rev actuation frequencies tends to be closer to result obtained for maximizing amplitude for 5/rev actuation

frequency. This can be attributed to the higher cross-sectional stiffness in Max $\theta_{5/rev}$ case which in turn results in higher active twisting moment.

Chapter 5. New Strategy for Design of Composite Rotor Blade with Active Flaps

The optimization framework and strategy developed for the design of rotor blades with active twist is extended for the design of composite rotor blade with active flaps in this chapter. The optimum blade design must aim to maximize the flap authority for vibration reduction while satisfying the constraints on the chordwise location of cross-sectional center of gravity (CG) and shear center (SC), blade mass per unit length, torsional frequency, etc. Since the vibration reduction in rotors with active flaps is obtained through the servo-flap effect, the amplitude of tip twist obtained from flap actuation is a good metric for estimating the flap authority. Thus, in the analysis performed here, the amplitude of tip twist obtained due to the flap motion is used as the objective function which is maximized. The objectives of this chapter are:

a) To demonstrate the use of new optimization strategy with high fidelity analysis tools for designing a rotor blade with active flaps
b) To design a realistic composite rotor blade to enhance the effect of active flaps for vibration reduction.

5.1 Aeroelastic Analysis with Active Flaps

The aeroelastic analysis performed for analyzing a rotor blade with active flaps *is similar* to that described in Chapter 3 for analyzing an active twist rotor blade. The aeroelastic analysis performed using RCAS has been modified to account for the

presence of active flaps. The aerodynamic analysis for active flaps is performed in RCAS using the flexible airfoil theory [167] and 3-D dynamic inflow [168] model. The table lookup required for analyzing a rotor blade with active flaps in RCAS is generated using XFOIL.

5.2 Baseline Rotor Blade

A composite rotor blade that can be tested in the University of Michigan spin test stand (see Figure 5-1) is used as the baseline rotor blade. This test stand was used earlier for testing a $1/6^{th}$ Mach-scaled CH-47D rotor blade with active twist [58] and active flap [112]. The properties of the test stand and baseline rotor blade are given in Table 5-1. The rotor has a 10 ft diameter and it has articulated configuration with a root offset of 0.15R. The nominal operating RPM is 1336 which corresponds to Mach number of 0.6 at the blade tip in hover condition.

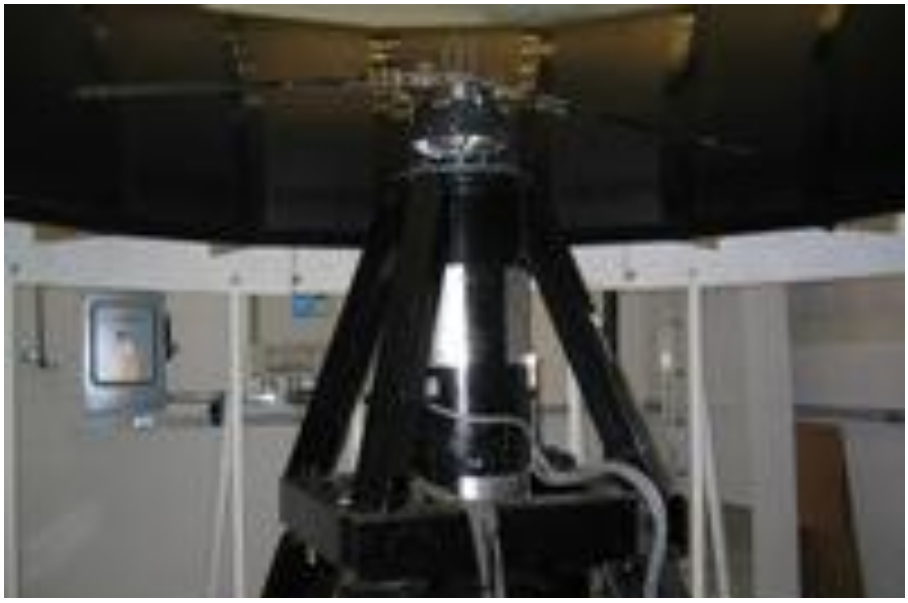

Figure 5-1: University of Michigan Spin Test Stand

The composite rotor blade is made up of E-Glass and IM7 graphite plies as shown in Figure 5-2. The baseline blade has leading edge ballast mass to bring the CG of the cross section close to the quarter chord. The D-shaped cross section consists of 2 layers of E-Glass plies oriented at ±45 deg as the overwrap plies. The main spar consists of 2 layers of IM7 at 0 deg and 2 layers of E-Glass at ±45 degrees. The vertical spar web located at 0.38c has 3 layers of E-Glass at 0/90 degree.

Table 5-1: Rotor Properties

Configuration	Articulated
Radius	1.54m
Chord	0.136m
Num of Blades	4
Air Density	1.225 kg/m^3
C_T	0.0066
RPM	1336
Hinge Location	0.15R
CG (%c)	25.32
SC (%c)	22.8
Airfoil	VR7

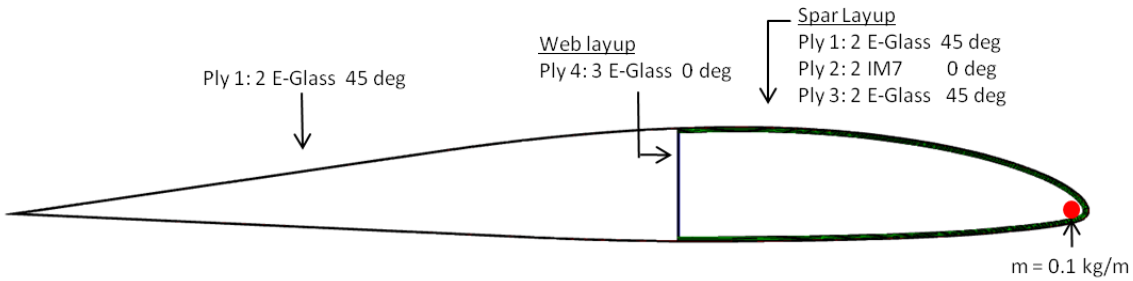

Figure 5-2: Cross-Sectional Layup for the Baseline Rotor Blade

For testing the rotor blade with active flaps, a piezoelectric actuator is mounted in the spar region of blade as shown in Figure 5-3. In order to mount the actuator and install the flap, cutouts are made in the spar region of blade and near the trailing edge. The loss in stiffness due to these cutouts is balanced by including additional plies in the cutout

region. However, the presence of actuator and flap supports leads to additional mass in the blade which adds to the inertia of the blade. In the aeroelastic analysis performed in this chapter, the effect of actuator and flap support inertia is included. The reference actuator used in this study is the X-frame actuator developed at MIT [119] and it is small enough to fit inside the spar of rotor blade cross section as shown in Figure 5-3. The details of the first single flap configuration considered in this study are presented in Table 5-2. The structural frequencies of the baseline rotor blade (with the actuator and flap support inertia) are listed in Table 5-3.

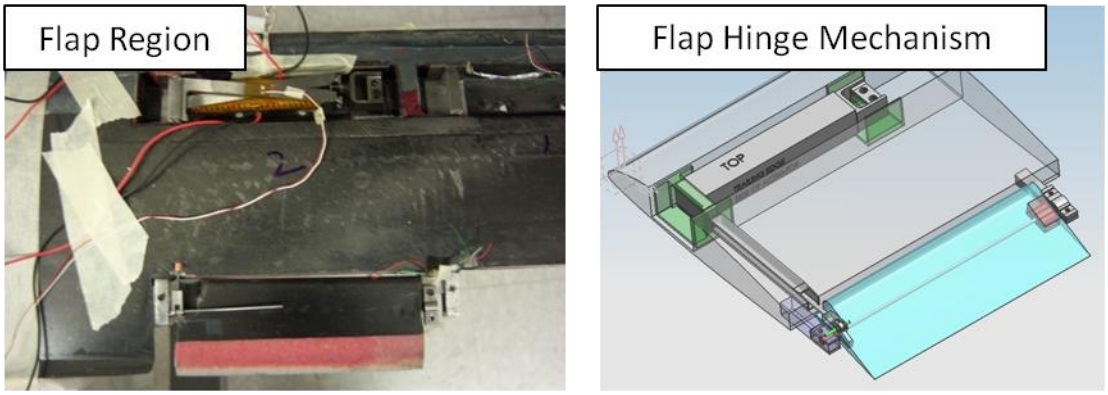

Figure 5-3: Active Flap Mechanism

Table 5-2: Flap and Actuator Dimensions

Flap Dimensions	
Flap Length	0.12R
Flap Chord (c_f)	0.25c
Flap Center (r_f)	0.78R
Actuator Details	
Size	3.6" x 0.9" x 0.5"
Actuator Location	0.25c and 0.78R
Actuator+Support Mass	96 gm

Table 5-3: Structural Frequencies of the Rotor Blade

Mode Shape	Frequency (/rev)
1st Chordwise	0.51
1st Flapwise	1.12
2nd Flapwise	3.57
1st Torsion	4.21
3rd Flapwise	6.86
2nd Chordwise	7.49

5.3 Preliminary Analysis

A "Periodic Analysis" was performed for analyzing the rotor blade with active twist instead of "Trim Analysis" in the optimization studies performed in the earlier chapter to reduce the computational time. The trim targets used in the "Trim Analysis" are: C_T = 0.0066, no cyclic moments ($M_x = 0$ and $M_y = 0$), and the blade pitch settings are used as the trim targets (wind tunnel trim). In the case of "Periodic Analysis", the blade pitch settings are kept constant and the equations of motion are solved in time domain till the system response is periodic. It was demonstrated using the results obtained from optimization in Chapter 3 that a "Periodic Analysis" is sufficient to obtain a design which maximizes the dynamic twist. Hence, in the case of active flap studies, both "Periodic Analysis" and "Trim Analysis" are performed in the preliminary analysis to verify if "Periodic Analysis" is sufficient to capture the amplitude of dynamic twist accurately.

In the first study, the frequency of actuation is varied from 3/rev to 5/rev in hover conditions for flap deflection of ±4 degrees and the mean value and amplitude of twist at the blade tip are obtained. The results obtained with "Periodic Analysis" and "Trim Analysis" is shown in Figure 5-4. The results show that although there is a significant difference in the mean value of twist at the blade tip, the amplitude of dynamic twist for

both the analyses are very close to each other. A higher mean value for the tip twist implies that the blade is experiencing higher aerodynamic loads in the trim analysis.

Next, the advance ratio was varied from 0.0 to 0.3 and the amplitude of dynamic twist was determined using "Trim Analysis" and "Periodic Analysis" for 4/rev actuation frequency. The variation of amplitude of tip twist with advance ratio is shown in Figure 5-5. For low advance ratios, the difference between the amplitude of tip twist predicted by both the analyses is small; however, it increases with an increase in the forward flight speed. The blade pitch settings obtained from the "Trim Analysis" (for analysis with and without the flap motion) and pitch settings used in the "Periodic Analysis" are shown in Figure 5-6. The results obtained with "Trim Analysis" show that for small values of μ, only the collective pitch angle is used for obtaining trim while the contribution from cyclic pitch angles is small. For these cases, the amplitude of dynamic twist obtained from "Periodic Analysis" and "Trim Analysis" match very well. As the advance ratio increases, there is a decrease in collective pitch angle and increase in cyclic pitch angles, which leads to a noticeable in the amplitude of dynamic twist obtained from these two analyses.

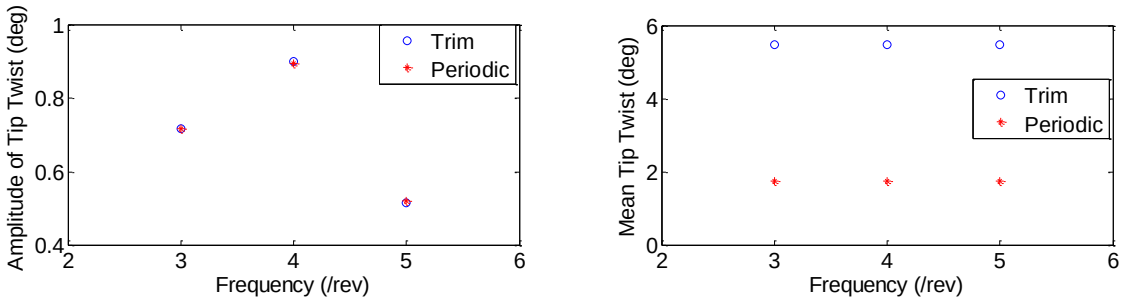

Figure 5-4: Variation of Tip Twist with Actuation Frequency

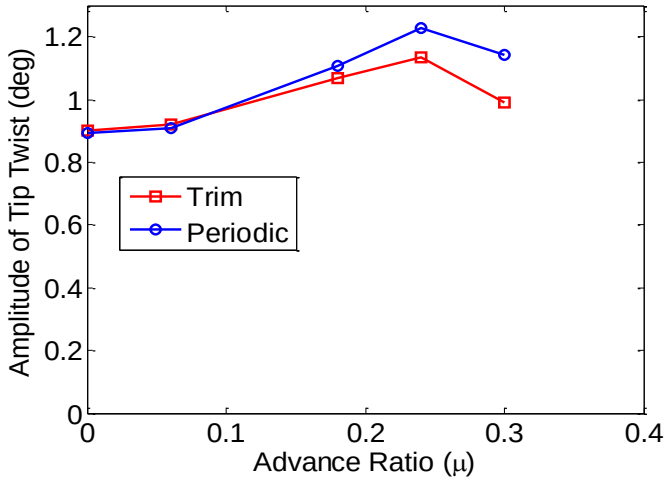

Figure 5-5: Variation of Amplitude of Tip Twist with Advance Ratio

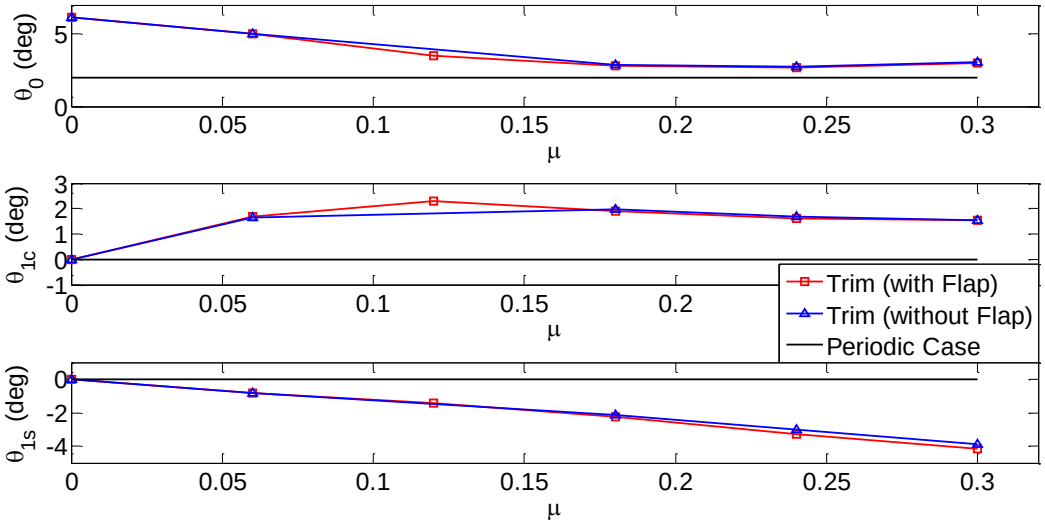

Figure 5-6: Variation of Trim Variables with Advance Ratio

In order to determine the optimum range of flap deflection required to obtain vibration reduction, the circle plot technique was used. To obtain a circle plot, the flap was actuated with 4 degree amplitude at 4/rev frequency and the phase of actuation was varied from 0 to 360 degrees in intervals of 30 degree. For each of the responses, the cosine component of the 4/rev load was plotted against the sine component of 4/rev load, as shown in Figure 5-7. The line drawn from the baseline vibration point joins the point on the circle plot which corresponds to a phase angle of 0 degree for flap actuation. For

each of the vibratory hub load component, the origin (which corresponds to zero vibration) is enclosed by the circle plot. This implies that the flap deflection of ±4 degrees at 4/rev actuation frequency is sufficient to reduce the 4/rev component of the vibratory load at hub.

Based on the results obtained in the preliminary analysis, it can be concluded that:

a) The amplitude of dynamic twist obtained from the "Periodic Analysis" is very close to that obtained from the "Trim Analysis" for different flap actuation frequencies at small values of μ.
b) The "Trim Analysis" shows that there is approximately 15% variation in the amplitude of dynamic twist for higher advance ratios. Thus, the amplitude of dynamic twist obtained in hover condition is representative of the amplitude of dynamic twist which will be obtained in forward flight conditions.
c) Hence, the amplitude of dynamic twist obtained in hover condition using "Periodic Analysis" can be used as the objective function for the optimization studies.

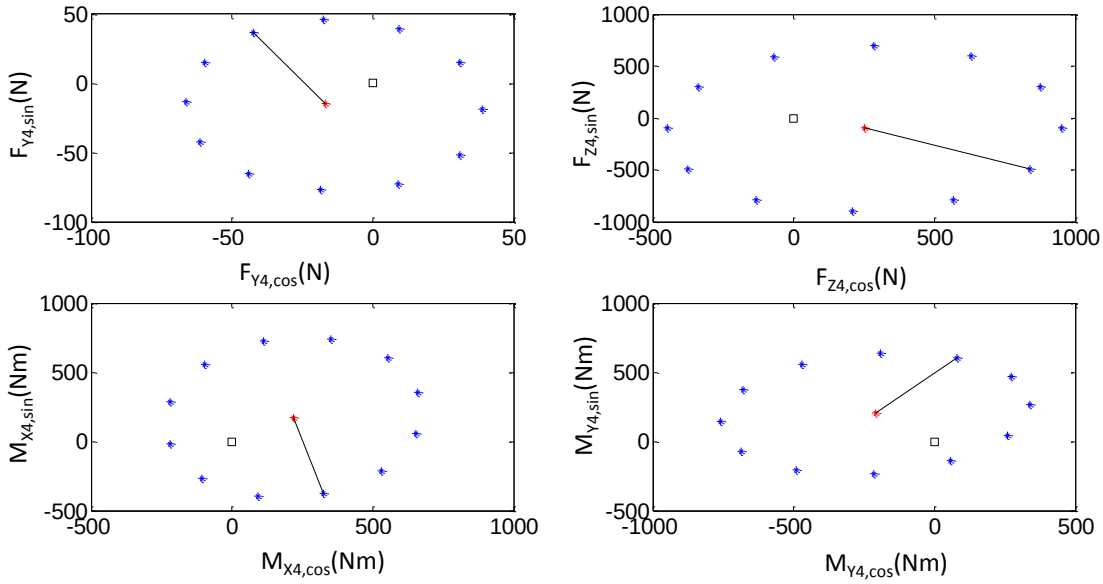

Figure 5-7: Circle Plot for 4/rev Actuation Frequency
(* = Vibration for the Baseline Case, * = Vibration for Flap Actuated Case, □ = Origin)

5.4 Optimization Problem Definition

In this section, optimization studies are presented in which the cross-sectional layup is determined for a composite rotor blade with active flap. The aim of the optimization study is to enhance the effectiveness of active flaps for vibration reduction. In order to achieve this target, optimization study is performed with the amplitude of dynamic twist in hover condition as the objective function. The objective function considered in this study is: Maximize the amplitude of tip twist for 4/rev flap actuation (Max $\theta_{4/rev}$). The optimization studies are performed for active flap located at three different spanwise locations, as shown in Figure 5-8.

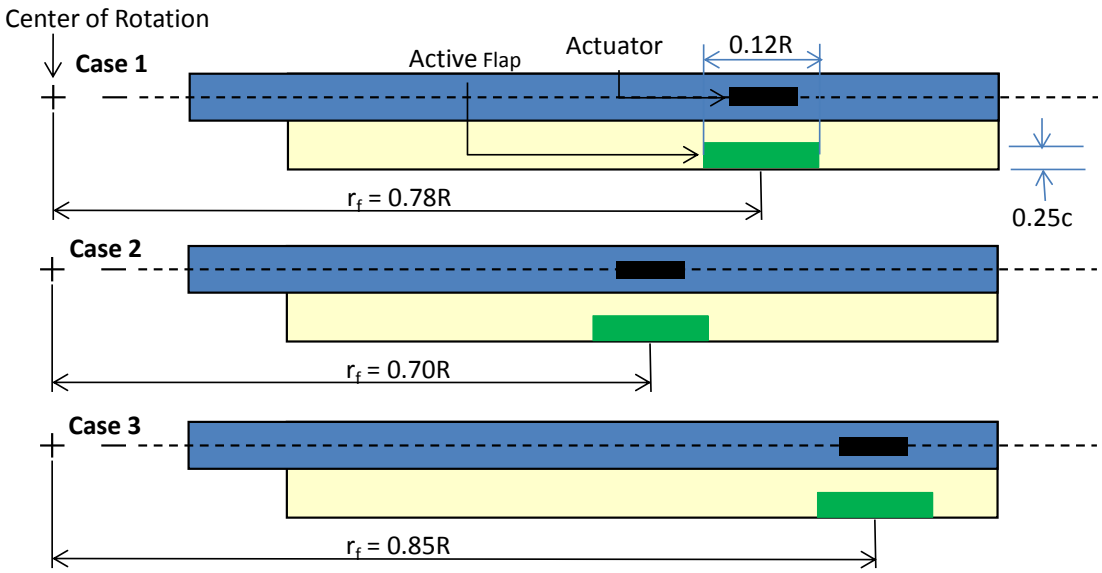

Figure 5-8: Spanwise Location for Active Flaps

The cross section for the baseline blade is shown in Figure 5-2. The design variables used in the optimization are listed in Table 5-4. The design variables used are: the chordwise location where the spar plies end, chordwise location of the vertical spar web, the two ballast masses, and the normalized ply thicknesses and ply angles for all the composite plies used in the cross section. Even though the baseline blade includes only one leading edge ballast mass, additional ballast mass is used as the design variable since it is useful in tuning the dynamic properties of rotor blade, as observed in the results presented in Chapter 3 and 4. In order to make the rotor blade design more realistic, the location of first ballast mass is fixed near the leading edge at x = 0.02c while the second ballast mass is located just in front of the vertical spar web. (This is done to ensure that the ballast mass is added in the region where passive plies can be used to support it and thus prevent the ballast mass for flying out during the operation). In order to prevent the mesh generator from crashing, the lower bound on ply thickness is fixed at 0.1 instead of zero. A value of 0.1 for normalized ply thickness in an optimum design implies that that

particular ply is not required in the cross section and should be removed in the next optimization. In this study, the lower bound for the normalized thickness of Ply 1 is "1," since the outermost ply cannot be removed from the cross section. The bounds used for ply angles depend upon the nature of the prepreg. For the unidirectional plies, the ply angle varies from -90 to +90 degrees, whereas for the bidirectional plies, the ply angle varies from 0 to 90 degrees.

Table 5-4: Design Variable used for Optimization Study

	Design variables	Baseline	Lower	Upper	Ply Type
1	Spar End (c)	0.4	0.2	0.85	
2	Main Spar Web Loc (c)	0.4	0.2	0.85	
3	Ballast Mass 1 (m_1) (kg/m)	0.1	0	0.25	
4	Ballast Mass 2 (m_2) (kg/m)	0	0	0.25	
Normalized Ply Thickness					
5	Ply 1 Thickness	2	1	4	E-Glass
6	Ply 2 Thickness	2	0.1	4	IM7
7	Ply 3 Thickness	2	0.1	4	E-Glass
8	Ply 4 Thickness	3	0.1	10	E-Glass
Ply Angle					
9	Ply 1 Angle	45	0	90	E-Glass
10	Ply 2 Angle	0	-90	90	IM7
11	Ply 3 Angle	45	0	90	E-Glass
12	Ply 4 Angle	0	0	90	E-Glass

Table 5-5: Constraints used in the Optimization

Constraints	Baseline	Min	Max
SC (%c)	22.8	17	25
CG (%c)	25.3	20	28
M_{11} (kg/m)	0.309	0.26	0.36
Tor Freq (/rev)	4.22	**3**	6
Max ε_{11} ($\mu\varepsilon$)	2605	0	3500
Max ε_{12} ($\mu\varepsilon$)	4042	0	5000

The constraints used in the optimization are shown in Table 5-5. The mass per unit length for the cross section is constrained to lie within ±15% of the baseline value. In the optimization studies performed earlier for active twist rotor, the maximum value of strains in the cross section was not considered as a constraint. The optimum results obtained for active twist rotor were always stiffer as compared to the baseline cross section and in general, they had lower cross-sectional strains. However, in the case of optimization studies with active flap, the tendency of the optimizer is to design a rotor blades cross section with lower cross-sectional stiffness. Hence, most of the designs obtained without the constraint on strains had very high cross sectional strains. It should be noted that the maximum value for allowable strains used in the constraints listed in Table 5-5 is well below the maximum strain limit for the material. Since a "Periodic Analysis" is performed here in hover condition, the blade does not experience worst-case aerodynamic loads. Hence, the strains observed in the cross section are mainly due to the large centrifugal force acting on the blade.

5.5 Optimization Results

The optimization problem is solved using the Mixed-Variable Optimization Framework described in Chapter 4. As observed in Chapter 4, the framework is capable of determining solution with both continuous design variables and with mixed design variables. In case of optimization with mixed design variables, the ply angles and ply thicknesses are treated as discrete. In this section, only the best result obtained with mixed design variables is presented and compared with the results obtained using continuous design variable. The final results obtained for objective function is shown in Table 5-6.

Table 5-6: Results for Flap centered at r_f = 0.78R

Cases	Max $\theta_{4/rev}$	Max $\theta_{4/rev}$	Baseline
Objective Function	**Cont**	**Mixed**	
$\theta_{4/rev}$ (deg)	1.02	1.01	0.89
Constraints			
Tor Freq (/rev)	4.13	3.91	4.21
M_{11} (kg/m)	0.27	0.28	0.31
SC (%c)	22.53	20.30	22.81
CG (%c)	27.79	24.01	25.32
Max ε_{11} ($\mu\varepsilon$)	1266	1216	2606
Max ε_{12} ($\mu\varepsilon$)	3558	3715	4041
Design Variables			
Spar End (c)	0.446	0.456	0.4
Spar Web Loc (c)	0.307	0.289	0.4
m_1 (kg/m)	0.050	0.051	0.1
m_2 (kg/m)	0.001	0.015	0
Normalized Ply Thicknesses			
Ply 1 (E-Glass)	1.27	1	2
Ply 2 (IM7)	3.72	4	2
Ply 3 (E_Glass)	1.04	1	2
Ply 4 (E-Glass)	7.51	8	3
Ply Angles			
Ply 1 (E-Glass)	61.2	64	45
Ply 2 (IM7)	8.2	8	0
Ply 3 (E-Glass)	55	53	45
Ply 4 (E-Glass)	56	57	0
Other Parameters			
S_{44} (Nm^2)	97.5	90.0	119.8
S_{55} (Nm^2)	532.3	573.4	332.9
2^{nd} Flap Freq (/rev)	3.91	3.98	3.57
3^{rd} Flap Freq (/rev)	7.89	8.51	6.86
Induced F_{Z4} (N)	319.08	318.92	272.22

The results obtained show 14% increase in the twist amplitude corresponding to 4/rev actuation frequency. The percentage increase in the amplitude of twist at the blade tip is small since the baseline case is close to the optimum design obtained by maximizing the

twist amplitude at 4/rev actuation frequency. The most important parameter while maximizing the dynamic twist amplitude is the first torsion frequency. The optimizer tries to get the first torsion frequency in the neighborhood of the flap actuation frequency. Besides this, the mass per unit length for each of the optimized cases is near its lower bound. The chordwise location of shear center stays close to the value obtained for the baseline case. The amount of ballast mass used in the cross section has reduced although there is a redistribution of ballast masses indicating that the optimizer is using the ballast masses to increase the torsional inertia in order to reduce the torsion frequency. The torsional stiffness for the cross section is mainly controlled by varying the thickness of Ply 3 which is the E-Glass ply. For the optimized case, the thickness of unidirectional IM7 ply (Ply 2) is at the maximum allowable value and its orientation is very close to 0 degree. Thus, the IM7 plies are mainly used to withstand the large centrifugal loads acting on the rotor blade cross section and thereby reduce the cross-sectional strains. The effect of increase in the thickness of unidirectional plies can also be seen in the value of cross-sectional bending stiffness (S_{55}) and second and third flapwise bending frequencies. The thickness of Ply 1 is at the minimum allowable value. The thickness of Ply 4 is important to keep the chordwise location of shear center within the bounds specified in constraints.

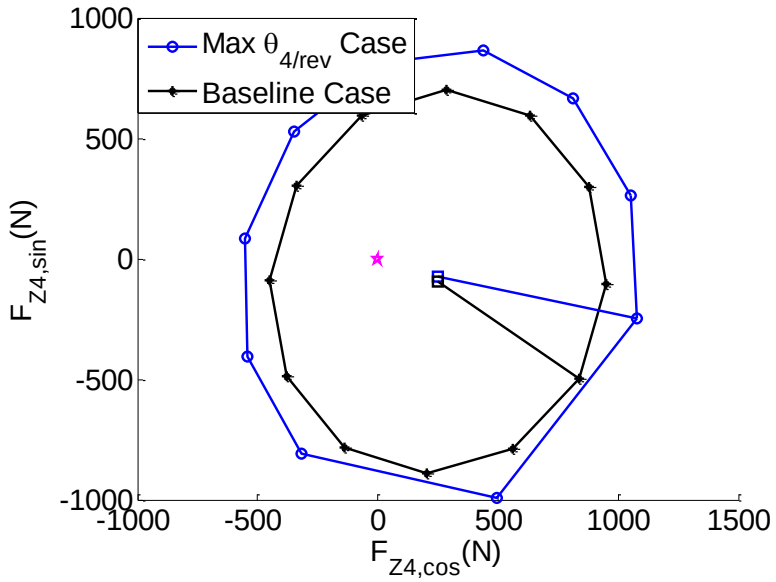

Figure 5-9: Circle Plot at r_f = 0.78R

The circle plot obtained for the optimized case is shown in Figure 5-9. It clearly shows the increase in control authority for vibration reduction in vertical component of the force at 4/rev frequency (F_{Z4}) at the hub.

In the next optimization study, the spanwise location of the flap (r_f) was fixed at 0.7R. The design variables and constraints used in the optimization are the same as those listed in Table 5-4 and Table 5-5, respectively. The final optimized result is shown in Table 5-7, for both the continuous and mixed design variable cases. The trend observed for design variables is the same as it was observed in previous results. The results show 9.32% increase in the amplitude of dynamic twist. The corresponding circle plot is shown in Figure 5-10. Here, the results show that when the flap is not actuated, the optimized case produces higher vibration but the increase in control authority for the optimized case over compensates for this.

Table 5-7: Results at r_f = 0.7R

Cases	Max $\theta_{4/rev}$	Max $\theta_{4/rev}$	Baseline
Objective Function	**Cont**	**Mixed**	
$\theta_{4/rev}$ (deg)	0.645	0.628	0.590
Constraints			
Tor Freq (/rev)	4.30	4.46	4.39
M_{11} (kg/m)	0.265	0.265	0.308
SC (%c)	24.9	21.9	22.5
CG (%c)	28.0	25.6	24.2
Max ε_{11} ($\mu\varepsilon$)	976	1552	2556
Max ε_{12} ($\mu\varepsilon$)	2143	4052	4042
Design Variables			
Spar End (c)	0.55	0.41	0.4
Spar Web Loc (c)	0.46	0.32	0.4
m_1 (kg/m)	0.06	0.04	0.1
m_2 (kg/m)	0.00	0.03	0
Normalized Ply Thicknesses			
Ply 1 (E-Glass)	1.01	1	2
Ply 2 (IM7)	4.00	4	2
Ply 3 (E-Glass)	0.28	1	2
Ply 4 (E-Glass)	2.58	6	3
Ply Angles			
Ply 1 (E-Glass)	64.30	49	45
Ply 2 (IM7)	4.50	5	0
Ply 3 (E-Glass)	7.90	61	45
Ply 4 (E-Glass)	86.10	15	0
Other Parameters			
S_{44} (Nm^2)	88.64	85.77	118.92
S_{55} (Nm^2)	785.27	556.76	332.83
2^{nd} Flap Freq (/rev)	4.03	3.74	3.34
3^{rd} Flap Freq (/rev)	8.85	8.18	6.71
Induced F_{Z4} (N)	233.12	219.99	204.98

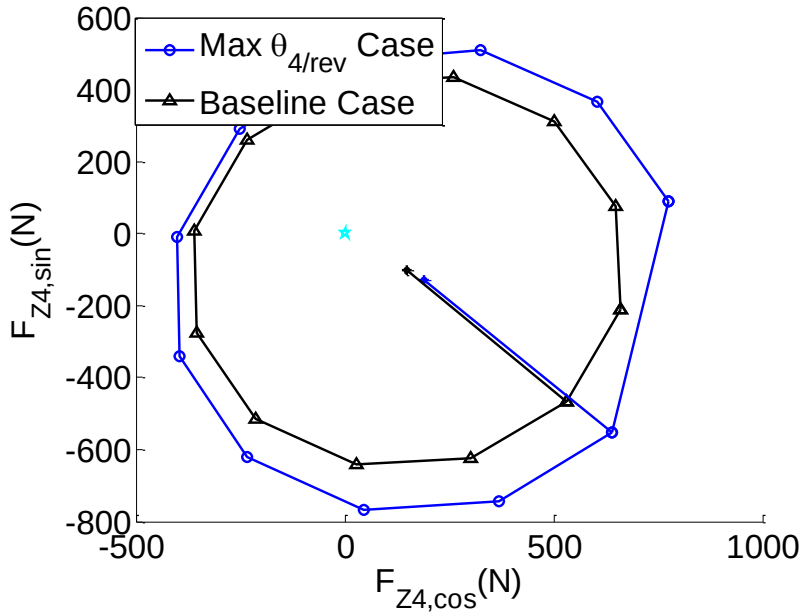

Figure 5-10: Circle Plot at 0.7R

Finally, the optimization was performed at r_f = 0.85R. The results obtained for this case is shown in Table 5-8. For this case, the final result obtained with continuous design variables and mixed design variables and the baseline case are very close to each other. The increase in the amplitude of dynamic twist for this case is only 4.58%. The circle plot for the optimized case and the baseline case for flap located at r_f = 0.85R is shown in Figure 5-11. The final results obtained for the three cases considered here are shown in Figure 5-12. The results show the expected trend where a higher flap deflection is obtained as the flaps are moved outboard. Also, the percentage increase in the amplitude of tip twist is different for each of the case. It is highest for the flaps located at 0.78R. It should be noted that, although the layup for the baseline cases is same in all the cases, the blade frequencies are different for the three baseline cases due to the inertia effects of flaps and actuator.

Table 5-8: Results for Flap at 0.85R

Cases	Max $\theta_{4/rev}$	Max $\theta_{4/rev}$	Baseline
Objective Function	**Cont**	**Mixed**	
$\theta_{4/rev}$ (deg)	1.14	1.14	1.09
Constraints			
1st Tor Freq (/rev)	4.26	4.26	4.16
M_{11} (kg/m)	0.266	0.272	0.308
SC (%c)	23.48	24.38	22.5
CG (%c)	27.39	26.84	24.23
Max ε_{11} ($\mu\varepsilon$)	2010	2004	2658
Max ε_{12} ($\mu\varepsilon$)	3961	3896	4143
Design Variables			
Spar End (c)	0.385	0.388	0.4
Spar Web Loc (c)	0.379	0.387	0.4
m_1 (kg/m)	0.026	0.03	0.1
m_2 (kg/m)	0.016	0.017	0
Normalized Ply Thicknesses			
Ply 1 (E-Glass)	1	1	2
Ply 2 (IM7)	3.04	3	2
Ply 3 (E-Glass)	3.98	4	2
Ply 4 (E-Glass)	6.06	6	3
Ply Angles			
Ply 1 (E-Glass)	68	68	45
Ply 2 (IM7)	-3	-3	0
Ply 3 (E-Glass)	75	75	45
Ply 4 (E-Glass)	0.9	7	0
Other Parameters			
S_{44} (Nm^2)	84.6	86.4	118.9
S_{55} (Nm^2)	473.7	467.4	332.8
2nd Flap Freq (/rev)	3.89	3.86	3.62
3rd Flap Freq (/rev)	8.4	8.31	6.98
Induced F_{Z4} (N)	361.8	360.4	350.3

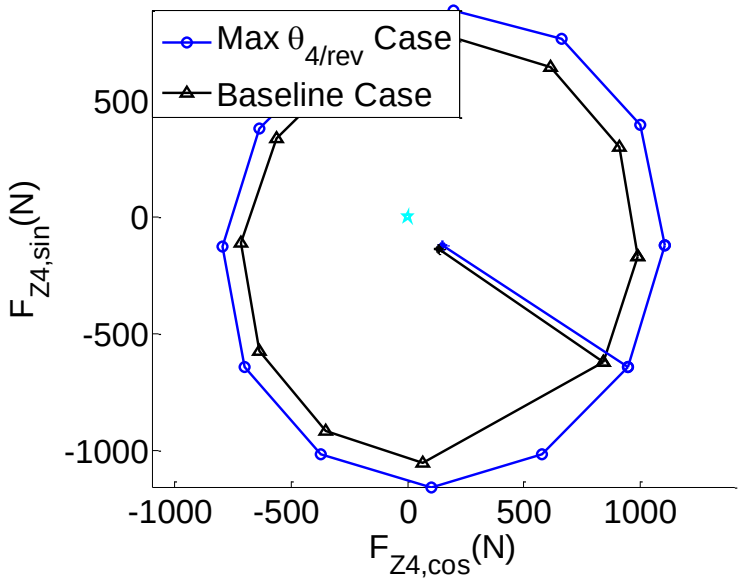

Figure 5-11: Circle Plot for Optimized Result at r_f = 0.85R

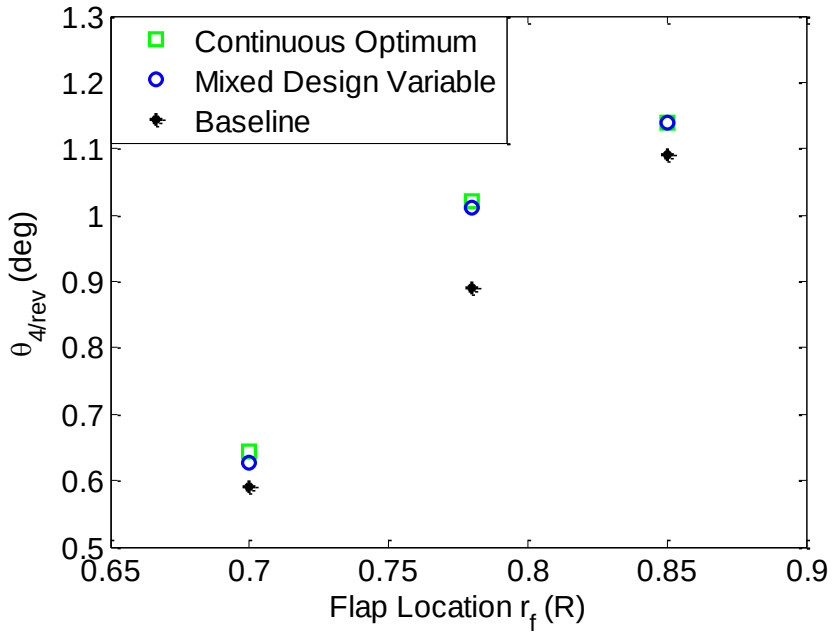

Figure 5-12: Optimized Results for different Spanwise Locations

The shape of the cross section for the baseline case and the optimized cases is shown in Figure 5-13. The results show that the spars get thicker as the spanwise location of flap

moves outboard. This is expected since the centrifugal force acting on the blade is highest when the actuator and flap mass is located near the tip region.

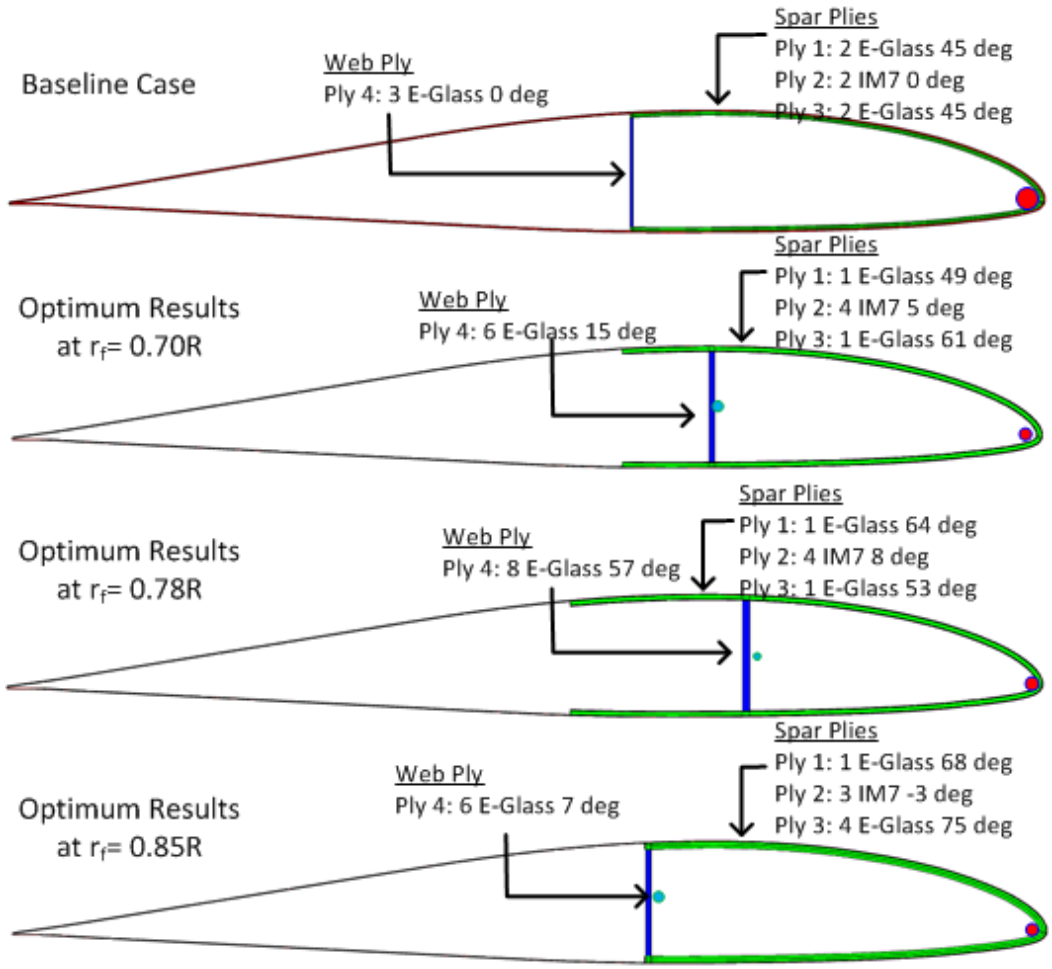

Figure 5-13: Optimized Cross Sections

5.6 Concluding Remarks

This chapter presented the modified version of the mixed design variable optimization framework for the design of a composite rotor blade with active flaps. The optimization framework was used to design composite rotor blade for a Mach-scaled rotor blade which can be tested in the University of Michigan spin test stand. In this chapter, optimization study was performed for the flaps located at three different spanwise locations. Here, the analysis includes the inertia effects of flap and actuator. The stiffness properties are

assumed to be uniform over the complete rotor blade (except the root region). The optimization studies were performed with ply thicknesses, ply angles, chordwise location of vertical spar web, and ballast masses as the design variables. The constraints are imposed on the chordwise location of CG and SC, first torsional frequency, mass per unit length and cross-sectional strains. In all the optimization studies, the amplitude of dynamic twist at 4/rev actuation frequency is used as the objective function which is maximized.

The optimization results showed:

a) 14% increase in dynamic twist for $r_f = 0.78R$

b) 9.32% increase in dynamic twist at $r_f = 0.7R$

c) 4.58% increase in dynamic twist at $r_f = 0.85R$

For each of the optimized cases, circle plots were obtained which show higher control authority for vibration reduction as compared to the baseline case. In all the optimized cases, there is a decrease in torsional stiffness and an increase in flapwise bending stiffness. Higher axial stiffness is helpful in reducing strains in the cross section due to the large centrifugal force. As observed in the case of active twist optimization studies, the optimizer tries to get the first torsion frequency of the blade closer to the actuation frequency. The dynamic tuning of the blade was performed by varying the ply angles for plies in the cross section and by varying the ballast masses used in the cross section. The optimization results are obtained using both continuous design variables and mixed design variables. In the case of the mixed variable optimization, ply angles and ply thicknesses were treated as discrete design variables. For all the optimized results

obtained, the results obtained with mixed design variables are close to those obtained with continuous design variables.

The framework developed here can be extended to analyze and design more complicated active flap configurations like blade with dual flaps or microflaps. The framework also allows for including more sections along the span which will result in an increase in the number of design variables.

Chapter 6. Performance Enhancement and Vibration Reduction in Dynamic Stall Condition using Active Camber Deformation

Deformable airfoils present a unique way to contribute to vibration reduction and performance enhancement in rotating wings. Camber deformation of the airfoil section is seen as an aerodynamically efficient alternative for controlling aerodynamic loads in order to obtain vibration reduction and performance enhancement. This chapter presents detailed analysis with cubic and quadratic camber deformation shape function to obtain these objectives.

In this study, the analysis is performed at $\mu = 0.33$, where the dynamic stall effects lead to high vibratory loads and poor performance. The aerodynamic analysis performed in this chapter includes a unified airloads model that allows arbitrary airfoil morphing with dynamic stall model, as described in [169]. In the next step, a global search over the parameter space – i.e., camber deformation amplitude, phase, and frequency of actuation – is conducted to identify the optimum points for the vibration and performance characteristics of the rotor blades with deformable airfoils. The optimization problem is solved using a surrogate-based approach as described in Chapter 3. Then starting from these optimum points of surrogated-based approach as initial points, gradient-based optimization is conducted using *fmincon* in MATLAB, to obtain the best results possible.

The objectives of this chapter are:

1) To demonstrate the implementation of unified airloads model for modeling the dynamic stall effects for arbitrary airfoil morphing.
2) To explore the possibility of performance enhancement and vibration reduction in dynamic stall condition using active camber deformation.
3) To compare the two different modes of camber deformation: camber deformation with a quadratic shape function and camber deformation with a cubic shape function.

6.1 Optimization Framework

The mathematical optimization problem can be stated as:

$$min\ f(x)$$

$$\text{subject to:} \quad x_l \leq x \leq x_u$$

where f is the objective function, which can be the vibratory vertical hub load at 4/rev frequency (F_{Z4}) or the performance related moment (M_{Z0}), x is the set of design variables that are bounded between a lower (x_l) and an upper (x_u) limits. The design variables used in this optimization problem are the amplitudes and phases of the camber deformation at different actuation frequencies.

The optimization process involves two different steps as shown in Figure 6-1. In the first step, initial range of design variables is given as input to create a surrogate model. Optimum results obtained from the surrogate based optimization (SBO) after multiple iterations are used as the initial values for the gradient based optimization (GBO) performed using MATLAB's *fmincon*. This process allows the gradient-based

optimization to start from different initial feasible points and perform local search for minima.

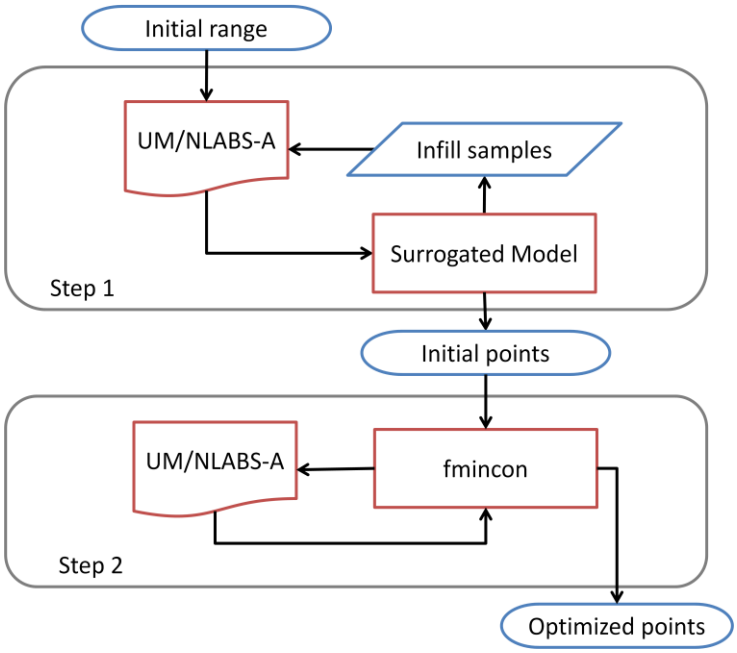

Figure 6-1: Two-step Optimization Process

6.1.1 Surrogate-based Optimization (SBO)

The SBO performed in this chapter is similar to that described in the earlier chapters. In order to form the surrogate, the objective function must first be evaluated over an initial set of design points. The surrogate is then generated by interpolating the initial design points. The MATLAB Latin hypercube function *lhsdesign* was used to generate the space-filling design of experiments used in this study. The points in the Latin hypercube represent design points at which aeroelastic simulations are to be conducted. Each simulation can be run independently of simulations at other design points; therefore the initial set of sample points is generated using distributed computers.

Once an initial set of fitting points have been produced, kriging interpolation [162, 170] is used to create the surrogate for the vibration and performance objective functions. After the surrogate objective function is created using kriging, the Efficient Global Optimization (EGO) algorithm [159] is used to determine optimum points. EGO algorithm accounts for uncertainty in the surrogate and is more efficient.

6.1.2 Gradient-based Optimization

The GBO is performed within MATLAB, using *fmincon* function from its optimization toolbox. The *fmincon* function minimizes a constrained nonlinear multivariable problem. In each of the iteration, the function solves a quadratic programming subproblem. Since the objective function is highly nonlinear, and since the design hyperspace is very complex, it is possible for *fmincon* to fall into a local extrema, leading to a sub-optimal solution. Therefore, it is necessary to run the optimization to completion, starting from different initial points. These initial points are determined from the optimization performed using the surrogate approach. At the end of the cycle, the gradient-based optimization provides a better optimum than if only the surrogated was used.

6.1.3 Aeroelastic Framework (UM/NLABS-A)

In order to analyze morphing-type rotors, one must consider several effects normally assumed to be unimportant in rotor problems. A quasi-3D geometrically nonlinear model for the aeroelastic analysis of an airfoil with camber deformation was developed in UM/NLABS-A (Non-linear Anisotropic Beam Solver - Aeroelastic) [145, 146].

Schematic of the various components in the aeroelastic framework is shown in Figure 6-2 and the details are described next.

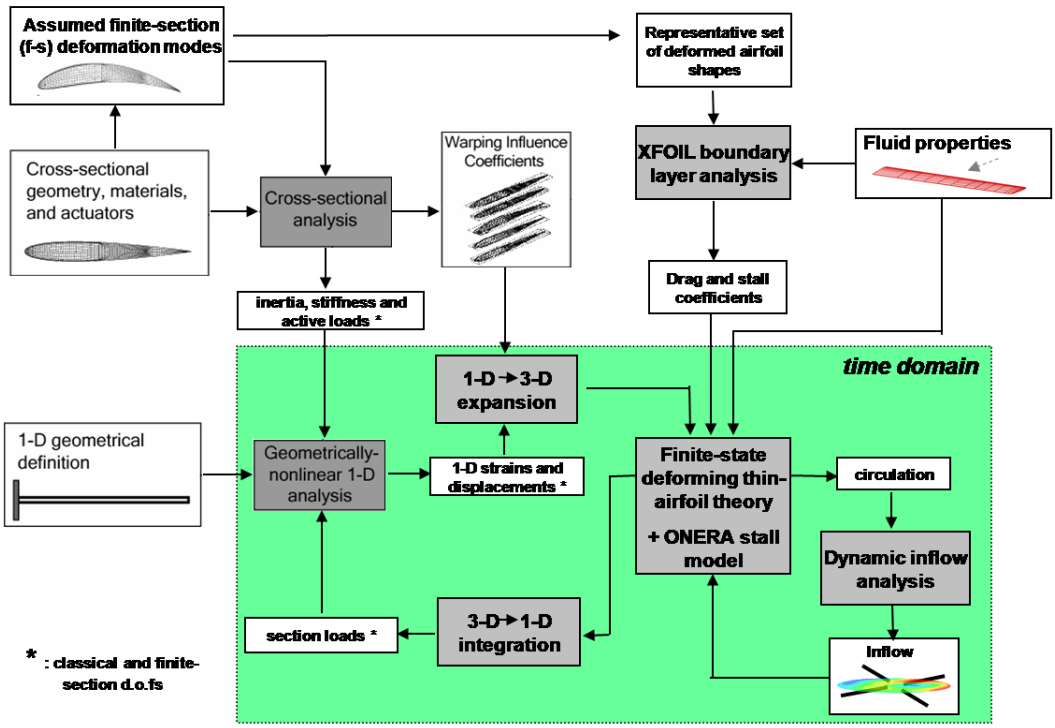

Figure 6-2: UM/NLABS-A Framework [145]

Structural model

The computational structural dynamics formulation used in the current study has been presented in [72, 171]. It follows the variational-asymptotic method for the analysis of composite beams [70]; that is, the equations of motion for a slender anisotropic elastic three-dimensional solid are approximated by the recursive solution of a linear two-dimensional problem at each cross section and a one-dimensional geometrically-nonlinear problem along the reference line. This procedure allows the asymptotic approximation of the three-dimensional warping field in the beam cross sections, which are used with the one-dimensional beam solution to recover the three-dimensional

displacement field. The present implementation adds an arbitrary expansion of the displacement field through a set of functions approximating the sectional deformation field to capture "non-classical" camber deformations, which are referred to as finite-section modes.

Aerodynamic Model

The aerodynamic analysis requires a unified model that allows for arbitrary airfoil motion, unsteady freestream, morphing airfoil shape and dynamic stall. The three key elements of the unified model are: the Peters flexible airfoil theory, the 3D dynamic inflow model, and the modified ONERA dynamic stall model. The schematic of the unified airloads model is shown in Figure 6-3.

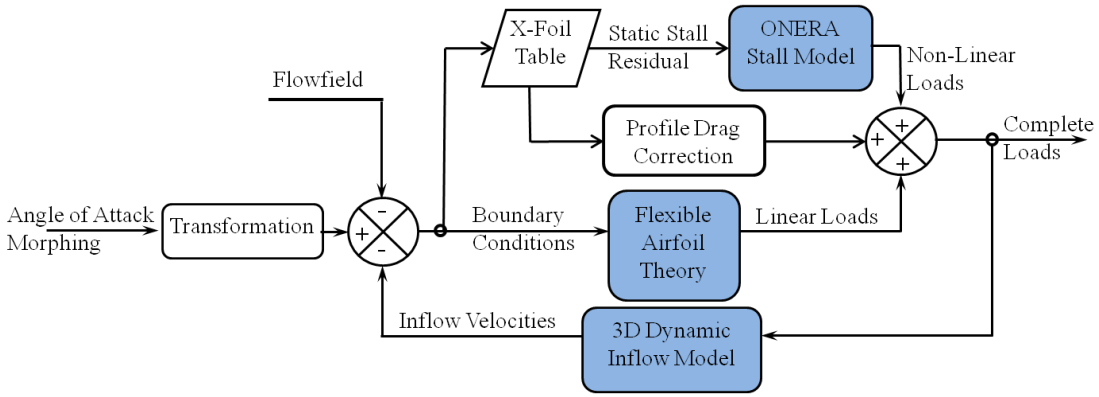

Figure 6-3: Schematic of Unified Airloads Model

The low-order aerodynamic model uses the two-dimensional finite-state formulation for deformable airfoils presented in [167]. It is based on a Glauert expansion of the potential flow equations for a deformable airfoil of infinitesimal thickness. The camber-wise airfoil deformation is written using the Chebyshev polynomials of the first kind, which defines the generalized camber-wise displacement amplitudes. The wake-induced

velocity is solved using the dynamic inflow theory. It assumes that the velocity normal to the rotor disk can be expressed in terms of radial and azimuthal expansion functions. The dynamic inflow model is sufficient to capture effects of N_b/rev vibrations and it can be used in the design of controllers, however, it cannot be used for modeling blade-vortex interactions or acoustical phenomena [168]. Also, at $\mu = 0.33$, the effect of blade vortex interactions are expected to be less dominant as compared to the dynamic stall effects.

Drag and Dynamic Stall

A potential benefit of camber actuation is the ability to alter profile drag and stall characteristics, which have implications in power and vibration. To include these effects in the low-order aerodynamic model, the potential flow airload expressions are augmented with a quasi-static profile drag term as well as a dynamic-stall correction that is based on the ONERA model. The ONERA model assumes that the dynamic stall states are governed by a second-order differential equation, and requires static loading coefficients near and beyond stall. These are determined using the two-dimensional boundary layer analysis code XFOIL (which is valid to slightly post stall conditions), along with a simple, empirically derived approximation for deep-stall. The coefficients are obtained under varying Reynolds number, angle-of-attack and camber deformation. A detailed account of the method used for determining the coefficients is available in Thepvongs et al. [145]. The dynamic stall formulation was appended with a first order model to capture the delay in angle of attack. The steps involved in determining the effect of dynamic stall on aerodynamic loads are described in Appendix B.3.

Coupling with Finite-State Aerodynamics

The finite-state aerodynamics formulation uses Chebyshev polynomials to form a basis for the camber deformations and associated airloads, while the choice of basis functions for the finite-section modes are arbitrary. The motion and force variables of the aerodynamics formulation are related to those of the structural formulation by a simple linear expression, as derived in Thepvongs et al. [145]. This straightforward connection between the aerodynamic and structural states allows the same space and time integration methods to be used for both formulations as well as a simultaneous solution. The governing structural dynamics equations, aerodynamic load expressions, dynamic stall equations and wake equations together define the time-domain problem. An explicit method is used with iterative refinement to achieve the desired convergence. A simple three-point backwards Euler time-integration scheme is used in accordance with the first-order form of the structural and potential flow governing equations. A four-point scheme is used to integrate the second-order dynamic stall equations.

Trim Analysis

The enforcement of vehicle equilibrium adds more variables and constraints to the aeroelastic problem. The present work assumes a wind-tunnel setup, where the variables are taken to be the collective, sine and cosine components of the cyclic pitch, and equilibrium is represented by specifying values for the time-averaged thrust, pitch and roll moments. These are provided by an autopilot that makes incremental changes to the control settings at every time step. The "trimmability matrix" can be approximated by

numerically computed Jacobian, determined by stepping the controls and examining the response at an instant one revolution later.

6.2 Camber Deformation Shape

The non-dimensionalized cubic (Ψ_{cubic}) and quadratic (Ψ_{quad}) camber deformation shape functions used in this analysis are shown in Figure 6-4. The expressions for these camber deformation are given by:

$$\Psi_{quad}(\xi) = \xi^2 - \frac{1}{3}$$

$$\Psi_{cubic}(\xi) = \frac{5}{4}\left(\xi^3 - \frac{3}{5}\xi\right)$$

where ξ is the airfoil chordwise coordinate non-dimensionalized by its half chord such that $-1 \le \xi \le 1$.

Camber deformation in the current analysis is simulated by assigning an arbitrarily high cross-sectional stiffness associated with the camber degree of freedom and applying a conjugate finite-section force in the structural simulation. This method allows the user to control airfoil deformation without defining the particular actuation mechanism. The amplitude of camber deformation is obtained by taking the difference between the maximum camber deformation and the minimum camber deformation along the airfoil chord. In all the results presented in this study, the camber deformation is shown as a percentage of the airfoil chord. Airfoil cross section with a 5% camber deformation for both cubic shape function and quadratic shape function are shown in Figure 6-5.

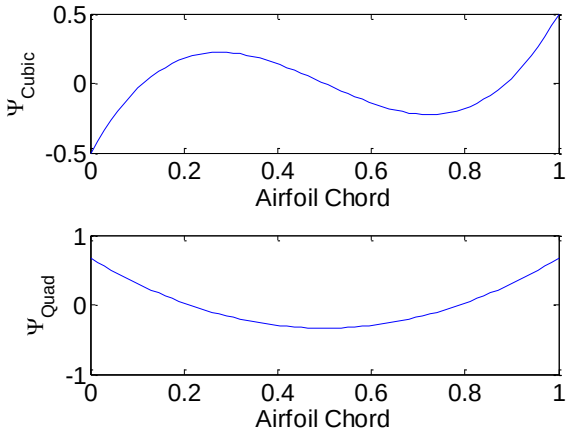

Figure 6-4: Camber Deformation Shape Function

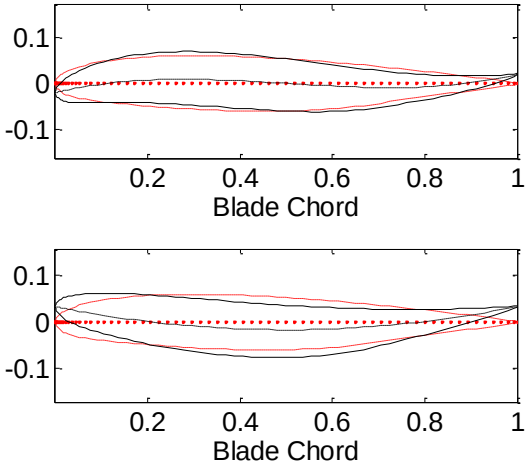

Figure 6-5: Airfoil Cross Section with 5% Camber Deformation
(Dotted red line: Undeformed NACA 0012 Airfoil, solid black line: Deformed Airfoil)

Note that a 5% camber deformation is shown in Figure 6-5 only for visualization purpose. Based on the preliminary analysis performed, it was observed that approximately 0.5%c camber deformation is sufficient for vibration reduction and performance enhancement.

The NACA 0012 airfoil is used as the baseline airfoil cross section in these studies. The aerodynamic properties of the airfoil cross section with and without the prescribed camber deformation are obtained using XFOIL analysis for a range of Mach numbers and Reynolds numbers. These are used to generate the table lookup for calculating the static

stall residual for the ONERA dynamic stall model and for including the profile drag correction in the aerodynamic forces. Variation of aerodynamic coefficients with the angle of attack for M = 0.5 and Re = 1.41×10^6 is shown in Figure 6-6 for 1% camber deformation. The lift (c_l) and the drag (c_d) coefficient obtained with cubic and quadratic camber deformation shape function are close to each other below the stall condition while the same is not true for coefficient of moment (c_m). The difference between their aerodynamic properties is more apparent in the post-stall regime and hence, they are expected to provide different results in the dynamic stall condition.

The optimum camber deformation required for performance enhancement and vibration reduction is obtained using a two-step optimization process that combines surrogate-based optimization (SBO) with gradient based optimization (GBO) in order to obtain a more stable optimization process and to reduce the computational time.

Preliminary analysis performed using the aeroelastic analysis code UM/NLABS-A using both the camber deformation shape functions in dynamic stall condition are described next.

6.3 Preliminary Numerical Results

The baseline model is a scaled BO105 rotor with four blades, as used in the HART II experiments. Properties of the baseline rotor are summarized in Table 6-1 and more detailed information can be found in [145]. All the cases considered here are at an advance ratio of **0.33** and at a rotor thrust level of 6584 N ($\mathbf{C_T = 0.008}$).

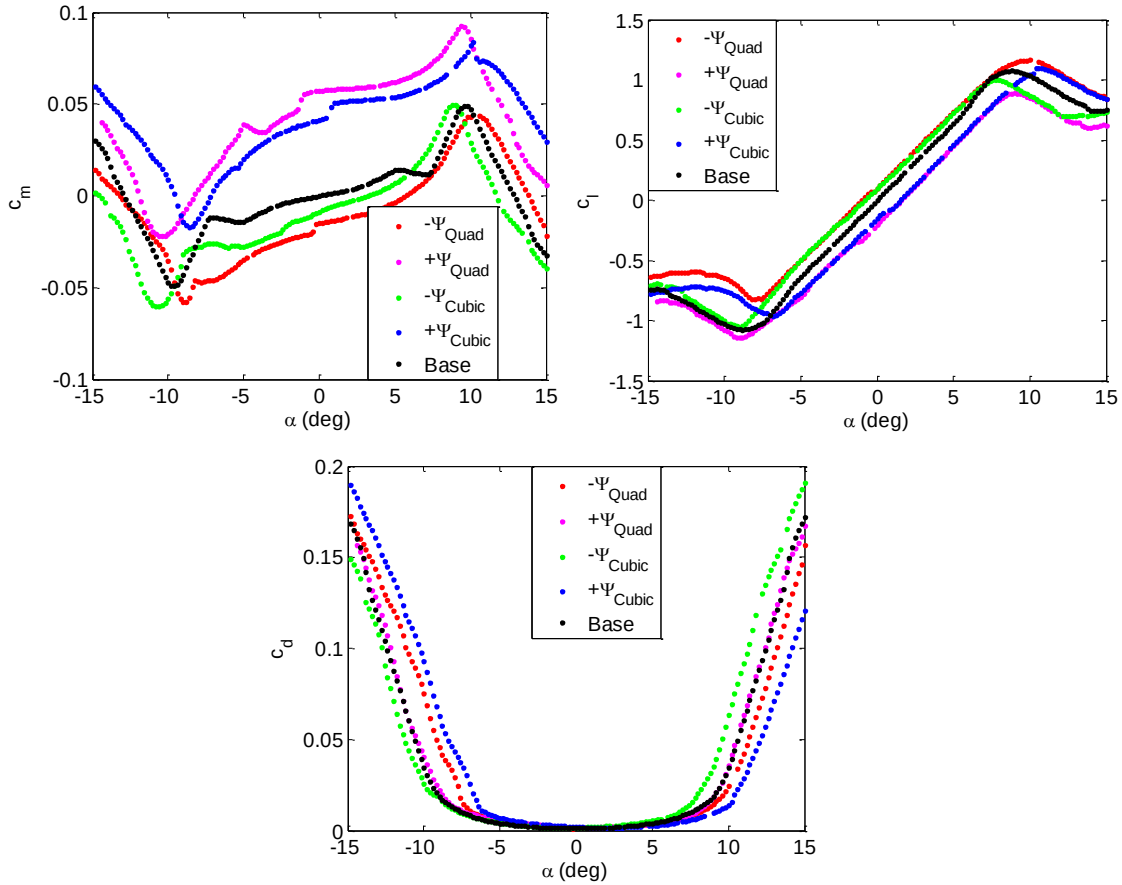

Figure 6-6: Aerodynamic Properties of Cambered and Baseline Airfoil Section (Reference Airfoil: NACA 0012**)**

Table 6-1: Baseline Blade Properties

Property	Value
Type	Hingeless
Number of blades	4
Radius	2m
Root offset	0.44m
Chord	0.121m
Airfoil Section	NACA 0012
Operating RPM	109 rad/s
Advance Ratio	0.33
Shaft angle	-5 deg

In order to observe the effect of camber actuation on rotor performance in dynamic stall condition, a uniform camber actuation force was applied along the blade span at

different actuation frequencies and for different phase of actuation. The resulting distribution of camber deformation along the blade radius for both the camber deformation shape function is shown in Figure 6-7 which indicates a maximum camber deformation of 0.07%c at the blade tip. Since, in the current analysis, the same stiffness is assumed for both the camber deformation modes, the resulting camber distribution along the blade span is identical. Note that the camber actuation force is only applied from 0.23 < r/R < 1.00.

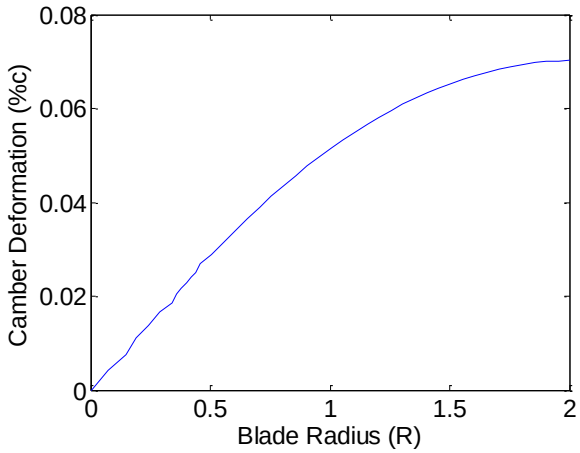

Figure 6-7: Variation of Camber Deformation along the Blade Span

6.3.1 Effect of Camber Actuation on M_{Z0}

The effect of camber actuation on the mean value of the torque (M_{Z0}) for cubic and quadratic camber deformation for different actuation frequencies is shown in Figure 6-8. Results show that the 2/rev actuation frequency is the most effective while the 5/rev actuation frequency is the least effective frequency for influencing performance of the rotor blade, for both the camber deformation shape functions considered here. Preliminary observation show that it is possible to obtain atleast 2% improvement in M_{Z0} by quadratic camber actuation at 2/rev frequency and phase difference of 240 degree or

by cubic camber actuation at 2/rev frequency and phase difference of 60 degree. Even though the minimum value of M_{Z0} that can be obtained from camber actuation is similar for the both the camber deformation shape functions, the adverse effect of camber actuation in increasing M_{Z0} is higher for the quadratic camber deformation.

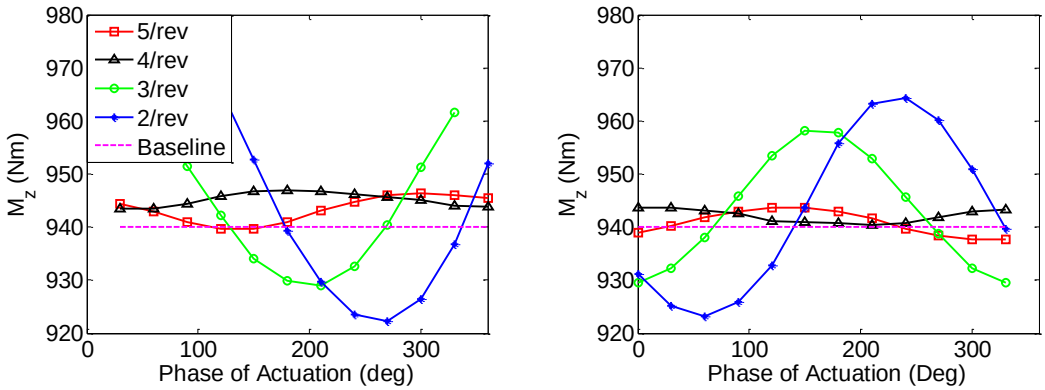

(a) With Ψ_{quad} **(b) With Ψ_{cubic}**

Figure 6-8: Effect of Camber Actuation on M_{Z0} at $\mu = 0.33$

6.3.2 Circle Plot for Different Actuation Frequencies

As described in the earlier chapters, circle plots are used to determine if the active vibration control method has sufficient authority for vibration reduction. In this case, camber actuation is provided at different actuation frequencies and the phase of actuation at each frequency is varied from 0 degree to 360 degree in intervals of 30 degree.

The circle plots obtained for the fixed system hub load at 4/rev frequency for F_z and M_x component are shown in Figure 6-9 and Figure 6-10, respectively. For each of the camber actuation cases, the camber deformation along the blade span is as shown in Figure 6-8. Circle plot results show that both 3/rev and 4/rev actuation frequencies are the most effective for reducing 4/rev vibration in the vertical component of the hub force

(F_{z4}) for both the camber deformation shape functions. Similarly, 3/rev actuation frequency is the most effective for reducing M_{X4} for both the camber deformation shape functions. These results show that the frequency of actuation that is most effective for reducing 4/rev vibratory hub loads depends upon the hub load component. Hence, in the analysis performed in this chapter, the actuation signal consists of 2/rev to 5/rev actuation frequencies.

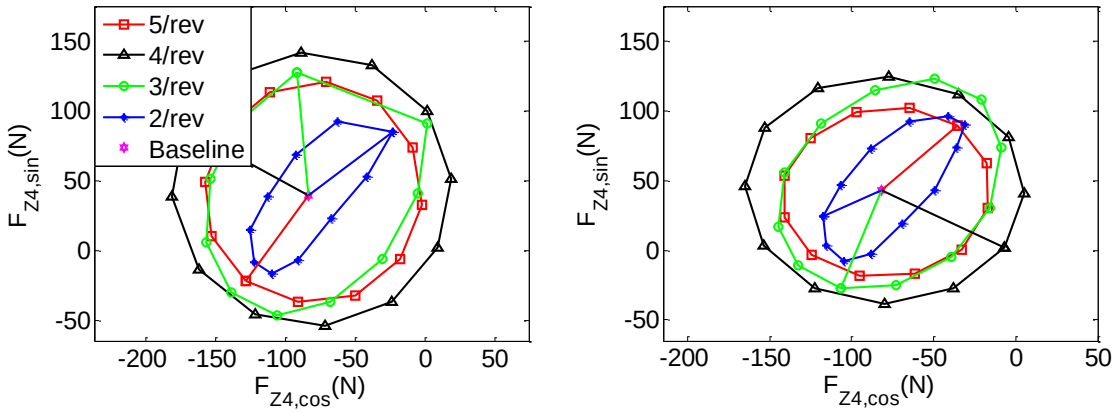

(a) With Ψ_{quad} **(b) With Ψ_{cubic}**

Figure 6-9: Circle Plot for F_{Z4}

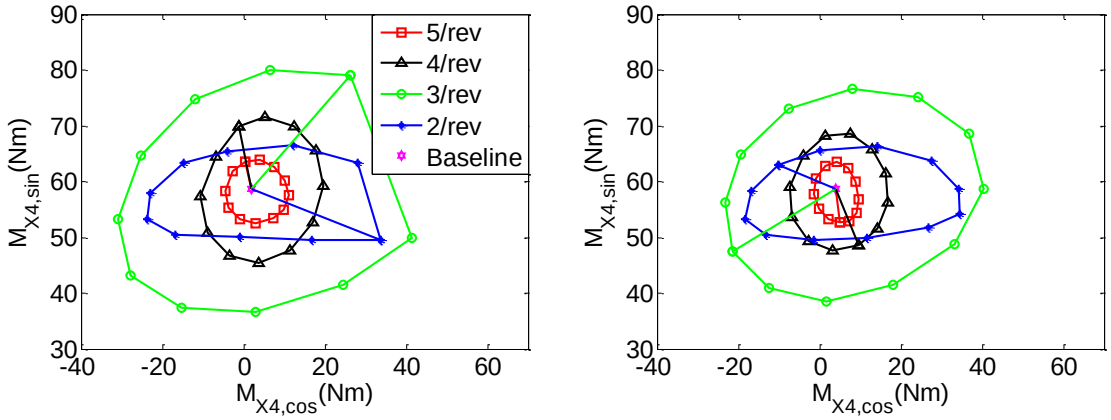

(a) With Ψ_{quad} **(b) With Ψ_{cubic}**

Figure 6-10: Circle Plot for M_{X4}

6.3.3 Effect of Amplitude of Actuation

In order to see the effect of amplitude of actuation, the amplitude of actuation for both the camber deformation shape function was doubled and the analysis was performed for 3/rev actuation frequency. The effect of amplitude on circle plot for F_{Z4} is shown in Figure 6-11. The results show an increase in size of the circle plots for both the camber deformation cases with increase in the amplitude of actuation indicating an increase in the authority for vibration reduction. However, the results shown in Figure 6-12 for M_{Z0} show that the effect of camber actuation on performance reduces with an increase in the amplitude of actuation for 3/rev actuation frequency.

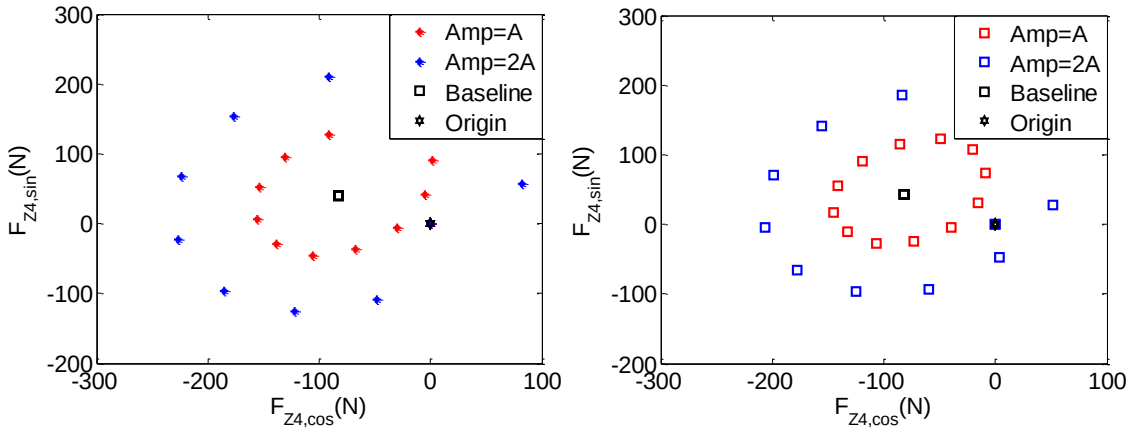

(a) With Ψ_{quad} **(b) With Ψ_{cubic}**

Figure 6-11: Effect of Amplitude on Circle Plot for F_{Z4}

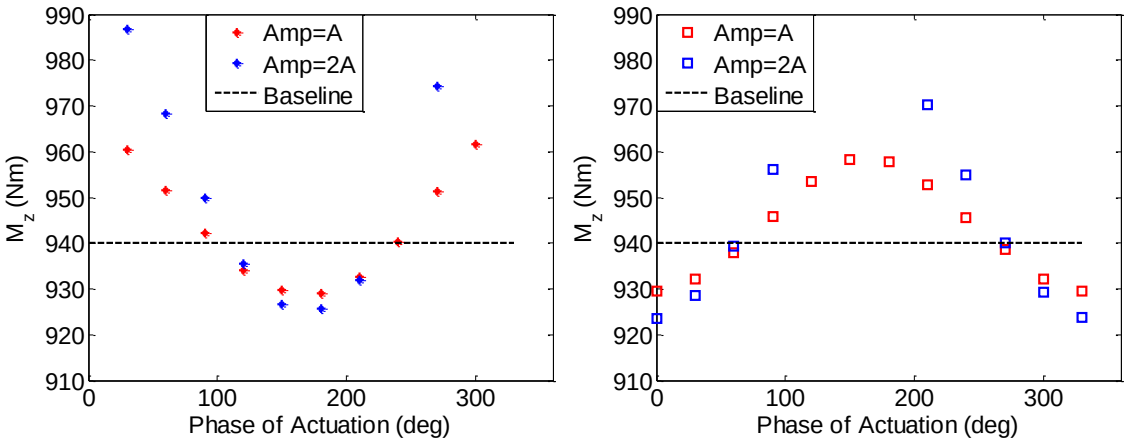

(a) With Ψ_{quad} **(b) With Ψ_{cubic}**

Figure 6-12: Effect of Amplitude of Actuation on M_{Z0}

6.4 Optimization Problem Definition

The problem of vibration reduction and performance enhancement has been converted to an optimization problem in this study. The design variables used in the study are the amplitude and phase of actuation corresponding to actuation frequencies of 2/rev to 5/rev. Hence, this problem has eight design variables. The objective functions considered in this study are:

a) Minimize F_{Z4} (minimize vibration in vertical component of hub force)

b) Minimize F_{H4} (minimize vibration in all the hub load components)

where, $F_{H4} = \sqrt{F_{X4}^{\ 2} + F_{Y4}^{\ 2} + F_{Z4}^{\ 2}} + \frac{1}{R}\sqrt{M_{X4}^{\ 2} + M_{Y4}^{\ 2} + M_{Z4}^{\ 2}}$

c) Minimize M_{Z0} (improve performance)

The camber deformation force is assumed to be constant along the blade span which results in the camber deformation profile as described in Figure 6-7. Without loss

of generality, the uniform actuation force required to obtain a camber deformation of 0.07% chord at the blade tip is referred to as 1*A*. The initial range for camber amplitude was chosen between no actuation and 2*A* for each actuation frequency, whereas the phase of camber actuation varies from 0 to 2π for each actuation frequency, as shown in Table 6-2. Same range was used for the optimization conducted with Ψ_{quad} and Ψ_{cubic} shape function.

Table 6-2: Range for Design Variable used in the Optimization Study

	Amplitude (*A*)				Phase (radians)			
	2/rev	3/rev	4/rev	5/rev	2/rev	3/rev	4/rev	5/rev
	A_2	A_3	A_4	A_5	Φ_2	Φ_3	Φ_4	Φ_5
Lower Bound	0.00	0.00	0.00	0.00	0.00	0.00	0.00	0.00
Upper Bound	2.00	2.00	2.00	2.00	2π	2π	2π	2π

Thus, a generic camber deformation signal provided to the rotor blade can be expressed as:

$$\Psi_{Blade1} = A_2 \sin(2\omega_0 t + \frac{\Phi_2}{2}) + A_3 \sin(3\omega_0 t + \frac{\Phi_3}{3}) + A_4 \sin(4\omega_0 t + \frac{\Phi_4}{4}) + A_5 \sin(5\omega_0 t + \frac{\Phi_5}{5})$$

where, ω_0 is the 1/rev frequency in radians.

6.4.1 Optimization Results

The optimization results obtained at the end of two-step optimization process using Ψ_{quad} and Ψ_{cubic} shape functions are listed in Table 6-3. Results obtained show a 99.6% reduction in F_{Z4} vibratory load with Ψ_{cubic} shape function, while 97.6% vibration reduction can be obtained using Ψ_{quad} shape function. Similarly, the percentage improvement in combined vibratory load (F_{H4}) and performance (M_{Z0}) is higher in the case of analysis with Ψ_{cubic} shape function.

Table 6-3: Optimization Results

Objective Function	Percentage Reduction With Ψ_{cubic}	With Ψ_{quad}
F_{Z4} (%)	99.60	97.60
M_{Z0} (%)	3.70	3.30
F_{H4} (%)	51.6	45.20

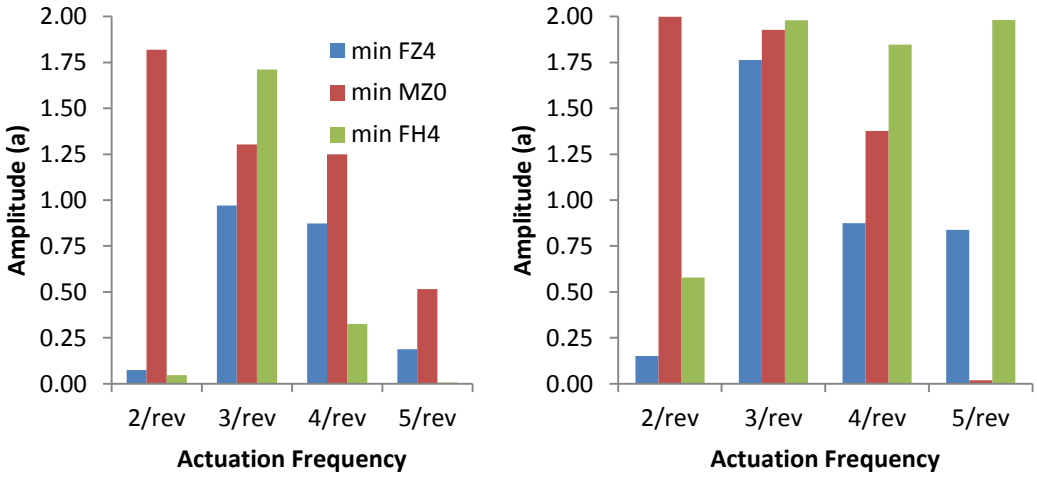

(a) With Ψ_{quad} (b) With Ψ_{cubic}

Figure 6-13: Amplitude of Actuation for Optimized Cases

The value of design variables for these optimized cases is shown in Figure 6-13. The trend observed for the amplitude of camber deformation corresponding to different actuation frequencies for the optimized cases is similar for the case with Ψ_{quad} and Ψ_{cubic} shape functions. In both the cases, the amplitude corresponding to 2/rev actuation frequency is highest for the "min M_{Z0} case". This is consistent with the trend observed in Figure 6-8 where 2/rev actuation frequency showed maximum influence on M_{Z0}. The contribution from higher actuation frequencies for minimizing M_{Z0} is smaller for both the camber deformation shape functions. For the vibration reduction cases, 2/rev actuation frequency is the least effective while 3/rev and 4/rev are the most effective frequencies. In general, the amplitude of camber deformation corresponding to the optimized cases

with Ψ_{cubic} shape function is higher than that required for the optimized cases with Ψ_{quad} shape function.

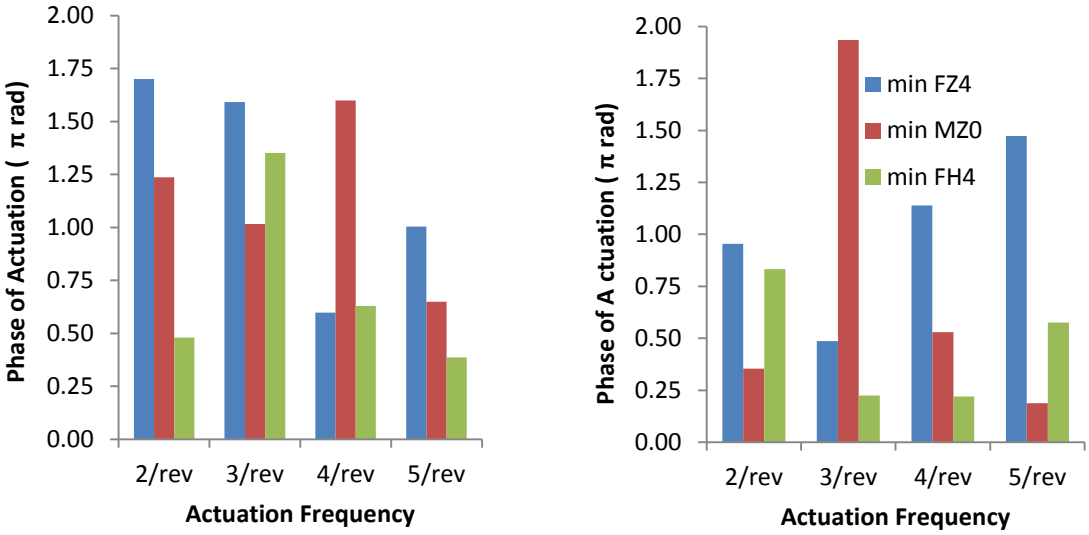

(a) With Ψ_{quad} (b) With Ψ_{cubic}

Figure 6-14: Phase of Actuation for Optimized Cases

The variation for phase of actuation corresponding to different actuation frequencies for the optimized cases is shown Figure 6-14 .

6.4.2 Advantage of Two-step Optimization Process

The two-step optimization process used in this paper provides robust solution and is very well suited for exploring a large design space where multiple solutions exist. As discussed in the earlier section, initially the non-gradient optimization is performed using surrogate method and the results obtained from the surrogate based optimization (SBO) are used as the starting point for gradient based optimization (GBO).

The variation of objective function with iteration number for the optimizations performed using SBO is show in Figure 6-15. Note that an additional iteration was

performed for the Ψ_{cubic} case in order to obtain the pareto front described in Section 6.4.5. Results indicate that design points very close to the optimum value are obtained in first 2-3 iterations.

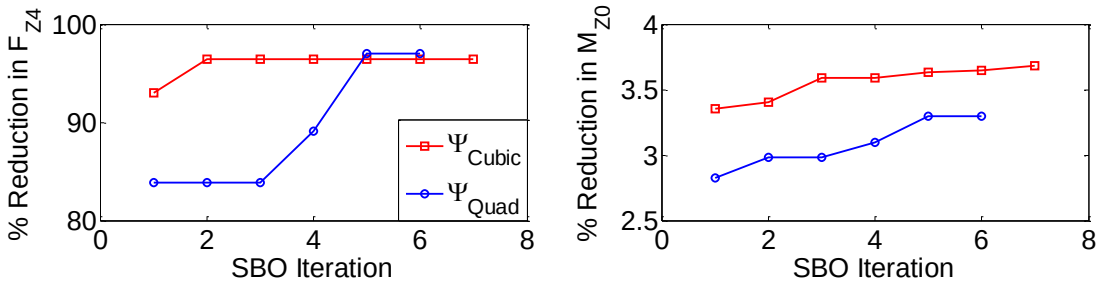

Figure 6-15: Variation of Objective Function with Iteration Number for SBO

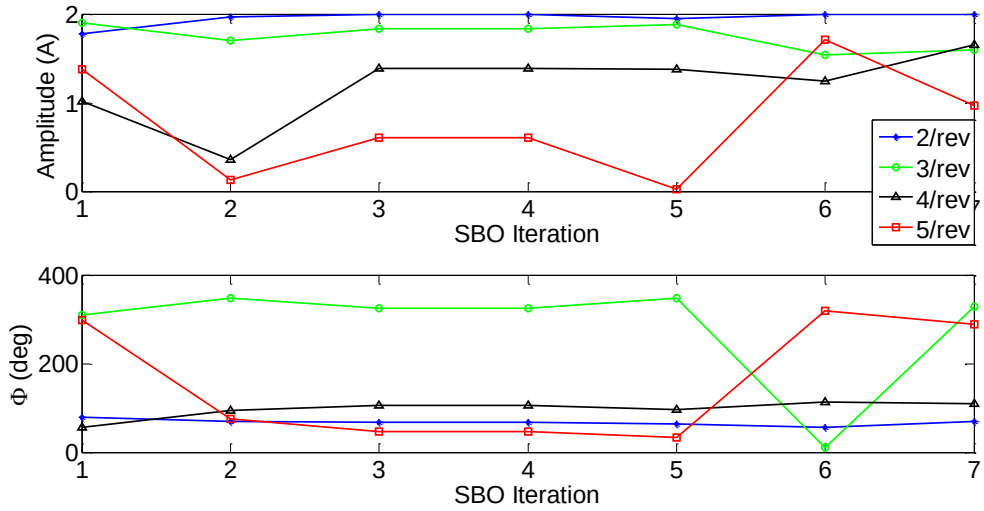

Figure 6-16: Variation of Design Variables with Iteration Number for SBO for Min M_{Z0} case for analysis with Ψ_{cubic}

The variation of design variables with SBO iteration for Min Mz0 case for analysis performed using Ψ_{cubic} is shown in Figure 6-16. The trend observed highlight that 2 and 3/rev actuation frequencies are the most effective for performance enhancement. For these frequencies, the variation in amplitude and phase of actuation is small. These

results also show that the 5/rev actuation frequency is least effective for improving the performance of rotor blade, as observed earlier in the parametric studies.

For each of the objective functions considered, three best points obtained from the surrogate optimization are selected as the starting points for gradient based optimization as shown in Figure 6-17. Here, only the results for the "min F_{Z4}" case corresponding to Ψ_{cubic} shape function are shown; but a similar trend is observed for all the objective functions considered. In Figure 6-17, the bottom part of the column (in blue) represents the vibration reduction obtained just from the SBO, while the top part (in red) represents the additional improvement in the objective function due to the GBO. Results presented here show that, although the initial starting points obtained from SBO provide different level of vibration reduction, the final vibration reduction obtained at the end of GBO process for each of the three cases considered here are close to each other.

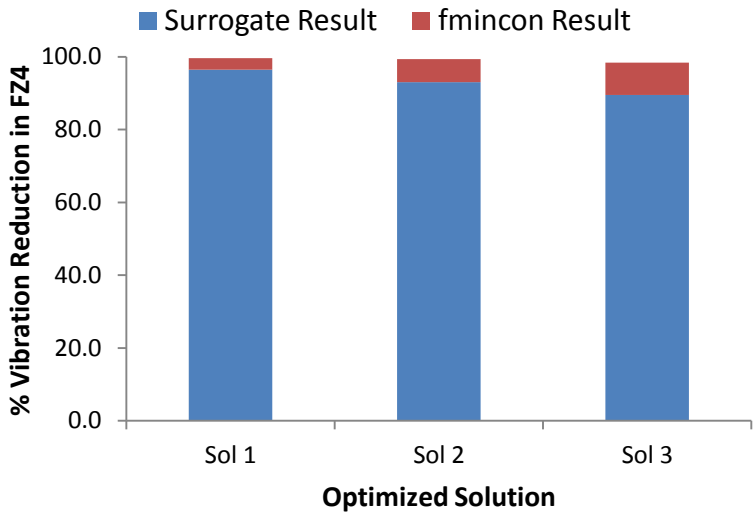

Figure 6-17: Percentage Reduction in F_{Z4} using Two-Step Optimization Process

The variation of design variables for these three cases is shown in Table 6-4. For each of the cases, the final solution obtained at the end of GBO is close to the corresponding starting point obtained from SBO. Also, the final value of design variables obtained for the three cases are very far from each other, even though the value of objective function for these cases are close to each other. This highlights the fact that multiple local minima exist in the design space which can provide a similar level of vibration reduction.

Table 6-4: Optimum Design Variables for min F_{Z4} Case

	Amplitude (*A*)				Phase (rad)				F_{Z4}
	2/rev	3/rev	4/rev	5/rev	2/rev	3/rev	4/rev	5/rev	% Change
SBO Sol 1	0.11	1.76	0.90	0.82	2.93	1.56	3.64	4.62	-96.5
GBO Sol	0.15	1.76	0.88	0.84	3.00	1.53	3.58	4.63	-99.6
SBO Sol 2	1.34	0.16	0.59	1.14	1.60	5.11	0.07	6.23	-93.0
GBO Sol	1.36	0.17	0.61	1.11	1.57	5.14	0.07	6.17	-99.4
SBO Sol 3	1.30	1.35	0.12	0.00	1.74	1.80	2.86	3.90	-89.6
GBO Sol	1.32	1.31	0.12	0.06	1.74	1.74	2.96	3.90	-98.4

6.4.3 Effect of Optimization on other Hub Load Components

In this section, the effect of vibration reduction and performance enhancement on the other hub loads is examined. The mean value of torque and the dynamic amplitude of various forces at the hub in fixed frame corresponding to 4/rev frequency and 8/rev frequency for the baseline case are shown in Table 6-5(a).

Table 6-5: Variation in Hub Loads for the Optimized Cases

(a) Absolute Value of the Hub Loads for the Baseline Case

	M_{Z0} (Nm)	F_{X4} (N)	F_{Y4} (N)	F_{Z4} (N)	M_{X4} (Nm)	M_{Y4} (Nm)	M_{Z4} (Nm)	F_{Z8} (N)	F_{H4} (N)	F_{H8} (N)
Baseline	-939.9	312.8	160.7	91.7	58.4	34.2	6.8	51.7	397.4	62.8

(b) Percentage Changes in Hub Loads with Ψ_{cubic} Shape Function

% Changes	M_{Z0}	F_{X4}	F_{Y4}	F_{Z4}	M_{X4}	M_{Y4}	M_{Z4}	F_{Z8}	F_{H4}	F_{H8}
min F_{Z4} Case	1.1	-13.0	-50.4	**-99.6**	-30.7	92.7	-71.5	-7.6	-18.9	-7.4
min M_{Z0} Case	**-3.7**	1.6	51.9	34.9	18.2	-34.7	34.0	-75.5	14.7	-58.6
min F_{H4} Case	0.2	-57.5	-39.2	-62.7	-78.3	33.8	-42.6	1.7	**-51.6**	-5.8

(c) Percentage Changes in Hub Loads with Ψ_{quad} Shape Function

% Changes	M_{Z0}	F_{X4}	F_{Y4}	F_{Z4}	M_{X4}	M_{Y4}	M_{Z4}	F_{Z8}	F_{H4}	F_{H8}
min F_{Z4}	2.2	-19.7	-49.1	**-97.6**	-22.7	83.5	-76.4	6.5	-23.8	2.4
min M_{Z0}	**-3.3**	7.6	57.3	-3.8	14.4	-37.3	11.7	-84.8	17.1	-66.8
min F_{H4}	1.0	-32.3	-77.0	-38.7	-64.3	105.7	-55.4	-27.4	**-45.2**	-26.2

The percentage changes in different component of hub loads for the optimized cases obtained with Ψ_{quad} and Ψ_{cubic} shape function is shown in Table 6-5(b) and Table 6-5(c), respectively. The result obtained for the "min F_{Z4}" case in Table 6-5(b) shows that the vibration reduction in F_{Z4} is accompanied by a 1.1% increase in torque. This case also results in 18.9% reduction for F_{H4}, however it is smaller than the optimum reduction that can be obtained when F_{H4} is minimized. For the "min F_{Z4}" case, minimizing the amplitude at 4/rev frequency also results in small decrease in vibratory loads at 8/rev frequency. Similarly, the 3.7% improvement in performance for the "min M_{Z0}" case is accompanied by a 34.9% increase in F_{Z4} and 14.7% increase in F_{H4}. Surprisingly, minimizing M_{Z0} also results in significant vibration reduction for 8/rev frequency loads. In the "min F_{H4}" case, the optimizer tries to reduce the amplitude of vibration at 4/rev frequency for all the hub load components. Even though a small increase in vibration is observed for M_{Y4}, the absolute values listed in Table 6-5(a) shows that the magnitude for this component is small as compared to other hub load components. A similar trend is observed in the results obtained with Ψ_{quad} camber deformation shape function, as shown in Table 6-5(c).

6.4.4 Analysis of Optimized Cases

In this section, the optimization results are analyzed further in order to understand the mechanism through which vibration reduction and improvement in performance is obtained using camber deformation. Here, only the optimized results obtained from Ψ_{cubic} shape function are shown.

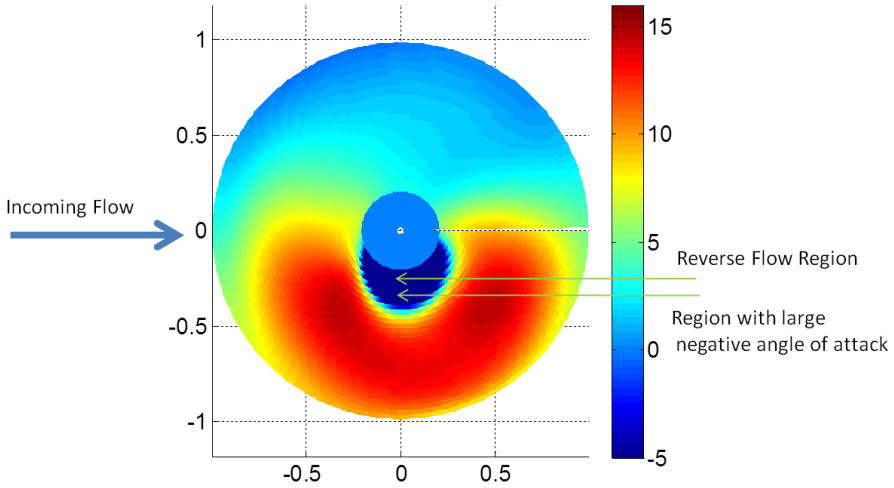

Figure 6-18: Variation of Angle of Attack for the Baseline Case (Units: Deg)

The variation of angle of attack over the rotor disk for the baseline case ($\mu = 0.33$, $C_T = 0.008$, no camber actuation) is shown in Figure 6-18. The distribution of angle of attack shown here highlights small angle of attack observed on the advancing side (almost negative near the tip) and large angle of attack on the retreating side which result in dynamic stall. (Note that on the retreating side, near the root region, there is a region of reverse flow and a region with very large negative angle of attack. The angle of attack in these two region is well below -5deg, however, the lower limit for the "colorbar" used in this figure has been set to -5 to focus more on the region with large positive angle of attack.)

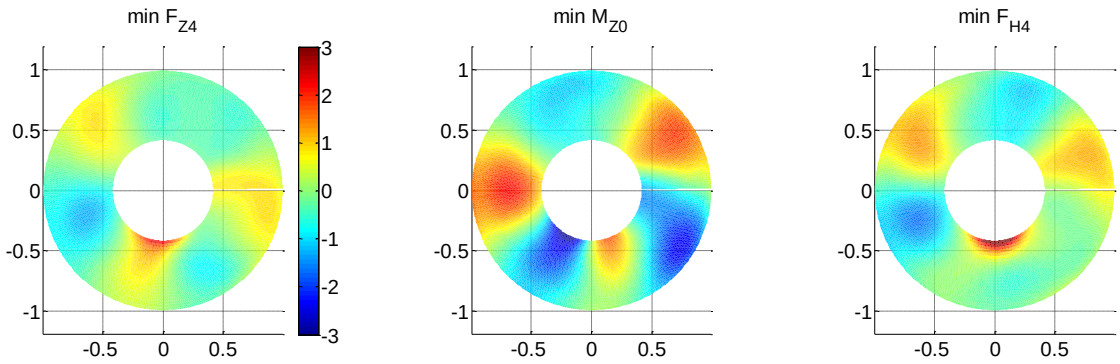

Figure 6-19: Difference in Angle of Attack for the Optimized Cases (Unit: Deg)

The angle of attack variation obtained for the optimized cases is subtracted from that observed for the baseline case and the results obtained are shown in Figure 6-19. Note that the reverse flow region and region with large negative angle of attack is removed from the figure to highlight the dynamic stall region. The highest variation in angle of attack from the baseline case is observed for the "min M_{Z0}" case, where the optimizer is trying to reduce large angle of attack encountered on the retreating side (shown by dark blue region). For the "min F_{Z4}" and "min F_{H4}" cases, the decrease in vibration is obtained by manipulating the phase of the additional loads obtained from camber deformation. Thus, in these cases, the variation in angle of attack from the baseline case is not significant as it was observed in the "min M_{Z0}" case. The same trend can also be seen in Figure 6-20 which shows the angle of attack variation with azimuth angle at r = 0.74R.

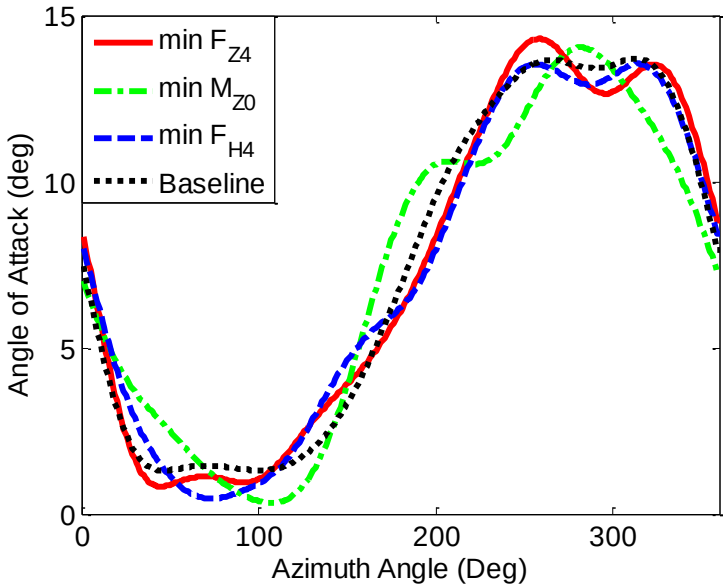

Figure 6-20: Variation of Angle of Attack at r = 0.74R

The camber deformation profile for the optimized cases over the rotor disk is shown in Figure 6-21 while Figure 6-22 shows the camber deformation at the blade tip. Results show that the camber deformation required is highest for the "min F_{H4}" case. For all the cases, a maximum camber deformation of 0.35%c is sufficient to obtain the objective function listed in Table 6-3.

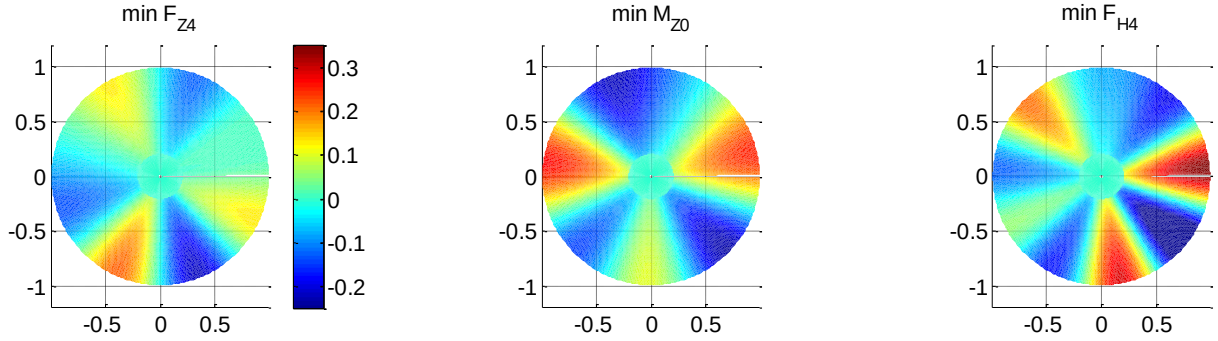

Figure 6-21: Variation of Camber Deformation for the Optimized Cases (Unit: %c)

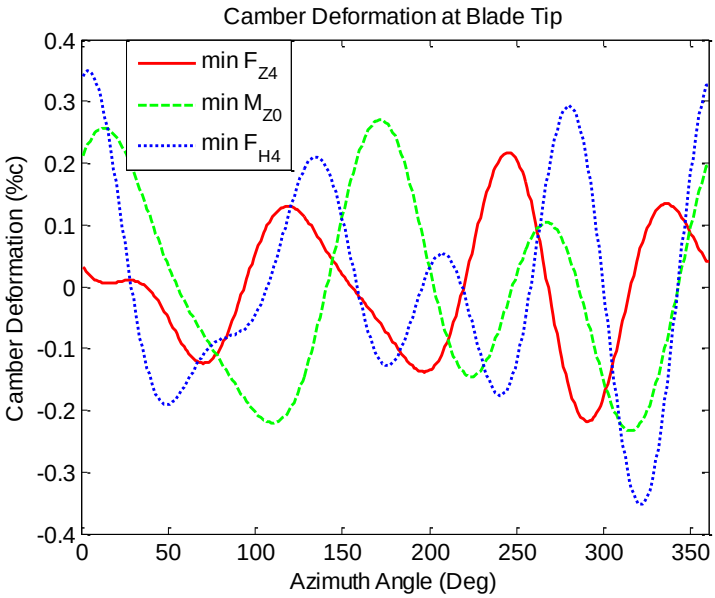

Figure 6-22: Camber Deformation at the Blade Tip

6.4.5 Pareto Optimization

In this study, a multi-objective optimization was conducted using the Ψ_{cubic} shape function where vibration reduction (min F_{H4}) and performance enhancement (min M_{Z0}) were considered as the objective functions. Optimization was performed using the GODLIKE toolbox developed for unconstrained optimization in MATLAB. The Pareto front obtained for these two objective functions is shown in Figure 6-23. The results presented here show that it is possible to obtain simultaneous reduction in vibration and improvement in performance with camber deformation.

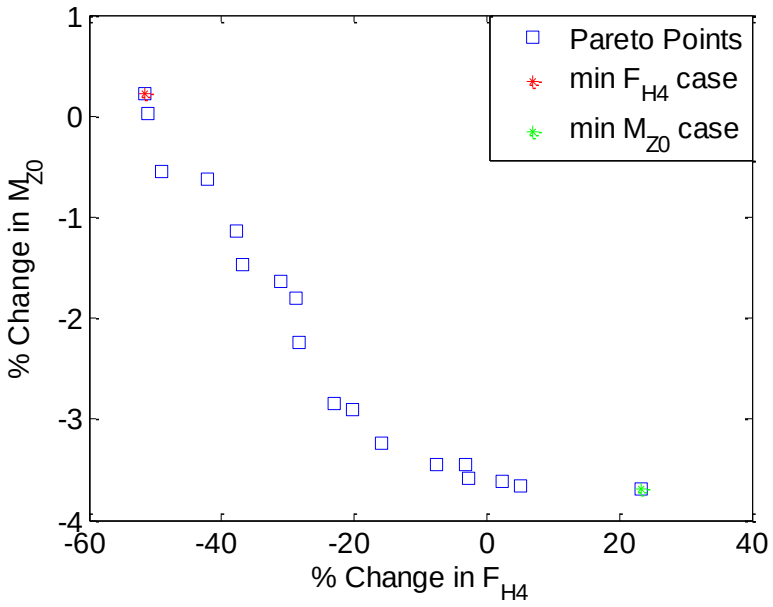

Figure 6-23: Pareto Front for Vibration Reduction and Performance Enhancement

6.5 Concluding Remarks

In this chapter, the use of quadratic and cubic camber deformation shape functions for vibration reduction and performance enhancement in dynamic stall condition was studied. A modified version of the ONERA dynamic stall model which can account for morphing airfoil section was included in the aeroelastic analysis performed using UM/NLABS-A. Preliminary parametric studies at different actuation frequencies showed the capability of camber deformation in influencing both vibratory loads and performance of the rotor blade.

In the next step, a novel two-step optimization process was used to obtain reduction in vibratory loads and hub torque (as a metric of rotor performance). In the first step of the process, a global search is performed using surrogate modeling to provide a good feasible initial design for the second step in the process: gradient-based optimization. The use of

gradient-based optimization allows the objective function to converge to a minimum, from the initial designs provided by the surrogate approach. Thus, a more stable optimization process is achieved, thereby reducing the overall required computational time.

In the optimization studies, the amplitude and phase of camber actuation at 2/rev, 3/rev, 4/rev and 5/rev actuation frequencies were used as the design variables and the analysis was performed with both cubic and quadratic camber deformation shape function. The optimization results showed:

a) 99.6% reduction in vertical component of 4/rev vibratory load at the hub (F_{Z4})

b) 3.7% improvement in performance (M_{Z0})

c) 51.6% reduction in combined 4/rev vibratory load the hub (F_{H4})

with cubic camber deformation shape function. The results obtained for these objective functions with quadratic shape function were slightly less as compared to those obtained with the cubic shape function. Post-processing of the optimized results obtained showed that the performance improvement is obtained by reducing the angle of attack in the dynamic stall region while vibration reduction is obtained by adjusting the phase of camber actuation in such a way that the vibratory loads at 4/rev frequency at the hub are minimized. Finally, a multi-objective optimization study was performed where vibration reduction and performance enhancement was obtained simultaneously and a Pareto front was determined for these objective functions.

Chapter 7. Conclusions and Future Work

This chapter provides a summary of the work presented in this thesis and outlines the key results and contribution made. And finally, few recommendations are made for the future work.

7.1 Summary

The aim of the work presented in this thesis was to develop a multidisciplinary analysis and design framework and exercise it to explore various approaches available for vibration reduction.

As a first step, an aeroelastic analysis/design environment was developed which can be used to design composite rotor blades with vibration reduction or performance enhancement as the objective function. The design environment included several well-established analysis codes from different sources: IXGEN for mesh generation, UM/VABS for cross sectional analysis, RCAS for rotorcraft simulation and ModelCenter for optimization and parametric studies. This design environment enables conceptual/early preliminary multidisciplinary rotor blade design, allowing rapid design trade studies early in the design process with realistic structural properties for modern composite rotor blades. The design environment was successfully used to perform detailed parametric and optimization studies on a full scale model of a UH-60 composite rotor blade.

For design of rotor blade with active twist, a new design strategy and framework was developed where dynamic twist was maximized instead of maximizing the static twist. The optimization framework included the aeroelastic design environment described earlier along with surrogate based optimization technique. The surrogate based optimization is performed in combination with Efficient Global Optimization algorithm which is better suited for aeroelastic problems where the runtime for each iteration is very high and there are significant amount of failed cases due to convergence issues within the analysis cycle. Results showed that the amplitude of dynamic twist is a true indicator of control authority of active twist rotor for vibration reduction. Optimization was performed at different actuation frequencies to maximize the control authority for vibration reduction at a range of frequencies. For the optimization studies presented here, the NASA/Army/MIT active twist rotor, which had been tested in TDT, was selected as the baseline rotor blade.

In the next step, the optimization framework was extended to include discrete design variables in the optimization and the solution for mixed design variable problems was obtained using different techniques. In this extended framework, the genetic optimization algorithm was combined with the gradient based optimization to obtain an optimum design with continuous design variables and an optimum design with mixed design variables in an efficient manner. The results obtained highlighted the effect of discretizing design variables and helped in obtaining a realistic composite rotor blade design.

Although active flaps have been around for last two decades, very few studies in the literature have focused on the detailed design of a composite rotor blade with active flaps.

In this research, composite cross sections along the blade span for a Mach-scaled rotor blade were designed using the mixed-design variable optimization framework described above.

This thesis also includes (in Appendix) work related to design and fabrication of a composite rotor blade with dual active flaps which can be tested in a Mach-scaled spin test stand. The work done highlights the steps involved in the design process and discusses difficulties and issues encountered during the testing phase. At the end, possible corrections for the issues are presented and modifications which can be made for future tests are listed.

Finally, within the same framework introduced here but with a different analysis tool, the use of quadratic and cubic camber deformation shape function for vibration reduction and performance enhancement in dynamic stall region was studied. A modified version of the ONERA dynamic stall model which can account for morphing airfoil section was included in the aeroelastic analysis performed using UM/NLABS-A. Optimization results obtained shows 50% reduction in 4/rev vibratory loads at the hub and more than 3.5% improvement in the performance using camber actuation at advance ratio of 0.33.

7.2 Main Results

This section summarizes the main results obtained in the thesis. These conclusions support the contributions made in this thesis which are listed in Section 7.3.

The new rotor blade design environment was used to design a composite cross section for a full scale model of a UH-60 rotor blade. The optimization results showed:

c) 52% vibration reduction in F_{Z4} (Objective function: min F_{Z4});

d) 28% vibration reduction in F_{H4} (Objective function: min F_{H4});

where F_{Z4} is the amplitude of the 4/rev vibratory vertical force at the hub and F_{H4} is the amplitude of the combined 4/rev vibratory load at the hub. The results obtained indicated that the reduction is F_{Z4} is obtained by reducing the coupling between the structural modes while a decrease in F_{H4} can be obtained by increasing the torsional stiffness of the cross section.

With an optimization framework/strategy developed for the design of active composite rotor blades, the new framework was set to use the amplitude of dynamic twist as the objective function. Using the NASA/Army/MIT Active Twist Rotor design as the baseline rotor blade, the optimized designs showed:

a) 18.5% increase in static twist per unit length;

b) 63.6% increase in tip twist amplitude for 4/rev twist actuation;

c) 52.6% increase in tip twist amplitude for 3/rev twist actuation;

d) 101% increase in tip twist amplitude for 5/rev twist actuation;

e) 71% increase in twist amplitude for actuation at a range of frequencies (3, 4 and 5/rev).

without varying ply thicknesses and ply angles.

Further it was shown that the blade designs obtained by maximizing the amplitude of dynamic twist have higher authority for vibration reduction as compared to the blade design obtained by maximizing the static twist amplitude. Based on the optimization studies conducted, important factors identified for maximizing the dynamic twist are: a)

first torsional frequency of the rotor blade, b) active moment generated by active material, and c) aerodynamic loads acting on the rotor blade.

An augmented version of this optimization framework was used to design active twist rotor blades with both continuous and discrete design variables. In this analysis, ply thicknesses and ply angles were treated as discrete design variables. The optimization studies with ply thicknesses showed:

a) A thick prepreg layer is required near the leading edge (Ply 2a) to obtain higher active twisting moment;
b) Increasing the chordwise coverage of active plies is better than increasing the thickness of active plies, in order to get higher static and dynamic twist;
c) A boxed-shaped spar design, in which the chordwise location where the spar plies end and the chordwise location of vertical spar web are close to each other, is suitable for maximizing the dynamic twist amplitude;
d) The two ballast masses are very useful for tuning the dynamic properties of the rotor blade, which eventually results in an increase in the dynamic twist amplitude.

Besides this, the framework was useful for quantifying the effects of discretizing design variables for different objective functions considered.

The same analysis framework was also used to design composite blade with active flaps after modifying the aeroelastic analysis performed by RCAS. In this analysis, optimum rotor blade cross sections along the blade span were determined for different spanwise locations of the flap. The analysis included the effect of actuator and flap inertia. For these studies, the amplitude of dynamic twist at 4/rev flap actuation frequency

was used as the objective function. A 5-ft radius Mach-scaled composite rotor blade that can be tested in the University of Michigan spin test stand was selected as the baseline rotor blade. The optimization results showed:

d) 14% increase in dynamic twist for a 12% flap located at 0.78R;

e) 9.32% increase in dynamic twist for a 12% flap located at 0.7R;

f) 4.58% increase in dynamic twist for a 12% flap located at 0.85R.

All the optimized blade designs showed a decrease in the torsional stiffness and an increase in the axial stiffness.

The optimization studies conducted showed that a torsionally stiff blade is desired in order to obtain higher active twist whereas a torsionally soft blade is desired in order to obtain higher control authority from flap actuation.

For the analysis of a rotor blade with camber actuation in forward flight condition, a modified version of the ONERA dynamic stall model was included in UM/NLABS-A. In the optimization studies with camber actuation, the amplitude and phase of camber actuation at 2/rev, 3/rev, 4/rev and 5/rev actuation frequencies were used as the design variables and the analysis was performed with both cubic and quadratic camber deformation shape function. The optimization results showed:

d) 99.6% reduction in vertical component of 4/rev vibratory load at the hub (F_{Z4});

e) 3.7% improvement in performance (M_{Z0});

f) 51.6% reduction in combined 4/rev vibratory load the hub (F_{H4});

with cubic camber deformation shape function. Post-processing of the optimized results obtained showed that the performance improvement is obtained by reducing the angle of attack in the dynamic stall region while vibration reduction is obtaining by adjusting the

phase of camber actuation in such a way that the vibratory loads at 4/rev frequency at the hub are minimized.

7.3 Key Contribution

The key contributions made in the thesis are:

- Created a new framework for the design and analysis of composite rotor blades with and without on-blade devices for vibration reduction. This new framework enables the designer to optimally size (at the ply level) realistic composite rotor blades. Among the active ones, this dissertation studied: active twist rotors, active camber scheduling, and multiple flaps for lower vibration, higher performance solutions.
- Introduced dynamic twist as the objective function to be used when designing active twist rotor blades. Through examples, it was shown that the dynamic twist is a true indicator of control authority for vibration reduction and not the static twist as done in the past.
    a. Extended the dynamic twist beyond a single actuation frequency and introduced an objective function to capture a range of frequencies when designing a composite rotor blade.
    b. Established that the optimization studies can be performed in hover condition (instead of multiple advance ratios) using periodic analysis (instead of full trim analysis) within a design cycle in order to reduce the computation time.

- Developed an optimization strategy for the design of composite rotor blade with mixed design variables. The framework provides three different techniques to ensure that a global optimum solution is obtained.
- Extended the optimization strategy and framework to also include the design of composite rotor blades with multiple flaps.
- Modified the aeromechanics solution of the new framework so to use UM/NLABS-A for the analysis of composite rotor blades with active camber deformation.
    a. Introduced the ONERA dynamic stall model in UM/NLABS-A so to capture the performance and vibration effects associated with dynamic stall.
    b. Showed effectiveness of camber deformation as a mean to improve performance and reduce vibration. The numerical studies conducted in dynamic stall conditions at μ=0.33 showed that the cubic camber deformation is more effective than the quadratic one.
- Designed, fabricated and tested the first composite rotor blade with dual flaps. It was a $1/6^{th}$ Mach-scaled CH-47D blade for testing in the UM spin stand.

7.4 Future Work

Based on the research conducted in this thesis, the following areas have been identified for further studies:

a) Failure Analysis: The blade failure approach used in this research was based on the loads observed in hover condition (and hence lower values were used for maximum allowable strain in the optimization studies to correct for that). This

could be modified by directly including the worst-case loadings determined for a given design and different advance ratios within an optimization loop. The framework can also be extended to include fatigue analysis based on the dynamic loads acting on the blade.

b) Improvement in Surrogate Modeling: The surrogate modeling techniques used needs to be improved further, especially when a large number of design variables are involved to reduce the error in the prediction. Improved accuracy in the prediction of the response function will also reduce the number of iterations required to obtain the optimum solution.

c) Including Closed Loop Controller: In this thesis, the design of composite cross section to enhance the vibration reduction capabilities of active rotor blade at different operating conditions was performed. For a direct evaluation of vibration performance under actuation, a control strategy needs to be introduced. The framework is, in principle, capable of evaluating a given controller. But the design of such may require further reduced order modeling coming from the current approach. This is a rich area of research that should be pursued in the future.

d) Effect of Advance Ratio: All the optimization studies for the design of composite rotor blade were performed in hover condition. Although it was shown that the optimum design obtained in hover condition is close to the optimum in forward flight, this should be formally demonstrated and its limitations established. Also, propulsive trim needs to be considered instead of the wind tunnel trim used in this thesis for forward flight conditions.

e) Effect of Actuator-flap Dynamics: In the optimization studies performed in this thesis, only the inertia effect of actuator and flap was included in the aeroelastic analysis. However, the dynamics of the combined flap-actuation mechanism also should be modeled to completely capture its effects when assessing the effectiveness of the flap system for vibration reduction. The dynamic properties of the flap actuation mechanism can be determined by performing experimental analysis on the bench as described in Appendix C.

f) Non-Harmonic Camber Actuation: To obtain performance enhancement, it was observed that camber actuation is required only in the retreating side of the blade. Thus, non-harmonic periodic actuation (instead of harmonic) should be investigated for performance enhancement in dynamic stall conditions.

APPENDICES

Appendix A. Surrogate Based Optimization

This section provides mathematical expressions related to the development of surrogate models and Efficient Global Optimization (EGO) algorithm used in the thesis. Further details about these concepts can be found in [96, 172].

A.1 Construction of Surrogate

The purpose of creating a surrogate model is to map a function $y=y(x)$ to a black-box function which can be evaluated very quickly. The generic solution method is to collect output values $y^{(1)}$, $y^{(2)}$, …., $y^{(n)}$ that result from a set of inputs $x^{(1)}$, $x^{(2)}$, ….. $x^{(n)}$ and find a best guess $\hat{y}(x)$ for the mapping, based on these known observations. The set of points $\boldsymbol{x}$ are selected from the chosen range of design variables using Latin Hypercube Sampling (LHS) technique. In this method, the points are selected in such a way that the distance between these points in the design space is maximized.

Kriging is based on the fundamental assumption that the errors involved in the prediction $\hat{y}(x)$ are correlated. This implies that error obtained at two close points together will be close. In kriging method, the unknown function $\hat{y}(x)$ is assumed to be of the form:

$$\hat{y}(x) = f(x) + Z(x)$$

where, $f(x)$ is an assumed function (usually a polynomial) and $Z(x)$ is a realization of a stochastic process. The function $f(x)$ can be thought of as a global approximation of $y(x)$,

while *Z(x)* accounts for local deviation which ensures that the kriging model interpolates the data points exactly. The function *Z(x)* is assumed to follow a distribution (Gaussian or normal distribution) with zero mean value and variance of σ^2_{var} . The covariance matrix of *Z(x)*, which is a measure of how strongly correlated two points are, is given by:

$$\mathrm{Cov}\left[Z\left(x^{(i)}\right),\ Z\left(x^{(j)}\right)\right] \ = \ \sigma^2_{var} R_{krg}$$

where each element of the correlation matrix R_{krg} is given by:

$$\left(R_{krg}\right)_{ij} = R_{krg}\left(x^{(i)}, x^{(j)}\right)$$

and $R_{krg}\left(x^{(i)}, x^{(j)}\right)$ is a correlation function which accounts for the effect of each interpolation point on every other interpolation point.

Correlation Models

The DACE Toolbox [163] used for developing the surrogate models in this thesis provides following options for correlation function:

1) Gaussian Function

$$R_{krg}\left(x^{(i)}, x^{(j)}, \theta\right) = \exp(-\theta \mid x^{(i)} - x^{(j)} \mid^2)$$

2) Exponential Function

$$R_{krg}\left(x^{(i)}, x^{(j)}, \theta\right) = \exp(-\theta \mid x^{(i)} - x^{(j)} \mid)$$

3) Spline Function

$$R_{krg}\left(x^{(i)}, x^{(j)}, \theta\right) = \begin{cases} 1 - 15\xi^2 + 30\xi^3 & for\ 0 \le \xi \le 0.2 \\ 1.25(1-\xi)^3 & for\ 0.2 \le \xi \le 0.1 \\ 0 & for\ \xi > 1 \end{cases}$$

where, $\xi = \theta \mid x^{(i)} - x^{(j)} \mid$.

4) Linear Function

$$R_{krg}\left(x^{(i)}, x^{(j)}, \theta\right) = \max(0, 1-\theta\,|\,x^{(i)} - x^{(j)}\,|)$$

The variation of correlation function for different values of parameter θ is given in Figure A-1.

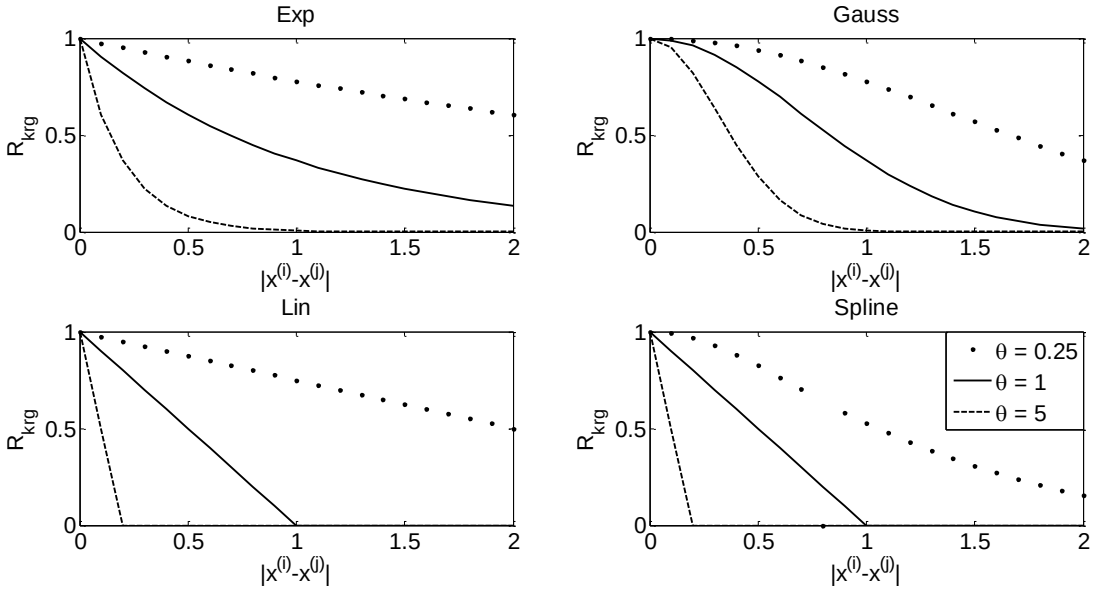

Figure A-1: Correlation Functions

The fitting parameter θ is an unknown correlation parameter which needs to be determined. The value of θ in turn depends on the form of *f(x)* chosen for the surrogate model.

Regression Models

In order to predict the value of *f(x)*, a regression model is used which is a linear combination of *p* chosen functions f_i . Thus, *f(x)* can be written as:

$$f(x) = \beta_1 f_1(x) + \beta_2 f_2(x) \ldots\ldots + \beta_p f_p(x) = F\beta$$

where, $F = [\, f_1(x^{(1)})\ \ f_2(x^{(1)})\ \ \ldots\ldots\ f_p(x^{(1)})\,]_{n \times p}$.

The coefficients β are called regression parameters. The toolbox provides regression models with polynomials of the order 0, 1 and 2. The value of f_i (x) for each of these cases is given by:

a) Order 0, p = 1:

$$f_1(x) = 1$$

b) Order 1, p = n+1:

$$f_1(x) = 1, \quad f_2(x) = x_1, \ \ldots\ldots, \quad f_{n+1}(x) = x_n$$

c) Order 2, $p = \frac{1}{2}(n+1)(n+2)$

$$f_1(x) = 1$$

$$f_2(x) = x_1, \quad f_3(x) = x_2, \ \ldots\ldots, \quad f_{n+1}(x) = x_n$$

$$f_{n+2}(x) = x_1^2, \quad f_{n+3}(x) = x_1 x_2, \ \ldots\ldots, \quad f_{n+1}(x) = x_1 x_n$$

$$\ldots\ldots\ldots\ldots\ldots\ldots\ldots\ldots\ldots\ldots \quad f_p(x) = x_n x_n$$

For each response, the correlation function and the regression model which gave the minimum error in the prediction of response function was selected for developing the surrogate model.

Estimating Kriging Parameter θ

The value of kriging parameter θ is determined by using the likelihood (L) estimates. The likelihood function is a measure of probability of the sample data being drawn from a probability density function associated with a Gaussian process. The maximum likelihood estimate of θ represents the "best guess" for fitting parameter. Although, any value of parameter θ would result in a surrogate that interpolates the sample point exactly, the "best" kriging surrogate is obtained by maximizing the likelihood function.

The log of likelihood function (also known as *concentrated ln-likelihood function* in literature) is given by:

$$\ln(L) = -\frac{\left[n\ln(\hat{\sigma}^2_{\text{var}}) + \ln|R_{krg}| \right]}{2}$$

where , $\hat{\sigma}^2_{\text{var}}$ is the generalized least square estimate of σ^2_{var} and is given by :

$$\hat{\sigma}^2_{\text{var}} = \frac{(y - F\hat{\beta})^T (R_{krg})^{-1} (y - F\hat{\beta})}{n}$$

and $\hat{\beta}$ is given by:

$$\hat{\beta} = (F^T (R_{krg})^{-1} F)^{-1} F^T (R_{krg})^{-1} y$$

The auxiliary optimization process of determining optimum θ can result in significant fitting time depending upon the size of the system. During this optimization process, scaling of the design space from 0 to 1 is very useful to ensure that the value of θ does not vary significantly for different design variables. Hence, kriging is only appropriate when the time needed to generate the interpolation points is much larger than the time to interpolate the data, which is true for all the aeroelastic analyses performed in this thesis. This auxiliary optimization for determining the parameter θ is performed using the MATLAB function "UMDIRECT" described in [173].

When all the parameters are known, the kriging approximation to a function *y(x)*, for any order regression function, can be written as:

$$\hat{y}_{krg} = F\hat{\beta} + r_{krg}(x)^T (R_{krg})^{-1} (y - F\hat{\beta})$$

where,

$$r_{krg} = [R_{krg}(x, x^{(1)}), R_{krg}(x, x^{(2)}), ..., R_{krg}(x, x^{(n)})]^T$$

The column vector r_{krg} of length n is the correlation vector between an arbitrary point x and the interpolation points, $x^{(1)}$, ……, $x^{(n)}$.

Error Estimate

The mean square error (MSE), at any point in the design space, of the kriging predictor can be written as:

$$s^2(x) = \hat{\sigma}^2_{\text{var}} \left[1 - r_{krg} R_{krg}^{-1} r_{krg}{}^T + \frac{(1 - 1^T R_{krg}^{-1} r_{krg})^2}{1^T R_{krg}^{-1} 1} \right]$$

The error described above is a measure of uncertainty in the prediction.

A.2 EGO Algorithm

After the surrogate models are obtained for objective function and constraints, optimization analysis can be performed directly on these surrogate models using gradient based or non-gradient based techniques like genetic algorithm. In this case, the result obtained at the end depends on the accuracy of the surrogate models and the final result may be a poor design. In order to obtain accurate surrogate over the complete design space, large number of function evaluations are required which can be very time consuming. The alternative to this "one-shot" approach is to account for the uncertainty in the surrogate model. This can be achieved using the Efficient Global Optimization (EGO) algorithm which accounts for uncertainty in the surrogate *and* is more efficient.

The optimization performed using EGO algorithm is iterative in nature, as described in Chapter 3. In EGO, a small number of initial design points are used to fit a kriging approximation in the first iteration, instead of starting with a large number of fitting points to obtain an accurate surrogate model. In the next step, the objective

function to be minimized or maximized is replaced by the Expected Improvement Function (EIF) which is maximized during the optimization process. The optimized set of points obtained by maximizing EIF are referred to as "Infill Samples" and are chosen to be in the region where there is a high probability of producing a superior design over the current best design and/or where the predictions of the surrogate are unreliable due to the high amount of uncertainty. Thus, these infill samples represent a balance between the local consideration of finding an optimal design based on the information in the surrogate, and the global consideration of sampling in the design space where there is much uncertainty in the surrogate's predictions. The objective function and constraints are determined again at these "Infill Sample" points and the surrogate models are updated using the old and new set of fitting points. This process is repeated multiple times till the stopping criterion is satisfied.

Therefore, the EGO algorithm is able to adapt to potential errors in the approximate objective function by sampling at points at which there is much uncertainty in the surrogate's predictions.

Expected Improvement Function

The expected improvement function can be written as:

$$EIF(x) = \chi_1 + \chi_2 \quad \text{if s > 0}$$

$$= 0 \qquad \text{if s = 0}$$

where,

$$\chi_1 = (y_{\min} - \hat{y}_{krg})\Phi_{dist}\left(\frac{y_{\min} - \hat{y}_{krg}}{s}\right)$$

and

$$\chi_2 = s\phi_{den}\left(\frac{y_{\min} - \hat{y}_{krg}}{s}\right).$$

The functions $\Phi_{dist}(*)$ and $\phi_{den}(*)$ represent the standard normal distribution function and the standard normal density function respectively. The first term in the *EIF*, χ_1, is the difference between the current best objective function value and the response at an arbitrary design, *x*, multiplied by the probability that *y(x)* is better than $y_{\min}$. This term is large when $\hat{y}_{krg}$ is likely to be better than $y_{\min}$. The second term, χ_2, is large when the error metric *s(x)* is large which signifies significant uncertainty in the surrogate's prediction. The design point with the highest EIF value represents the balance between finding a better point and finding regions of high uncertainty. In MATLAB, *EIF*(*x*) can be evaluated using the following expression:

$$EIF(x) = (y_{\min} - \hat{y}_{krg})\left[\frac{1}{2} + \frac{1}{2}erf\left(\frac{y_{\min} - \hat{y}_{krg}}{s\sqrt{2}}\right)\right] + s\frac{1}{\sqrt{2\pi}}\exp\left(\frac{-(y_{\min} - \hat{y}_{krg})^2}{2s^2}\right)$$

where, *erf*(*) is the error function defined in MATLAB.

Appendix B. UM/NLABS-A Aerodynamics Model

This section provides detailed description of the unified aerodynamic model used in UM/NLABS-A. The unified airloads model includes three key elements: Peters flexible airloads theory, the 3D dynamic inflow model and the modified ONERA stall model. The schematic of the unified airloads model is shown in Figure B-1. The unified airloads model accounts for arbitrary airfoil motion, morphing airfoil shape, and the dynamic stall effects. The description provided in this section is based on the detailed analysis given in [145, 168, 169].

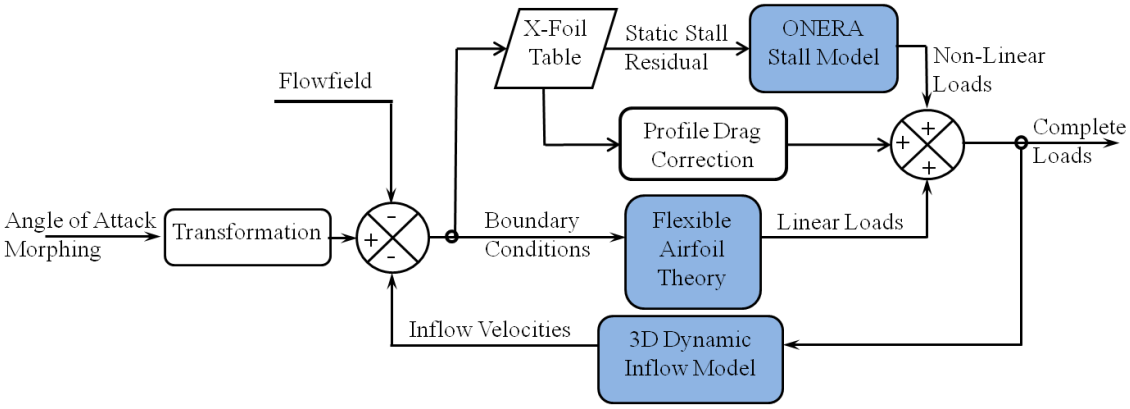

Figure B-1: Unified Airloads Model

B.1 Peters Flexible Airfoil Theory

The 2D aerodynamic analysis is based on 2-D finite state formulation for a flexible airfoil, as originally presented in [167]. Consider a thin airfoil of arbitrary shape moving through the thin air as shown in Figure B-2. As shown in the figure, the co-ordinate system is centered at the mid-chord and *b* is the semichord. With respect to the frame, the

fluid moves with horizontal velocity u_0, vertical velocity v_0 and rotation v_1. The deformation of the airfoil is given by the distribution $h(y,t)$, which is defined positive down. It is assumed that the deformation within the reference frame is small, such that, $h \ll b$, $\partial h/\partial y \ll 1$ and $\partial h/\partial t \ll u_0$. Trailing edge vorticity is assumed to be emitted in the direction of +Y axis.

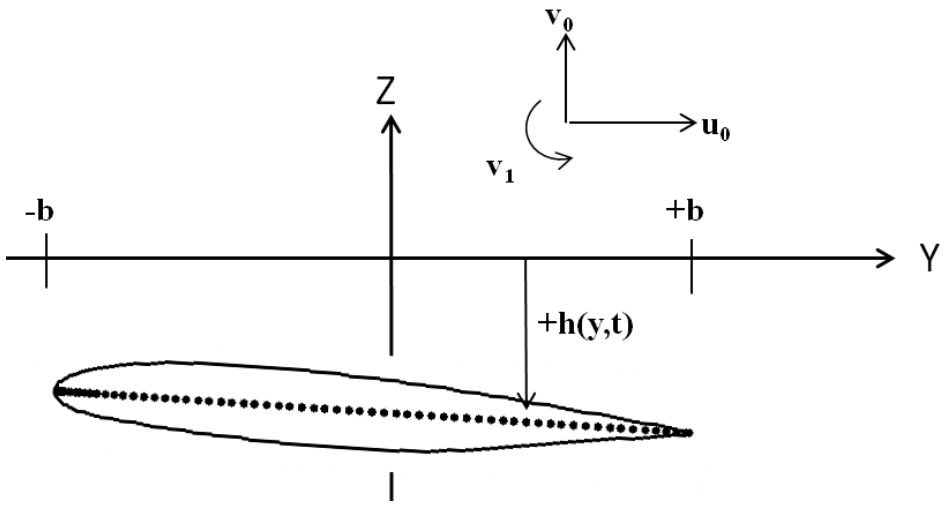

Figure B-2: General Airfoil Coordinate System

For this airfoil configuration, the non-penetration boundary condition can be written as:

$$w = \bar{v} + \lambda = u_0 \frac{\partial h}{\partial y} + \frac{\partial h}{\partial t} + v_0 + v_1 \frac{y}{b}$$

where, w is the total induced flow, λ is induced flow from the trailed circulation and $\bar{v}$ is the induced flow from bound circulation. Expressing $\bar{v}$ in terms of bound circulation per unit length γ_b:

$$\bar{v} = \frac{-1}{2\pi} \int_{-b}^{+b} \frac{\gamma_b(\xi,t)}{y-\xi} d\xi$$

The vorticity equation gives the loading due to circulation as:

$$\Delta P = \rho u_0 \gamma_b + \rho \int_{-b}^{y} \frac{\partial \gamma_b}{\partial t} d\xi \qquad \text{where, } (-b \le y \le b)$$

The spatial gradient of the induced flow due to shed wake is related to the temporal gradient of the induced flow:

$$\frac{\partial \lambda}{\partial t} + u_0 \frac{\partial \lambda}{\partial y} = \frac{1}{2\pi} \frac{d\Gamma}{(b-y)dt}$$

Above equations define the flexible airfoil theory, which must be expressed in terms of frame motion, and blade deformation. To carry out this transformation, all the variables are expressed with respect to the Glauert variable, φ. The change of variables is given by:

$$y = b\cos\varphi$$

where, $-b \le y \le +b,$ and $0 \le \varphi \le \pi$.

After the substitution, the expansions are as follows:

$$\gamma_b = 2\left[\frac{\gamma_s}{\sin\varphi} - \frac{\gamma_0 \cos\varphi}{\sin\varphi} + \sum_{n=1}^{\infty} \gamma_n \sin(n\varphi)\right]$$

$$\Delta P = 2\rho\left[\frac{+\tau_s}{\sin\varphi} - \frac{\tau_0 \cos\varphi}{\sin\varphi} + \sum_{n=1}^{\infty} \tau_n \sin(n\varphi)\right]$$

Similarly, the blade deformation, velocity and induced flow may be expressed as expansions in the Glauert variable:

$$h = \sum_{n=0}^{\infty} h_n \cos(n\varphi)$$

$$w = \sum_{n=0}^{\infty} w_n \cos(n\varphi)$$

$$\lambda = \sum_{n=0}^{\infty} \lambda_n \cos(n\varphi)$$

The $\cos(n\varphi)$ terms in the equation above correspond to the Chebyshev polynomial of the first kind along the nondimensional chordwise direction. Thus, there is a physical meaning for each term in the expansion. The first three terms correspond to plunge, pitch and camber respectively.

The airloads can be expressed in terms of the airfoil motion w_n and the uniform component of the induced flow, λ_0, by use of the vorticity equation:

$$u_0(w_0 - \lambda_0) = \tau_0$$

$$b(\dot{w}_0 - \frac{1}{2}\dot{w}_2) + u_0 w_1 = \tau_1$$

$$\frac{b}{2n}(\dot{w}_{n-1} - \dot{w}_{n+1}) + u_0 w_n = \tau_n, \text{ for n > 2}$$

The generalized loads are determined by substitution into the pressure distribution and integrating over the airfoil, that is:

$$L_n = -\int_{-b}^{+b} \Delta P \cos(n\varphi) dx = -\int_{-0}^{\pi} b\Delta P \cos(n\varphi)\sin\varphi d\varphi$$

The final results for the generalized loads are:

$$L_0 = -2\pi\rho b f u_0(w_0 - \lambda_0) - \pi\rho b u_0 w_1 - \pi\rho b^2(\dot{w}_0 - \frac{1}{2}\dot{w}_2)$$

$$L_1 = \pi\rho b u_0(w_0 - \lambda_0) - \frac{1}{2}\pi\rho b u_0 w_2 - \frac{1}{8}\pi\rho b^2(\dot{w}_1 - \dot{w}_3)$$

$$L_2 = \frac{1}{2}\pi\rho b u_0(w_1 - w_3) + \frac{1}{2}\pi\rho b^2(\dot{w}_0 - \frac{1}{2}\dot{w}_2) - \frac{1}{12}\pi\rho b^2(\dot{w}_2 - \dot{w}_4)$$

$$L_n = \frac{1}{2}\pi\rho b u_0(w_{n-1} - w_{n-3}) + \frac{1}{4(n-1)}\pi\rho b^2(\dot{w}_{n-2} - \frac{1}{2}\dot{w}_n) - \frac{1}{4(n+1)}\pi\rho b^2(\dot{w}_n - \dot{w}_{n+2})$$

The first two generalized loads, which correspond to lift and moment about the midchord, are completely defined by the first few terms of the velocity expansion. The lift and pitching moment are completely defined by the plunge, pitch and camber of the airfoil. The load L_0 is uniform force acting in the negative Z direction, that is, the negative of the conventional definition of lift. The load L_1 is a linear force distribution, so the quantity $L_1 x/2$ is the conventional nose up pitching moment about the midchord. Writing the velocities in terms of the frame motion and blade deformation:

$$w_0 = v_0 + \dot{h}_0 + u_0 \sum_{n=1,3,5}^{\infty} \frac{n h_n}{b}$$

$$w_1 = v_1 + \dot{h}_1 + 2u_0 \sum_{n=2,4,6}^{\infty} \frac{n h_n}{b}$$

$$w_m = \dot{h}_m + 2u_0 \sum_{n=m+1,m+3}^{\infty} \frac{n h_n}{b}, \quad \mathrm{m} \geq 2$$

Using these expressions, the final load equation can be written in matrix form.

The total circulation is found to be:

$$\Gamma = 2\pi b f (w_0 - \lambda_0) + \frac{1}{2} w_1 - \frac{1}{2} \lambda_1$$

The chordwise loading includes the induced drag and the leading edge suction force. It can be written as:

$$D = \int_0^{\pi} b(\Delta P) \frac{\partial h}{\partial x} \sin\varphi d\varphi - 2\pi\rho b f (w_0 - \lambda_0)^2$$

B.2 Dynamic Inflow Model

The dynamic inflow theory proposes the following solution to the velocity normal to the rotor disk in terms of radial and azimuthal expansion function:

$$w(s,\psi,t)=\sum_{r=0}^{\infty}\sum_{j=r+1,r+3}^{\infty}\phi_j^r(s)\left[\alpha_j^r(t)\cos(r\psi)+\beta_j^r(t)\sin(r\psi)\right]$$

where, s and t are the non-dimensionalized radius and time and ψ is the azimuth angle. The inflow states, α_j^r and α_j^r correspond to coefficients of the coupled terms containing the azimuthal harmonics and radial expansion functions, ϕ. Using the circulatory part of the lift obtained from flexible airfoil theory, wake skew angle, and the freestream velocity, the coefficients corresponding to the inflow states can be determined. Detailed description is provided in [168]. The zero-order inflow coefficient needed for the airloads expression is obtained from:

$$\lambda_0=\sum_{r=0}^{\infty}\sum_{j=r+1,r+3}^{\infty}J_0\left(\frac{rb}{s}\right)\phi_j^r(s)\left[\alpha_j^r(t)\cos(r\psi_q)+\beta_j^r(t)\sin(r\psi_q)\right]$$

The expression contains the Bessel function of the first kind, J_0, which can be approximated by taking first few terms of the Taylor series expansion, under the assumption that b/s is small for blades of typical aspect ratio, at sufficient distance from the rotor center.

B.3 Dynamic Stall Model

Dynamic stall occurs when some of the sections along the blade span oscillate in and out of the stall regime, as the blade rotates around the azimuth, resulting in hysteresis behavior for lift, moment and drag coefficeints. The static loss of lift acts as the forcing function to drive the ONERA differential equation for dynamic stall. When dynamic stall occurs, airloads display a *time delay* and *an overshoot* due to the passing of shed vorticity. In order to allow for this phenomenon, a second order transfer function is introduced.

Different steps involved in determining the loads generated due to dynamic stall effects are as follows:

a) Calculate 2D Aerodynamic Loads

As described in earlier section, Peters flexible airfoil theory is used to determine the aerodynamic forces. At the end of the analysis, load vector L_n and induced drag force component D are obtained.

b) Calculate the Angle of attack

It should be noted that in the Peters flexible airfoil theory, the angle of attack is not calculated explicitly. However, the angle of attack needs to be determined in order to calculate the static stall residuals and the coefficient of drag for profile drag correction term. In the current analysis, the angle of attack is defined as:

$$\alpha = \tan^{-1}\left(\frac{v_t}{u_0}\right)$$

where, u_0 is the incoming freestream velocity and v_t is defined as:

$$v_t = \dot{h}_n(0) + v_n(0) - \lambda_0(0)$$

c) Determine Critical Angle of attack

In the current analysis, critical angle of attack (in degree) is defined as

$$\alpha_{cr} = 13(1 - M^2)$$

where, M is the local mach number at the airfoil cross sections.

d) Calculate Delayed Angle of Attack

The time delay equation for determining the delayed angle of attack is given by:

$$\dot{\alpha}_d + \lambda_d \alpha_d = \lambda_d \alpha$$

where, α_d is the delayed angle of attack and $\lambda_d = U/\tau_d b$. In the current analysis, $\tau_d = 12$, however, its correct value needs to be determined using experimental results.

e) Calculate Static Stall Residual

As described in the earlier section, static stall residuals are the forcing parameters for the second order differential equation. Static stall residual represent the difference between the thin airfoil values for the airloads with appropriate static correction – and the experimental observation. In the current analysis, the experimental observations are substituted by the results from X-FOIL analysis. Static stall residual for lift and drag coefficient are shown in Figure B-3. For this particular case, Δc_l is positive while Δc_d is negative. Static stall residuals for different aerodynamic coefficient are defined below:

For lift coefficient:

$$\Delta C_L = C_{L\alpha}\sin(\alpha) - C_{L,Table} \quad \text{for } \alpha_d > \alpha_{cr}$$

$$\Delta C_L = 0 \qquad \text{for } \alpha_d \le \alpha_{cr}$$

For moment coefficient:

$$\Delta C_M = C_{M\alpha}\sin(\alpha)\cos(\alpha) + \frac{a}{2}C_{D,Table}\sin(\alpha) - C_{M,Table} \quad \text{for } \alpha_d > \alpha_{cr}$$

$$\Delta C_M = 0 \qquad \text{for } \alpha_d \le \alpha_{cr}$$

For Drag coefficient:

$$\Delta C_D = C_{D0} - C_{D,Table} \quad \text{for } \alpha_d > \alpha_{cr}$$

$$\Delta C_L = 0 \qquad \text{for } \alpha_d \le \alpha_{cr}$$

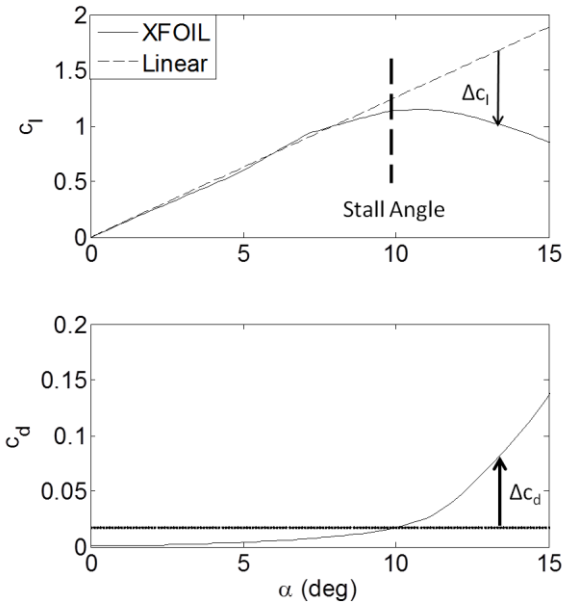

Figure B-3: Static Stall Residual

f) Calculating Loads due to Dynamic Stall Effect

The loads generated due to the dynamic stall effects, for each of the generalized coordinate, are computed using the following differential equation:

$$\frac{b^2}{u_T^2}\ddot{\Gamma}_n + \hat{\eta}\frac{b}{u_T}\dot{\Gamma}_n + \hat{\omega}^2\Gamma_n = -bu_T\hat{\omega}^2\left[\Delta C_n + \hat{e}\frac{d\Delta C_n}{dt}\frac{b}{u_T}\right]$$

The parameters $\hat{\omega}$, $\hat{\eta}$ and $\hat{e}$ are assumed to be of the functional form:

$$\hat{\omega} = \omega_0 + \omega_2\left(\Delta C_L\right)^2$$

$$\hat{\eta} = \eta_0 + \eta_2\left(\Delta C_L\right)^2$$

$$\hat{e} = e_0 + e_2\left(\Delta C_L\right)^2$$

where, the parameters e_0 ,e_2, ω_0, ω_2, η_1 and η_2 are determined by parameter identification.

g) Profile Drag

The effect of profile drag is included here in the quasi-steady sense using the table-lookup generated using XFOIL.

h) Combining all the loads

Since the stall model is based on flow-based reference system, it is assumed that the stall corrections to lift and drag are perpendicular to and parallel to the local freestream velocity, as shown in Figure B-4. The total life and drag forces in the large angle reference frame obtained by including the effect of dynamic stall loads and profile drag effects are given by:

$$L_{T0} = L_0 - \rho \bar{u}_0 \Gamma_0 - \rho b c_d u_T \bar{v}_L$$

$$D_T = D - \rho \bar{v}_L \Gamma_0 + \rho b c_d u_T \bar{u}_0$$

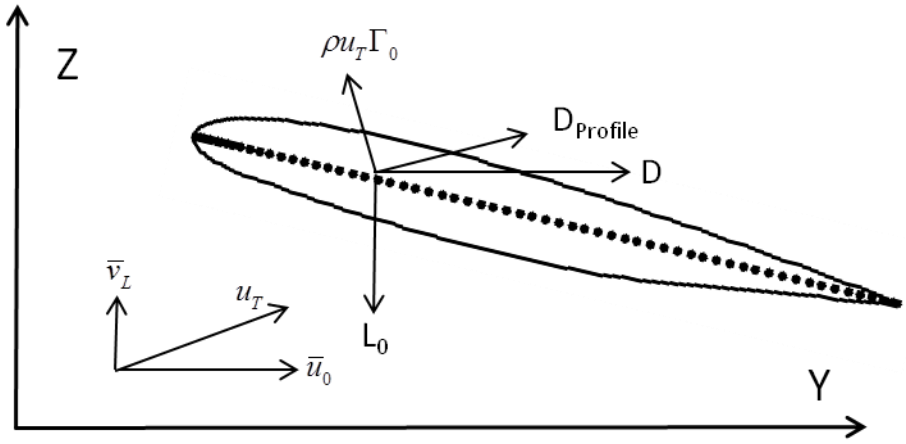

Figure B-4: Direction of Aerodynamic Forces

Appendix C. Design of Active Flap

Active flaps have proven to be very effective in reducing vibratory loads at the hub, minimizing noise and in some cases improving performance. Among active flaps, dual flaps have shown promising results in reducing vibrations and improving performance on a rotor as compared to a single flap. A number of experiments have been conducted to show the potential of active flaps in influencing hub loads. However, the performance penalty associated with oscillating flaps is yet to be quantified using experimental data. This performance penalty is critical for the implementation of active flaps on a rotor. The data obtained would be useful for validating the results obtained from CFD based simulations and ROM (reduced order models) based on CFD. Thus, the aim of the experimental analysis is to:

1) Test the effectiveness of dual flaps in influencing vibratory loads at the hub on a rotor in hover conditions.
2) Experimentally determine the performance penalty associated with oscillating dual flaps on a rotor blade in hover conditions.

For this purpose, an active 5ft long Mach-scaled composite rotor blade with dual flaps was designed and fabricated which could be tested in a hover spin test stand.

In this chapter, the design and fabrication of a flap-actuation mechanism is presented, which can be installed on a Mach-scaled rotor blade for testing the effects of dual flaps. The analysis performed includes detailed characterization of the two X-frame

piezoelectric actuators for determining their stiffnesses. In the next step, different components in the flap-actuation mechanism were sized to ensure sufficient flap deflection and strength of different components. The sizing was performed by determining the stiffness of the actuation system and the load path and using the impedance matching criteria to ensure maximum energy transfer. Finally, the flap supports were fabricated and tested on a bench set up and the amplitude of flap deflection and the output force obtained were measured.

The active flaps mounted on a rotor blade require high frequency of actuation for vibration reduction which is difficult to obtain using a servo-valve/hydraulic actuator [38]. The typical requirement for actuation frequency ranges from 2/rev to 5/rev frequency, depending upon the number of rotor blades in the helicopter. This corresponds to a frequency range of 20Hz to 50Hz for a rotor blade rotating at 600RPM. Besides the high bandwidth of actuation, piezoelectric actuators offer the advantages of: direct conversion of electrical energy into linear motion, less number of parts like pipes which are required for the hydraulic actuators, and smaller weight penalty. Piezoelectric material are capable of providing a large force, however the stroke provided by the piezos is very small and is limited by the inherent 0.1% cap on the free induced strain. Thus, for the practical implementation of piezoelectric material for active flap application, some form of amplification mechanism is required.

The requirements for an actuator [119, 128], which can be used for actuating flaps on a rotor blade, are based on the fact that they provide sufficient mechanical output of force and displacement without incurring any penalty on the structural and aerodynamic properties of the blade. The actuator must provide sufficient force to act against the

aerodynamic hinge moment and the stiffness of the flap-hinge mechanism and demonstrate flap deflection of ±4 deg at nominal RPM in different dynamic operating conditions. The actuator should be light in weight and the increase in mass of the blade due to the actuation system should be less than 20%. The installation of the actuator near the leading edge of the airfoil is beneficial from the aeroelastic stability point of view. The actuator must be capable of oscillating flaps at high frequencies (for an N bladed rotor, the actuator should provide sufficient amplitude of flap deflection up to (N+2)/rev frequency of actuation). To avoid any undesirable aerodynamic effects due to the actuation system, the actuator must be small enough such that it can fit in the blade spar. Actuators which extend over the large chordwise span create an issue of mass imbalance and are difficult to incorporate in the rotor blade. The actuator designed should have sufficient fatigue life and it should be able to perform in the presence of large vibration, unsteady aerodynamic loads and thermal environment. In most of the piezoelectric actuators, piezoelectric material is in the form of piezostacks which are connected in parallel to maximize the output displacement. In order to maintain the integrity of piezostacks and prevent them from discharging, a constant prestress is required. Thus, the actuator/actuation mechanism should be capable of providing prestress to the piezostacks. The control system operating the active flap should provide resolution and position sensing accuracy of 3% or less of the full range.

Among the current programs testing active flap, the SMART rotor program at Boeing [115] is using a double X-frame actuator developed by Hall et al. [174], while at the Eurocopter's ADASYS (Adaptive dynamic systems) rotor system [46], an amplified piezoelectric actuator developed by Cedrat Technologies in France [175] is being used.

More recently, the on-blade electro-mechanical actuator (EMA) developed by Hamilton Sundstrand Claverham and UTRC [116] was used by Sikorsky in their whirl and wind tunnel testing. Since the design of an actuator was not the main aim of this thesis, an off-the shelf actuator had to be obtained. Based on the literature survey conducted for different kinds of actuators available, the X-frame actuator manufactured by Axis Engineering Technologies, Boston and the Amplified Piezoelectric Actuator (APA) manufactured by Cedrat Technologies, France were short listed.

Table C-1: Comparison between X-frame Actuator and APA Actuators

Features	X-frame	APA 200M	APA 400 M	APA 900 M
Physical				
Length (mm)	80.9	55	48.4	49
Width (mm)	18.99	17	13	11.5
Height (mm)	10.72	9	11.5	10
Mass (gm)	40	15.7	19	19
Mechanical				
Displacement(μm)	1404	230	400	900
Blocked Force (N)	95	73	38	16
Stiffness (N/μm)	0.06	0.32	0.1	0.02
Resonance Freq	NA	900	495	248
Electrical				
Max Voltage (V)	1000	150	150	150
Capacitance (μF)	0.113	3.2	3.15	3.15
Calculated				
Lever Arm (s) (mm)	2.88	1.03	1.85	4.13
Flap deflection(δ) (deg)	19.42	8.63	8.38	8.44

Physical size of the actuator and the mechanical displacement and force provided by the actuator were the main driving factor for selection of the actuator. The actuators shown above were shortlisted based on their size and the size of supports required to hold them inside the blade. Among all the actuators listed in Table C-1, the X-frame actuator provides the maximum mechanical displacement and blocked force. During earlier experiments with active flaps [112], it was observed that the friction in rotating condition

due to high RPM can lead to a reduction in the amplitude of flap oscillations. Hence, it is desired that the actuator with maximum energy output is selected to ensure sufficient flap deflection at nominal RPM.

C.1 Quasi-static Tests

Quasi-static test of the actuator is performed to study the performance of the actuator and to determine its stiffness. The actuator performance is monitored by observing the actuator deflection as a function of input voltage and externally applied elastic load.

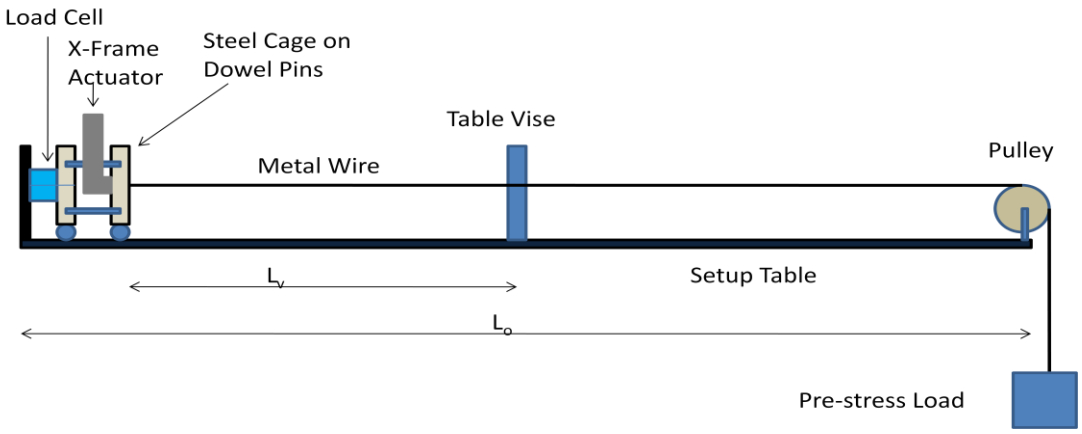

Figure C-1: Schematic of Quasi-Static Test

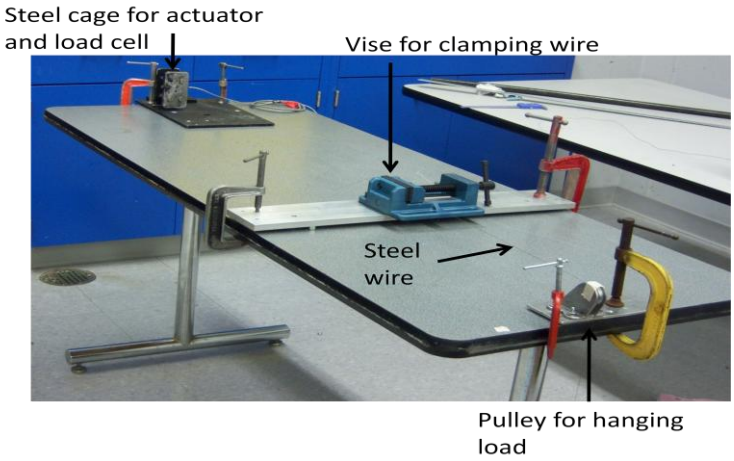

Figure C-2: Experimental Setup for Quasi-Static Tests

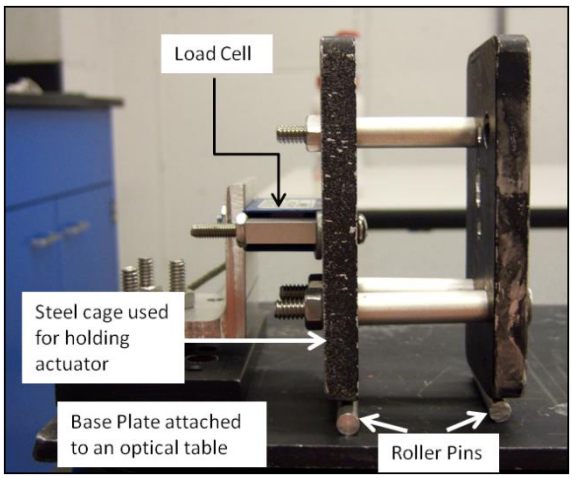

Figure C-3: Cage Region for holding the Actuator

The schematic of the experimental setup which was used for the quasi-static tests is shown in Figure C-1. The actual components of the setup are shown in Figure C-2 and Figure C-3. As shown in Figure C-2, the initial setup was done on a normal table but the initial tests results showed large unexpected vibrations. As a result, the experimental setup had to be transferred to an optical table for final testing. The setup consists of a steel cage in between which the actuator is held as shown in Figure C-3. The output end of the X-frame actuator is attached to a steel wire which runs across the table. At the other end of the steel wire, a constant mass of 19lb is attached through a pulley to provide a constant pre-stress to the actuator. The stiffness of the elastic load acting on the actuator is varied by changing the length of the wire (L_v) between the actuator and the table vise. This is obtained by clamping the wire at different locations along the length of the table during the tests. The length L_v was varied between 16" to 61" during the quasi-static tests. The actuator pre-stress was measured using a single axis load cell mounted behind the X-frame actuator. The displacement produced by the actuator was measured using a laser extensometer. The laser extensometer used for the tests has an accuracy of 0.1 mils (The expected value of displacement for these tests was around 20 mils). Both the load

cell and the laser extensometer were calibrated prior to the tests. The diameter of the metal wire was selected in such a way that the load stiffness due to the wire is in the range of expected aerodynamic hinge moment stiffness. Table C-2 shows the value of load stiffness provided by the metal wire for different lengths. Based on the approximate aerodynamic hinge moment loads calculated, a steel wire with diameter of 0.018 inch was used for these tests.

Table C-2: Variation of Load stiffness with the Length of Wire

Sr. No	L_v (in)	Stiffness (lbf/in)
1	16	481.0
2	20	384.8
3	25	307.8
4	45	171.0
5	61	126.2

The tests were performed at peak-to-peak voltages of 500V, 600V, 700V and 800V at 1Hz frequency to simulate the quasi-static conditions. In all these cases, the DC offset for the input voltage was adjusted such that the minimum value of the voltage applied was 0V. This is required to ensure that no negative voltage is applied to the actuator, which is detrimental to the health of piezo-stacks used in the actuator. FFT analysis was performed on the data obtained from the load cell and laser extensometer using MATLAB and the amplitude corresponding to 1Hz frequency was obtained.

Figure C-4 shows the results obtained from the quasi-static tests on both the X-frame actuators for characterization. The results obtained are compared to results obtained in [112] for $800V_{p-p}$ actuation. It can be seen that the value of displacements and loads obtained for both the actuators are close to those obtained for the reference case. The

reference case corresponds to the data obtained for an X-frame actuator of similar size tested at MIT [112]. The actuator stiffnesses obtained from Figure C-4 are listed in Table C-3. It can be seen that the stiffness obtained from the current set of experiments is higher than that obtained in [112]. This was expected, since a small modification was made in the new X-frame design to improve the performance of X-frame actuator.

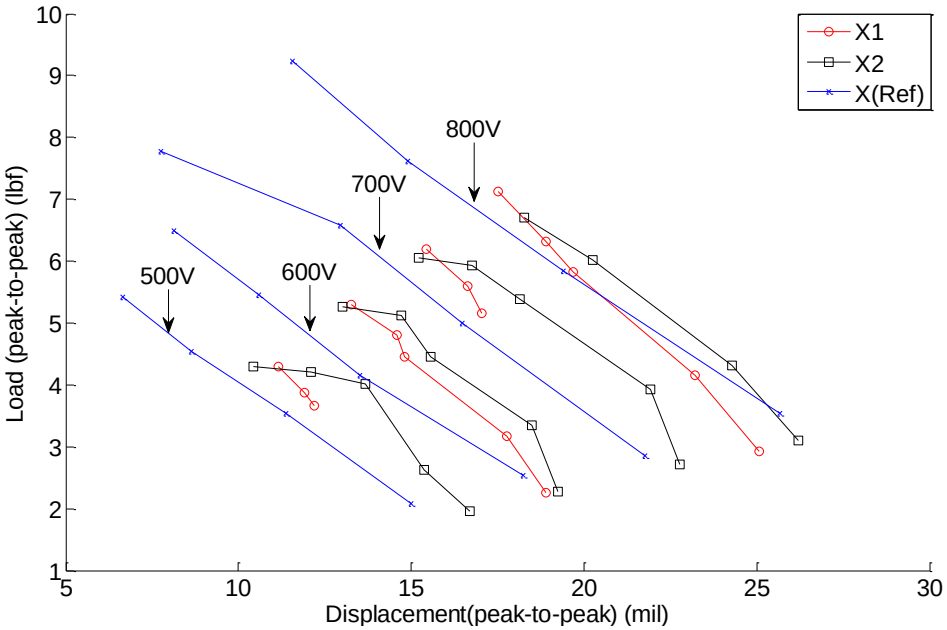

Figure C-4: Characterization of X-frame Actuators

Table C-3: Actuator Stiffness obtained from Quasi-Static Tests (Units: lbf/in)

Voltage	X1	X2	X (Ref)[112]
500V	592.5	396.0	397.0
600V	527	465.2	393.2
700V	617.3	424.7	357.1
800V	541.2	446.3	399.0
Average	569.5	433.0	386.6

C.2 Dual-flap Design

Based on the requirements for the tests, following parameters were fixed for the dual-flap design as shown in Figure C-5:

1) Chord length of the flap was fixed to 0.25c and the span-wise length of each flap was fixed to 0.06R
2) The first flap of the dual flaps extends from 0.72R to 0.78R while the second flap extends from 0.79R to 0.85R. Flaps could not be moved further towards the tip since there is a decrease in the thickness of the airfoil cross section beyond 0.85R. Both the flaps were kept close to each other so that when both the flaps operate with zero degree phase difference in the actuation voltage supply, it is approximately equivalent to a single 12% flap.
3) The actuators were mounted in the blade spar such that they are centered at 0.25c. As a result of this, the maximum thickness is available in the airfoil cross-section to mount the actuator and no additional ballast mass is required to balance the actuator weight.

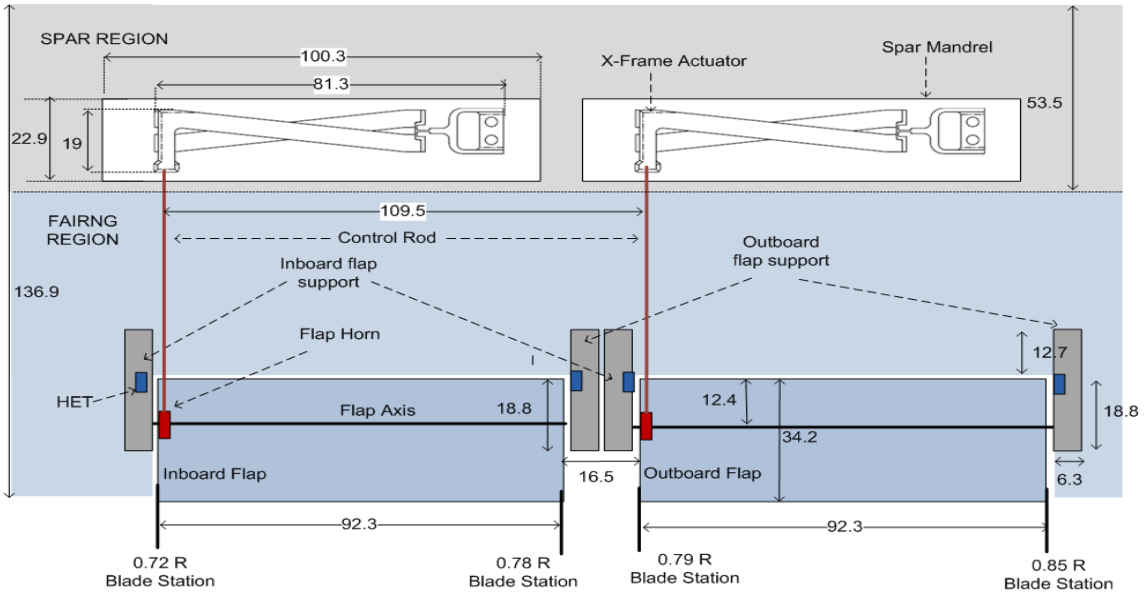

Figure C-5: Location of Flaps and Actuators

C.2.1 Aerodynamic Hinge Moment

The aerodynamic hinge moment had to be determined prior to designing the components for flap hinge mechanism. In order to minimize the aerodynamic hinge moment against which the active flaps needs to operate, an optimum position for the flap axis needs to be determined. For the purpose of these tests, a flap chord of 0.25c was used as discussed above.

The geometry of the VR7 airfoil with a 25% plain flap is defined in Figure C-6. A hinge gap of 1%c is present between the airfoil and the flap, as illustrated in Figure C-6. In order to determine the optimal flap hinge location so as to minimize the flap actuation power requirement, simulations using the CFD++ code were conducted for this two-dimensional airfoil/flap configuration. The CFD++ code is a compressible Reynolds-averaged Navier-Stokes flow solver which uses a finite volume formulation. Airfoil and flap grids were generated using ICEM-CFD, and an overset mesh approach is employed where a separate body-fitted mesh for the flap is generated in addition to the airfoil mesh, as illustrated in Figure C-7.

The simulations are conducted for the flow condition of M=0.538 and Re=1.79×10^6, which corresponds to the flow at the 0.85R spanwise location of the Mach-scaled model rotor. The Spalart-Allmaras (S-A) turbulence model is used and a fully turbulent boundary layer is assumed.

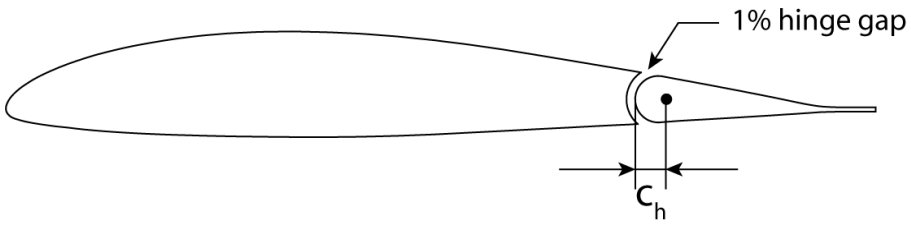

Figure C-6: VR7 airfoil with a Plain Flap

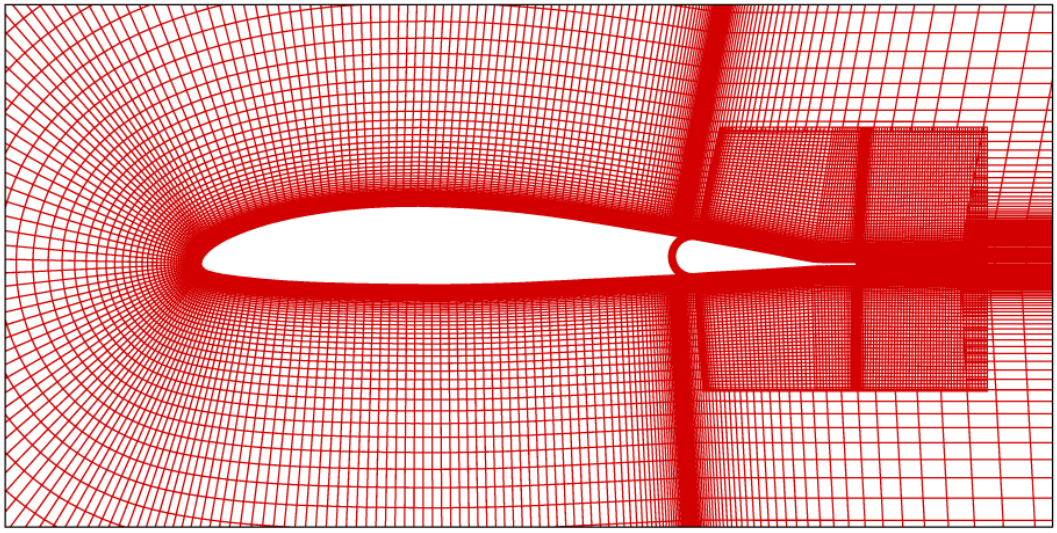

Figure C-7: Grids for the Airfoil with Flap

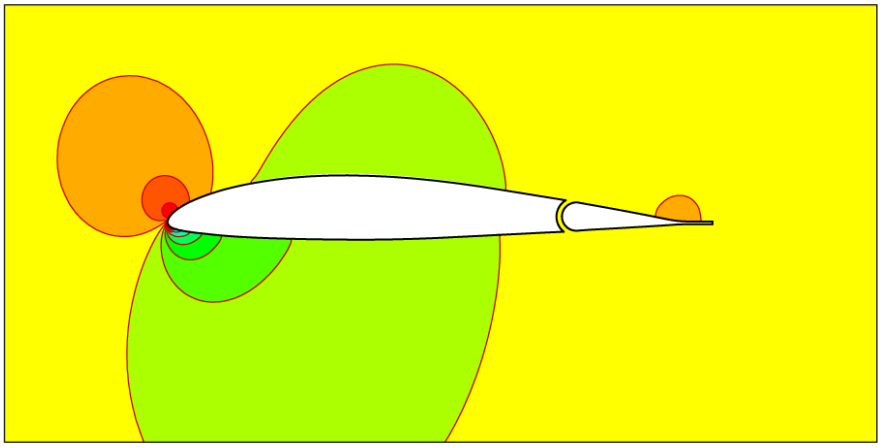

Figure C-8: Pressure Contour for α=4° and M=0.538

A sample result of pressure contour from the CFD simulation is shown in Figure C-8, for the case of α=4°. To determine the optimal flap hinge location, hinge moment curve slope $C_{H\delta}$ is calculated as a function of various hinge locations, defined by the distance c_h

from the leading edge of the flap, as illustrated in Figure C-9. The hinge location c_h is given as a percentage of flap chord c_f. Figure C-9 shows the variation of $C_{H\delta}$ versus c_h, at various airfoil angles of attack. A negative hinge moment curve slope implies an unstable configuration. From this figure, a flap location of $0.365c_f$ appears to be a good tradeoff between low flap actuation power and stability, for this flap configuration. The value of hinge moment coefficients for flap-hinge located at $0.365c_f$ are: $C_{H\delta} = 0.948x10^{-4}$ and $C_{H0f} = -0.0016$.

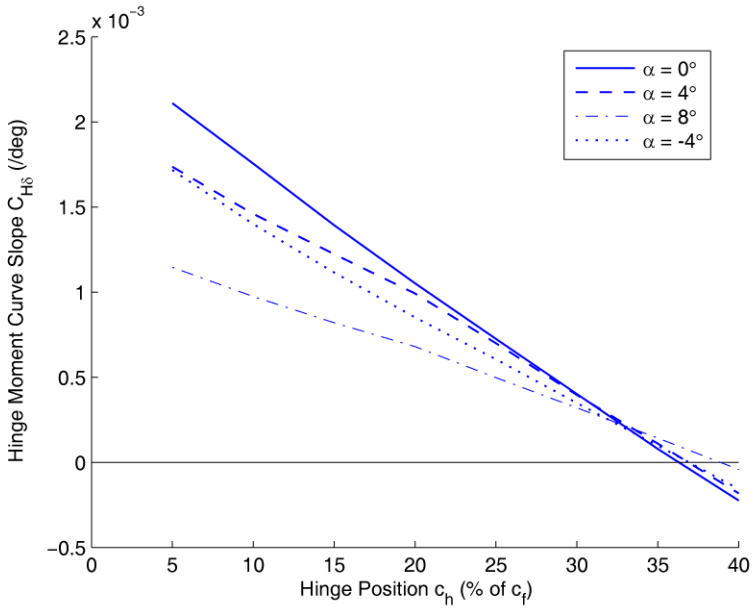

Figure C-9: Hinge Moment Curve Slope ($C_{H\delta}$)

In order to make sure that the flap effectiveness was not affected by moving back the hinge axis location, the lift generated by flap deflection was determined for different hinge axis location at angle of attack of 0 deg and 8 deg, as shown in Figure C-10. The results obtained from CFD show a very small difference in the lift coefficient curves corresponding to different flap axis locations. Very small decrease in the $C_{L\delta}$ is observed

due to flap hinge location as shown in Figure C-11. Thus the flap effectiveness was not compromised by moving back the flap hinge location.

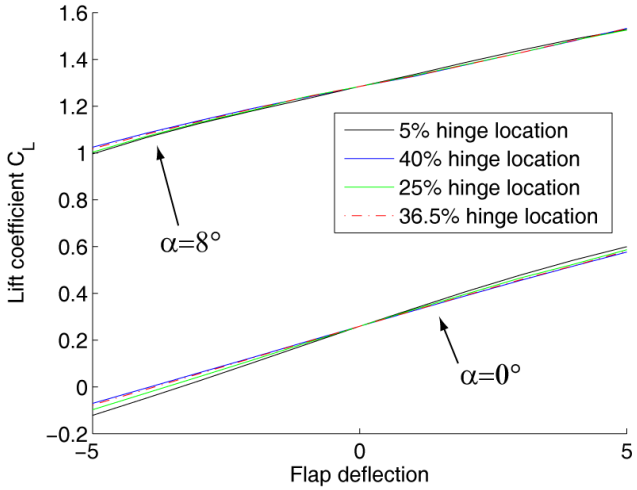

Figure C-10: Variation of Lift Coefficient due to Flap Deflection

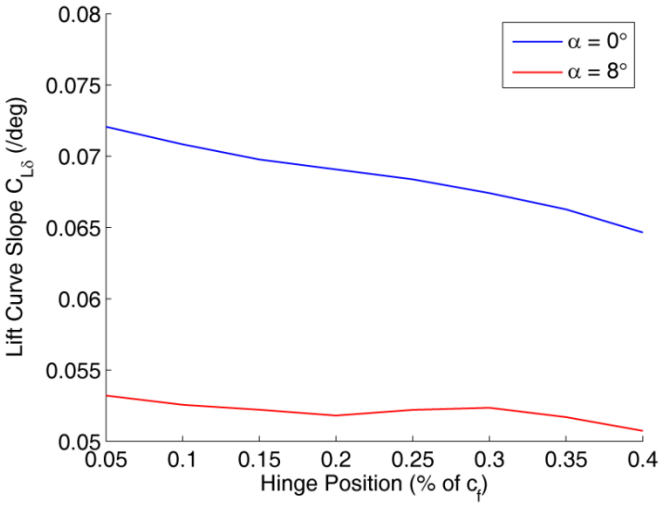

Figure C-11: Variation of $C_{L\delta}$ with Hinge Location

C.2.2 Sizing of the Parts for Flap Hinge Mechanism

Different components of the flap-hinge mechanism had to be sized properly and analyzed to ensure:

1) sufficient flap deflection,
2) sufficient strength and fatigue life,
3) small size of the parts so that they can be installed inside the blade easily,
4) small mass so that there is no mass penalty, and
5) low friction during operation at full RPM

Based on the above criteria and design used in [112], an approximate design for the flap hinge mechanism was developed. Many improvements were made in the new design to reduce friction and compliance in the system. As shown in Figure C-12, the airfoil cross section includes a cutout in the spar to hold the actuator. The supports required for holding the actuator and the flaps are integrated inside the blade during the fabrication process. Figure C-13 shows the detailed view for one of the flaps. The flap hinge-mechanism used for the both the flaps was identical.

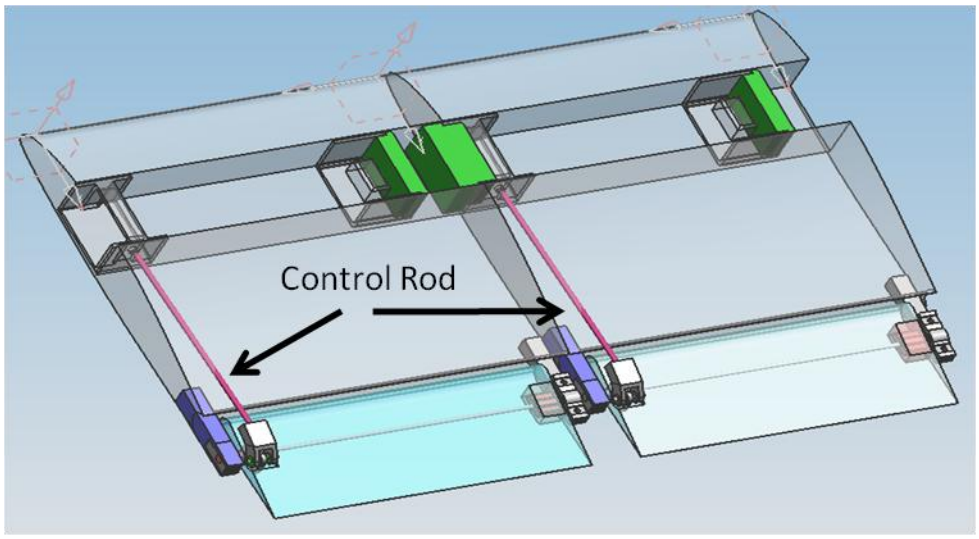

Figure C-12: Schematic of the Dual Flap Section of Rotor Blade

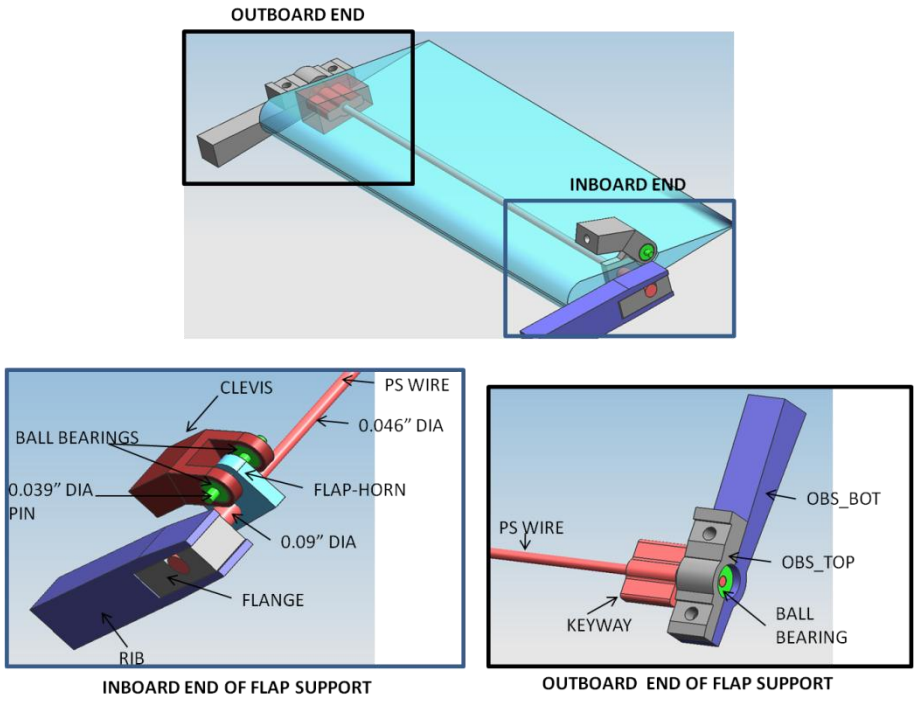

Figure C-13: Detailed View of the Flap Supports

Important components involved in the flap actuation system are:

1. *Control rod:* It is used to transfer actuation from the actuator to flaps (to clevis which is linked to flap horn on the active flap) as shown in Figure C-12. Its dimension was fixed by the size of the 0-80 threading used in the actuator and clevis pin. The minimum diameter corresponding to 0-80 threading is 0.056" (1.42 mm). It is expected to carry the load due to the prestress (~ 19lb) and actuation (max of 12lb). This corresponds to maximum load of 31lb on the control rod. For this load, the axial stress obtained in control rod is 85MPa.

2. *Prestress (PS) wire (Flap axis):* It acts as the rotational axis for the flap rotation. It has a torsional pre-twist which helps to keep the control rod in tension and thus, the piezo-stacks in compression. In this design, a steel rod with diameter of d_{ps} = 0.0465" (~1.18mm) was used as the prestress wire. This corresponds to a

torsional stiffness of 1.5862 in-lbf/rad for a 6% flap. The reasons of using this particular diameter are :

a) its torsional stiffness is of the order of expected aerodynamic stiffness,
b) it is easily available,
c) it matches the inner diameter of the ball bearing that was used at outboard end, and
d) twisting this steel rod by 60deg was sufficient to obtain required prestress without yielding the material.

3. *Inboard end of prestress wire*: The inboard end of the pre-stress wire is welded to a wire flange which in turn goes inside the reaction rib. The inboard end of the prestress wire should have very small compliance and the welded region should be able to carry the shear force due to pretwist and actuation. The diameter of the inboard end of the prestress wire used was 0.086".

4. *Wire flange*: It is welded to the inboard end of the prestress wire inside the flap. It includes two 0-80 threaded holes, which are used for holding the flaps during the operation. The wire flange is welded at an angle of 60 degree to the horizontal to provide prestress to the actuator.
5. *Flap Horn*: It is used to convert the linear motion of the actuator in to rotational motion for the flaps. Flap horn includes two holes, one for the prestress wire inside the flap and the other for clevis. The vertical distance between these two holes is the moment arm for converting the linear motion to rotational motion. The flap horn is fixed inside the inboard end of the flap during the fabrication of composite flap.

6. *Clevis*: Clevis is the link between the control rod and the flap horn. It includes a 0-80 threaded hole at one end which holds the control rod. At the other end, it is shaped like a fork and holds the flap horn in between using a steel pin.

C.2.3 Calculation of Compliance in the System

The effective stiffness of the actuator reduces mainly due to the compliance of following components in the flap actuation system: the axial strain in control rod, the bending of servo-flap horn, the torsion of flap skin and the bending of inboard end of the prestress wire. The effective compliance of the actuator is obtained by adding the compliance for all the components in the actuation load path. The compliance of different components in the actuation path is described below:

a) *Compliance of actuator:* The actuator 1 has a stiffness of 569.5 lb/in while the actuator 2 has stiffness of 433.01 lb/in (as shown in Table C-3). This corresponds to a compliance of C_{act1} = 0.0018 in/lb for actuator 1 and a compliance of C_{act2} = 0.0023 in/lb for actuator 2.

b) *Compliance of control rod*: The control rod has a diameter of 0.056" at its ends so that it can be fixed to moving frame of the actuator at one end and clevis at other end. In the middle, it has diameter of 0.125" to avoid bending of the control rod. This corresponds to a stiffness of 5942 lbf/in or compliance of $C_{cr} = 1.682 \times 10^{-5}$ in/lb.

c) *Torsion of flap skin*: The flap skin consisted of 2 layers of E-glass 120 oriented at ±45 deg and a layer of unidirectional IM7 ply added to front 55% of the flap. A finite element mesh for the cross section of the flap was developed in order to

determine its torsional stiffness. From the UM/VABS output, the torsional stiffness (GJ) of the cross section was obtained and it was equal to 2.02 Nm^2. The torsional stiffness for the flap was obtained by using the expression $T_{FS} = (GJ/L)_{flap}$ (= 21.99 Nm/rad). Assuming a moment arm of 0.12", this is equivalent to stiffness of 2.36×10^6 N/m. Thus, the compliance due to torsion of flap is $C_{FS} = 7.395 \times 10^{-5}$ in/lbf (=4.223×10^{-7} m/N).

d) *Inboard end of the pre-stress wire*: The flexing of the inboard end of the pre-stress wire adds compliance to the system. The diameter of this wire is $d_{ips} = 0.086$" and its length is $L_{ips} = 0.2$". The compliance of this section is approximately given by $C_{ips} = L_{ips}^3/3EI$, where $I = \pi d_{ips}^4/64$. Substituting these values, the compliance due to the inboard end of the pre-stress wire was obtained and it was equal to $C_{ips} = 3.26 \times 10^{-5}$ in/lbf (= 1.862×10^{-7} m/N)

e) *Bending/Shearing of flap horn:* The bending stiffness of flap horn was approximated using Timoshenko beam analysis and it was equal to 1.343×10^6 lbf/in. This corresponds to a compliance of $C_{fh} = 7.44 \times 10^{-7}$ in/lbf.

Net compliance of actuation path is given by:

$$C_a = C_{act} + C_{cr} + C_{FS} + C_{ips} + C_{FH}$$

Final stiffness of the actuation system is given by:

$$K_a = 1/C_a$$

The final stiffness obtained for the actuation path after all the calculation was equal to 527.3 lbf/in for actuator 1 and 408.2 lbf/in for actuator 2.

C.2.4 Stiffness of the Load Path

The load stiffness consists of torsional stiffness due to the aerodynamic hinge-moment, torsional load due to stiffness of the pre-stress wire and stiffness of cross-flexures of the centrifugal flexure in the X-frame actuator. An approximate analysis to predict each of these components is given below.

a) *Aerodynamic stiffness:* The aerodynamic torsional stiffness for a flap mounted on a rotor blade with inboard end at R_i and outboard end located at R_o is given by :

$$K_{aero} = \frac{1}{6}\rho\Omega^2 c_s^{\,2}(R_o^{\,3} - R_i^{\,3})C_{H\delta}$$

where $C_{H\delta}$ is the flap hinge moment obtained from aerodynamic analysis and c_s is the chord of the airfoil section. Substituting values of the different variables (ρ = 1.226 kg/m^3, Ω = 140rad/sec (1336 RPM), c_s = 5.388 in, R_o = 0.78R and R_i = 0.72R for inner flap and R_o = 0.85R and R_i = 0.79R for outer flap and $C_{H\delta}$= 0.948x10^{-4} /deg) in the above expression, aerodynamic stiffness values for two flaps are obtained and they are given by :

$$K_{aero,1} = 1.331 \text{ in-lb/rad} \quad \text{and} \quad K_{aero,2} = 1.590 \text{ in-lb/rad}$$

(Note: Subscript '1' corresponds to inboard flap while subscript '2' corresponds to outboard flap)

b) *Torsional stiffness of prestress-wire*: The prestress wire helps in providing prestress for the X-frame actuator and it acts as the hinge for the flap rotation. Torsional stiffness of prestress wire is given by :

$$K_{ps} = \frac{GJ_{ps}}{L_{ps}} \text{ where } J_{ps} = \frac{\pi d_{ps}^{\,4}}{32}$$

The torsional stiffness of prestress wire obtained after substituting all the values is: 1.586 in-lb/rad.

c) *Stiffness of flexure*: Stiffness of the flexure used in Ref [112] was 0.152 in-lb/rad. Assuming 10% increase in the stiffness (as mentioned by manufacturer), stiffness of flexure in our case can be approximately given by **K_f = 0.167 in-lb/rad**.

Thus, the total load stiffness is given by:

$$K_L = K_{aero} + K_{ps} + K_f$$

Summing up all the stiffness, load stiffness obtained for the two flaps are:

$$K_{L1} = 3.084 \text{ in-lbf/rad and } K_{L2} = 3.344 \text{ in-lbf/rad}$$

C.2.5 Impedance Matching

Moment arm required to obtain the impedance match condition is:

$$s = \sqrt{\frac{K_L}{K_a}}$$

This gives, moment arm of s_1 = 0.074 inch for the inboard flap and moment arm of s_2 = 0.088 inch for the outboard flap.

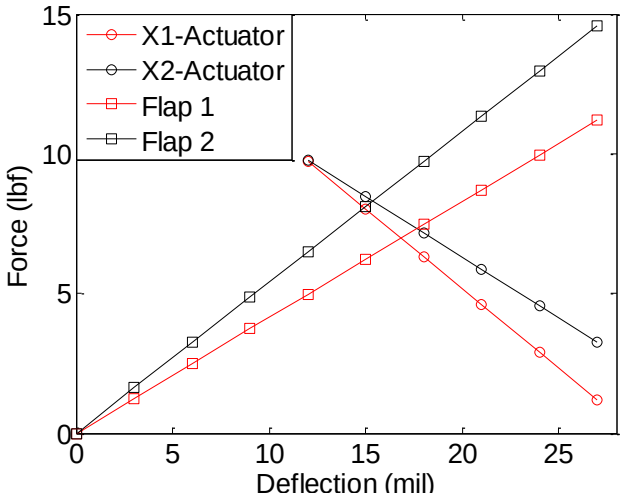

Figure C-14: Ideal operating point obtained using impedance matching

Combining flap 1 with actuator 1 (set1) and flap 2 with actuator 2 (set 2), we get peak-to-peak displacements of 33.6 mil and 30.74 mil for set 1 and set 2 respectively, and peak-to-peak forces of 13.94lbf and 16.64 lbf for set 1 and set 2 respectively.

Due to manufacturing constraints, it was difficult to fabricate parts with very small moment arms. Hence, the moment arm used for both the flaps was fixed to 0.12 in. As a result, there were small changes in the results obtained earlier as shown in Table C-4 and Figure C-15. The results obtained with modified moment arm show higher flap deflection but reduced forces. Based on above analysis, different parts were designed and fabricated as shown in Figure C-18.

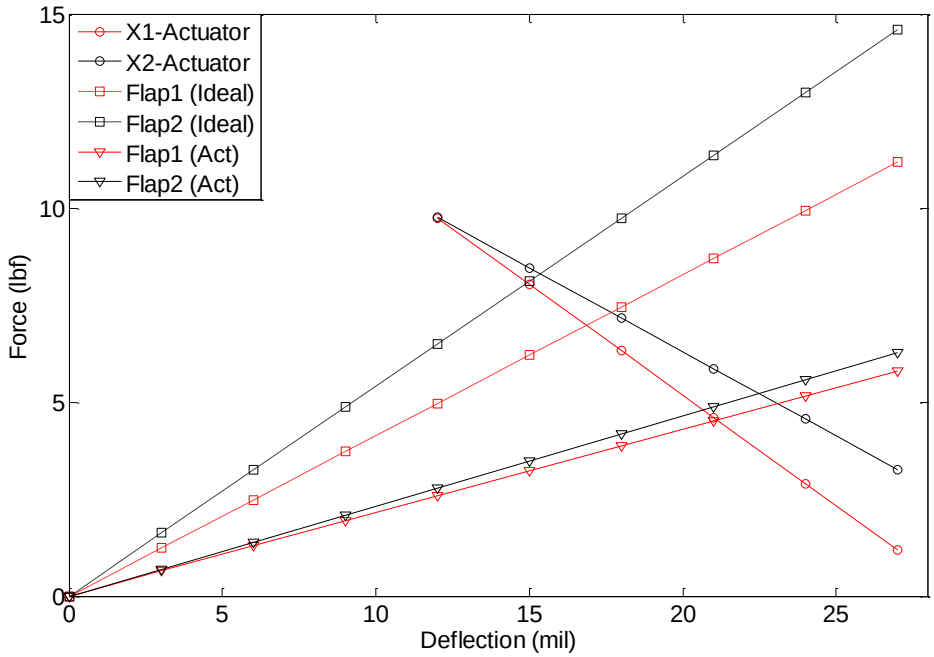

Figure C-15: Effect of Moment Arm Modification on Operating Point

Table C-4: Difference between Ideal and Actual Operating Condition

	Ideal Case		Actual Case	
	Set1	Set2	Set1	Set2
Mom Arm (mil)	75.6	89.8	120	120
Actuator Disp (mil)	33.6	30.74	44.9	42.27
Actuator Force (lbf)	13.94	16.6	10.44	9.05
Flap Deflection (deg)	12.85	9.91	10.59	9.98
Prestress (lb)	22.56	18.89	13.84	13.84

C.3 Bench Test for Active Flaps

Bench test was performed to validate the flap hinge mechanism designed for oscillating the flaps on a rotor blade. The parts which were designed for the bench test were such that they can be easily incorporated on the active blade with very minor changes. The bench test conducted with flap proved to be very useful in improving the flap-hinge mechanism design to get maximum flap deflection output from the actuator. For example, the initial design used for clevis was a curved one as shown in Figure C-12

and Figure C-17. This design was chosen so that a shorter moment arm, as required by the impedance matching condition, can be obtained. However, during the early bench tests, it was noticed that a curved clevis lead to bending of the control rod during its motion which increased the compliance of the actuation mechanism. As a result, very small flap deflections were obtained when the flap was actuated. This was corrected by using a flat clevis as shown in Figure C-16. Small modifications were also made in the inboard flap support in order to reduce the compliance. The CAD models for final parts used in the flap hinge mechanism are shown in Figure C-16. Since these parts had to be installed inside the rotor blade, they follow the airfoil contour, wherever possible. As a result of this complicated profile, some of the parts had to be cut using water-jet cutting technique in order to obtain an accurate profile. The final machined parts obtained are shown in Figure C-17. All these components, along with active the flap, were installed on a base plate for bench tests as shown in Figure C-18.

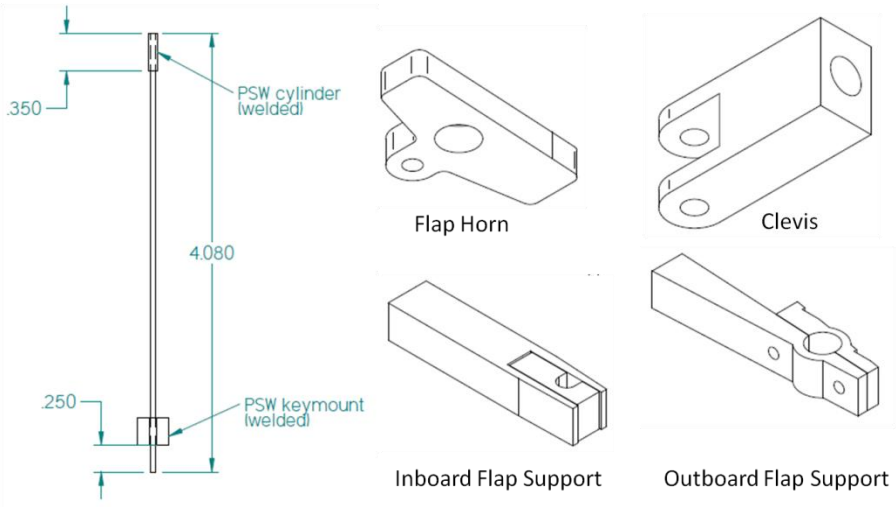

Figure C-16: CAD Model of the Flap Parts

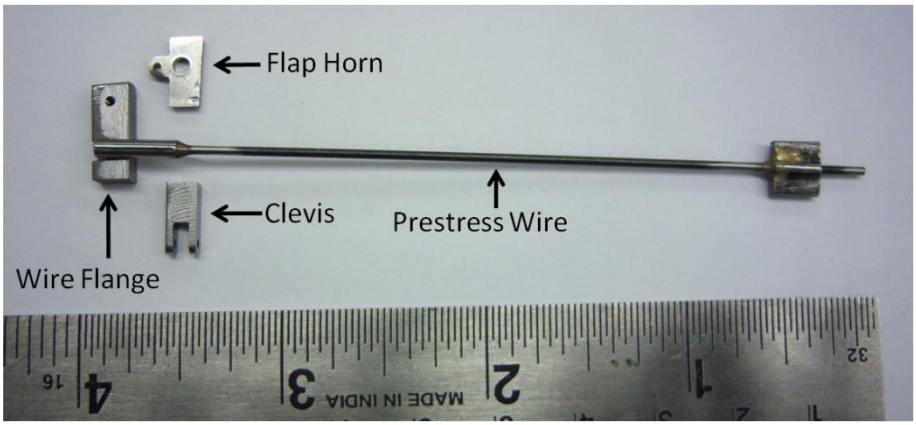

Figure C-17: Actual Fabricated Parts for Flap Hinge Mechanism

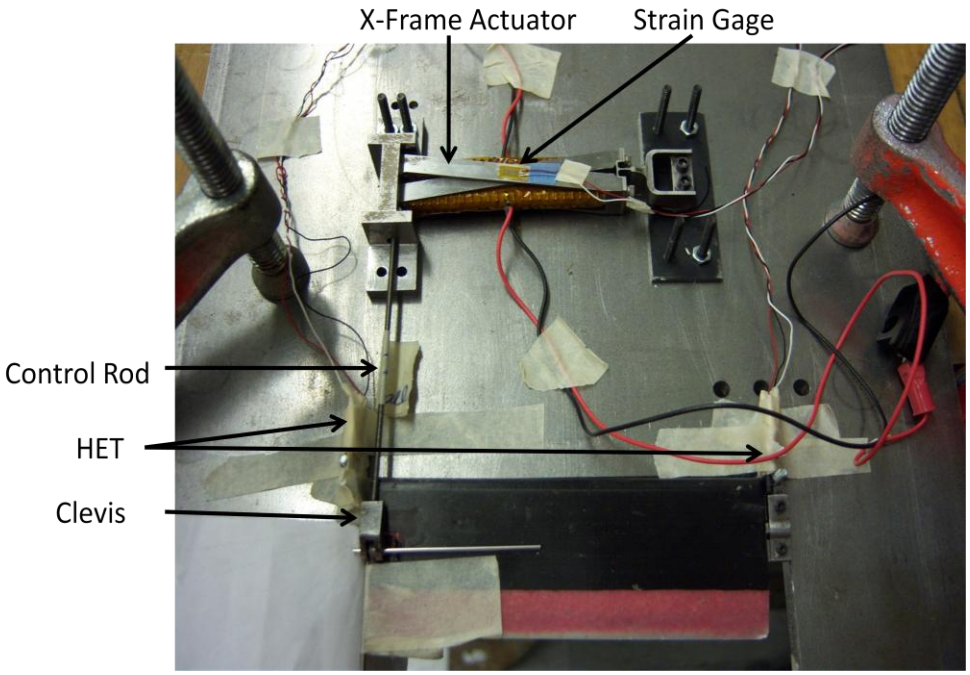

Figure C-18: Setup for Bench Test of Active Flap

Experimental results obtained for flap deflection and peak-to-peak force at different actuation frequencies are shown in Table C-5. Results show that the variation in amplitude of flap deflection and output force is small at low actuation frequencies. At high actuation frequencies, increase in flap deflection was observed at the cost of small decrease in the prestress force. In all the cases, the actuation voltage was kept constant at

approximately 760V_{p-p} with an offset of 400V. The hysteretic behavior observed in the flap-actuation mechanism is shown in Figure C-19. The presence of hysteresis is common in piezoelectric material and several attempts have been made to capture this effect in vibration reduction studies using active flaps [176].

Table C-5: Experimental Results for Bench Tests

Test	Freq (Hz)	Peak-to-peak (V)	Offset (V)	Pre-Stress (lbf) (peak-to-peak)	Mean load (lbf)	Deflection (deg) (peak-to-peak)
5	1	563.52	293.33	10.61	19.31	4.86
6	1	751.24	392.77	12.54	20.67	6.74
7	10	732.92	393.14	10.92	20.65	6.41
8	22	748	393.1	11.86	20.72	7.83
9	44	748	393.1	11.18	20.4	7.24
10	66	756.68	392.94	8.68	20.14	9.56
11	88	757.04	392.86	11.55	18.56	9.49
12	110	765.28	392.99	14.1	17.69	10.45

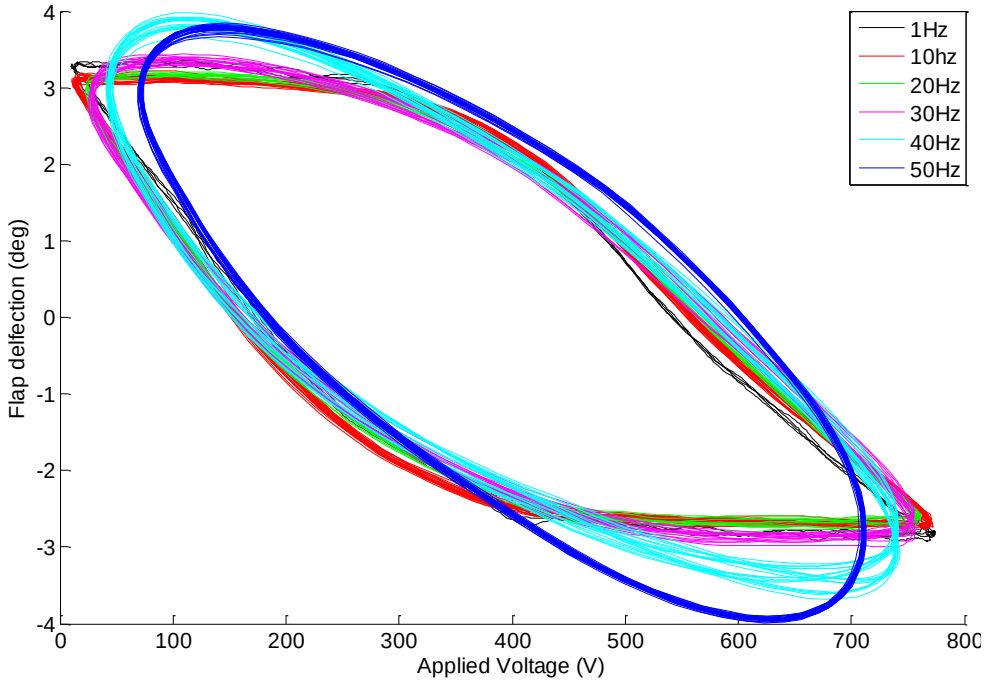

Figure C-19: Hysteresis in Flap Actuation

C.4 Conclusion

This chapter presented the design and experimental analysis of a flap-actuation mechanism that can be installed in a Mach-scaled rotor blade for testing the effect of dual active flaps. The analysis performed in this chapter is based on the X-frame actuator which was developed at MIT in 2000. As a first step, quasi-static tests were performed on the X-frame actuator to determine its stiffness and load-deflection relationship. This property was used in the design of supports for active flap using the impedance matching criteria. All the parts required for flap-actuation mechanism were designed and fabricated in order to maximize the dynamic flap deflection amplitude while ensuring sufficient output force to act against the prestress in flap and the aerodynamic loads. The final flap actuation mechanism was bench-tested and sufficient flap deflection and output force was observed. The experimental results showed flap deflection amplitude of more than 6deg at high frequencies of actuation (till 5/rev actuation frequency which corresponds to 110 Hz, for nominal operating condition at 1336 RPM).

The flap actuation mechanism designed in this chapter was installed on a 10 ft diameter Mach-scaled rotor blade and tested in the spin-test stand at the University of Michigan. Further details related to the design and fabrication of rotor blade and experimental tests are provided in following appendices.

Appendix D. Active Blade Design

The composite rotor blade to be used for testing the dual active flaps had to be designed to meet the requirements for strength and sufficient fatigue life. Besides this, the active blade includes cut-out in the spar to make space for mounting the X-frame actuator and cut in the fairing to hold the flaps. Before fabricating the final blade, sample sections of the blade were fabricated and tested in a tensile testing machine to check the blade strength. The active blade also includes instrumentation like strain gages, accelerometers to measure the blade deformation and hall effect sensors to measure flap deflection angles during the tests. The shape of the blade was fixed by the mold being used for the fabrication of rotor blade. In the current study, a $1/6^{th}$ scaled version of the CH-47D blade was used which has a radius of 5ft and chord of 5.38 in. Although, the outer mold line of the blade (and hence the geometry) was already fixed, the composite layup required to meet the design requirements had to be determined.

D.1 Geometry of the Baseline Blade

A $1/6^{th}$ mach-scaled Chinook CH-47D blade is used as the baseline for integral blade design. The spin test stand used for this test was designed with this particular blade in view. The fact that the same blade was used in earlier tests on a similar test stand was useful for obtaining preliminary data for design and validation purpose [58, 112]. Basic dimensions of the blade are given in Table D-1 and the planform view of the passive blade (without the active flaps) is shown in Figure D-1. The spin test stand hub is

articulated with the flap hinge axis located at 0.028R and the lead-lag hinge located at 0.15R. Blade pitch is fixed at a particular angle depending upon the required collective setting.

Table D-1: Blade Properties

Property	Value
Geometric Scaling	$1/6^{th}$
Radius	60.619 in (1.539 m)
Chord	5.388 in (0.1368 m)
Number of blades	2
Rotor Type	Articulated
Flap Hinge Location	0.028R
Lag Hinge Location	0.15R
Rotor Speed	1336 RPM

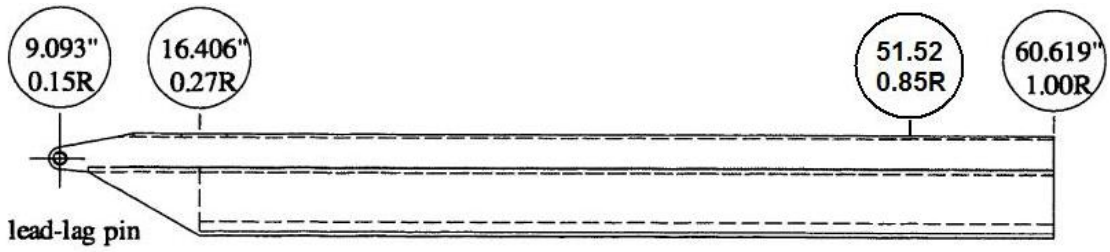

Figure D-1: Blade plan-form View [58]

The rotor blade has a non-uniform chord and thickness variation near the root region. From 0.27R to 0.85R, rotor blade has a uniform cross section of VR7 airfoil. The blade tapers from VR7 airfoil at 0.85R to VR8 airfoil at the tip. Both the airfoil sections are shown in Figure D-2. The VR7 airfoil is a 12% thick airfoil while the VR8 airfoil is 8% thick. Linear interpolation is used to obtain cross section shape for $0.85\ R < r < 1.0R$. The built-in twist for the rotor blade is shown in Figure D-3.

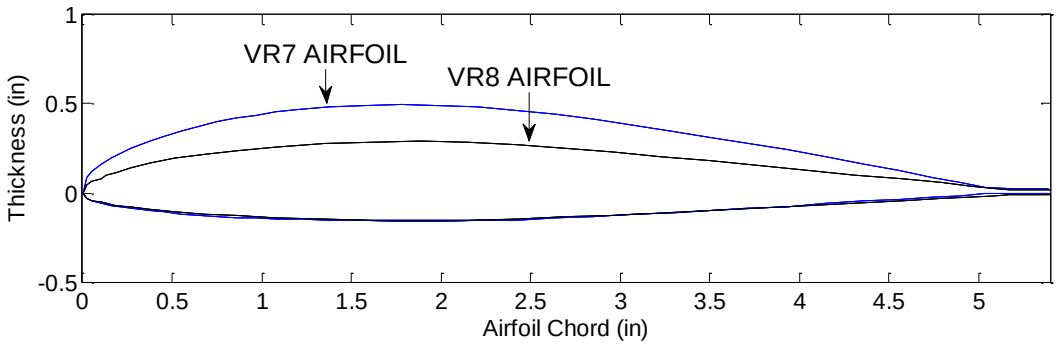

Figure D-2: Blade Cross Section

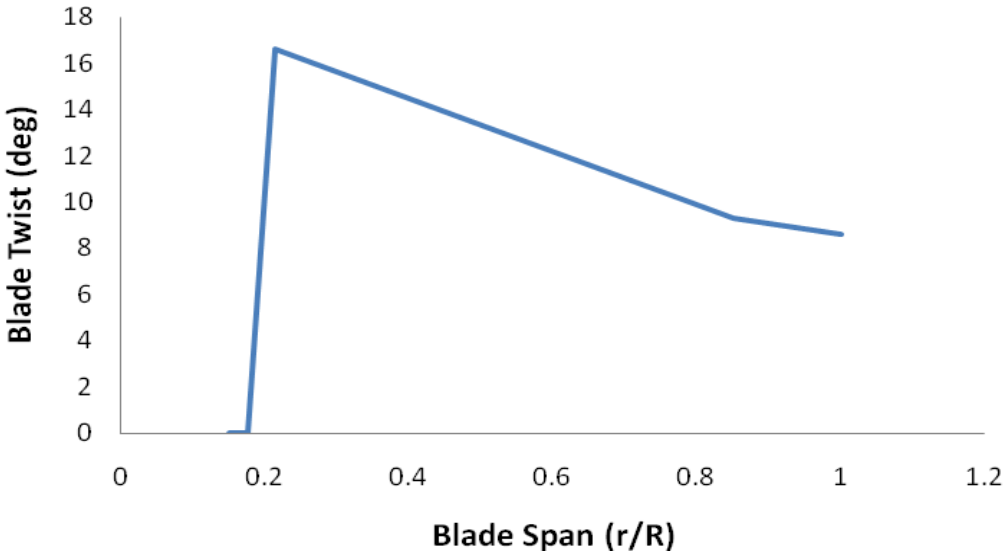

Figure D-3: Blade Twist Distribution

Cross-sectional details for the composite rotor blade are shown in Figure D-4. It consists of prepreg plies wrapped around the foam core. In the first cure, the front D spar of the blade is cured, while the fairing is attached to the front spar in second cure. Nose weights are added near the leading edge while fabricating the spar to get the CG of the cross section closer to the quarter chord. The number of plies for spar, web region and fairing and their ply angles had to be determined prior to fabrication.

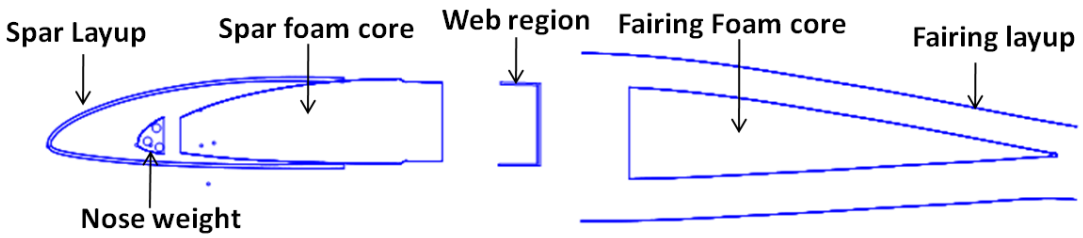

Figure D-4: Cross Section of the Rotor Blade

D.2 Blade-Layup Design Process

This section provides details about the blade structural analysis and the design process used for obtaining the final composite blade design. The spanwise view of the rotor blade with dual active flaps is shown in Figure D-5.

Figure D-5: CH47D Rotor Blade with Dual Active Flaps

Blade Analysis

The complete 3D analysis of the rotor blade is broken down into two steps, as discussed in Section 2.2. In the first step, a linear cross-sectional analysis of the composite rotor blade is performed to determine the cross-sectional properties of the blade at different spanwise locations. And in the second step, aeroelastic analysis of the rotor blade is performed on the 1D beam model. This breakdown of the analysis is valid for slender structures like aircraft wing and rotor blades. For the cross-sectional analysis, the blade shape and the layup information is required. Depending upon the complexity in rotor blade geometry and variation in the layup, the blade is divided into several spanwise sections. Blade properties are assumed to be constant in each section. In the current

analysis, the blade is divided into ten spanwise sections as described Table D-2. Since the blade's geometry and layup, both vary significantly in the root region, the number of sections is more in the root region.

Table D-2: Spanwise Regions for Cross-sectional Analysis

Sections	Span
Section 1F	0.33R to 0.728R
Section 2F	0.728R to 0.781R
Section 3F	0.781R to 0.844R
Section 4F	0.844R to 1.0R
Section 1R	0.33R to 0.246R
Section 2R	0.246R to 0.223R
Section 3R	0.223R to 0.2R
Section 4R	0.2R to 0.173R
Section 5R	0.173R to 0.151R
Section 6R	0.151R to Root

Cross-sectional shape of different sections was determined based on the description provided for the mold geometry by the mold manufacturer. The layup used for the root section of the blade (from 0.15R to 0.33R) was same similar to that used in [58]. Once the layup information and the cross section profile was available, a MATLAB based mesh generator was used to generate the finite element mesh for UM/VABS. The finite element mesh generated for different root sections is shown in Figure D-6. Reference axis for the full airfoil region (Section 1R to Section 4F) is at the quarter chord, while for the root region (section 6R and 5R); it is located at the mid chord. For sections 2R to 4R, the reference line varies between the midchord and quarter chord. The reference point for each section was determined such that the reference points for all the sections are collinear points, as in the actual blade. Figure D-7 shows the finite element mesh generated for the main blade (without the foam). In order to obtain the baseline values for

strains and aeroelastic loads, the blade with a single flap manufactured in [112] was also modeled. The cross-sectional analysis was done using UM/VABS to obtain the inertia and stiffness properties for 1-D aeroelastic analysis and strain influence coefficients for the failure analysis.

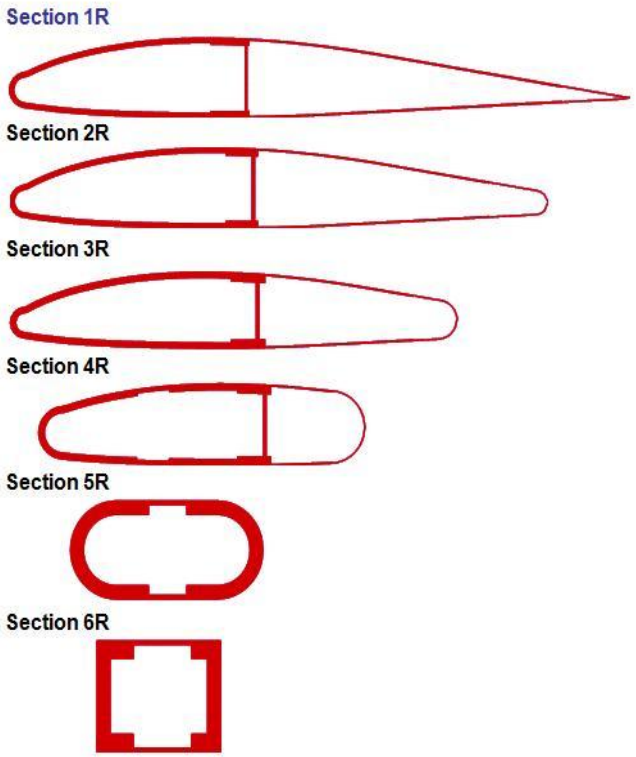

Figure D-6: Finite Element Mesh for Root Section

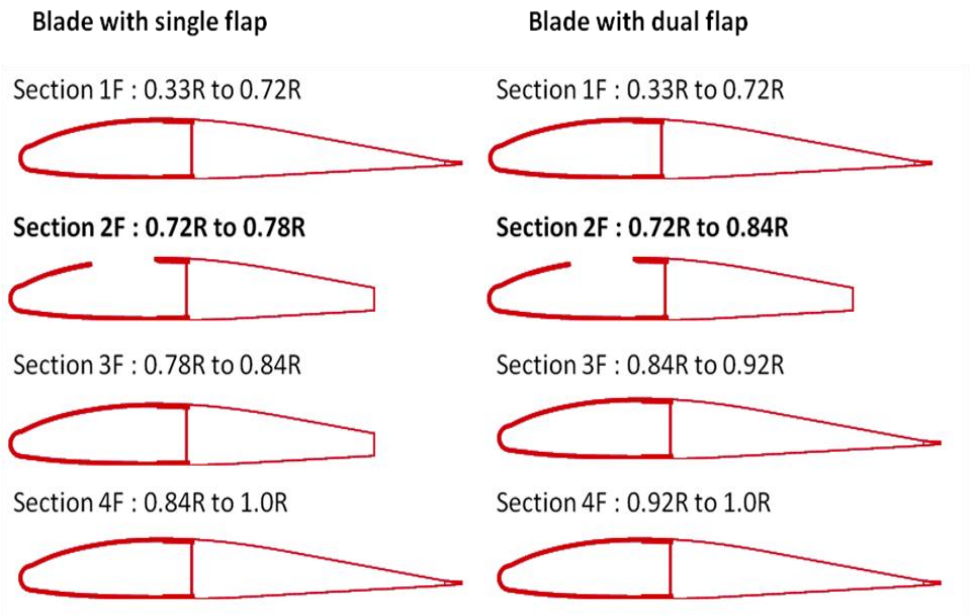

Figure D-7: Finite Element Mesh for Main Blade Sections

The 1-D beam model for the whole blade was developed in both AVINOR and RCAS for aeroelastic analysis. The model designed takes into account the position of hinges as described in Figure D-8.

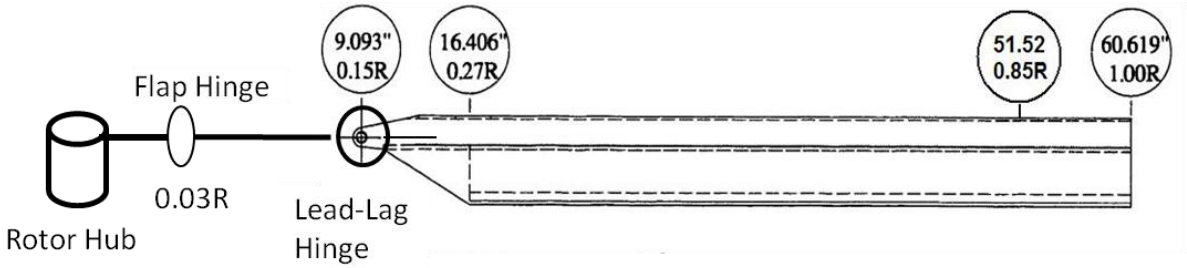

Figure D-8: Location of Hinges in Spin Test Stand

Design Process

Figure D-9 shows the steps followed in the design process used for the design of active blade. Different components of the design process are described below.

Initial starting point: The initial starting point for the layup is similar to that used in [112]. For the purpose of analysis, blade is divided into 10 span-wise sections as discussed in the previous section.

Stiffness and Inertia Properties: The cross-sectional layup and geometry is assumed to be constant within each span-wise section. Cross-sectional inertia and stiffness matrix for each of the cross section are obtained using UM/VABS [70]. These properties are used as input for the aeroelastic analysis of the rotor blade using the AVINOR code [97].

Worst Case Loading: In the analysis performed using AVINOR, the flaps are actuated at different frequencies from 2/rev to 5/rev and the blade loading is extracted for each of the cases. From these cases, maximum value of the load for each of the six components is determined at each station. Also, the maximum amplitude of oscillatory component of the load is determined for the fatigue analysis at each section.

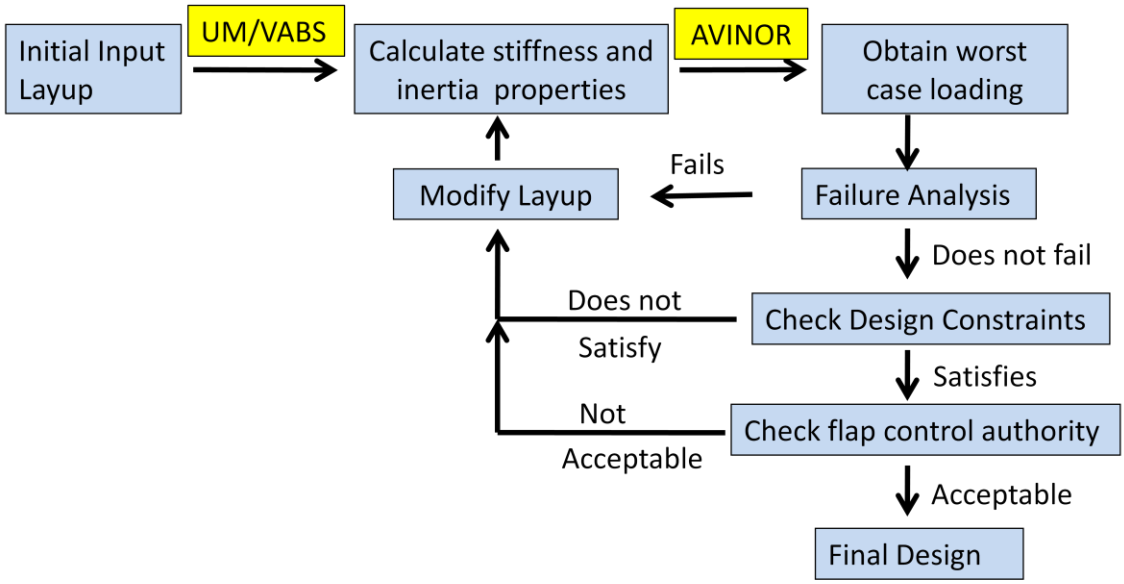

Figure D-9: Steps used in Blade Design

Failure Analysis: Worst case loading obtained from the AVINOR analysis is used as the input for the Failure Analysis. Strain influence coefficients obtained from UM/VABS analysis are used for determining all the six strain components for each element of the cross-sectional mesh. The maximum strain criterion is used to determine the failure point for the blade. Maximum allowable value of the strain for each of the six components is determined from a similar analysis of the baseline blade (blade with a single flap described in [112]). Similarly, the maximum dynamic strain for each of the component is determined using the amplitude of the oscillatory loads determined using AVINOR in the previous step.

Design constraints: Design constraints used in the analysis include upper and lower bounds on the location of the shear center, cross-sectional center of gravity and blade dynamic frequencies.

Flap control authority: Flap control authority depends upon the dynamic properties of the blade. It is a measure of oscillatory load generated by per unit deflection of the flap. In the current set of experiments, measurement of the unsteady aerodynamic drag was the main aim of the experiment. Thus, it was desirable that the blade torsional stiffness be very high to ensure that the contribution of aeroelastic loads to the hub loads is minimal.

Blade Analysis Tools

Detailed description of UM/VABS and RCAS is given in earlier chapters. This section provides details about the aeroelastic code AVINOR and the MATLAB based mesh generator.

AVINOR

The AVINOR (Active Vibration and Noise reduction) code [97] has been developed over the years at UCLA and University of Michigan. It performs aeroelastic rotorcraft analysis with emphasis on computational efficiency while retaining sufficient fidelity. The AVINOR aerodynamic model consists of four main components – (1) an attached 2D time domain unsteady aerodynamic model that accounts for compressibility and time-varying free stream Mach numbers, (2) a semi-empirical dynamic stall model for separated flow regime at high advance ratios, (3) a free-wake model which calculated non-uniform inflow distribution, and (4) a reverse flow model. The structural model is based on 1D finite element method that accounts for moderately large deflections. The structural dynamic model used in the code can use cross-sectional properties provided by UM/VABS for modeling composite rotor blade. The simulation code has been primarily used to investigate active and passive approaches to improve rotor blade design. For active control, code allows for single or multiple actively controlled flaps along the blade span. The optimal flap deflections for various combinations of vibration reduction, noise reduction and performance enhancement are determined by a variant of the higher harmonic control.

Mesh Generator

The finite element mesh required for 2D cross-sectional analysis was generated using a MATLAB-based mesh generator specially developed for UM/VABS. To create a general airfoil wetted surface, pairs of co-ordinate points defining the contour of the airfoil must be supplied. From the wetted surface, layers of given material are defined in order to create the stacking sequence needed for internal structural configuration.

Material properties for each material are defined using table lookup. The inertial effects associated with the ballast masses are added directly to the inertia matrix generated by UM/VABS.

Final Blade Design

The initial layup used for the blade cross section was based on tests conducted at MIT in 2000 [112]. As shown in Table D-3, the front spar consisted of 4 layers of fiberglass and 1 layer of IM7 graphite, vertical web consisted of 3 layers of E-Glass while the blade fairing consisted of one layer of E-Glass fiber.

Table D-3: Initial and Final Blade Design

Baseline

Spar		Fairing		Web	
1. E-Glass	0 deg	1. E-Glass	±45 deg	1. E-Glass	±45 deg
2. IM7	0 deg			2. E-Glass	±45 deg
3. S Glass	+45 deg			3. E-Glass	±45 deg
4. S Glass	-45 deg				
5. S Glass	0 deg				

Final Blade Design

Spar		Fairing		Web	
1. E-Glass	0 deg	1. IM7	+ 45 deg	1. IM7	+ 45 deg
2. IM7	0 deg	2. IM7	- 45 deg	2. IM7	- 45 deg
3. IM7	+ 45 deg			3. E-Glass	± 45 deg
4. IM7	- 45 deg			4. E-Glass	± 45 deg
5. IM7	0 deg			5. E-Glass	± 45 deg
6. E-Glass	0 deg				

During the design process, various ply configurations were tried. Final composite layup configuration obtained which satisfied failure and design criteria are shown Table D-3. Since the blade with dual active flaps includes two actuators, it experiences higher centrifugal force. Hence, the number of plies in the blade cross section had to be

increased. Also, one of the design criteria was to obtain high torsional stiffness such that the contribution to hub loads from aeroelastic effects is minimized. Thus, IM7 graphite plies oriented at ±45 deg were used in the fairing and the blade web.

Table D-4: Cross-sectional properties for Section 1F and Section 2F

Section 1F	Baseline	Final	**Section 2F**	Baseline	Final
$E_{11}(x10^6)$ (N)	4.97	11.9	$E_{11}(x10^6)$ (N)	4.58	9.54
$E_{44}(x10^2)$ (N/m^2)	1.23	4.27	$E_{44}(x10^2)$ (N/m^2)	0.50	2.25
$E_{55}(x10^2)$ (N/m^2)	2.03	3.40	$E_{55}(x10^2)$ (N/m^2)	1.76	2.25
m ($x10^{-1}$) kg/m	3.02	3.62	m ($x10^{-1}$) kg/m	2.41	3.76
SC(%c)	29.8	32.3	SC(%c)	39.85	40.66

Table D-4 shows the cross-sectional properties of Section 1F and Section 2F for the baseline case and for the final design obtained. Table D-5 shows the structural dynamic frequencies of the baseline blade and the final design in vacuum at 1336 RPM (100% RPM). All the frequencies for the final design are higher than that for the baseline blade. The torsional frequency of the final design is 33% higher than that of the baseline blade.

Table D-5: Dynamic Blade Frequencies

Type	Baseline	Final
1^{st} Flap Freq (/rev)	1.02	1.019
2^{nd} Flap Freq (/rev)	3.05	3.43
3^{rd} Flap Freq (/rev)	5.38	5.84
1^{st} Lag Freq (/rev)	0.51	0.502
2^{nd} Lag Freq (/rev)	5.84	9.18
1^{st} Torsion Freq (/rev)	**4.4**	**5.88**

D.3 Failure Analysis

Failure analysis performed for the composite rotor blade is based on the maximum strain criteria. All the six components of strain for each element of the cross section at

different stations along the blade span were determined. The maximum value of strain for each component was compared to the corresponding value for the baseline case. Table D-6 shows the maximum strain for each of the 10 stations in compression and tension in both longitudinal and transverse direction. Results indicate that the blade section 5, 6 and 7 experience the maximum strains. These sections correspond to the transition region between the blade root and rest of the blade. Since the blade root has additional plies and thus higher stiffness, strains in the root region are smaller even though it experiences larger internal force. Table D-7 shows the maximum strain for the final design while Table D-8 shows the percentage difference in the maximum strains experienced by the baseline case and the final design case. As observed in the baseline case, the new blade designed also experiences maximum strains in the transition region. The percentage difference obtained for the maximum strains indicate that the new blade design has smaller strains as compared to the baseline case.

Table D-6: Maximum Strains for the Baseline Case (Units: με)

Section	ε_{11}	ε_{22}	ε_{11}	ε_{22}
1	1563	1643	-1077	-1053
2	1175	1199	-751	-704
3	2614	3695	-2455	-1402
4	2907	3810	-2602	-1597
5	3549	3599	-2371	-2278
6	**3684**	3510	-2494	**-2722**
7	3553	**4829**	**-3681**	-2579
8	2497	2936	-2252	-1797
9	1345	2034	-1617	-864
10	1065	1497	-1253	-786
max	3684	4829	-3681	-2722

Section	ε_{12}	ε_{13}
1	3557	3630
2	2472	1465
3	5153	5640
4	6588	5971
5	**6699**	5491
6	4689	5669
7	4654	**7591**
8	3193	4422
9	2168	3118
10	1547	2471
max	6699	7591

Table D-7: Maximum Blade Strain for the Final Design (Units: με)

Section	ε_{11}	ε_{22}	ε_{11}	ε_{22}
1	901	958	-662	-662
2	955	962	-694	-692
3	1904	2458	-1500	-1268
4	1912	2588	-1647	-1289
5	1990	2908	-1495	-1360
6	1758	2331	**-1688**	**-1241**
7	**2950**	**4133**	-1482	-2185
8	2315	1660	-743	-1639
9	1339	1641	-601	-975
10	763	1320	-567	-612
max	2950	4133	-1688	-2185

Section	ε_{12}	ε_{13}
1	4372	3022
2	2118	942
3	4463	6517
4	5280	**7361**
5	**5550**	7119
6	3330	6729
7	5417	4307
8	5525	4824
9	2425	1726
10	1389	1379
max	5550	7361

Table D-8: Percentage Variation in Cross-Sectional Strains

Section	ε_{11}	ε_{22}	ε_{11}	ε_{22}
1	-42.4	-41.7	-38.5	-37.1
2	-18.7	-19.7	-7.6	-1.7
3	-27.2	-33.5	-38.9	-9.6
4	-34.2	-32.1	-36.7	-19.3
5	-43.9	-19.2	-37.0	-40.3
6	-52.3	-33.6	-32.3	-54.4
7	-17.0	-14.4	-59.7	-15.3
8	-7.3	-43.5	-67.0	-8.8
9	-0.5	-19.4	-62.8	12.8
10	-28.3	-11.8	-54.7	-22.2
max	-19.9	-14.4	-54.2	-19.7

Section	ε_{12}	ε_{13}
1	22.9	-16.7
2	-14.3	-35.7
3	-13.4	15.6
4	-19.9	23.3
5	-17.2	29.7
6	-29.0	18.7
7	16.4	-43.3
8	73.0	9.1
9	11.9	-44.6
10	-10.2	-44.2
max	-17.2	-3.0

Similar analysis was also carried out for the dynamic strains. The maximum amplitude of dynamic strain for each component of the strain was obtained and compared with the corresponding strain for the baseline case. The final result obtained is shown in Table D-9, Table D-10 and Table D-11.

Table D-9: Alternating Strains for the Baseline Case (Units: με)

section	ε_{11}	ε_{22}	ε_{12}	ε_{13}
1	271.1	279.5	813.8	624.9
2	226.3	229.2	511.5	324.9
3	434.2	425.4	518.5	876.2
4	447.2	448.1	615.7	950.6
5	406.4	415.6	593.4	857.7
6	382.4	394.9	586.4	798.8
7	402.1	406.6	490.3	766
8	638.1	593.3	432	814.4
9	283.4	299.6	248.4	537.8
10	267.6	274	189.8	511.5
Max	638.1	593.3	813.8	950.6

Table D-10: Alternating Strains for the Final Design (Units: με)

Section	ε_{11}	ε_{22}	ε_{12}	ε_{13}
1	128.7	133.1	468.1	324.5
2	98.3	100.9	236.9	149.5
3	135.8	257.4	209.5	457.8
4	140.3	261.4	239.9	489.7
5	121.1	265.5	212.6	440.5
6	117.4	236.8	217.1	401
7	83.1	263.5	232.3	267.8
8	164.9	183.4	195.5	681.1
9	92.2	115.7	169.7	107.4
10	73.3	84	137.1	87
Max	164.9	265.5	468.1	681.1

Table D-11: Percentage Difference for the Alternating Strains

Section	ε_{11}	ε_{22}	ε_{12}	ε_{13}
1	-52.5	-52.4	-42.5	-48.1
2	-56.6	-56.0	-53.7	-54.0
3	-68.7	-39.5	-59.6	-47.8
4	-68.6	-41.7	-61.0	-48.5
5	-70.2	-36.1	-64.2	-48.6
6	-69.3	-40.0	-63.0	-49.8
7	-79.3	-35.2	-52.6	-65.0
8	-74.2	-69.1	-54.8	-16.4
9	-67.5	-61.4	-31.7	-80.0
10	-72.6	-69.3	-27.8	-83.0
Max	-74.2	-55.3	-42.5	-28.4

D.4 Strength Test

Pull (tensile) test was conducted on sample section to test the strength for the layup designed in the previous section. Sample sections were fabricated specifically for the pull test with metal inserts (see Figure D-10) at the end such that it can be easily held in the MTS testing machine. During the test, a pure tensile load was applied to simulate the centrifugal force which is the most dominant force. Based on the computational analysis, two critical areas were identified for structural testing, namely, the root section and the cutout section for holding the actuators. Since, most of the structural strength of the blade is due to the front spar, only spar part of the airfoil cross section was used for testing. Only a small addition to strength and stiffness is expected by including fairing to the airfoil section. However, its main purpose is to provide a smooth aerodynamic surface.

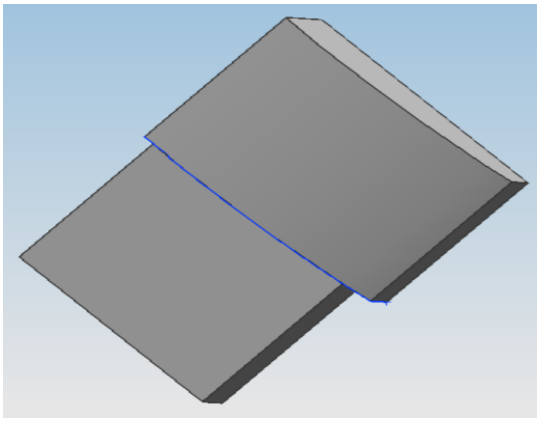

Figure D-10: CAD Model of the Metal insert used for Pull Tests

Pull Test for Root Section

For testing the root section, a 0.5R long blade section was fabricated with blade root at one end and the metal insert at the other end. Metal insert was fixed inside the blade section during the fabrication process to ensure that the joint has sufficient strength. Sample section was then mounted on the tensile testing machine as shown in the Figure D-11. In order to monitor blade strains during the tension test, 2 pairs of strain gages were mounted on the top and bottom surface of the blade at 0.2R and 0.34R. As shown in Figure D-12, this corresponds to section 4R and 1F in the blade design.

The tension test was performed in a quasi-static manner. The displacement at the moving end was increased at the rate of 0.001 inch per sec. The load was allowed to increase till the failure point. At tensile load of 4800 lbf, damage was observed in the region where the metal insert was attached to the blade as shown in Figure D-13. (It should be noted that, in this case, the hole used for attaching the metal insert to testing machine was drilled in the metal insert after the blade was fabricated. As a result of drilling this hole, some of the joint-strength between the rotor blade section and metal

insert was lost. And hence the damage occurred at the joint. This issue was avoided in the next pull test by drilling the hole in the metal insert prior to fabrication.) During the test, no damage was observed in rest of the blade. Thus the root section of the blade was able to withstand tensile load of atleast 4800 lbf without any damage which is 20% higher than the maximum load expected at the root at 100% RPM (13336 RPM) determined from numerical analysis.

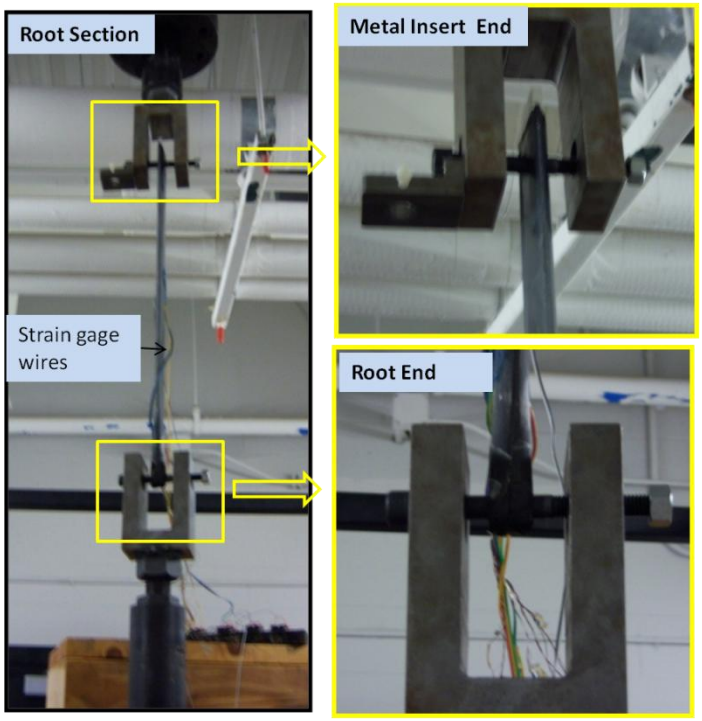

Figure D-11: Set up for pull test of blade root section

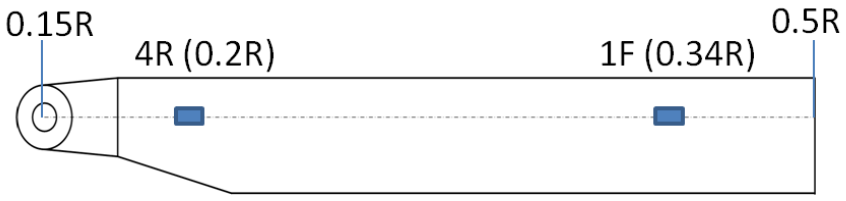

Figure D-12: Location of Strain Gages used for the Pull Test of Root Section

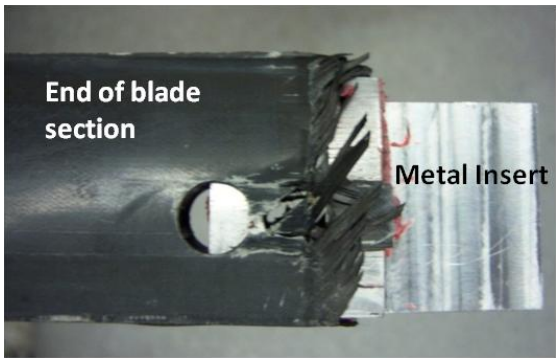

Figure D-13: Damaged Section after the Pull Test for Root Section

The variation of tensile load and blade strains with time is shown in Figure D-14 and Figure D-15 respectively. The output produced by strain gage on top surface of section 4R shows some unexpected variation from the general trend which may be due to loose electrical wiring. The strain observed for section 4R is consistently less than that observed for section 1F as expected, since the root section has more plies. Also, for section 1F, the strain gage on the top surface indicates higher strain as compared to the strain gage on the bottom surface. This may be due to some asymmetry in the applied load which can arise from the cambered profile of airfoil section. It should be noted that the blade cross section consists of VR7 airfoil which is not a symmetric airfoil. In general, all the strain components vary linearly with the applied load indicating that no damage occurred to the blade section during the tension test. Thus, the blade root section was able to withstand loads more than 20% of the maximum expected load without any damage.

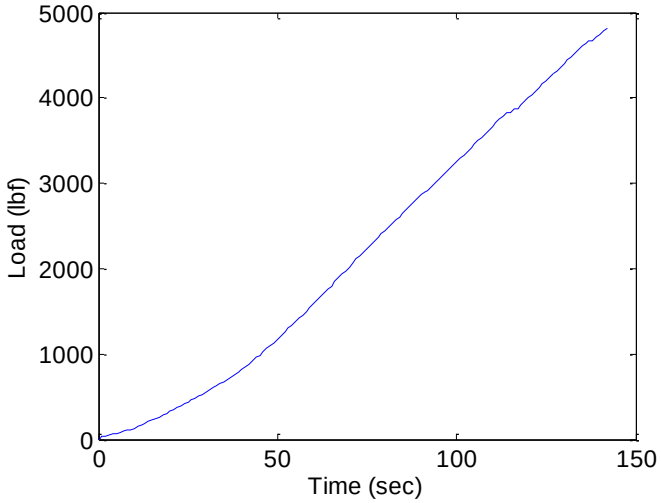

Figure D-14: Blade Loading Profile used for the Pull Test of Root Section

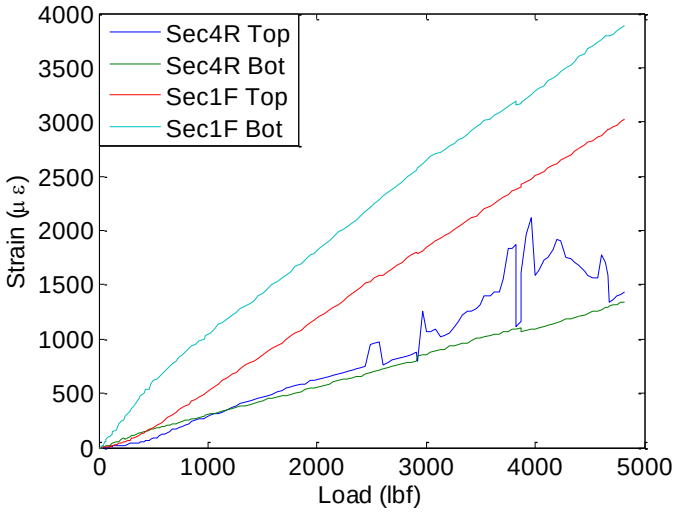

Figure D-15: Strain Recorded by different Strain Gages during the Blade Loading

Pull Test for Cut-out Section

A sample section was fabricated for pull test of cutout region with metal inserts at both ends of the specimen as shown in Figure D-16. The sample section mounted on the tensile testing machine is shown in Figure D-17. In this case, the metal inserts used had drilled holes to avoid drilling holes after the blade fabrication. In order to monitor the

blade strain at critical locations, strain gages were mounted on the blade as shown in Figure D-18.

Figure D-16: Test Section Fabricated for Pull Test of Cutout Section

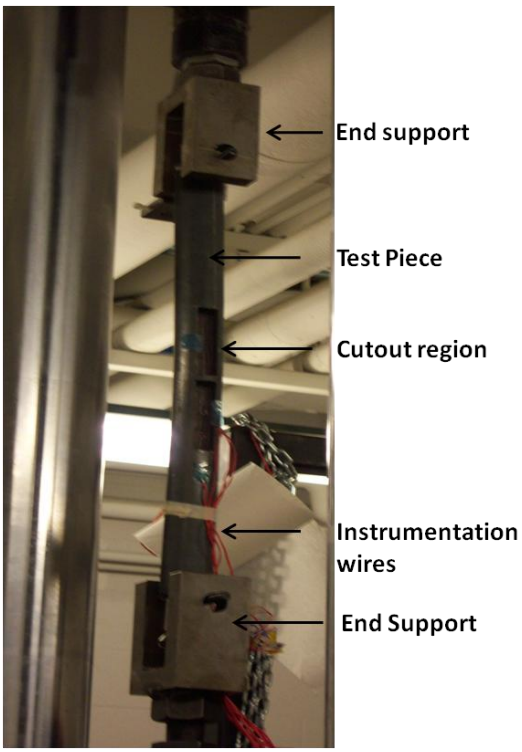

Figure D-17: Setup used for the Pull Test for the Cutout Region

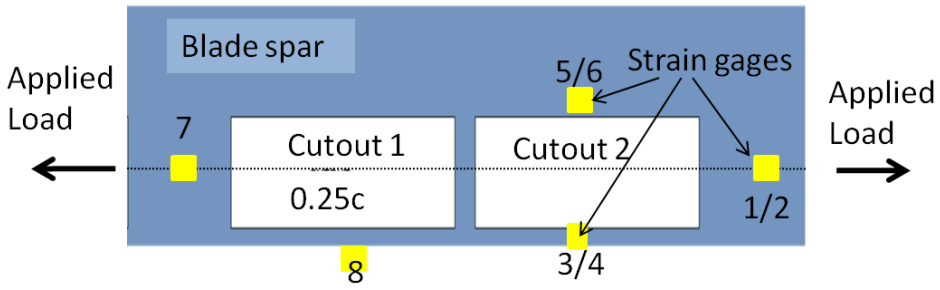

Figure D-18: Location of Strain Gages used for the Pull Test of Cutout region

In this test, the loading cycle was modified to observe the hysteresis effect in the stress-strain curve. The applied axial load was increased to 1000lbf and then decreased by 500lbf and then increased by 1000lbf again till the maximum expected load of 3500lbf was reached. After that, the blade load was allowed to increase steadily till 6500 lbf as shown in Figure D-19. The blade strain given by strain gages is shown in Figure D-20. All the strains observed show a linear relationship with the applied load and the effect of alternating the load cycle is minimal. This indicates that no significant damage occurred to the blade during the tensile test. As expected, higher strains are recorded by strain gages 8, 3 and 4 which are mounted in the web region of actuator bay. In this region, additional plies were included to reduce the effect of cutout in the cross section. The maximum strain observed in this region is well below the maximum allowable strain limit for the fiberglass material. The strain value observed by strain gages 7, 1 and 2 are of similar magnitude. Also, as observed in the earlier pull test, there is some difference in the strains recorded by the top and bottom strain gages at the same spanwise location.

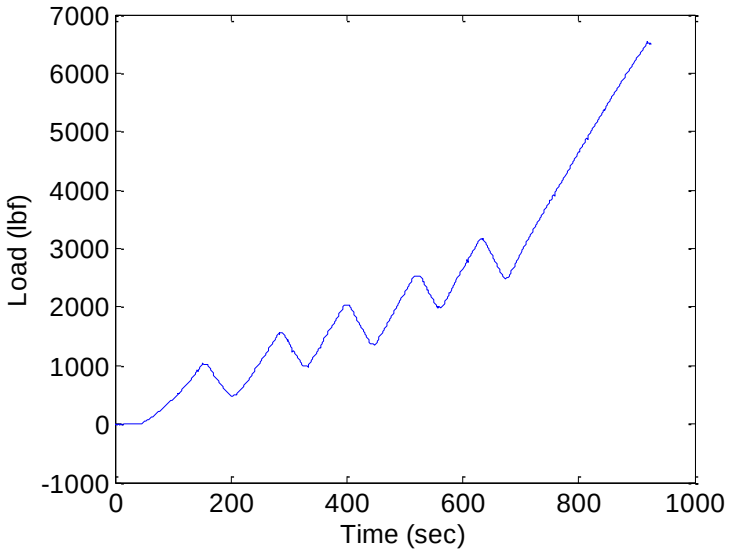

Figure D-19: Loading Cycle used for Pull Test of Cutout Region

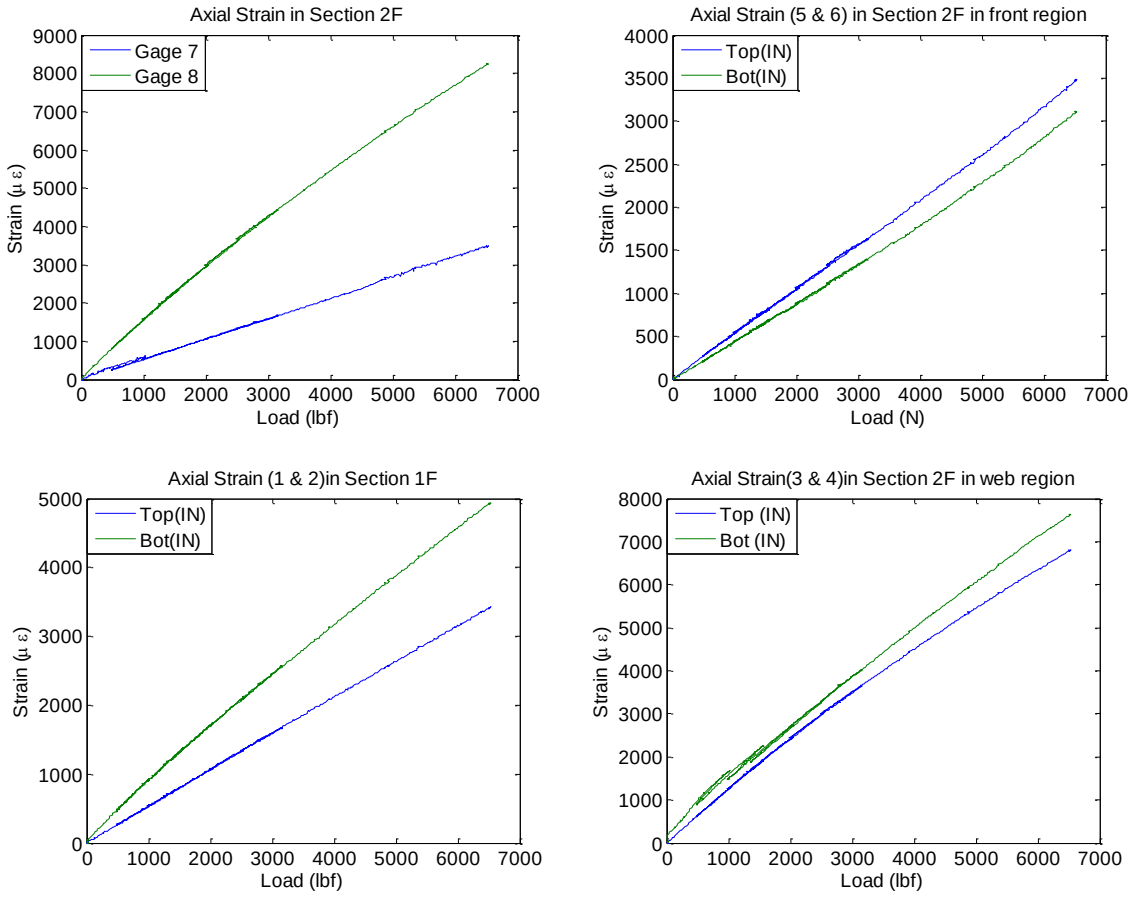

Figure D-20: Strain Gage Output

D.5 Blade Instrumentation

The active blade was instrumented with a variety of sensors to monitor the blade response in real time. Instrumentation used in the active blade included strain gages to determine blade strains, hall effects sensors to measure flap deflections and accelerometers at the blade spanwise tip to measure tip twist and acceleration. For all the sensors used in this blade, a 36AWG wire was used for making the wiring connections. The wires were run along the blade spar and pulled out near the root. Detailed description of all the sensors used on the active blade is given Table D-12 and Figure D-21.

Table D-12: Details of the Sensors used on the Active Blade

Strain Gages in the spar

Sensor	Sensor Description	Type	Location (%R)
1	Chordwise Bending Strain	Half	0.18
2	Flapwise Bending Strain	Half	0.19
3	Torsional Strain	Full	0.2
4	Flapwise Bending Strain	Full	0.39
5	Flapwise Bending Strain	Full	0.59
6	Chordwise Bending Strain	Full	0.52
7	Torsional Strain	Full	0.35
8	Torsional Strain	Full	0.55
9	Torsional Strain	Full	0.69
10	Torsional Strain	Full	0.89
11	Axial Strain in Actuator bay 1	Quarter	0.75
12	Axial Strain in Actuator bay 2	Quarter	0.82

Accelerometers

Gage No	Sensor Description	Location (%c)
1	Near Leading edge	6%
2	At quarter chord	25%
3	Near Leading edge	44%

Hall Effect Sensor

No	Sensor Description (at 0.75c)	Location (%R)
1	For actuator 1	72%
2	For actuator 2	79%

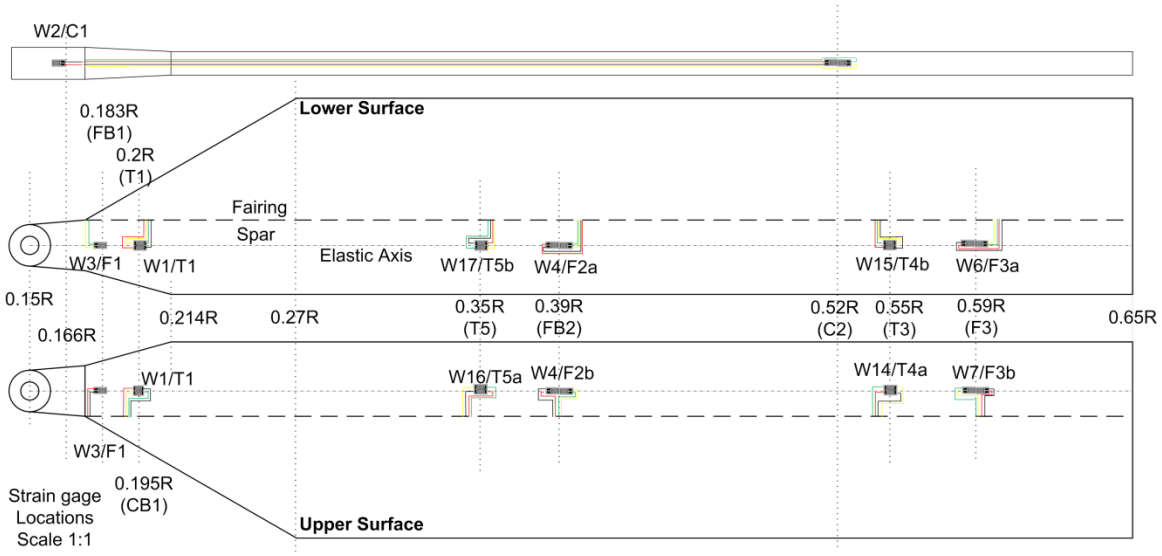

Active Blade Instrumentation (Part A)

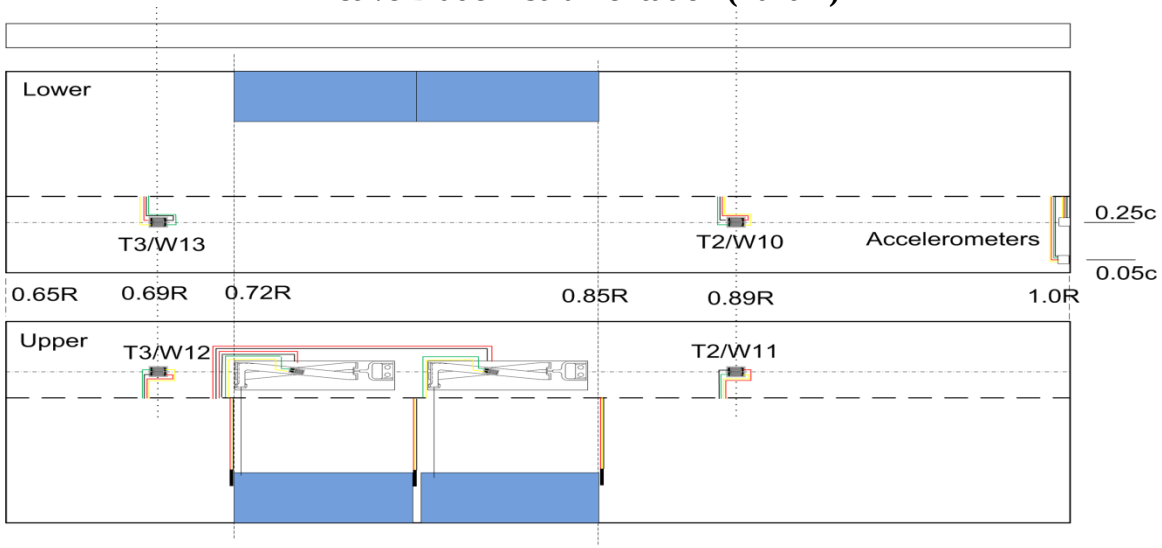

Active Blade Instrumentation (Part B)

Figure D-21: Instrumentation used in the Active Blade

Besides the instrumentation wires, high voltage wires were also run along the blade spar which were used to power the piezoelectric actuators. The high voltage wires were shielded by aluminum foil.

D.6 Passive Blade design

The passive blade used in spin test was designed to have similar dynamic properties as the active blade. Thus the passive blade also included the cutout region and similar

composite layup. In place of the actuator and flaps, ballast masses were used in the passive blade to obtain similar inertia properties. As compared to the active blade profile, only difference for the passive blade was in the flap region where it did not include any cutout.

Detailed description of the fabrication process used for manufacturing active and passive blade is provided in the Appendix E.

Appendix E. Blade Manufacturing

The manufacturing steps involved in the fabrication of the composite rotor blade are similar to that highlighted in [58, 112]. In order to account for the presence of dual flaps, some modifications were made, which will be discussed in detail in the following sections.

The basic cross section of the rotor blade is shown in Figure E-1 and Figure E-2. It consists of prepreg layers wrapped around the foam core with tungsten ballast mass at the leading edge. The blade cross section is cured in two stages: namely, the spar cure and the fairing cure. In the spar cure, the front spar of the blade is cured which also includes the root section. In order to create space for mounting the actuators, spar includes cutouts near the actuator location. Most of the instrumentation for active blade is included in the spar region, thus it also houses the wires for transferring the sensor output to hub. Similarly, the fairing includes cutouts for mounting flaps.

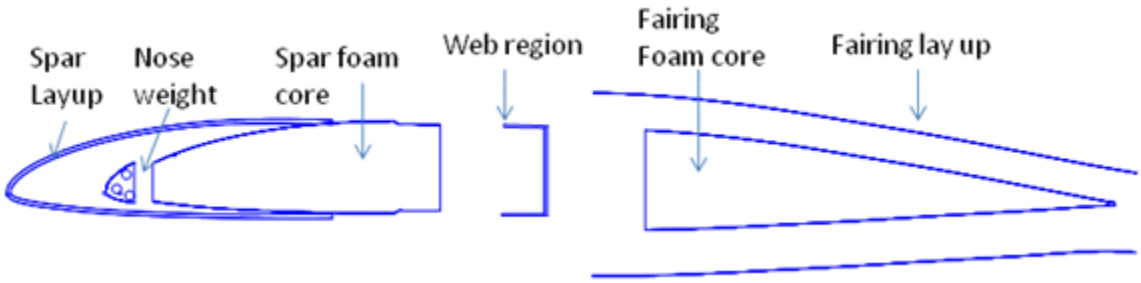

Figure E-1: Exploded View of the Airfoil Cross Section

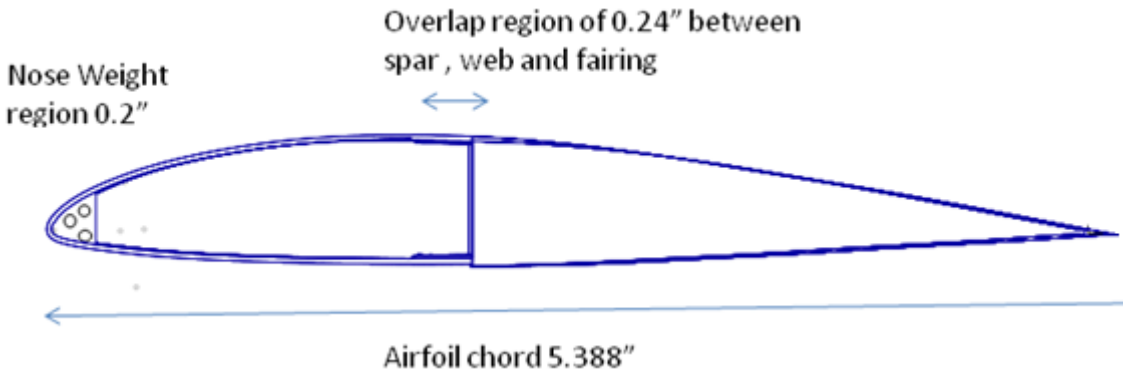

Figure E-2: Assembled View of the Airfoil Cross Section

E.1 Fabrication of Foam Core

Foam core is required in the fabrication process to provide sufficient back pressure for prepreg plies during the curing process inside the mold. The presence of foam core has very little effect on the stiffness properties for the cross section; however, its effect is more apparent on the inertial properties. In the cross-sectional analysis performed in this chapter for the active-flap blade design, the effect of foam is included for all the blade cross sections along the span. The shape of the foam section is determined using the shape of outer mold line (OML), the number of prepreg layers used in the cross section and the backpressure required for curing. To ensure sufficient backpressure, the foam core used in spar section (71IG) was oversized by 5 mils while the foam core used in the fairing section (31 IG) was oversized by 20 mils. These values were determined by fabricating sample sections and observing the quality of cured parts.

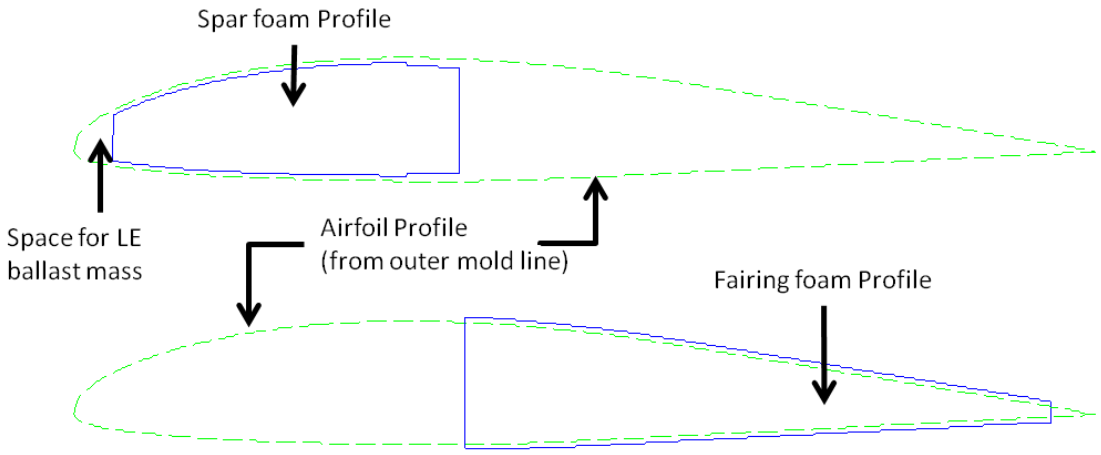

Figure E-3: Shape of the Foam Core for Spar and Fairing Section

Initially, the CNC method was explored to fabricate the foam core sections. However, it did not work well due to the cutting time required for getting a smooth finish and the flexibility of foam section. As a result, a different method was used. Here, plexiglass profiles were fabricated using a laser cutting machine. Laser cutting method provides very high accuracy which is required for the foam core fabrication. These profiles are attached on the either ends of a 6" long foam section and the foam was sanded using a sanding machine and hand files. The root section of the blade has a non-uniform profile which varies along the span. In order to accurately capture the non-uniformity, four different sections were selected along the root part of the blade and the cross-sectional shape was determined using the mold geometry. A tolerance of 5 mils in the thickness was used for the fabrication of foam core. All the 6" foam pieces were joined together by 5min epoxy. The joined pieces of foam core in the root region are shown in Figure E-4. Before joining the foam pieces, it was verified that the five-minute epoxy does not lead to gassing of the foam section when heated inside autoclave at 250 deg F.

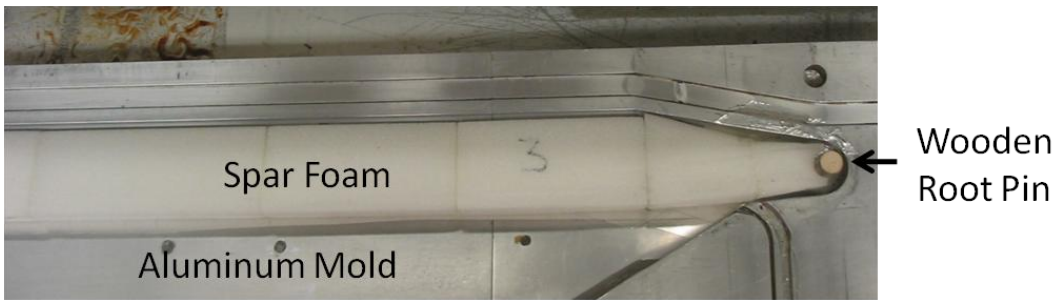

Figure E-4: Joined pieces of Foam Core

The foam core used for the spar section included cutouts as shown in the Figure E-5. Similarly the foam core used for the fairing section included cutout in the flap region. These cutouts were made with a sharp knife after joining all the foam pieces together.

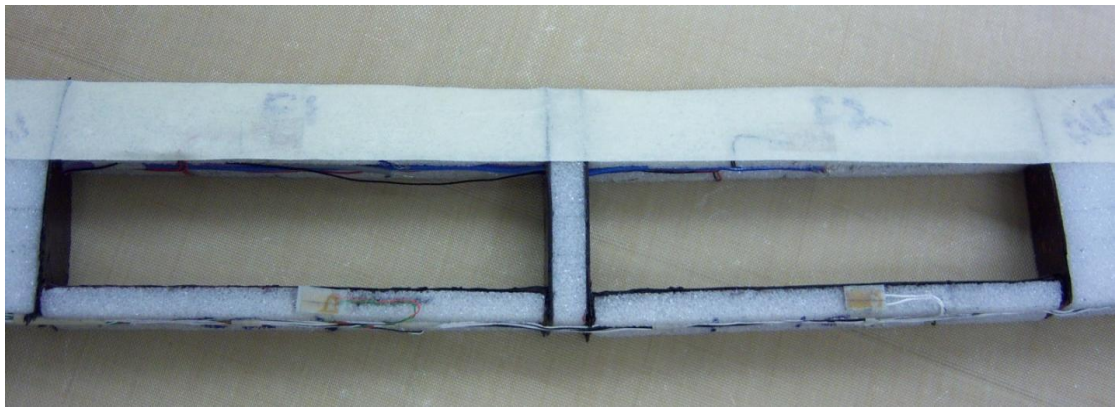

Figure E-5: Cutout made in the Spar Region for Actuators

E.2 Instrumentation

The active blade included strain gages, HET sensors and accelerometers as the sensors for measuring the blade deformation and flap deflection. Details and specifications of the sensors and wires used in the blade are given in Table E-1. Wires for these sensors were run along the trough made in the blade spar (shown in Figure E-7) and they exit near the root as shown in Figure E-6. For installing the strain gages, precured E-Glass tabs were used and strain gages were glued on them. These tabs with strain gages were glued upside

down on the foam core such that the strain gage records strain for the innermost layer of the prepreg. Wiring diagram for the flap-wise bending strain gages and the torsional strain gages are shown in Figure E-8 and Figure E-9, respectively. The front spar also included two accelerometers near the blade tip as shown in Figure E-11. Wires running along the blade spar also included high voltage wires for providing power supply to the actuators in the cutout region as shown in Figure E-10.

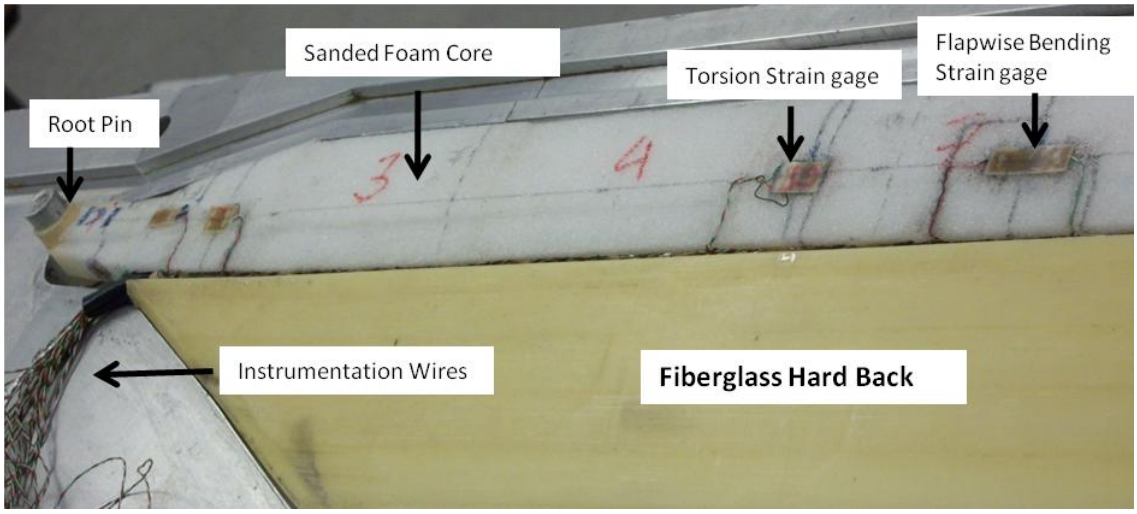

Figure E-6: Instrumented Spar Section

Table E-1: Instrumentation used in the Spar Section

	Manufacturer	Part Number
Strain gages Flapwise Chordwise Torsion	 Vishay Micro measurements Vishay Micro measurements Vishay Micro measurements	
Accelerometer	Analog Devices	ADXL 193
HET	Micronas	Hal 815
Wires	Vishay Micro measurement	36 gage

Figure E-7: Trough made in the Blade Spar for Instrumentation Wires

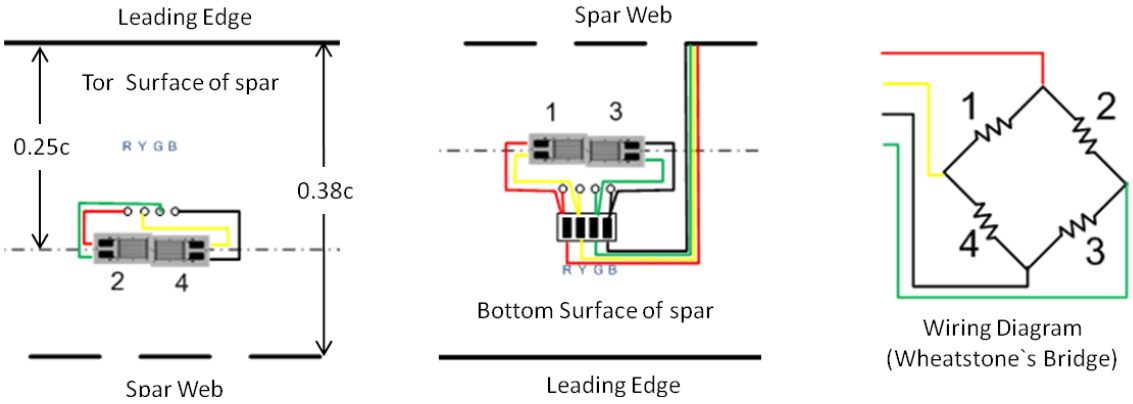

Figure E-8: Wiring Diagram for Full Bridge Flap wise Bending Strain Gage

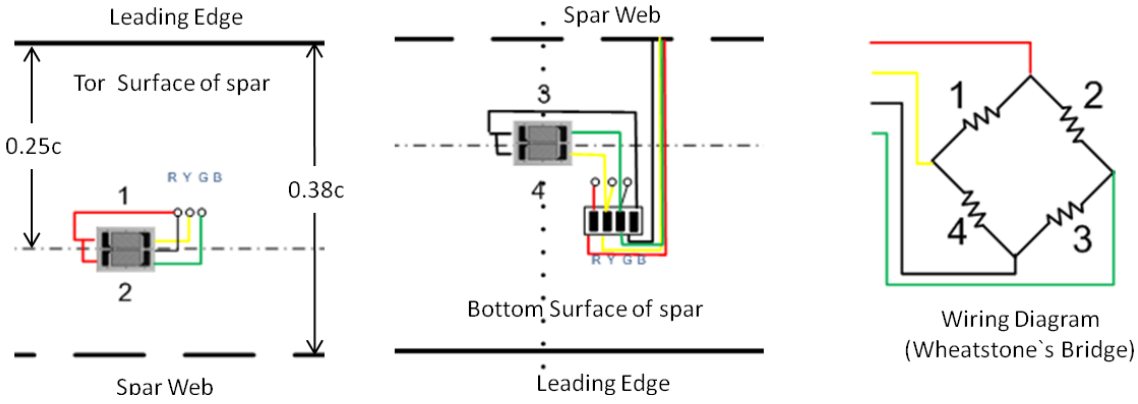

Figure E-9: Wiring diagram for Full Bridge Torsion Strain Gage

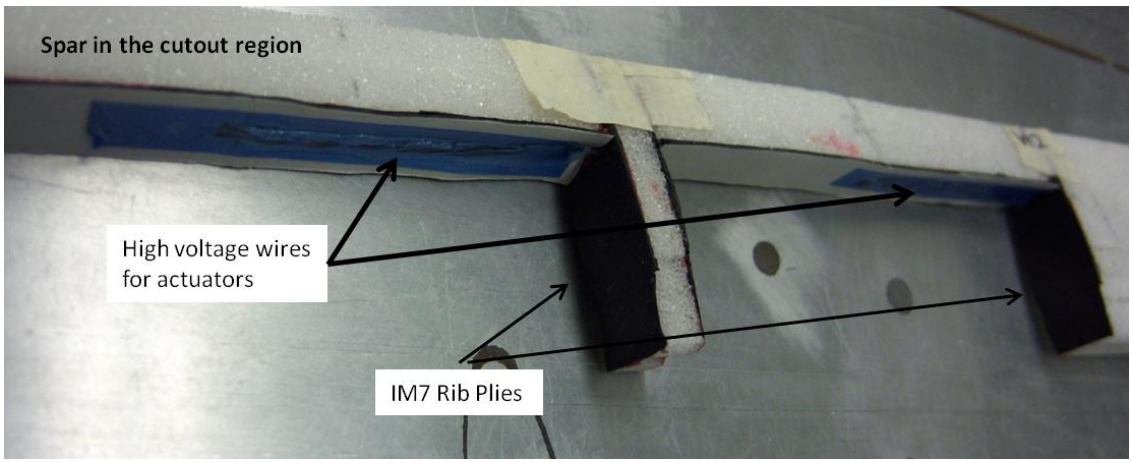

Figure E-10: High Voltage Wires in the Cutout Region

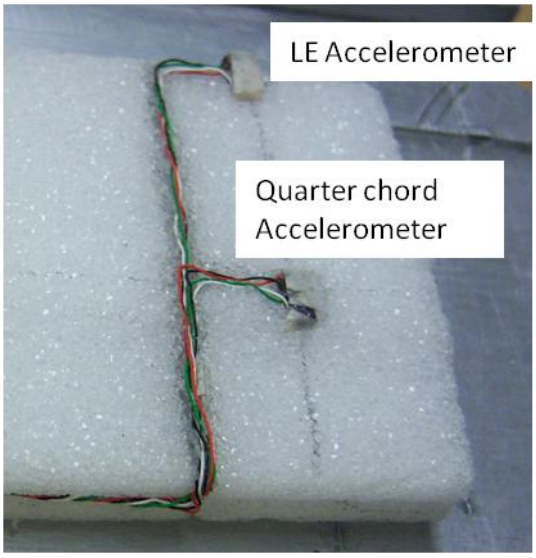

Figure E-11: Accelerometers mounted on the Blade Tip in the Spar Region

Calibration for the accelerometer was verified using the guidelines provided in the datasheet. Figure E-12 shows different configuration which can be used to calibrate the accelerometer. According to the datasheet, ADXL193 has a sensitivity of 8mV/g. Table E-2 gives the output voltage measured for 2 accelerometers. The obtained results are close to the sensitivity given in the datasheet. The Hall Effect transducer was calibrated after the fabrication of the rotor blade.

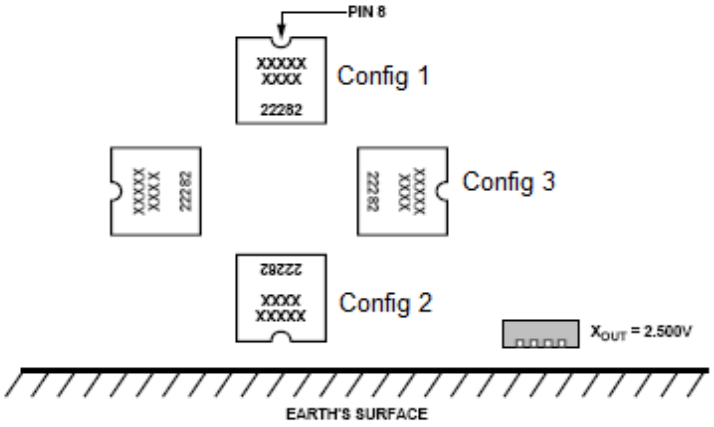

Figure E-12: Different Configurations used for Calibration of Accelerometer

Table E-2: Measured Voltage from Accelerometers

	Acc 1 (V)	Diff (mV)	Acc 2 (V)	Diff (mV)
Config 1	2.4977	-8.4	2.4979	-8.1
Config 2	2.5143	8.2	2.514	8
Config 3	2.5061	0	2.506	0

E.3 Spar mandrel Design

The blade includes two cutouts in the spar region for mounting actuators after the blade fabrication. In order to create space for the actuators, two spar mandrels are used. During the manufacturing process, inboard actuator support and outboard actuator support are installed in the blade spar. Actual fabricated parts used during the blade manufacturing are shown in Figure E-13. In order to fabricate these parts, detailed CAD models for each of the component were prepared as shown in Figure E-14. Final parts were fabricated in the Machine Shop (by Terry Larrow) in Department of Aerospace Engineering. In order to ease the process of removing spar mandrel from the cured blade,

two ¼” x 20 threaded holes were made in the middle spar mandrel and one in the inboard spacer as shown in Figure E-13.

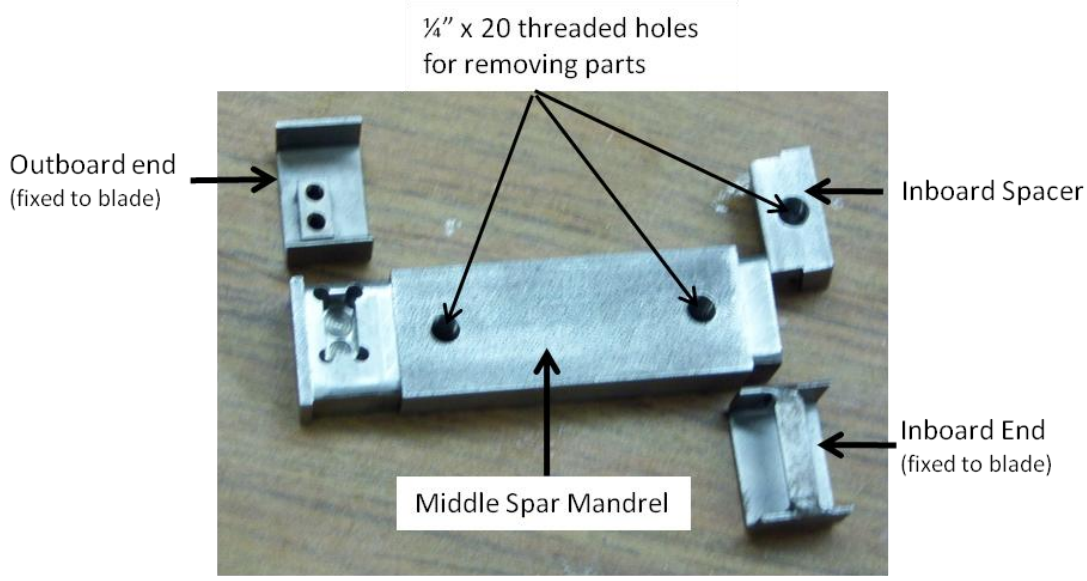

Figure E-13: Spar Mandrel Parts

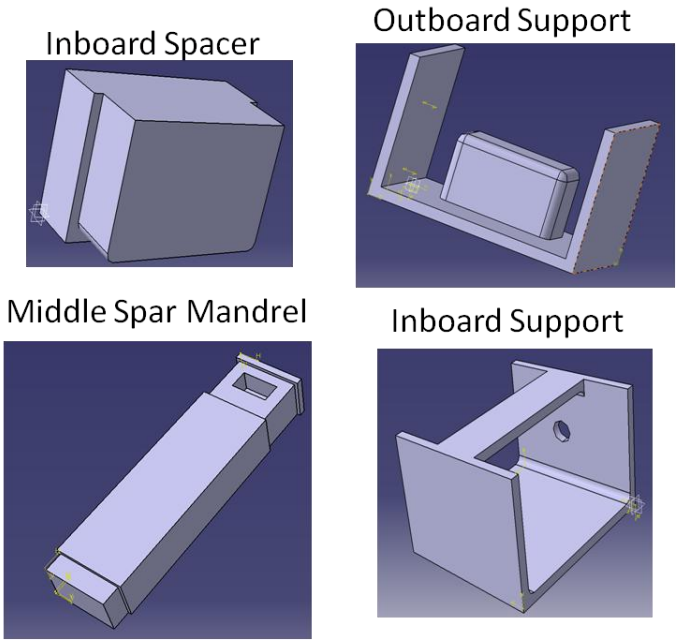

Figure E-14: CAD Model Developed for the Parts of Spar Mandrel

E.4 Spar Manufacture

Once the instrumented foam core was ready and the two spar mandrels were fabricated, the layup process for the blade spar was started. Based on the cross-sectional design finalized in Appendix D, all the plies were cut to the desired shape and size. The root section of the blade included additional plies to withstand the large centrifugal force. The root plies used in the cross section consisted of 0.52" wide IM7 ply strips which wrap around the root pin. For each layer (which consisted of 4 strips), two of these layers wrap around the root pin and cover the top surface of spar, while the other two layers wrap around the root pin and cover the bottom surface of blade spar. Unlike the root plies, the mail spar plies wrap (except Spar Ply 2) around the leading edge of airfoil section. Dimensions of all the plies used in the layup are shown in Table E-3. The main plies used in the cross section had to be cut on the top surface in actuator region. The cutout made in the plies is shown in Figure E-15. Ply 2 in the spar plies is a 0 deg IM7 ply to provide additional axial stiffness against the centrifugal loads. Similar to the process followed for the root plies, Spar 2 plies are split into 4 strips of 0.52" width and they wrap around the root region. In the cutout region, a diversion is made in these plies, which will be shown later. Based on the sizes given in Table E-3, all the plies are cut to the exact size as shown in Figure E-16.

Table E-3: Dimension of the Plies cut prior to Blade Fabrication

Root Plies					
Sr. No	Name	Ply	Length	Width	Angle
1	SPD 10b 1	IM7	2.4	0.52	0
2	SPD 10b 2	IM7	2.4	0.52	0
3	SPD 10b 3	IM7	2.4	0.52	0
4	SPD 10b 4	IM7	2.4	0.52	0

5	SPD 10a 1	IM7	2.4	0.52	0
6	SPD 10a 2	IM7	2.4	0.52	0
7	SPD 10a 3	IM7	2.4	0.52	0
8	SPD 10a 4	IM7	2.4	0.52	0
9	SPD 9a 1	IM7	3	0.52	0
10	SPD 9a 2	IM7	3	0.52	0
11	SPD 9a 3	IM7	3	0.52	0
12	SPD 9a 4	IM7	3	0.52	0
13	SPD 9b 1	IM7	3	0.52	0
14	SPD 9b 2	IM7	3	0.52	0
15	SPD 9b 3	IM7	3	0.52	0
16	SPD 9b 4	IM7	3	0.52	0
17	SPD 8 1	IM7	3.5	0.52	0
18	SPD 8 2	IM7	3.5	0.52	0
19	SPD 8 3	IM7	3.5	0.52	0
20	SPD 8 4	IM7	3.5	0.52	0
21	SPD7 1	IM7	4.1	0.52	0
22	SPD7 2	IM7	4.1	0.52	0
23	SPD7 3	IM7	4.1	0.52	0
24	SPD7 4	IM7	4.1	0.52	0
25	SPD6 1	IM7	4.6	0.52	0
26	SPD6 2	IM7	4.6	0.52	0
27	SPD6 3	IM7	4.6	0.52	0
28	SPD6 4	IM7	4.6	0.52	0
29	SPD5 1	IM7	5.2	0.52	0
30	SPD5 2	IM7	5.2	0.52	0
31	SPD5 3	IM7	5.2	0.52	0
32	SPD5 4	IM7	5.2	0.52	0
33	SPD4 1	IM7	7.9	0.52	0
34	SPD4 2	IM7	7.9	0.52	0
35	SPD4 3	IM7	7.9	0.52	0
36	SPD4 4	IM7	7.9	0.52	0
37	SPD3 1	IM7	10.7	0.52	0
38	SPD3 2	IM7	10.7	0.52	0
39	SPD3 3	IM7	10.7	0.52	0
40	SPD3 4	IM7	10.7	0.52	0
41	SPD2 1	IM7	13.5	0.52	0

42	SPD2 2	IM7	13.5	0.52	0
43	SPD2 3	IM7	13.5	0.52	0
44	SPD2 4	IM7	13.5	0.52	0
45	SPD1 1	IM7	24.5	0.52	0
46	SPD1 2	IM7	24.5	0.52	0
47	SPD1 3	IM7	24.5	0.52	0
48	SPD1 4	IM7	24.5	0.52	0

SPD: Spar Double Ply

Web Plies					
Sr. No	Name	Ply	Length	Width	Angle
49	Web 1	IM7	51.5	1.51	-45
50	Web 2	IM7	51.5	1.52	45
51	Web 3	E120	51.5	1.53	45
52	Web 4	E120	51.5	1.54	45
53	Web 5	E120	51.5	1.55	45
54	Web D1	E120	8	1.5	45
55	Web D2	E120	8	1.5	45

Main Plies					
Sr. No	Name	Ply	Length	Width	Angle
56	Spar Ply 1	E120	51.5	4.3	0
57	Spar Ply 2_1	IM7	105.5	0.52	0
58	Spar Ply 2_2	IM7	105.5	0.52	0
59	Spar Ply 2_3	IM7	105.5	0.52	0
60	Spar Ply 2_4	IM7	105.5	0.52	0
61	Spar Ply 3	IM7	51.5	4.3	45
62	Spar Ply 4	IM7	51.5	4.3	-45
63	Spar Ply 5	IM7	51.5	4.3	0
64	Spar Ply 6	E120	51.5	4.3	0

Root Pin					
Sr. No	Name	Ply	Length	Width	Angle
65	Root pin	IM7	50	0.85	0

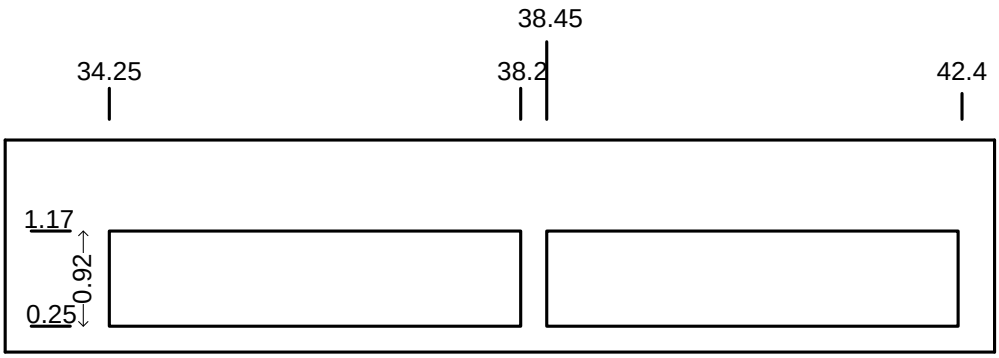

Figure E-15: Cutout made in Spar ply 1, 3, 4, 5 and 6.

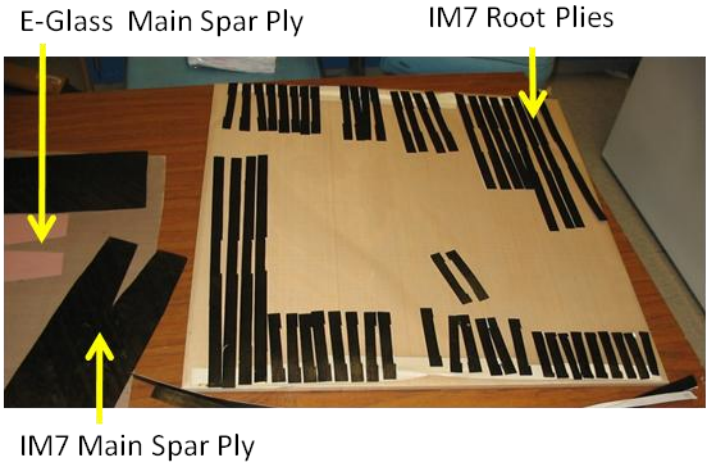

Figure E-16: Cut Prepreg Plies prior to Layup

Prior to the layup process, the foam core is heated in an oven for 30 min at 150F temperature to remove all the moisture. In the next step, the adhesive film (pink colored AF163-2U) is wrapped around the foam core. Adhesive film facilitates the bonding of prepreg to the foam core. It has a thickness of 3 mils and has the same curing temperature (250F) as the prepreg used in the cross section. Adhesive film wrapped around the root region and the cutout region is shown in Figure E-17 and Figure E-19. The cutout region also includes additional chordwise and spanwise plies to provide strength in the cutout region. These plies are added to the foam core prior to complete layup as shown in Figure E-18 and Figure E-19.

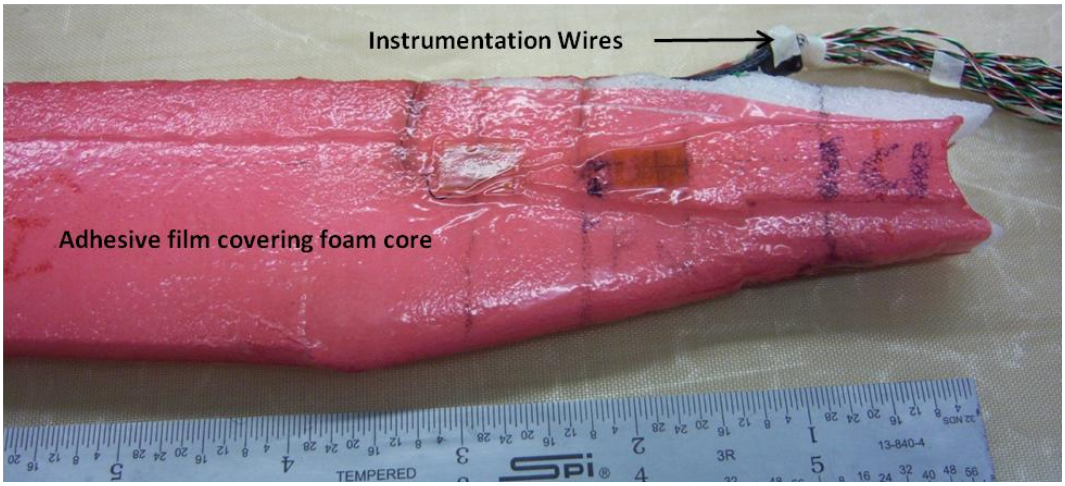

Figure E-17: Adhesive Film wrapped around Foam Core

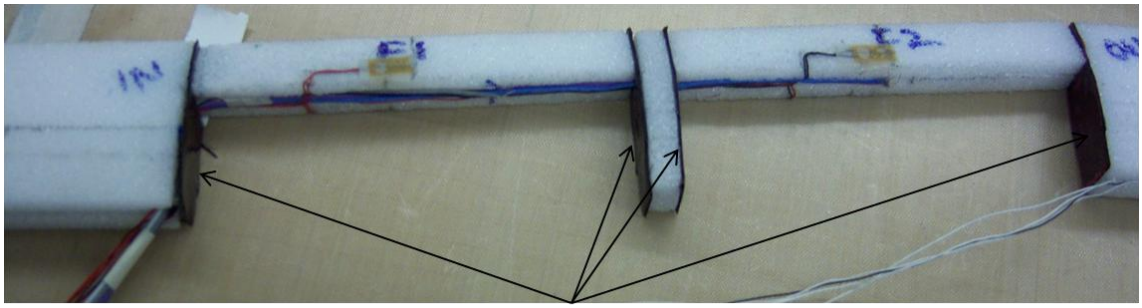

Figure E-18: Additional Plies in the Cutout Region

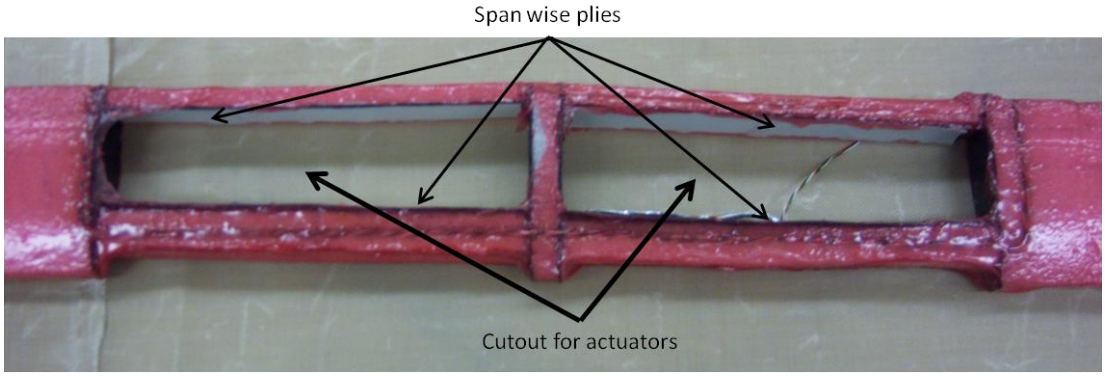

Figure E-19: Cutout Region with Ribs

In the next step, leading edge weight is added to the spar layup. This weight is added near the leading edge of the cross section such that the cross-sectional center of gravity lies near the quarter chord of airfoil section. The amount of ballast mass required is

determined from the cross-sectional analysis performed using UM/VABS. The ballast mass used in this research consists of tungsten rods with cross-sectional diameter of 0.04 inch and 0.125 inch. The leading edge weight (LEW) required and the number of tungsten rods needed to obtain that weight is shown in Table E-4. These tungsten rods are cut into 1 inch pieces (so that they do not result in additional cross-sectional stiffness) and rolled inside the IM7 ply as shown in Figure E-20. Since the flap region (section 2F) includes flap supports and flaps in the trailing edge region, higher leading weights are required in this region. Leading edge weights are attached to the spar section after the root layup is completed as shown in Figure E-23 and Figure E-24.

Table E-4: Ballast Mass used in each Cross Section

Section	LEW Reqd	0.04 Dia	0.125 Dia	LEW calc
	(gm/m)	(#)	(#)	(gm/m)
3R	0.014	5		0.111
2R	0.09	4		0.096
1R	0.143	7		0.148
1F	0.125	6		0.126
2F	0.35	2	2	0.355
3F	0.11	5		0.111
4F	0.108	5		0.111

In the next step, a root pin (required for alignment and for creating a 0.5” diameter hole for mounting the blade in the spin test stand) is added to the spar foam with adhesive film on it. The unidirectional IM7 ply is wrapped around the root pin such that the mounting hole has sufficient stiffness and strength. Root pin with wrapped IM7 plies and root plies added near the root section are shown in Figure E-21. As discussed earlier, root plies consist of 0.52” wide strips and they wrap around the root pin. Figure E-22 shows the root section when all the root plies are added to the root section.

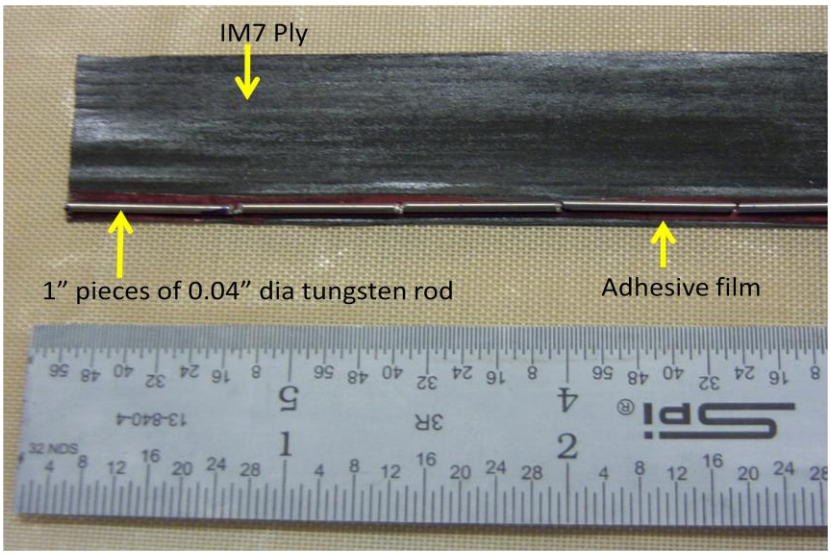

Figure E-20: Leading Edge Ballast Mass

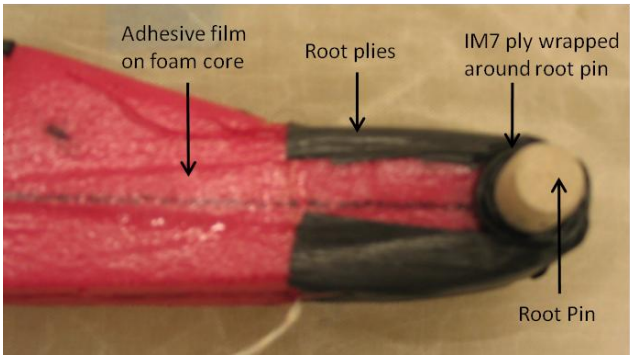

Figure E-21: Wrapping Root plies around the Root Pin

Figure E-22: All Root Plies wrapped around the Root Pin

After the root plies, leading edge weight and web plies are added to the spar as shown in Figure E-23. The cutout section of the blade includes larger ballast mass (Figure E-24) to account for the additional mass due to flap and flap supports in the trailing edge region.

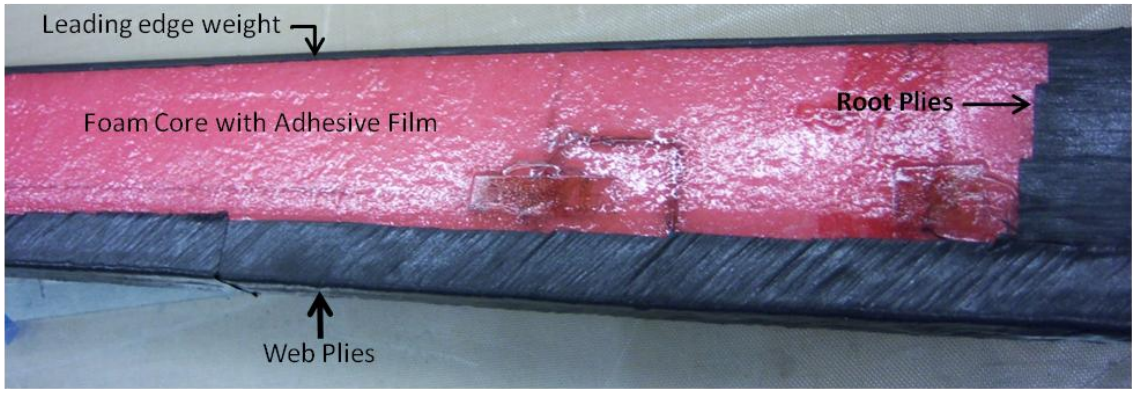

Figure E-23: Leading Edge Weights and Spar web plies

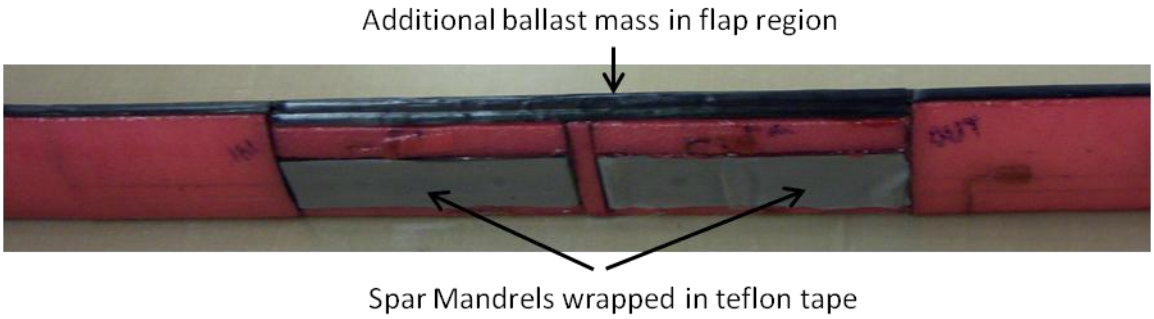

Figure E-24: Cutout Region with Spar Mandrel and Additional Leading Edge Weights

Next, the main spar plies are added. As discussed earlier, the main spar plies include a cut in the top part to account for the cutout. Figure E-25 and Figure E-26 show the first main spar ply (E-Glass at 0 deg) in the cutout region and the root region, respectively. A small modification had to be made in the main spar plies near the root region so that they conform better to the tapered and non-uniform root section. Figure E-27 shows the fourth main spar ply (IM7 ply at 45 deg) on the spar section. The unidirectional IM7 ply is

wrapped around the root pin like root plies. On the top surface, these plies are steadily moved around the cutout region as shown in Figure E-28.

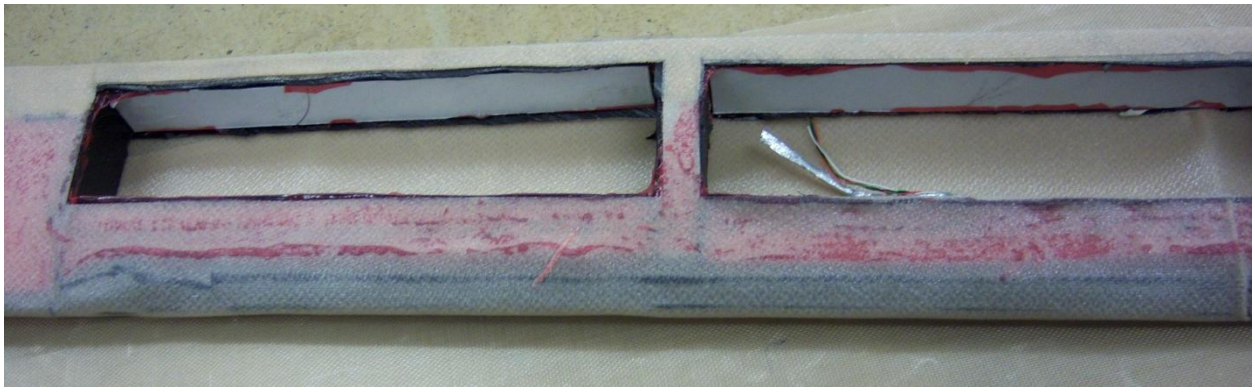

Figure E-25: First main Spar ply Wrapped Around Spar in the Cutout Region

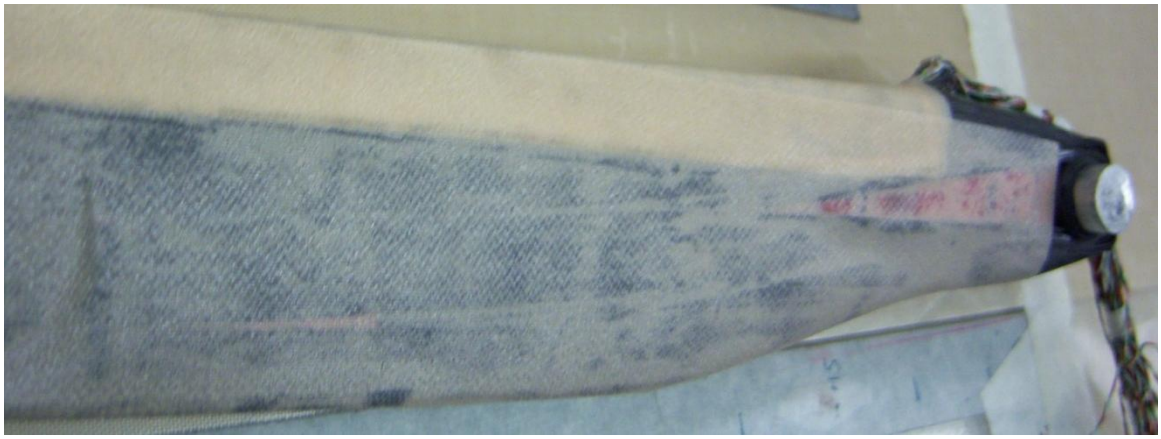

Figure E-26: First Main Spar Ply near the Root Region

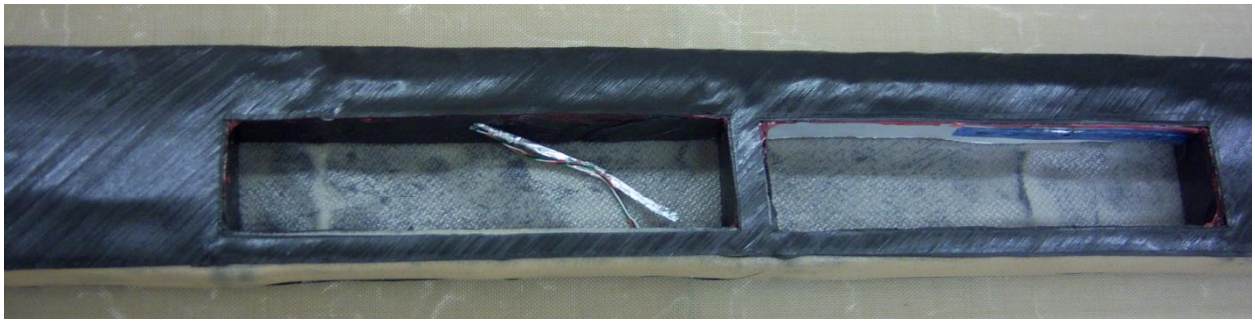

Figure E-27: 4th Spar Ply in the Cutout Region

Figure E-28: Unidirectional Plies moved around the Cutout Region

The cutout section of blade with all the main spar plies is shown in Figure E-29. It also shows the spar mandrel in the cutout region. In order to ease the process of spar mandrel removal from the cured spar, it is coated with the releasing agent (Frekote 700NC) and then taped with Teflon. This also prevents the residual epoxy from the prepreg from pouring into the threaded holes which are required for the removal of spar mandrel. The lower surface of the inboard and outboard actuator support are cleaned and covered with adhesive film to facilitate the attachment of supports to the lower surface of the cutout region in blade spar. In the next step, peel ply is added on the top and bottom surface of spar near the web region to create space for the overlapping fairing plies as shown in Figure E-29. Similarly, a spacer is used on the top of cutout region to create space for the spar cover which covers the actuators on blade. The bottom surface of the spar is shown in Figure E-31. Besides the peel ply, it also includes holes to allow the alignment pins from spar mandrel to pass through.

Figure E-29: Cutout Region with All Spar Plies

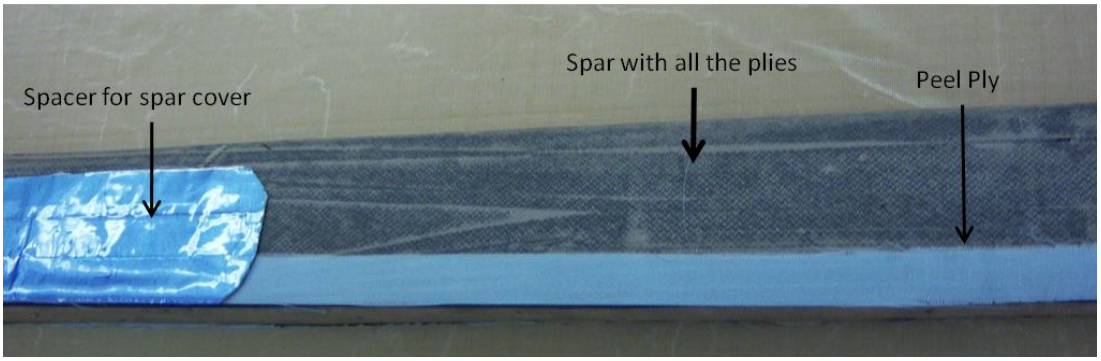

Figure E-30: cutout region with spacer and peel plies

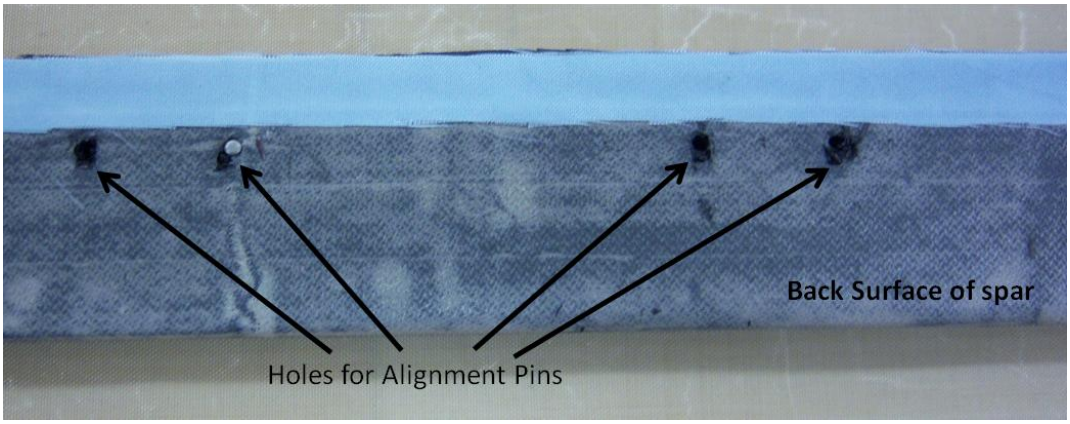

Figure E-31: Bottom part of the cutout region

All the instrumentation wires coming out from the root region are passed through a shrink tube as shown in Figure E-32. This prevents the prepreg epoxy from getting in contact with the wires which can make them brittle. Wires are also covered with the flash tape to prevent any kind of damage from rubbing which might happen while closing the molds. The instrumentation wires exit from the mold as shown in Figure E-33 through the cavity machined earlier in the mold.

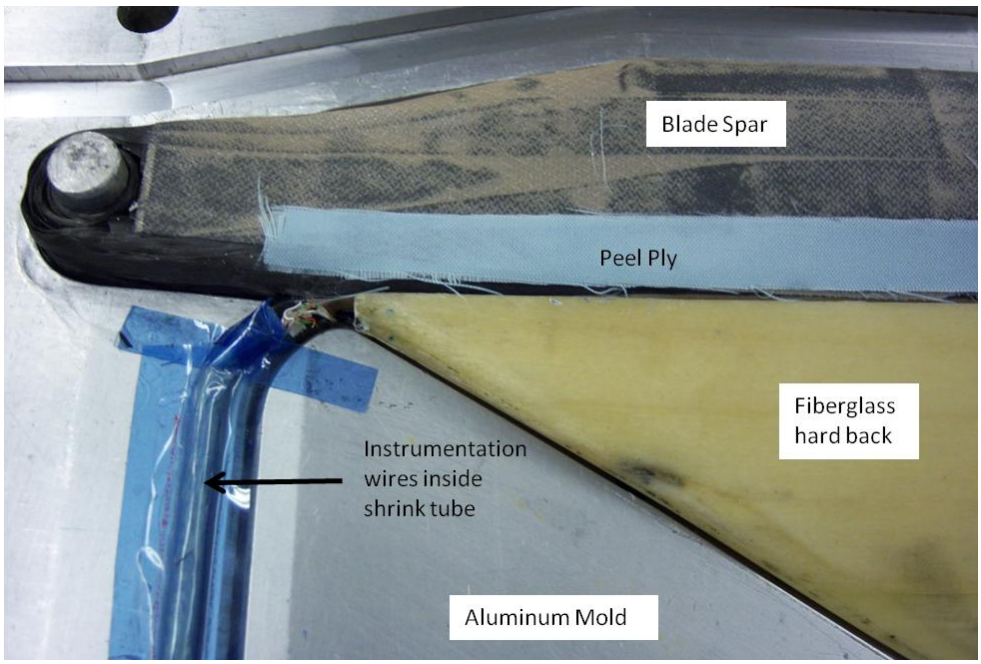

Figure E-32: Root region before spar cure

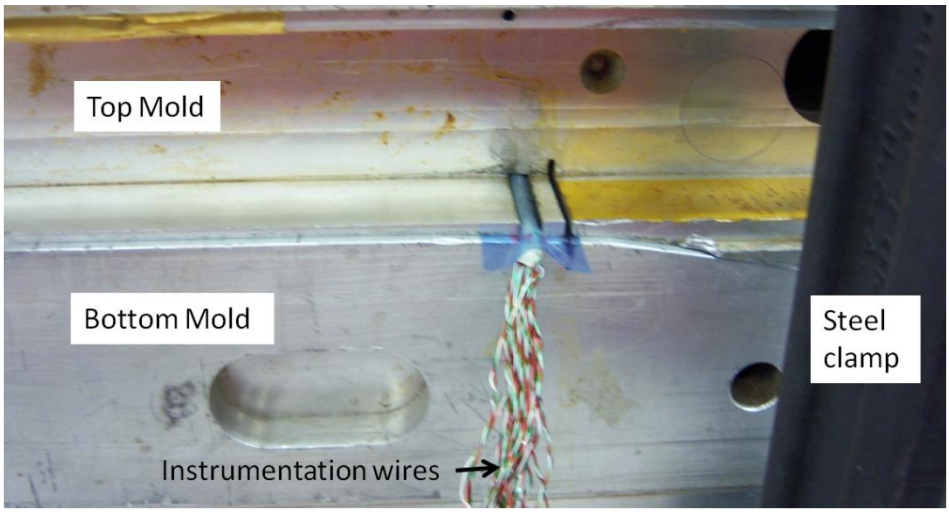

Figure E-33: Instrumentation wires exiting the mold

The bottom and the top molds are closed with the heavy duty steel clamps as shown in Figure E-34. The steel clamps are tightened such that the space between the molds is less than 8 mils along the entire perimeter. The blade section inside the closed mold is cured in a 6ft long autoclave at 250F for 90 min. In this research, an autoclave was used instead

of the traditional mold heater to provide a more uniform heating over the entire blade span and achieve a better control over the temperature profile. A very small pressure of 10 psi was used during the cure such that it is sufficient to ensure uniform heat transfer inside the autoclave without affecting the foam core in the blade cross section.

Figure E-34: Blade Molds Closed with Heavy Duty Steel Clamps

The cured blade spar is shown in Figure E-35 and Figure E-36. The peel ply and the spacers after the cure are shown in Figure E-36. It also shows the Teflon-taped spar mandrel in the cutout region which had to be removed. The spar mandrel was removed using the threaded hole in the middle spar as shown in Figure E-37. During the removal of spar mandrel, care is taken to make sure that the inboard and outboard actuators supports are not affected and they remain fixed in the blade spar. And finally, the high voltage wires in the cutout region are soldered to the solder taps on the wall of the cutout region.

Figure E-35: Active Blade Spar after Cure

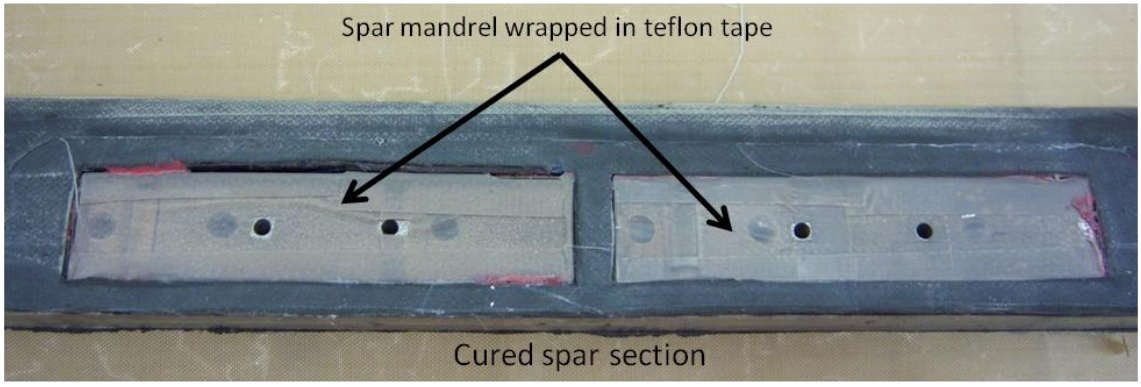

Figure E-36: Cutout Region after Cure

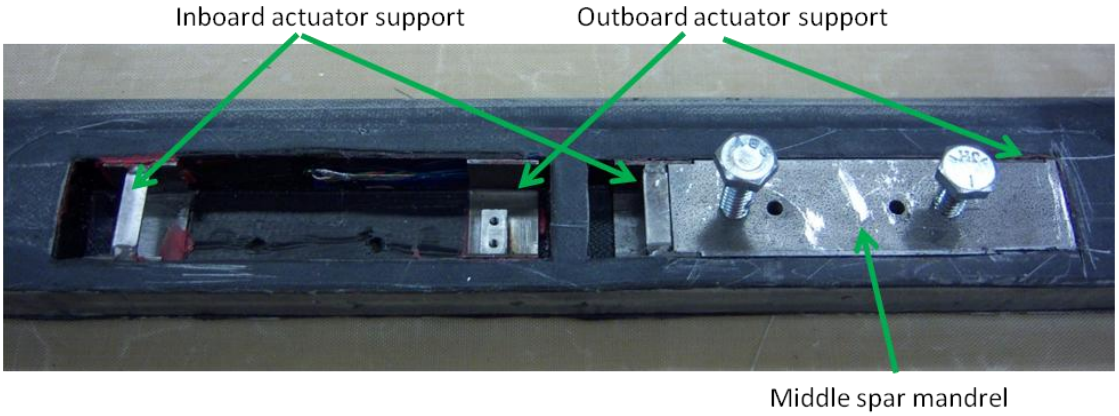

Figure E-37: Spar Region after removing Spar Mandrel

E.5 Fairing Manufacture

The process used in the faring cure is similar to that followed during the spar cure. In this case, the cure is complicated by the fact that the accurately aligned flap supports need to be installed in the flap region for holding the flaps. In order to help in the alignment, holes and notches are machined in the lower blade mold as shown in the Figure E-38. The position of these holes was fixed relative to the location of alignment holes used for the spar mandrel. Before the fairing cure, the flap mandrel had to be designed and fabricated which is used to create space for actual flaps. The CAD model of the flap

mandrel is shown in Figure E-39. It also includes extensions at the ends to hold the flap supports during the fairing cure.

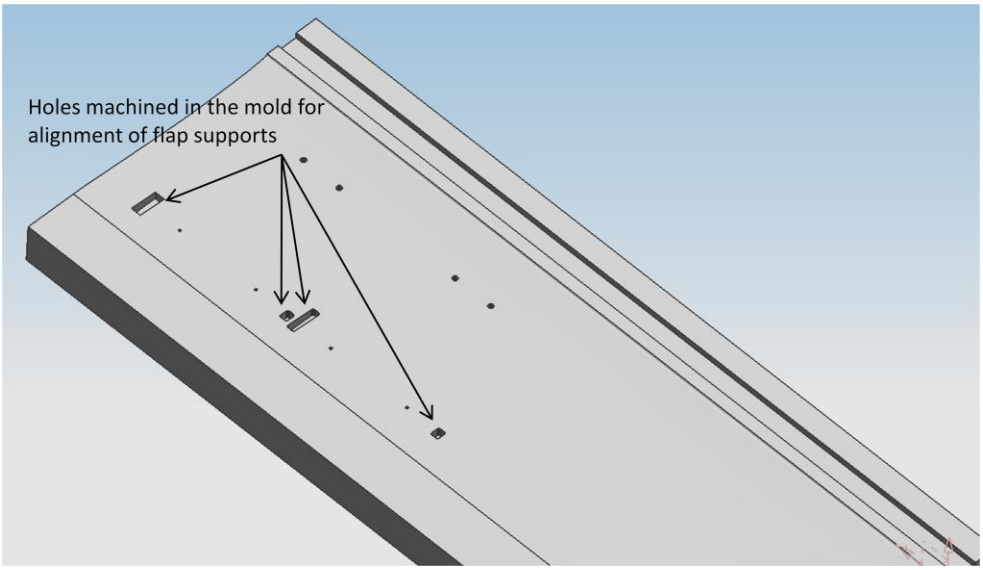

Figure E-38: Holes machined in the bottom mold for alignment of flaps during the cure

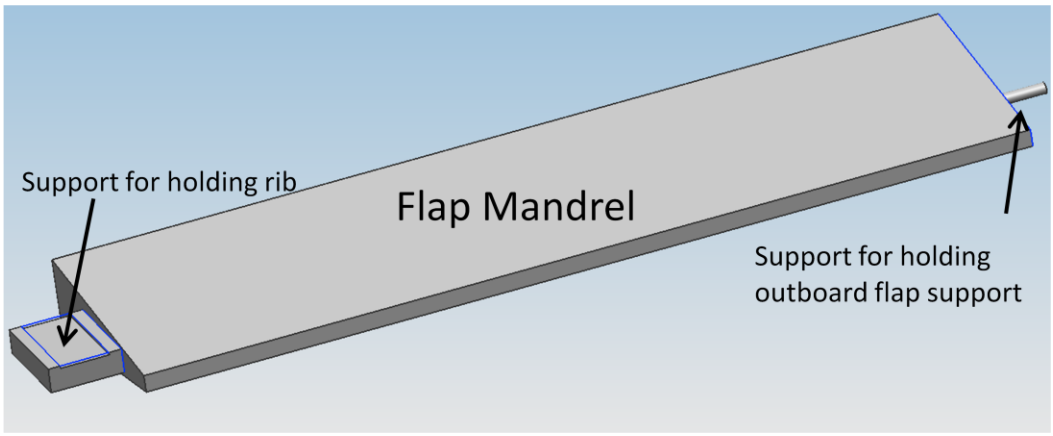

Figure E-39: CAD model of the flap mandrel used during fairing cure

The flap mandrel was machined out of aluminum. The CAD model of the inboard and outboard flap support that had to be installed on the blade during the fairing cure is shown in Figure E-40. The flap supports were fabricated using water jet cutting to get the precise shape. As in the case of spar foam, the fairing foam was also fabricated in 6 inch

long pieces and then joined together using the five-minute epoxy. The fairing foam had to be tapered near the root region to follow the mold profile as shown in Figure E-41. The fairing section includes wires from HET that are used to measure the flap deflection. Hall Effect transducers (HETs) are mounted after the fairing cure to protect them from high temperature during the curing process.

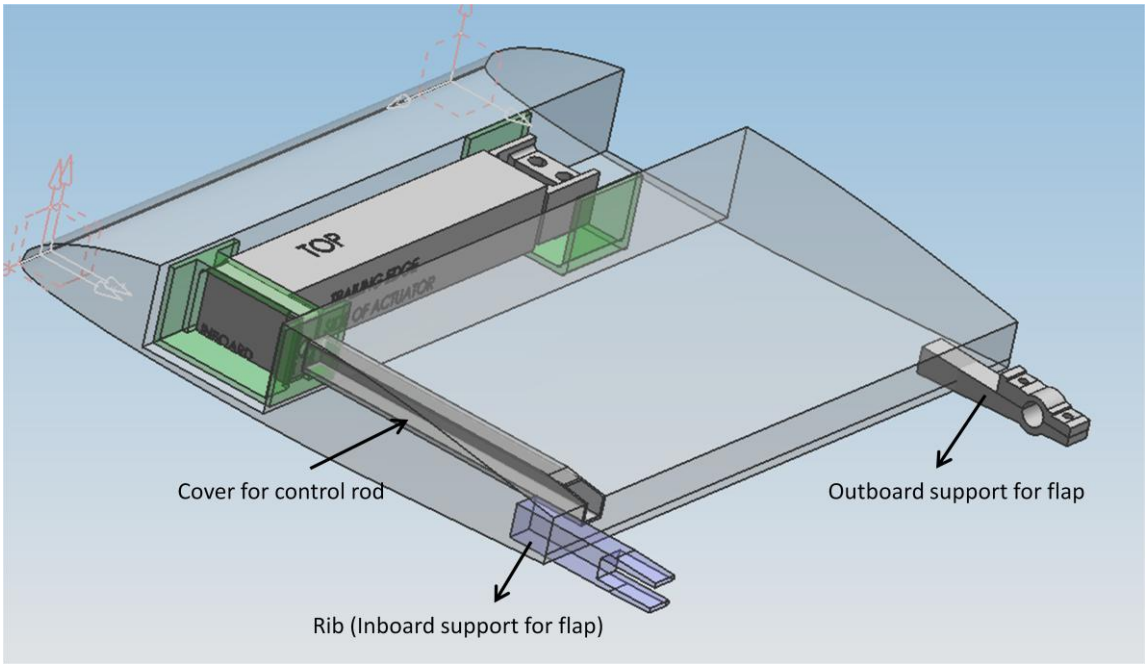

Figure E-40: Location of Flap Supports mounted in the Flap Region during Fairing Cure

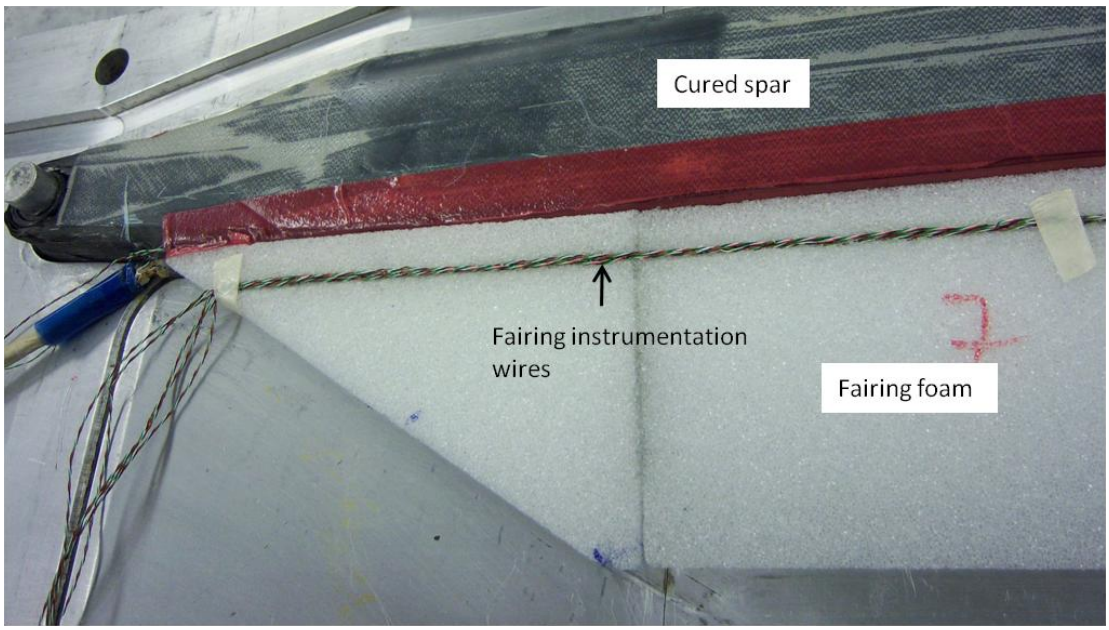

Figure E-41: Root Region with Fairing Foam Core

In order to attach the flap supports to blade section, super plies and ribs are used. Figure E-42 shows superplies wrapped around the inboard and outboard flap supports. This figure also shows the flap mandrel, the cut made in fairing foam core for the mandrel and the wires for connecting HET to the flap support. The ribs that are used to transfer the loads generated by flap supports to the blade spar are shown in Figure E-43. This figure also shows the TE stiffener (0.3 inch wide unidirectional IM7 ply) which runs along the blade span to provide longitudinal stiffness in the fairing region.

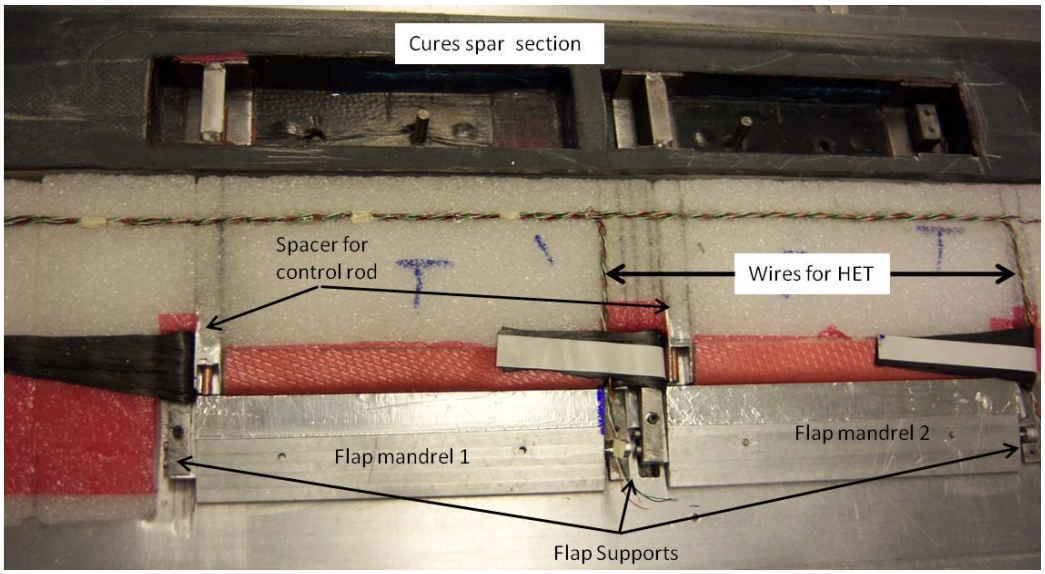

Figure E-42: Instrumented Flap Region for Fairing Cure with Flap Mandrel

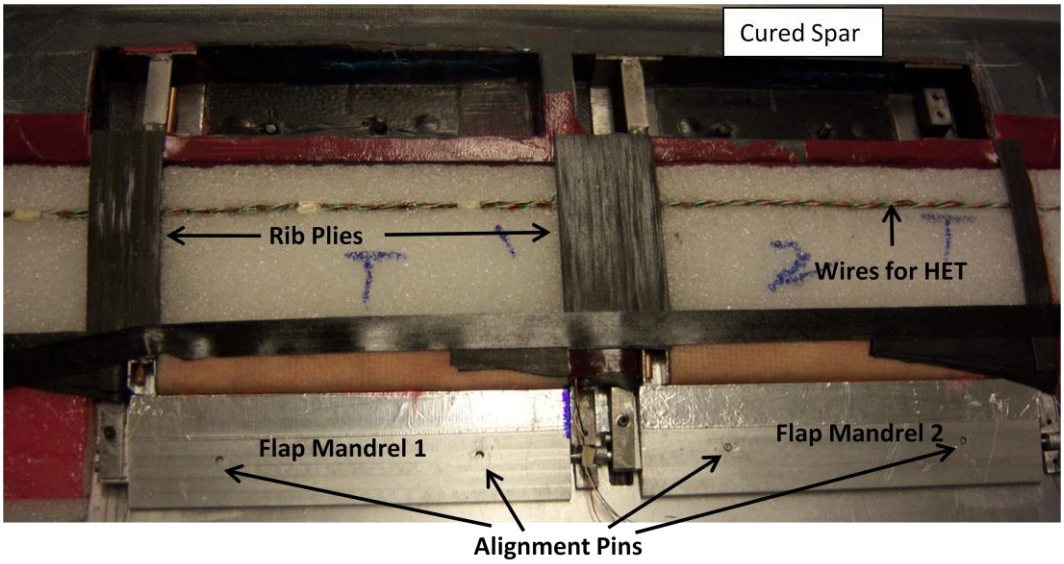

Figure E-43: Flap Region with Additional Plies for holding Flap Supports

Fairing plies (IM7 plies at +45 deg and -45 deg) were added on the top as shown in Figure E-44. As it can be seen in the figure, they overlap the cured spar region over a width of 0.3 inch. Similar rib plies and trailing edge stiffener were added on the bottom surface of the fairing foam core as shown in Figure E-45.

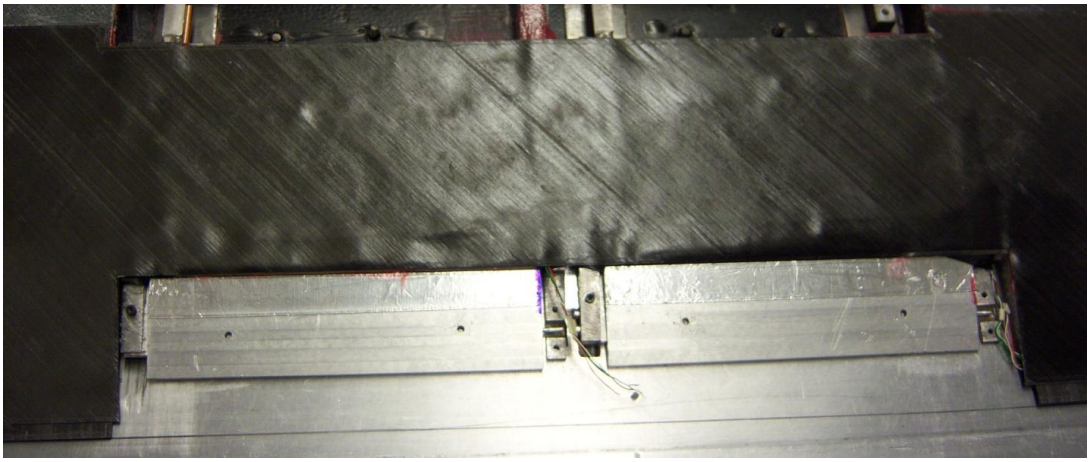

Figure E-44: Flap Region with Fairing Plies

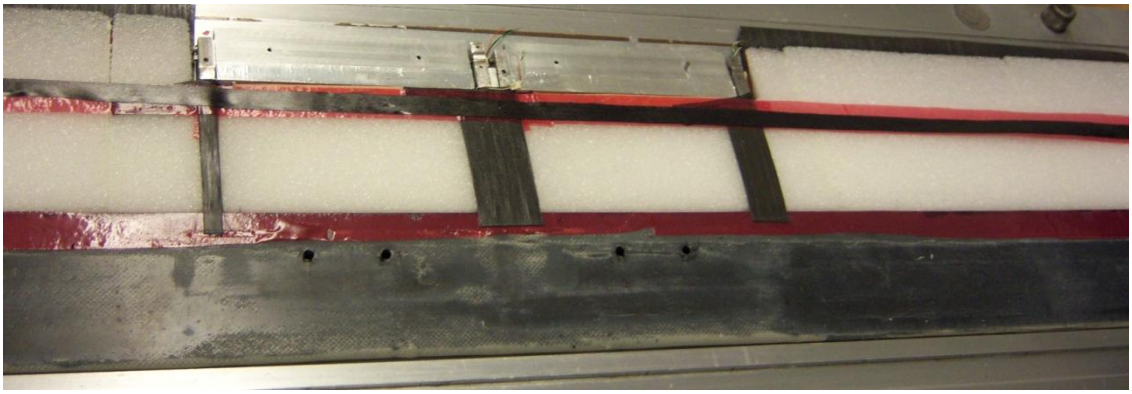

Figure E-45: Bottom Part of the Fairing Region

Before closing the mold for final cure, a spacer was used to create space for the spar cover in the cutout region and critical areas were covered with the flash tape to prevent extra epoxy from seeping into the parts as shown in Figure E-46. Final fairing layup near the root section is shown in Figure E-47. As in the case of spar cure, the instrumentation wires were run along the machined cuts in the mold to prevent them from damage during the curing process.

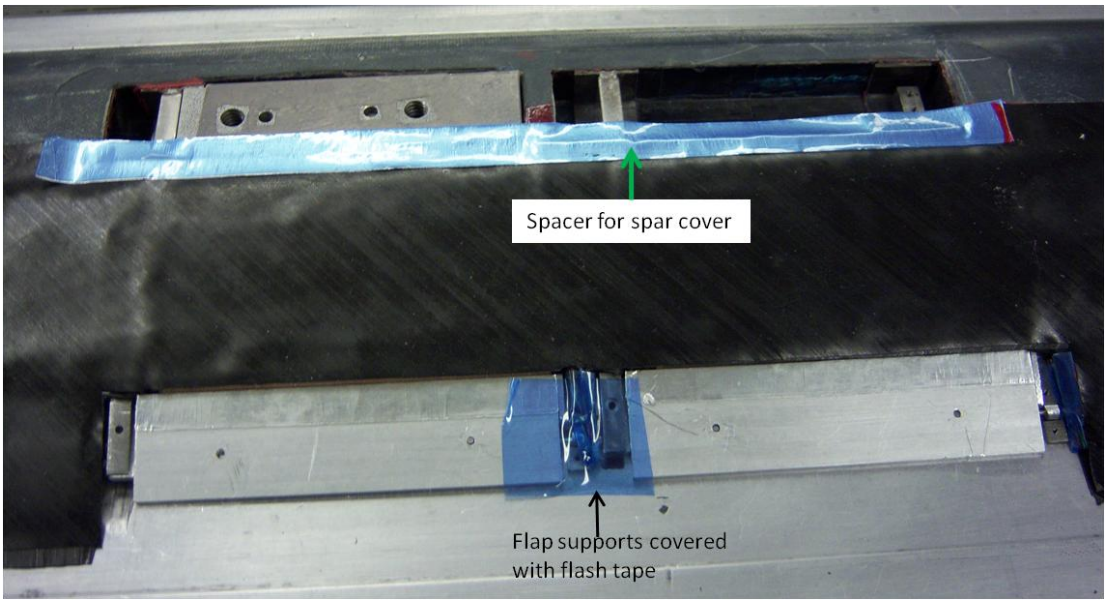

Figure E-46: Fairing region before Final Cure

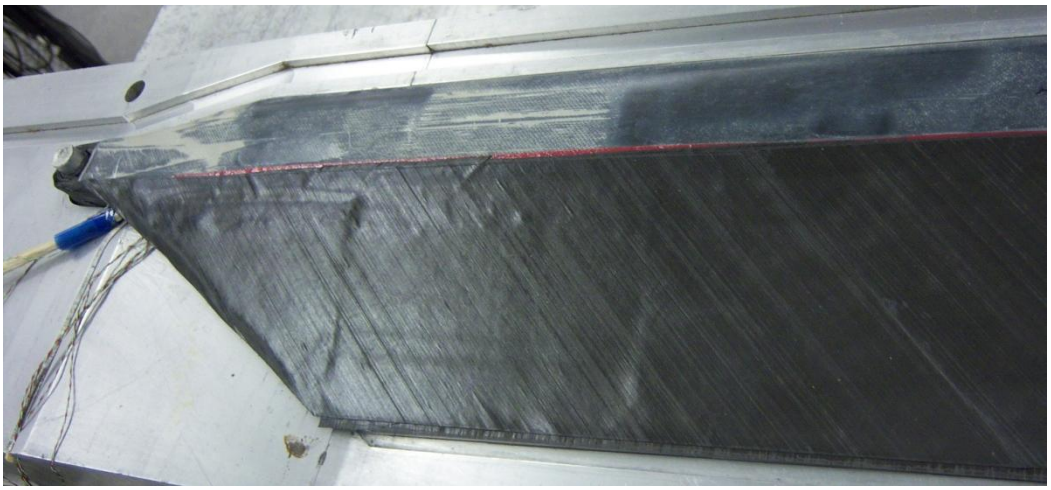

Figure E-47: Root part of the Blade before Fairing Cure

The final cured blade obtained after the fairing cure is shown in Figure E-48. It shows the flap supports attached to the fairing of blade and the flap mandrel which was used as spacer. The flap mandrels were carefully removed so as not to damage the HET wires and fixed flap supports as shown in Figure E-49.

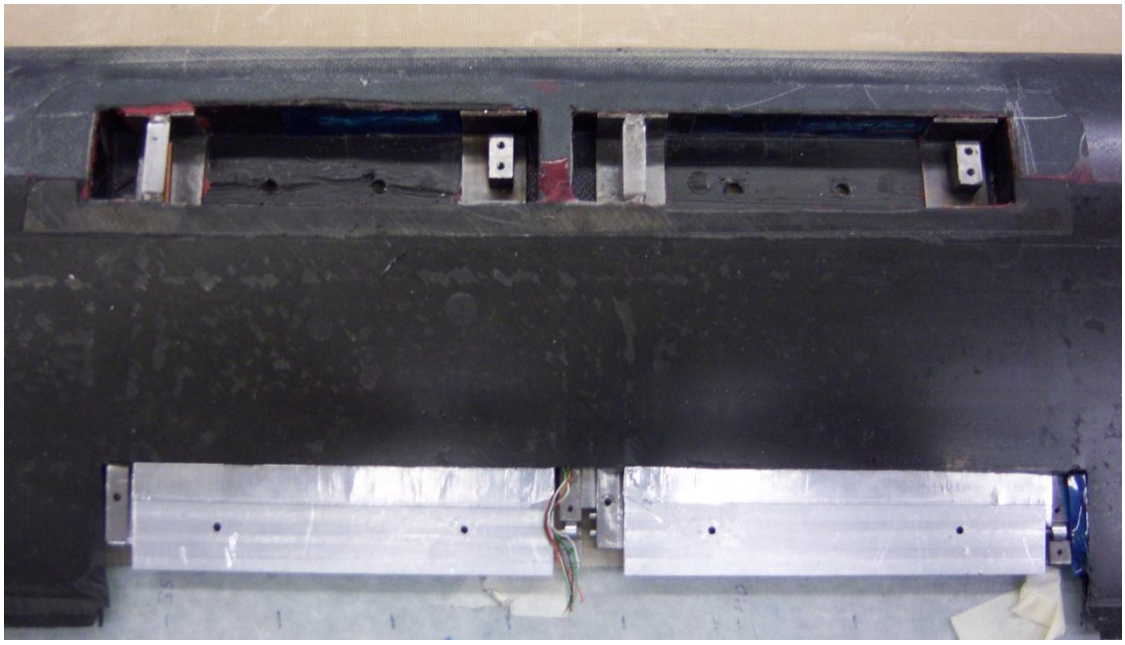

Figure E-48: Flap part of the Blade after Cure

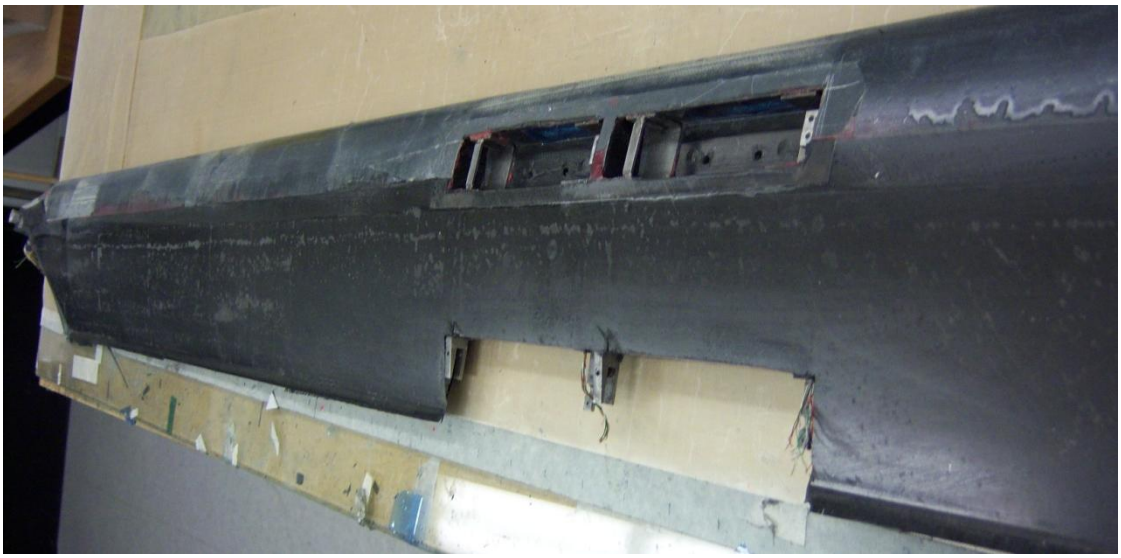

Figure E-49: Cured Active Blade

The second blade used for testing on the spin test stand did not include active flaps and is referred as “passive blade”. The passive blade used for testing was designed to have similar dynamic properties as the active blade to avoid undesirable loads due to the blade dissimilarities. Thus, the passive blade had cutout as in the case of active blade and

it included ballast masses in the spar region and in the flap region to account for the actuators and flaps, respectively. The passive blade also included one flapwise bending strain gage, one torsional strain gage and one chordwise strain gage near the root region. The final passive blade that was fabricated is shown in Figure E-50. The ballast masses used in the spar region in place of the actuator are shown in Figure E-51.

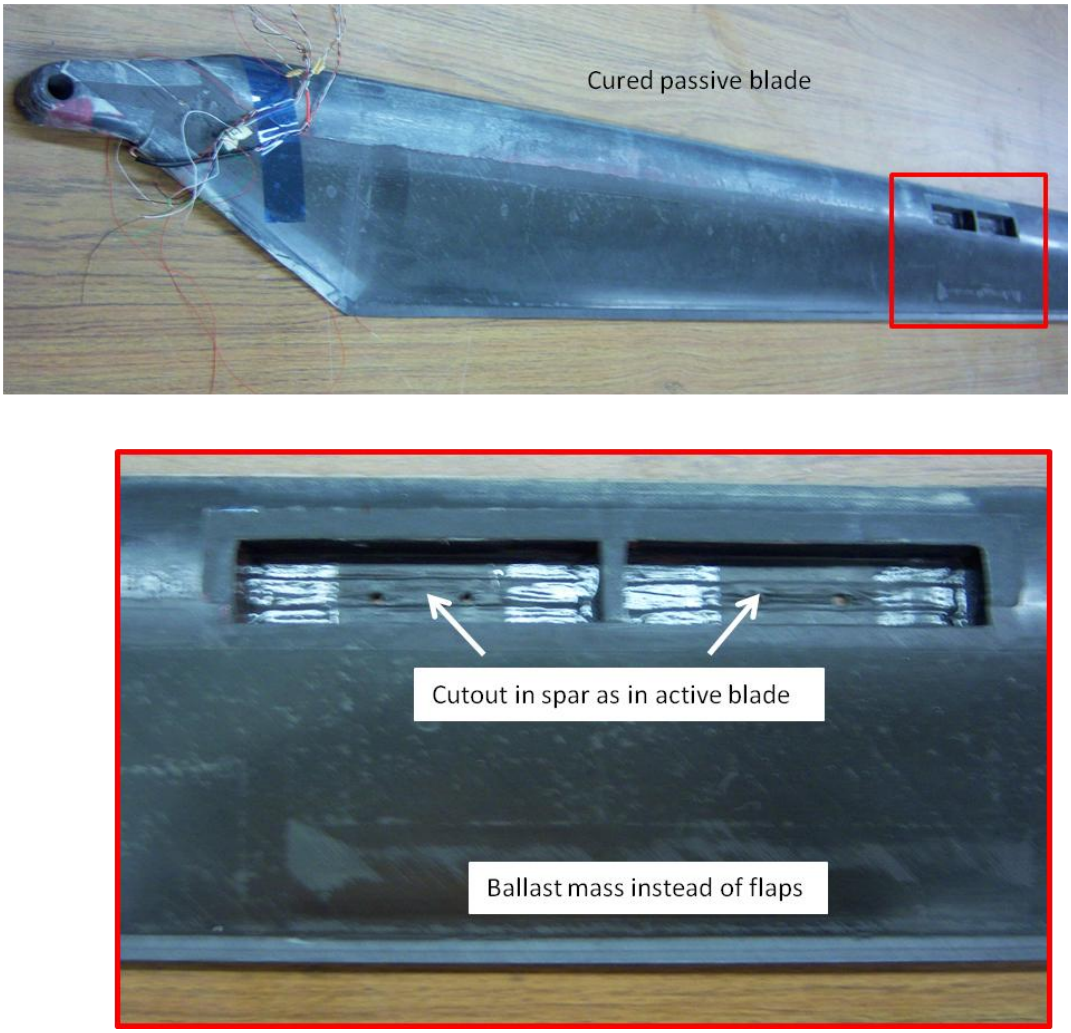

Figure E-50: Cured Passive Blade

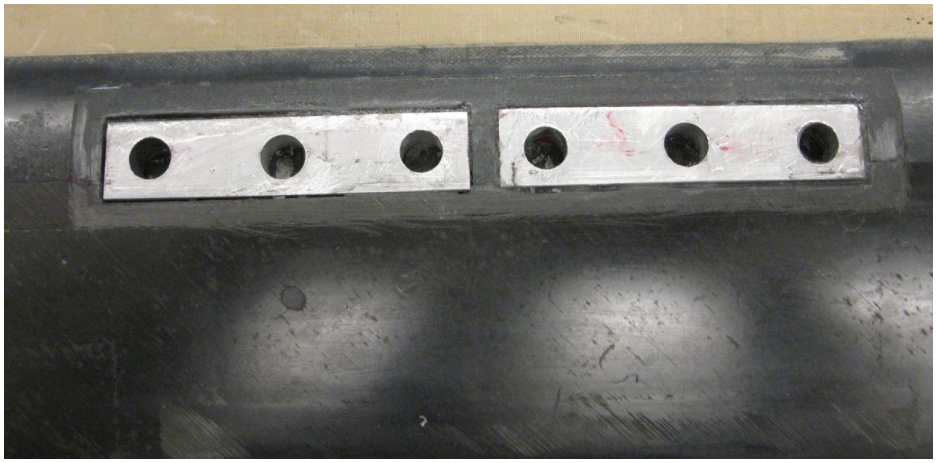

Figure E-51: Ballast mass added in passive blade instead of actuator

E.6 Fabrication of Active Flap

The fabrication process used for manufacturing the active flaps is similar to that used for fabricating the active blade. It consisted of prepreg plies wrapped around the foam core. It also included supports at the end to help in installation of the flaps on the active blade. The cross-sectional shape of the active flap is shown in Figure E-52. The final fabricated flap had a chord of 1.34 inch (~ 0.25c) and a span of 3.85 inch (~0.06R). As discussed in Section C.2.1, in order to minimize the hinge moment generated by aerodynamic forces, the active flap was designed to have an overhang. Based on the CFD analysis carried out for the airfoil-flap, the location of flap hinge axis was fixed at $0.365c_f$.

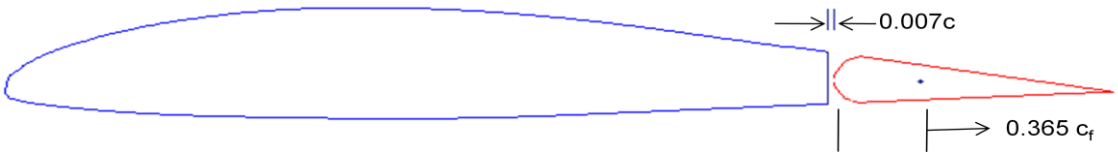

Figure E-52: Cross-sectional Shape of the Flap

During the CAD assembly of the flap and flap hinge mechanism, it was noticed that some part of the flap was interfering with the control rod which is used to transfer the

actuation from X-frame actuator to active flap. Thus, a small notch was made near the leading edge of the flap as shown in Figure E-53 to avoid the interference.

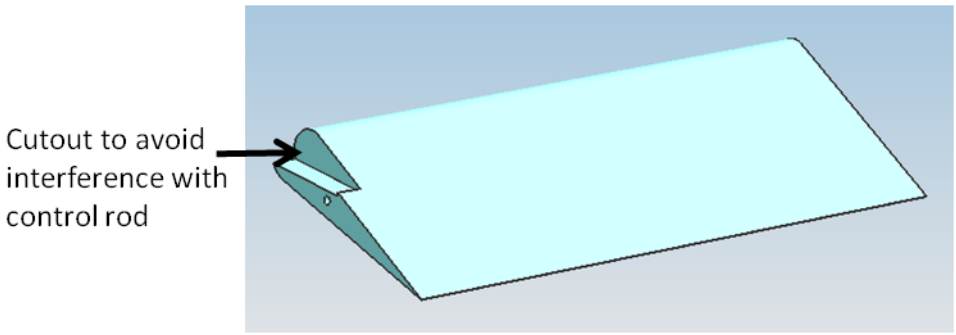

Figure E-53: CAD Model of the Active Flap

The foam core for active flaps was prepared in a similar manner as the foam core in blade spar and fairing were fabricated. Plexiglass template was designed and laser cut based on the number of plies and oversizing required to get sufficient back pressure for the mold cure. The flap section before the cure is shown in Figure E-54. The spacer used to create space near the leading edge of the flap and flap horn used in the flap can be seen in the picture. For curing the flaps, a new aluminum mold was designed and machined. It included small cutouts on the sides to help in the alignment of flap supports during the fabrication process as shown in Figure E-55. The active flap was also cured in the autoclave as shown in Figure E-56. The final fabricated flaps are shown in Figure E-57.

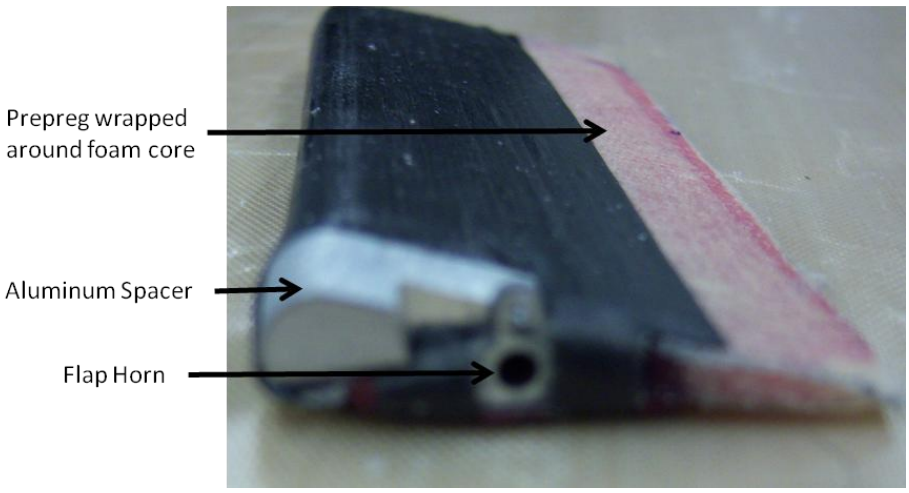

Figure E-54: Flap section before cure

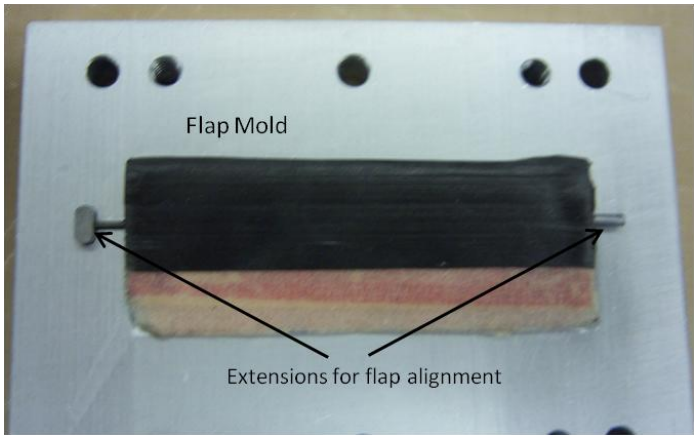

Figure E-55: Flap inside the Mold before Cure

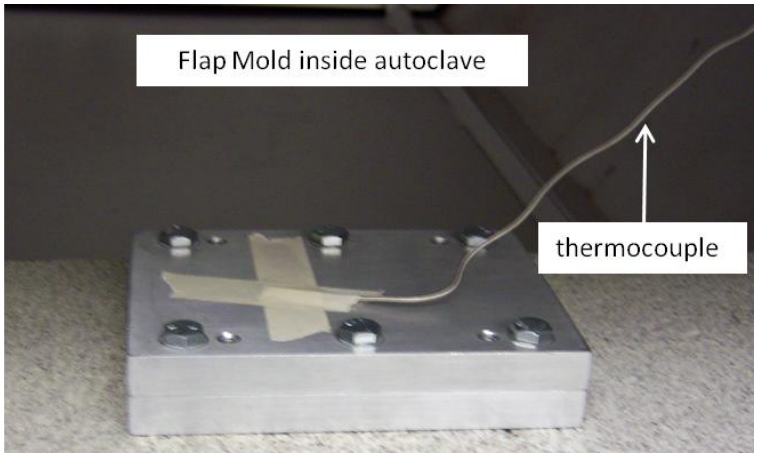

Figure E-56: Flap inside the Autoclave for Cure

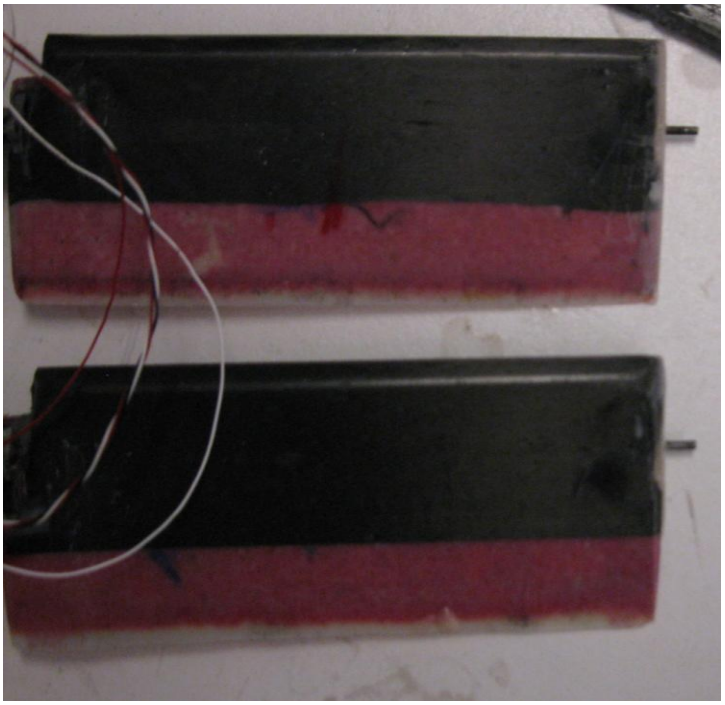

Figure E-57: Cured Flap Sections

E.7 Blade Section for Pull Test

For pull test, sample sections of the blade were fabricated with metal insert at the end. The CAD model of the metal insert used in the pull test is shown in Figure E-58. As shown in the figure, half of the metal insert resembles the shape of blade spar such that it can be easily attached to the blade, while the other half is a flat rectangular extension, where a hole is drilled, such that it can be easily attached to the tensile testing machine. The drilling of the hole or any other machining required for the metal insert should be performed prior to attaching the metal insert to the blade spar. In the next step, the metal insert is attached to the end of foam core as shown in Figure E-59. Thus, the metal insert becomes a part of the blade during the layup process.

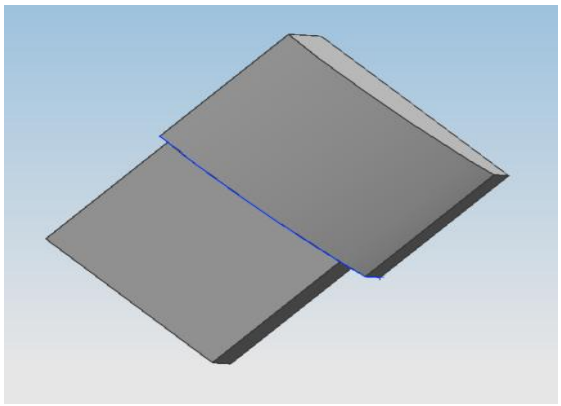

Figure E-58: CAD model for the Metal Insert

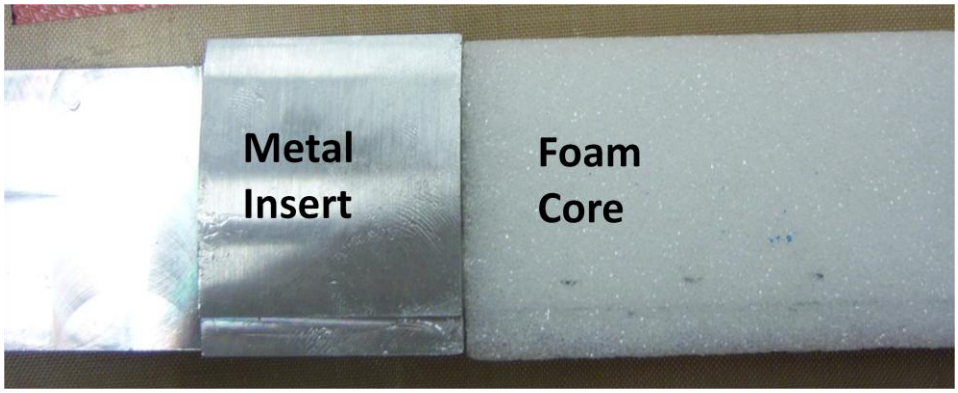

Figure E-59: Metal Insert Attached to the Foam Core

The final parts fabricated for pull test included strain gages to measure strains during testing. To allow the wires to pass through, a small grove was made in the metal insert along the spar thickness. Sample section for tensile testing with metal inserts attached at either ends is shown in Figure E-60.

Figure E-60: Fabricated Section for Pull Test

Appendix F. Results from the Dual Flap Experiments

This appendix provides a summary of the experimental results obtained from the tests conducted on spin-test stand with dual active flaps. The results obtained are compared with numerical analysis performed using RCAS code.

F.1 Introduction

The main aim of the experimental analysis was to measure the unsteady drag produced by active flaps in rotating conditions. With this objective in mind, a composite rotor blade with dual active flaps was designed and fabricated as described in Appendix C, Appendix D and Appendix E. The active flaps on the rotor blade were actuated by a couple of X-frame actuators developed at MIT. The characterization of the X-frame actuator and the development and testing of flap-actuation mechanism is described in Appendix C of the thesis. Once the blade was fabricated, it was tested on the spin test stand. Besides determining the unsteady drag produced by active flaps, other objectives of the experiment are to: a) test the effectiveness of dual active flaps in influencing vibratory loads at the rotor hub and b) generate experimental database for comparison with numerical analysis.

Summary of the Spin Test Stand

The UM/MIT spin stand facility was developed for testing a Mach–scaled two-bladed rotor with a diameter of 10ft. As shown in Figure F-1, the test stand consists of a steel

frame in a pyramid configuration which houses an electric motor with a direct coupled shaft which passes through a slip ring assembly. The base of the stand is isolated on rubber cushions to attenuate transmissions of floor vibration. The main characteristics of the spin-test stand are given in Table F-1.

Table F-1: Spin-test Stand Characteristics

Property	Value
Hover speed (for Mach scaling)	1336 RPM
Max rotor power	150 hp
Lowest stand elastic mode	> 150Hz
Flap articulation	0.0286R
Lag articulation	0.15R
Feathering degree of freedom	clamped at 0.0673R
Number of slipring channel for sensor signal	138
Number of slipring channel for high voltage signal	28
Number of blades	2
Radius	60.619 in (5ft)
Blade Chord	5.388 in

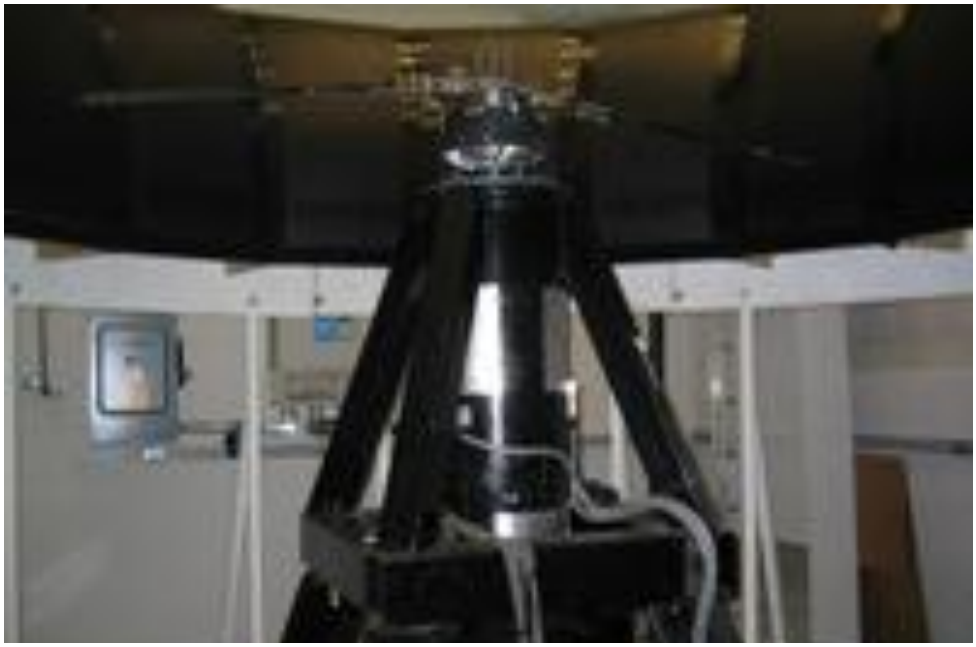

Figure F-1: Spin-test Stand

The primary sensor used for the measurement of unsteady aerodynamic loads due to flap oscillation is a six-axis JR3 load cell. It measures all the three forces and three moments at the rotor hub in the rotating frame. The maximum load carrying capacity for various load components of the load cell is given in Table F-2. Axes orientation for the load cell is shown in Figure F-2.

Table F-2: Maximum loads

Load Component	Max Load
F_x	± 300 lbf
F_y	± 300 lbf
F_z	2000 /-500 lbf
M_x	± 250 ft-lbf
M_y	±250 ft-lbf
M_z	200 / -800 ft-lbf

Note: 1. Data for Table F-2 is provided by the manufacturer
2. Except F_z and M_z, all other loads generated by the blades subtract at the hub

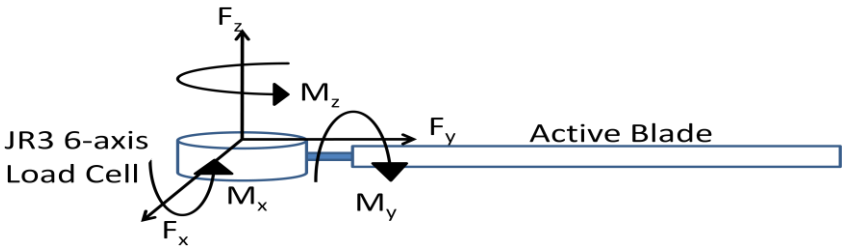

Figure F-2: Axes Convention for the Load Cell

During previous experiments conducted with the spin-test stand at the old MIT location [112], basic accuracy and resolution of the load cell under rotating conditions were characterized. Results are reproduced in Table F-3. Ideally, these calibration tests need to be conducted again for the new facility at the University of Michigan. However, it is expected that due to the improved flow conditions in the new facility, the flow fluctuations will be smaller than that detected earlier and the results shown in Table F-3 are expected to improve.

Table F-3: Preliminary Accuracy and Resolution of Various Load Components

Load Component	Accuracy	Resolution
F_x	1.5 lbf	0.08 lbf
F_y	1.5 lbf	0.08 lbf
F_z	6.2 lbf	0.25 lbf
M_x	1.2 ft-lbf	0.06 ft-lbf
M_y	1.2 ft-lbf	0.06 ft-lbf
M_z	2.5 ft-lbf	0.05 ft-lbf

List of working Sensors

During the process of active blade fabrication and instrumentation, some of the sensors were damaged. The list of all working sensors is given in Table F-4.

Table F-4: List of working Sensors

Strain gages in blade spar

Sensor	Sensor Description	Type	Location (R)	Status
1	Chordwise Bending Strain	Half	0.18	Quarter bridge working
2	Flapwise Bending Strain	Half	0.19	Working
3	Torsional Strain	Full	0.2	Working
4	Flapwise Bending Strain	Full	0.39	Half Bridge working
5	Flapwise Bending Strain	Full	0.59	Working
6	Chordwise Bending Strain	Full	0.52	Quarter bridge working
7	Torsional Strain	Full	0.35	Working
8	Torsional Strain	Full	0.55	Working
9	Torsional Strain	Full	0.69	Working
10	Torsional Strain	Full	0.89	Working
11	Axial Strain in Act Bay 1	Quar	0.75	Failed
12	Axial Strain in Act Bay 2	Quar	0.82	Failed

Note: Chordwise strain gages to measure axial strain in actuator bay were mounted again during fabrication of blade fairing

Accelerometers (at blade tip) in spar

Sensor	Sensor Description	Location (c)	Status
13	Near Leading edge	0.06	Failed
14	At quarter chord	0.25	Yes

Strain gages (in fairing)

Gage No	Sensor Description	Type	Location (R)	Status
15	Chordwise Bending Strain	Quarter	0.76	Working
16	Chordwise Bending Strain	Quarter	0.82	Working
17	Chordwise Bending Strain	Quarter	0.52	Working

Accelerometer (in spar)

Gage No	Sensor Description	Location (c)	Status
18	Near Leading edge	0.44	Yes

Note: HET sensors mounted in the sample blade can get damaged due to the high temperature and lack of sufficient space. Hence, HET wires were installed for HET which come out near flap`s outboard support. Actual HET are soldered near the flap supports after the blade is manufactured.

Data Acquisition and Flap Actuation

The data acquisition setup used for acquiring the data from spin test and power supply setup used to power the two X-frame actuators is shown in Figure F-3. The data collected from all the sensors on active and passive blades and the data from the load cell in rotating frame are transferred to the fixed frame through slip-rings in the spin test-stand hub. Data from the fixed frame on the spin-test stand is transferred through long intertwined wires to the National Instruments Data Acquisition Box in control room, as shown in the Figure F-3. The data acquisition, visualization and elementary post-processing analysis were performed using the LABVIEW software. It allows the user to observe the data in real time and store the acquired data at a desired sampling frequency in a text file. The output obtained in the text file can be used for further post processing using MATLAB. The LABVIEW was also programmed to include a warning system in case the output from any of the sensors exceeds a limiting value. For example, if the value of strain from one of the strain gages exceeds a critical value, the LABVIEW software issues a warning.

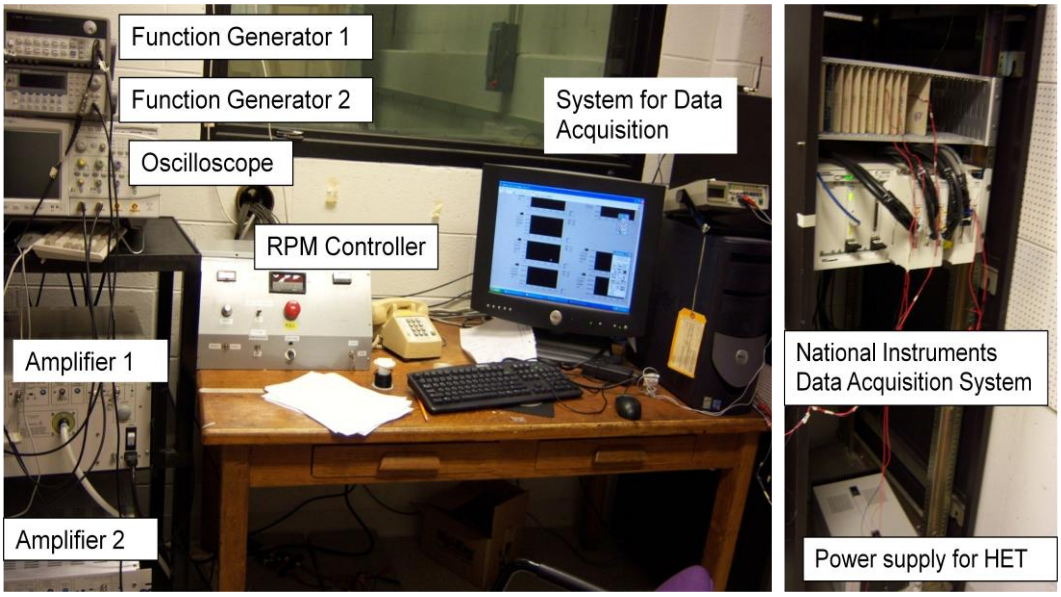

Figure F-3: Setup for Data Acqisition and Power Supply

The spin test stand room included four cameras at various locations in the room which can be used to record videos during the operation. Since the cameras had poor resolution, they could not be used for image processing or further analysis. One of the cameras was used for tracking purpose. Further details related to tracking and balancing is provided in the following section. The videos from all the four cameras can be seen by the user in real-time and it can also be recorded. One wireless camera was installed on the blade hub and it was made to point towards the tip of active blade from the hub. This helped in capturing the blade tip motion.

The two X-frame actuators used on the active blade were powered independently so that the motion of both the flaps can be controlled independently. The power supply to each actuator was provided by a set of function generator and amplifier. The function generator used for both the actuators can be synced, in case their phase difference or frequency needs to be controlled simultaneously. The 5V DC signal for the HET is provided through a separate power supply as shown in the Figure F-3.

Static Balancing and Tracking

Static balancing is performed in order to make sure that the total mass on the two blades used in the spin test stand are balanced. An aluminum fixture, where both the active and the passive blades used in the testing can be mounted, was designed and fabricated. The size of the fixture was the same as that of the spin-test stand hub. The setup used for static balancing is shown in Figure F-4 and Figure F-5.

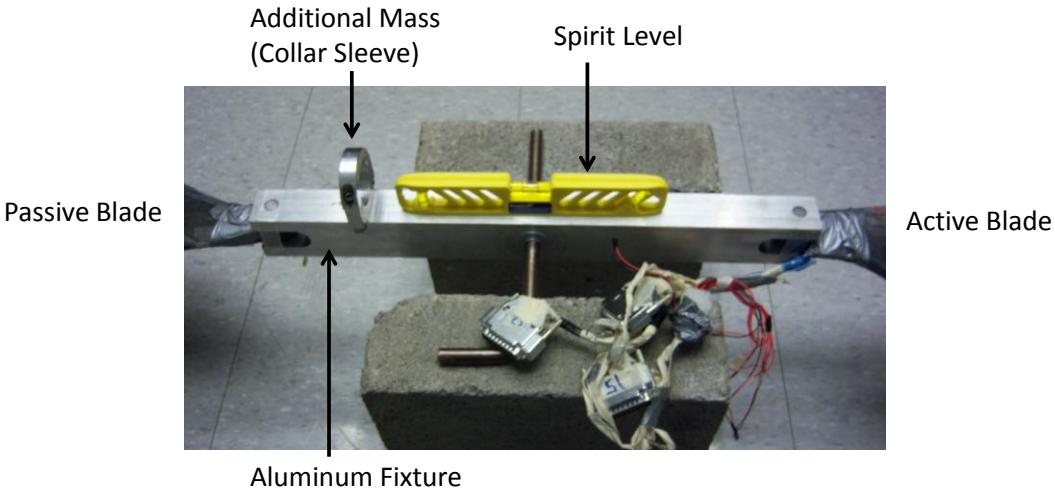

Figure F-4: Aluminum Fixture for Static Balancing

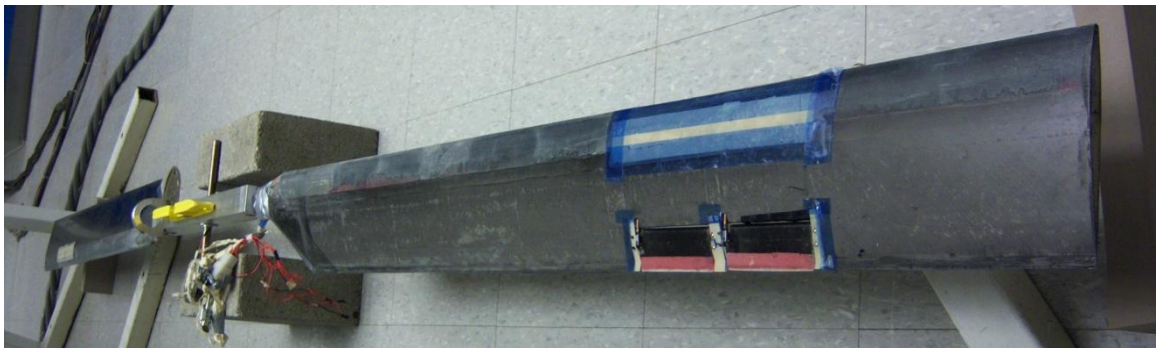

Figure F-5: Static Balancing of Blades

The active blade used for static balancing includes both the flaps and spar cap, as shown in Figure F-5. The additional ballast mass in the form of collar sleeve is used to

balance both the blades. The size of the collar sleeve is such that it can be easily fitted on the pitch shaft assembly. The advantage of using a collar sleeve is that it allows balancing of the two blades without adding any mass to the blade itself.

After the completion of static balancing, the collar sleeve was added to the pitch shaft. In the next step, blade tracking (or dynamic balancing) needs to be performed in order to make sure that the two blades are producing the same amount of lift. If the blades are not tracked, the pitch angle for one of the blades is adjusted till the balancing criterion is met. The procedure used for tracking is the same as that described in [112], where a combination of laser and camera were used. The schematic of the blade tracking process used in the current experiments is shown in Figure F-6. In this case, a high intensity laser was used to point on the blades. Whenever one of the blades hit the laser, a dot is produced at the point of contact and it is recorded by the camera. In case the blades are not balanced (as in the case of blades shown in Figure F-6), there is a shift in the point of contact, which can be easily seen on the camera output. If this occurs, then the blade pitch angle for one of the blades is adjusted till the dots almost coincide.

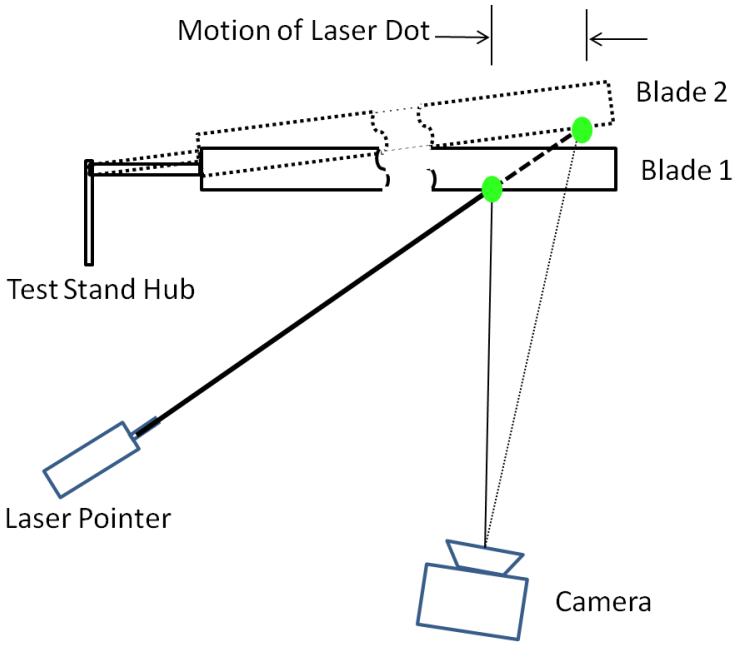

Figure F-6: Schematic of Blade Tracking

F.2 Testing Process

As discussed above, the main aim of the tests was to determine the unsteady aerodynamic loads produced by the rotor blades. In order to determine the vibratory loads, following steps were followed:

Step 1: Obtain Baseline Data

In this case, the rotor was spun at 900RPM while the flap position was fixed at zero degree. (For Mach scaling, the required rotor speed is 1336RPM. However, it was observed that at very high speeds, it was not possible to obtain sufficient flap deflections. Hence, the operating speed was reduced to 900 RPM). For this operating condition, the hub loads generated were recorded. For all the tests conducted in this thesis, a sampling frequency of 1000 samples per second was used. The data from hub load cell and other sensors was recorded once the steady state was obtained. In the steady state condition, the data was recorded for a period of 10 seconds that corresponds to 150 revolutions at 900

RPM. It should be noted that the default position of flaps (when flaps are installed on the blade) is not zero (usually it is close to +3 to +4 degree depending on the amount of prestress). Thus in order to bring this non-zero flap deflection to zero, a DC voltage supply was given to the actuators through the waveform generator and amplifier. Thus, the flaps were being controlled during the baseline tests. For the results presented in this section, the blades had a collective pitch setting of 6.5 degree which resulted in C_T = 0.0033 (C_T/σ = 0.0584).

Step 2: Obtain data with flap oscillations

In this step, the flaps on active blade were actuated at a desired frequency and phase difference. A sample test matrix for analysis at different actuation frequencies and phase angles of actuation is shown in Table F-5. In the sample results shown later in this Appendix, the data collected for Case 1 and Case 5 is used. As in the baseline case, the rotor was spun to the nominal speed of 900RPM and the data was collected in steady state condition for a period of 10 seconds.

Table F-5: Test Matrix for Analysis at Different Frequency

Freq\Phase	0^0	90^0	180^0	270^0
2/rev	**1**	2	3	4
3/rev	**5**	6	7	8
4/rev	9	10	11	12
5/rev	13	14	15	16

Step 3: Extraction of Vibratory Loads due to Flap

The data obtained from the spin test stand hub load cell was very noisy, as shown in Figure F-7 (a) for the F_z component. The spin test stand also included a RPM counter in the hub and the output from the counter was also recorded. This was used to plot the data

as a function of number of revolutions, as compared to plotting the data as a function of time. For the analysis of periodic systems, it was observed that this technique is more meaningful and eases the process of filtering noise. Next, the data collected for 150 revolutions was split into 10 sets where each set had the data for 15 revolutions. The data observed for all the 10 sets is shown in Figure F-7 (b). And finally, the data obtained for all the ten sets was averaged to get a single signal for 15 revolutions as shown in Figure F-7 (c). The results show that this process helped in getting a cleaner signal which was used for obtaining the mean value of the signal and frequency content using the FFT option in MATLAB, as shown in Figure F-8. In this figure, top part (in red) shows FFT of the raw data (shown in Figure F-7(a)), while the bottom part (in blue) shows FFT of the time averaged data (shown in Figure F-7 (c)).

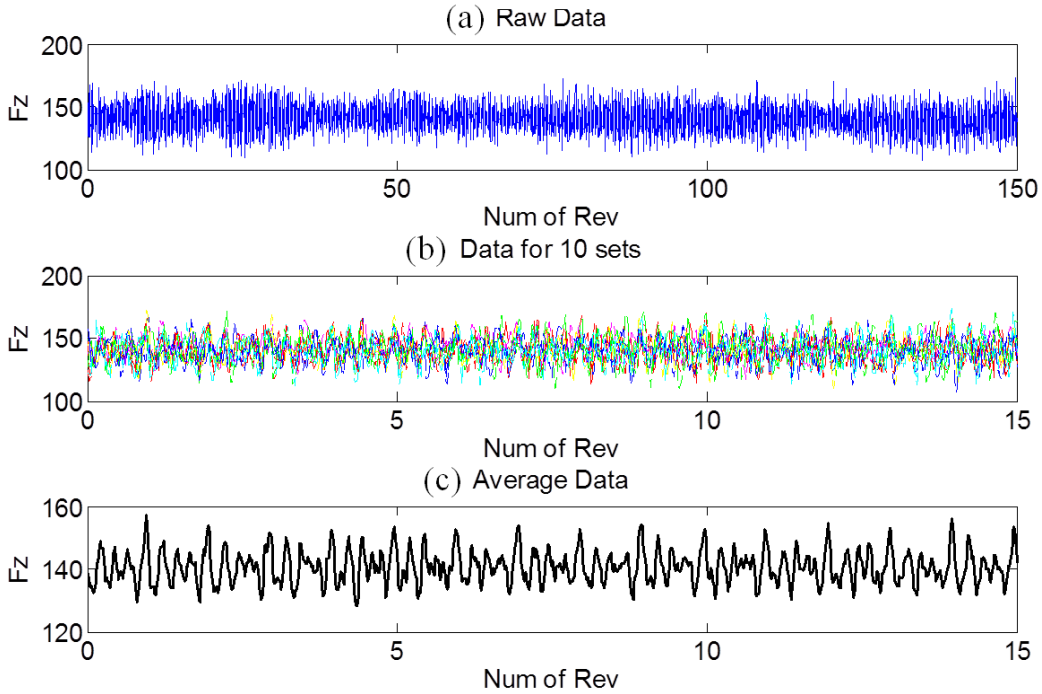

Figure F-7: Time Averaging of Data

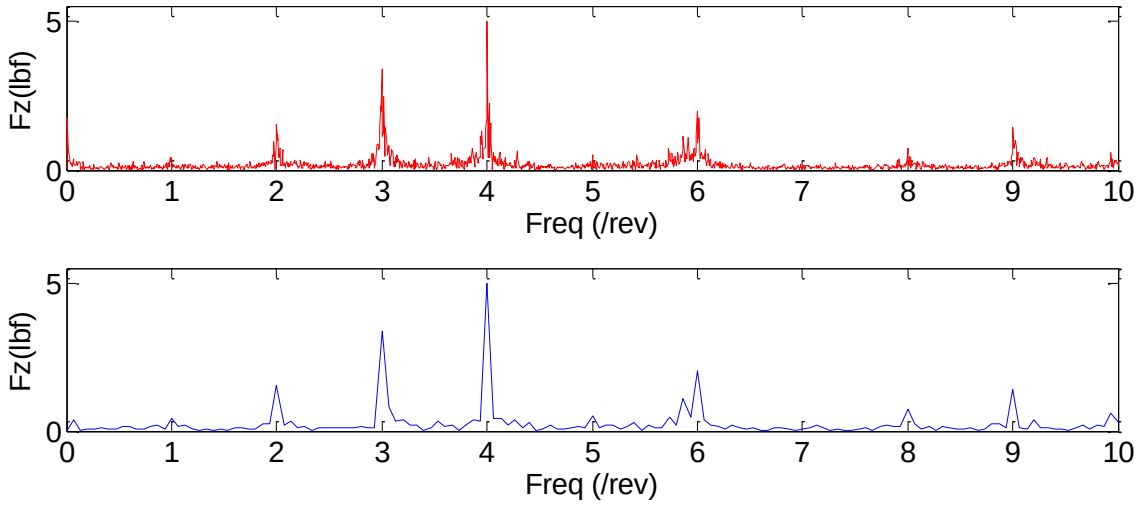

Figure F-8: Effect of Averaging on FFT

Step 4: System Identification

In step 3 of the analysis, the relation between an input variable and output response was obtained only at specific points in the design space. In order to obtain a transfer function between the input variable and the response which can be used later for controls related studies, a frequency sweep analysis is required. The process of obtaining an empirical transfer function estimate (ETFE) using the frequency sweep analysis is described below.

An empirical transfer function is the ratio of the FFT of the output signal to the FFT of input signal. As observed earlier, the response obtained from the test stand includes large noise and hence the ratio was also dominated by noise and thus, not very accurate. In a typical frequency sweep test, the frequency of the actuation voltage provided to the actuator was varied from 20Hz (1.33/rev) to 105Hz (7/rev) in a period of 10 seconds (one chirp) at constant voltage amplitude ($800V_{p\text{-}p}$ with an offset of 400V). After a gap of 2 seconds, the sine sweep signal was repeated again and 3 sets of data were obtained.

(Ideally, 10 sets of data would be more suitable to get a cleaner response, however in the current tests it was observed that the flap deflection was starting to reduce after the third repetition.) The collection of chirps was averaged in the frequency domain using the cross and auto spectrum to eliminate some of the noise.

If the Fourier transform of the output and input signal are given by $Y(f)$ and $U(f)$, respectively, then the averaged cross spectrum is given by:

$$\hat{\phi}_{yu} = \frac{1}{N}\sum_{i=1}^{N} Y_i(f)U_i^*(f)$$

where, $U_i^*(f)$ is the complex conjugate of the control signal, and N is the total number of chirps (N= 3 in this case). Similarly, the auto spectrum of the input is given by:

$$\hat{\phi}_{uu} = \frac{1}{N}\sum_{i=1}^{N} U_i(f)U_i^*(f)$$

Using these two spectrums, the average transfer function can be written as:

$$\bar{G}_1(f) = \frac{\hat{\phi}_{yu}}{\hat{\phi}_{uu}}.$$

F.3 Sample Results

Here some sample results obtained from the spin test are shown for the purpose of demonstration. After the blades were installed on the spin test stand, a number of tests were carried out during the course of one year in trying to remove the noise in the signal, improve the flap deflection at higher RPM, to obtain repetitive data, etc. The results presented here highlight the issues faced during the testing of blade with dual active flaps. In this section, the results are presented for the baseline case (Base-1 and Base-2 conducted at two different times) and Case 1 and Case 5 listed in Table F-5. As described

earlier, in Case 1, both the flaps were actuated at 2/rev frequency while in Case 5, flaps were actuated at 3/rev frequency. In both the cases, the phase difference is zero degree. It should be noted that all these tests were conducted on the same day.

Table F-6: Mean value of Flap Deflection

	$\delta_{2,mean}$ (deg)
Base-1	-0.72
Base-2	-0.67
Case 1	0.95
Case 5	1.09

The mean values of flap deflection for the baseline cases and for the cases with flap oscillation are shown in Table F-6. For the baseline cases, the mean value of flap deflection was set to 0 deg (approximately) at 100RPM by varying the DC voltage given to the actuator and observing the realtime output shown by the data acquisition system. Next the RPM was slowly increased to 900 and the flap deflection was recorded in the steady state condition. For the cases with flap oscillation, a fixed input voltage of 800Vp-p with an offset of 400V was provided to maximize the amplitude of flap deflection. As a result of this, there is a difference in the mean value of flap deflection for the baseline cases and the cases with flap oscillation. The FFT of the flap deflection response for both the flaps for Case 1 and Case 5 is shown in Figure F-9. For each of the cases, the FFT shows peak at the actuation frequency, as expected. The amplitude of flap deflection is higher for Flap 2 for the results shown here. In general, this trend is not consistent and it depends on the actuation frequency and the initial prestress in the flaps during the installation.

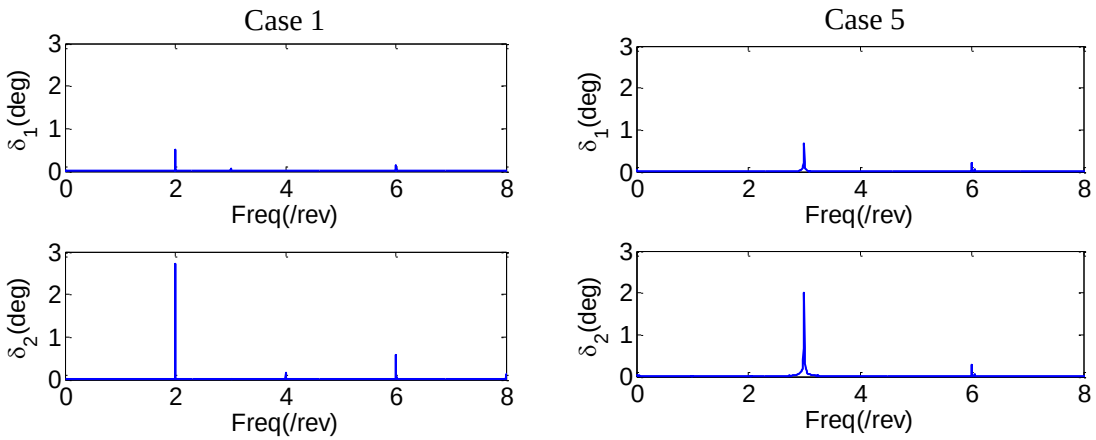

Figure F-9: FFT of the Flap Deflection

For the purpose of smoothing the data and to remove noise from the signal, the data collected for 150 revolutions was split into 10 sets and averaged. Figure F-10 shows the variation of mean value of the loads for each of these 10 sets for the baseline case. For all the components, the results show noticeable variation in the mean value, which is unexpected. The periodic variation in the result indicates the presence of some lower order harmonics in the system.

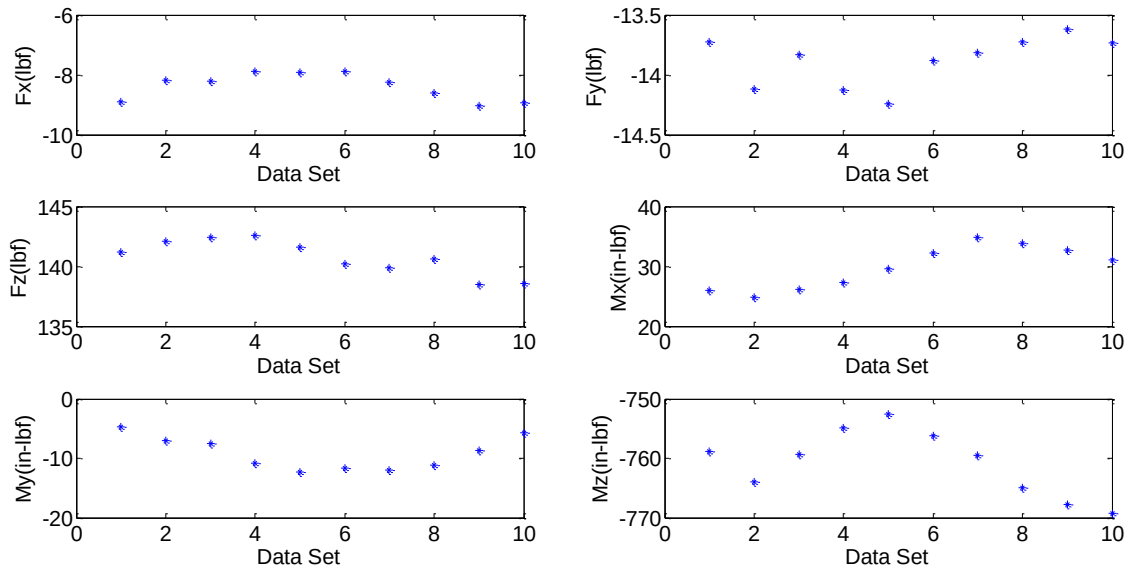

Figure F-10: Variation of Mean Loads for Base1

The variation in the mean value of the loads for the two baseline cases and the cases with flap oscillation is shown in Figure F-11. The error bars for these results were

obtained by using the data shown in Figure F-10. For the results shown here, no trend can be seen between the mean loads obtained for the baseline cases and the cases with flap oscillations. For some of the components, the variation between the baseline cases is higher than that between the baseline and flap actuated cases.

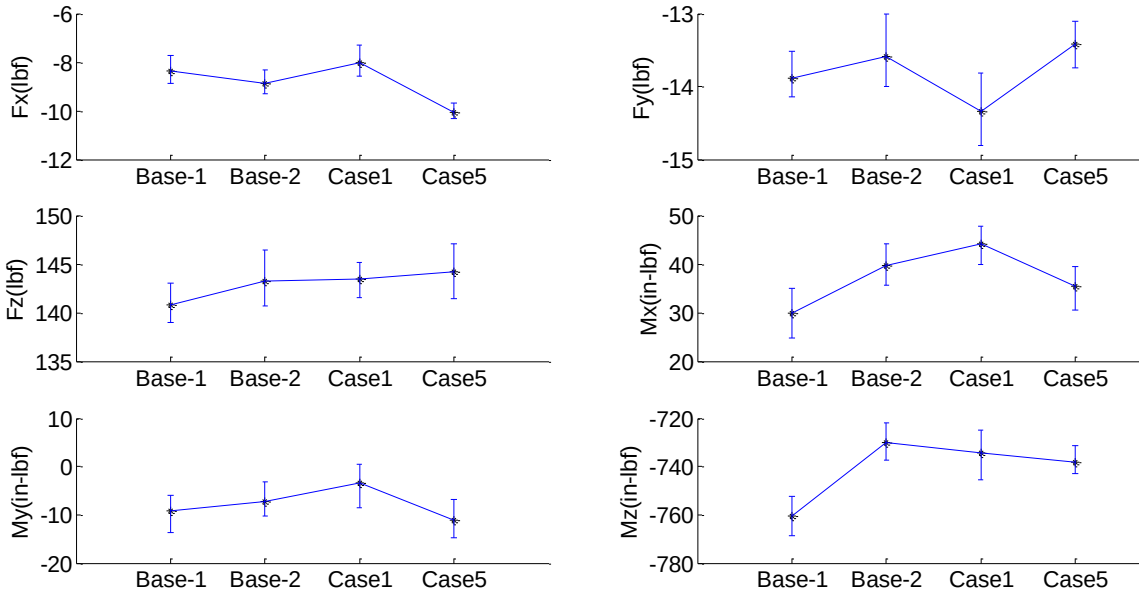

Figure F-11: Variation of Mean Loads for Different Cases

Next FFT is performed on the steady state response obtained for the baseline cases. Since the tests were performed in hover condition for similar rotor blades (although, only one of the blades has flaps, they are designed to be structurally and aerodynamically similar when the flaps are not oscillating), ideally there should not be any vibratory loads in F_z and M_z component. However, due to closed boundaries around the spin test stand and ground effects, baseline cases show significant vibration. Thus, these vibratory loads observed for the baseline cases represent noise in the system. (If the numerical simulations include the effect of walls and boundaries around the spin test stand, it is possible to capture these vibratory loads, as it was demonstrated by the research performed at Georgia Tech). Vibratory loads at different frequency observed for the F_z

and M_z components for both the baseline cases are shown in Figure F-12 and Figure F-13, respectively.

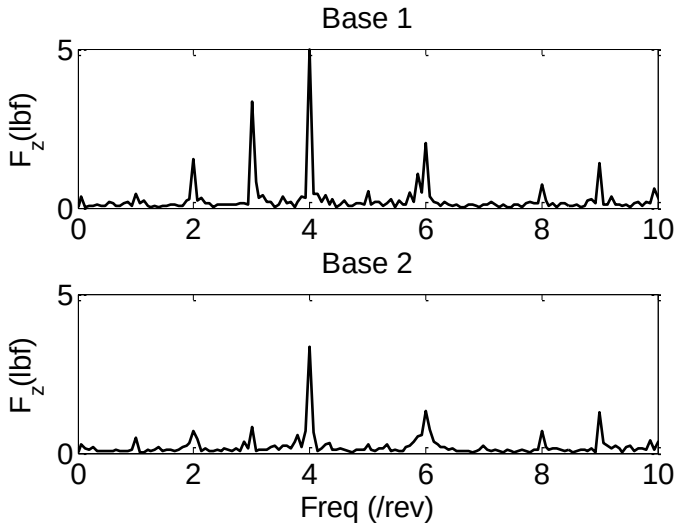

Figure F-12: FFT of F_z for the Baseline Cases

Results for F_z show most dominant amplitude at 4/rev frequency. In case of "Base 1" results, the contribution to vibratory loads from other harmonics is also significant. For these two cases, the average amplitude of vibratory loads is approximately 3.2% of the mean loads. Also, the hub loads show very small contribution from 1/rev frequency, which implies that the blades are dynamically balanced.

The results obtained for M_z component shows large vibratory loads at 1/rev frequency, which are unexpected since the blades are balanced. Besides the dominant 1/rev component, there are small contributions from 2/rev and 6/rev component for both the baseline cases. The amplitude of vibratory load for M_z component is approximately 4.1% of the mean M_z load.

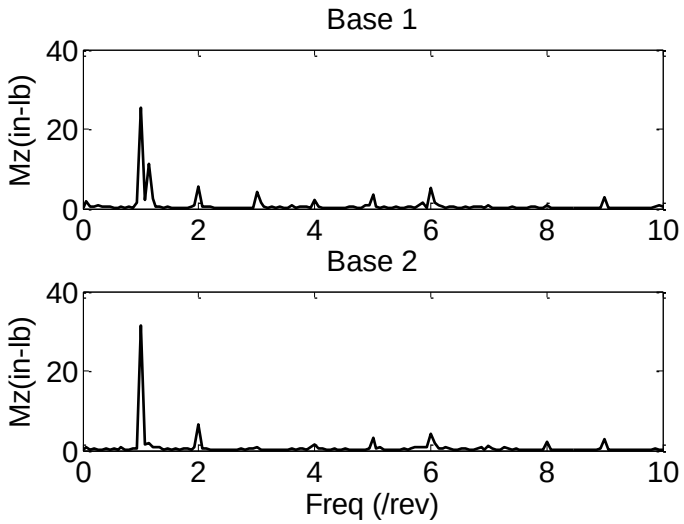

Figure F-13: FFT of M_z for the Baseline Cases

In order to capture the effects of flap actuation, the amplitude of vibratory loads obtained for the flap actuated cases is subtracted from the amplitude of vibratory loads obtained for the baseline cases. For the results presented here, the difference is taken with both the baseline cases shown in previous results. The difference in amplitude obtained for the F_z component is shown in Figure F-14. The results obtained vary depending upon the baseline case which was subtracted. When the result obtained for the Base 1 case was subtracted, the results showed increase in vibration for 3/rev frequency loads and decrease in vibration for 4/rev frequency loads, for both Case 1 and Case 5. Similarly, when the amplitude corresponding to Base 2 case was subtracted, results showed large increase in vibration at 3/rev frequency, for both Case 1 and case 5. Thus, the results show that the trend observed for the difference of amplitude from the FFT analysis is independent of the actuation frequency and the amplitude of vibration observed is within the noise level obtained for the system.

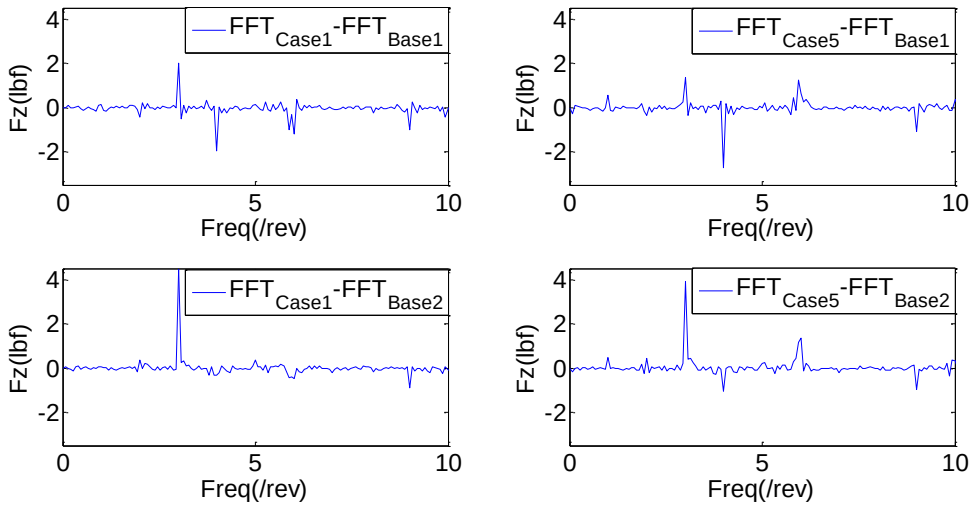

Figure F-14: Difference in FFT for F_z Component

Figure F-15 shows the difference in vibration level between the baseline cases and the flap actuated cases for M_z component. In all the cases, there is an increase in the amplitude of M_z loads at 1/rev frequency. Other than that, small increase is observed for 2/rev frequency and 3/rev frequency loads. However, the difference in amplitudes for these frequencies is much smaller than that observed for the 1/rev frequency. Thus, the experimental results show that flap actuation leads to an increase in M_z loads at 1/rev frequency independent of the actuation frequency.

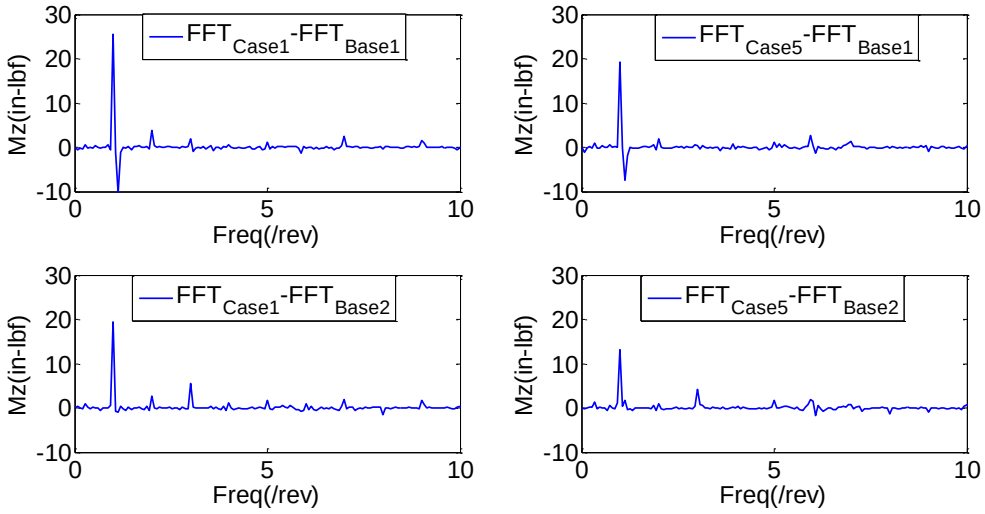

Figure F-15: Difference in FFT for M_z component

F.4 Comparison with RCAS

For numerical analysis, a model of the blade with dual active flaps was implemented in RCAS. As in the experimental setup, RCAS model included active flaps on only one of the two blades. The structural analysis was performed using the non-linear beam model while the aerodynamic analysis was performed using the Peters flexible airfoil theory. The analysis also included dynamic inflow model. For RCAS analysis, trim option was used where F_z force at the hub was trimmed to the average thrust obtained in the experiments. The aerodynamic analysis also required table-lookup for aerodynamic coefficients at different flap deflections. This table was generated using X-FOIL results. The table obtained was also updated with the results obtained using CFD analysis for the purpose of comparison.

The variation of mean F_z and M_z for all the cases is shown in Figure F-16, and the results obtained are compared with the RCAS results. Since trim analysis is performed, the thrust predicted by RCAS is same for all the cases. The torque predicted by RCAS is less than the experimentally obtained torque by atleast 25%.

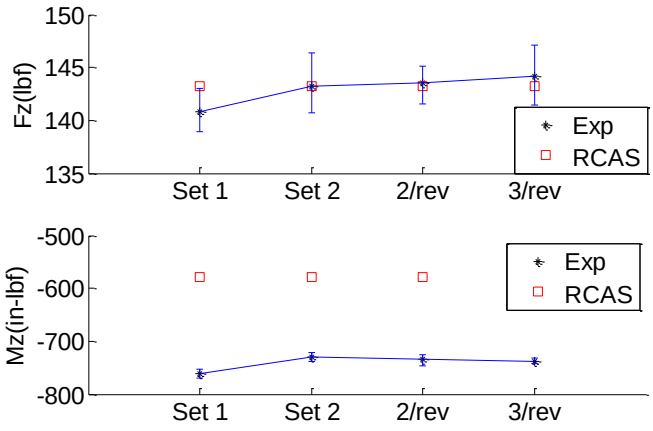

Figure F-16: Comparison for Mean Loads

The results for Case 1 (2/rev actuation frequency) for F_z component are shown in Figure F-17. The RCAS results show vibratory loads at the actuation frequency only, that is, at the 2/rev frequency. The amplitude of vibratory loads predicted by RCAS is of the same order as the loads observed in experiments. However, the experimental results show vibratory loads at 3/rev frequency. A similar trend is observed for Case 5 (3/rev actuation frequency) (Figure F-18) where the RCAS results show vibratory loads at the actuation frequency only, while the experimental results show increase in vibration for loads at 3/rev and 6/rev frequency and decrease in vibratory loads at 4/rev frequency. The amount of increase and decrease in the amplitude depends upon the baseline case selected for the analysis.

Similarly, in case of M_z component, the RCAS results in Figure F-19 and Figure F-20 show vibratory loads at the actuation frequency only and the amplitude of vibratory loads predicted by RCAS is of the same order of magnitude as the 1/rev loads observed in experiments.

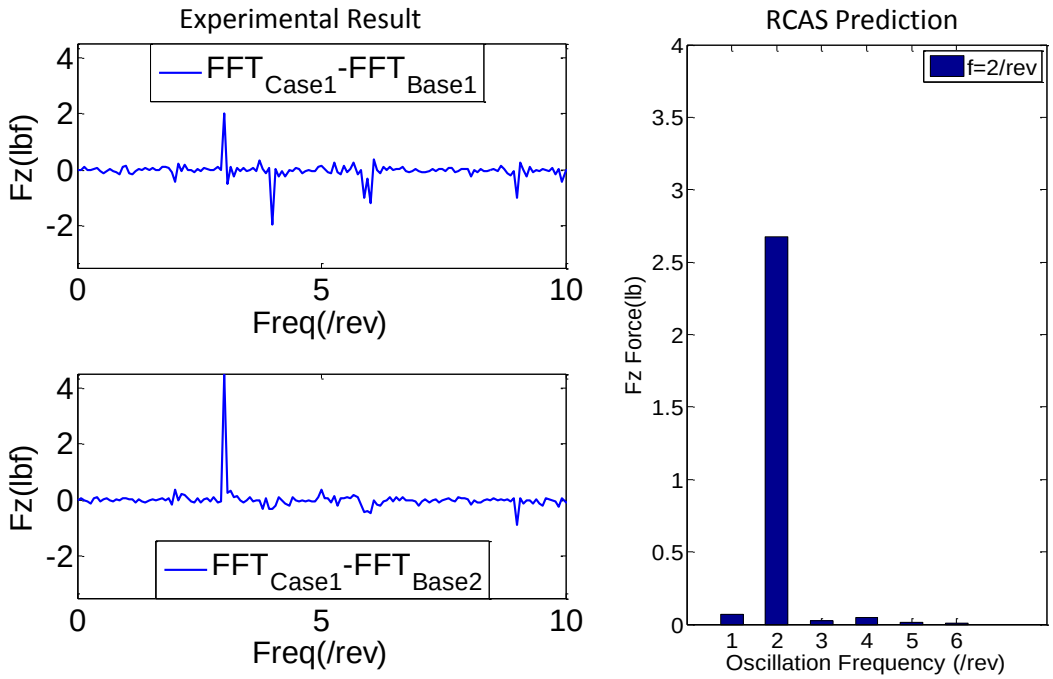

Figure F-17: Comparison for F_z component for Case 1

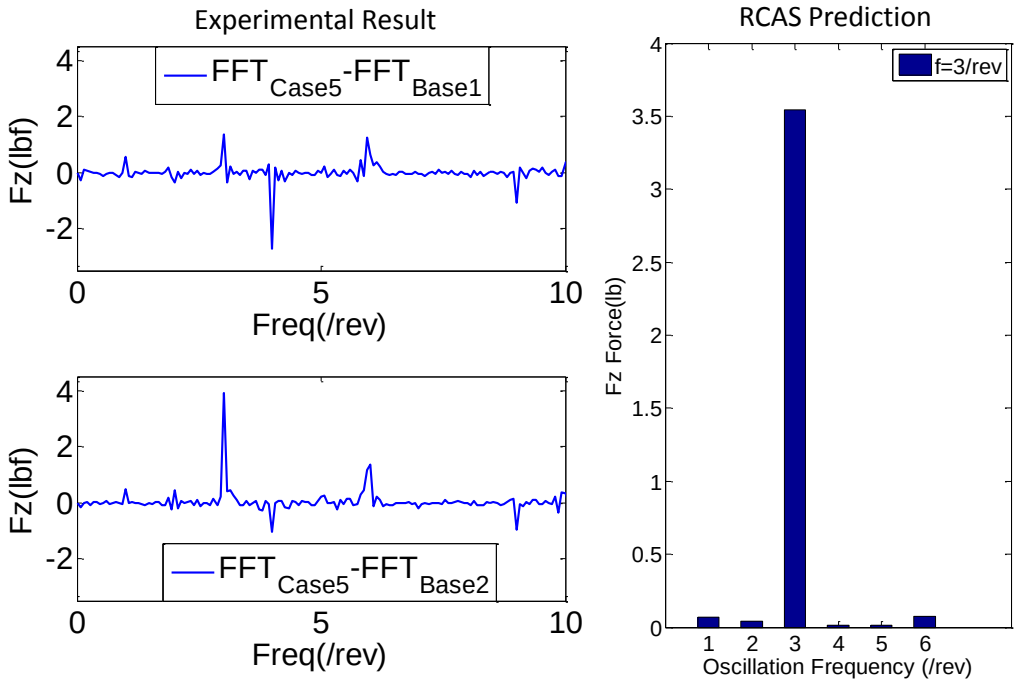

Figure F-18: Comparison for F_z component for Case 5

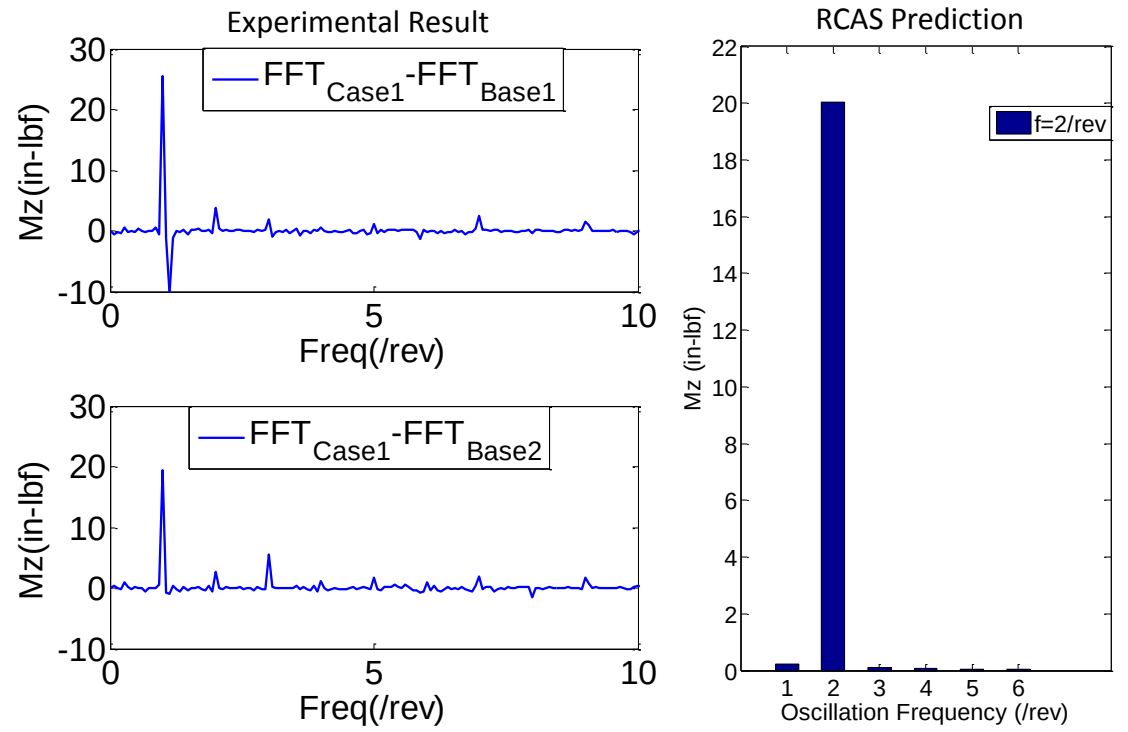

Figure F-19: Comparison for M_z component for Case 1

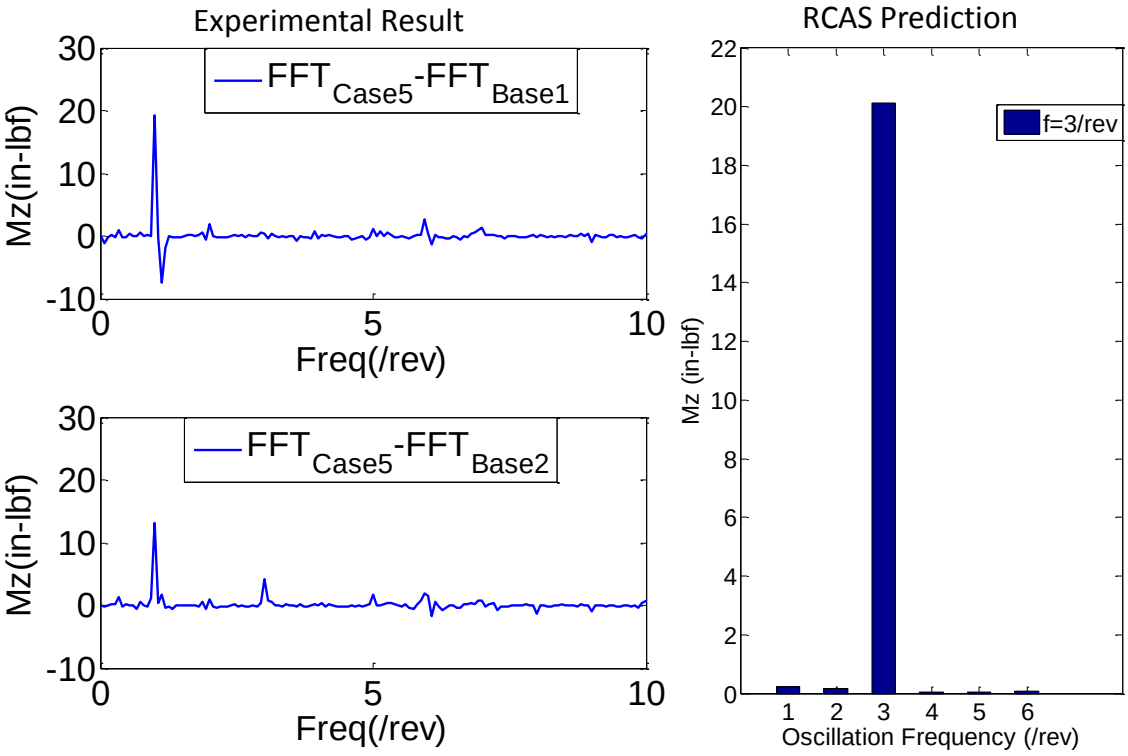

Figure F-20: Comparison for M_z component for Case 5

As described earlier, a frequency sweep analysis was performed to determine the transfer function between the actuation voltage and different responses. For these tests, the frequency of flap actuation was varied from 20 to 105 Hz in an interval of 10 seconds while the amplitude of input voltage was held constant and three sets of data were collected. Here four different cases were considered, namely, a) both flaps oscillating in phase, b) both flaps oscillating out of phase, c) only flap 1 was actuated and d) only flap 2 was actuated.

The transfer function obtained between the input voltage and the flap deflection for Flap 1 and Flap 2 is shown in Figure F-21 and Figure F-22, respectively. In both the cases, the results show the trend observed earlier where the amplitude of flap oscillation increased with an increase in the actuation frequency. The results obtained for Flap 2 are more consistent while the results for Flap 1 vary significantly depending upon the case. Also, there is very good coherence throughout the range of actuation frequency indicating good signal quality from the flap sensors. The variation of phase is similar for Flap 1 and Flap 2 for all the cases and the mean value of phase angle is close to 90 deg.

The transfer function obtained for the hub loads F_z and M_z is shown in Figure F-23 and Figure F-24, respectively. Unlike the results obtained from the flap deflection sensor, the results obtained from the load cell show significant amount of noise in the system due to which the coherence for both these transfer functions is very poor. The F_z component shows high amplitude at 3/rev frequency only, as it was observed in the experimental results obtained earlier.

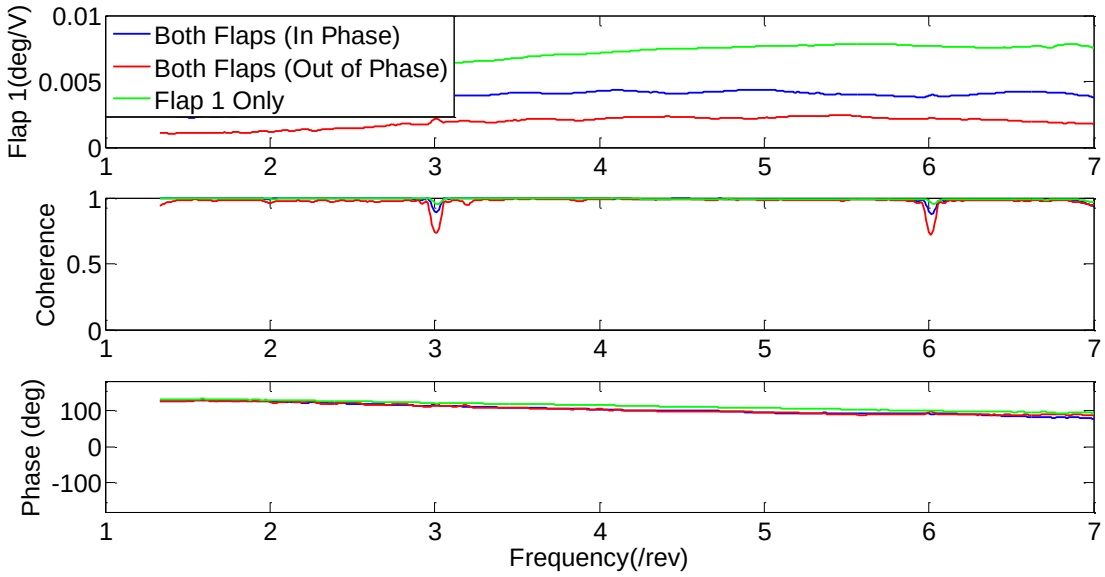

Figure F-21: Flap Deflection to Input Voltage Transfer Function for Flap 1

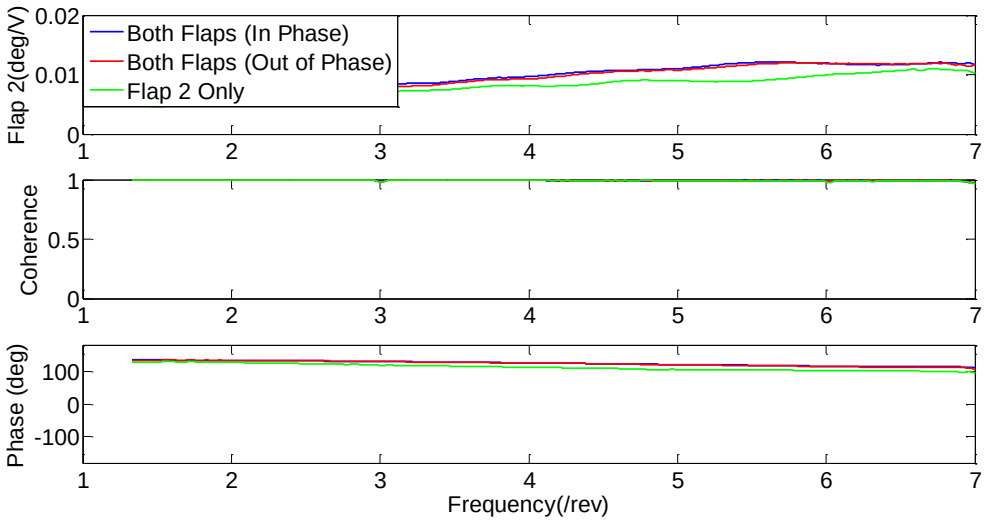

Figure F-22: Flap Deflection to Input Voltage Transfer Function for Flap 2

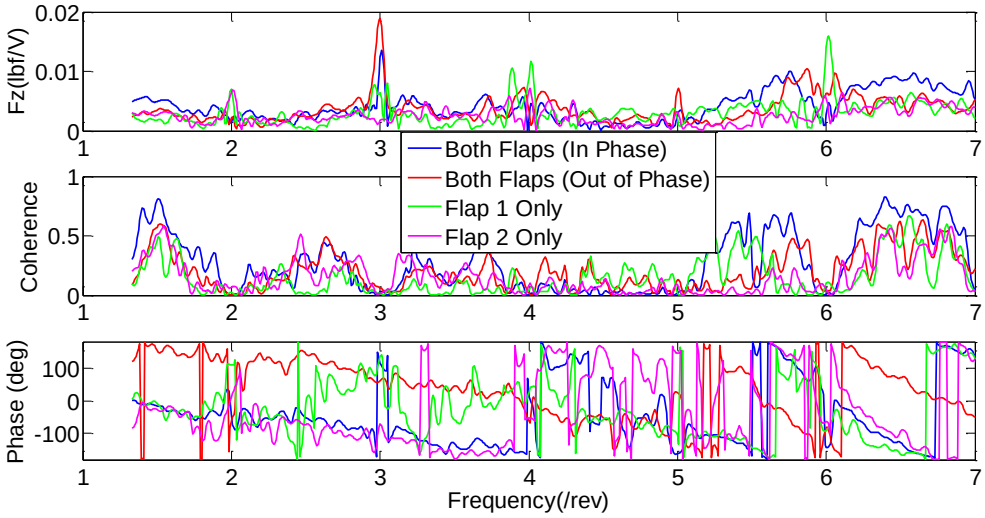

Figure F-23: Hub Thrust (F_z) to Input Voltage Transfer Function

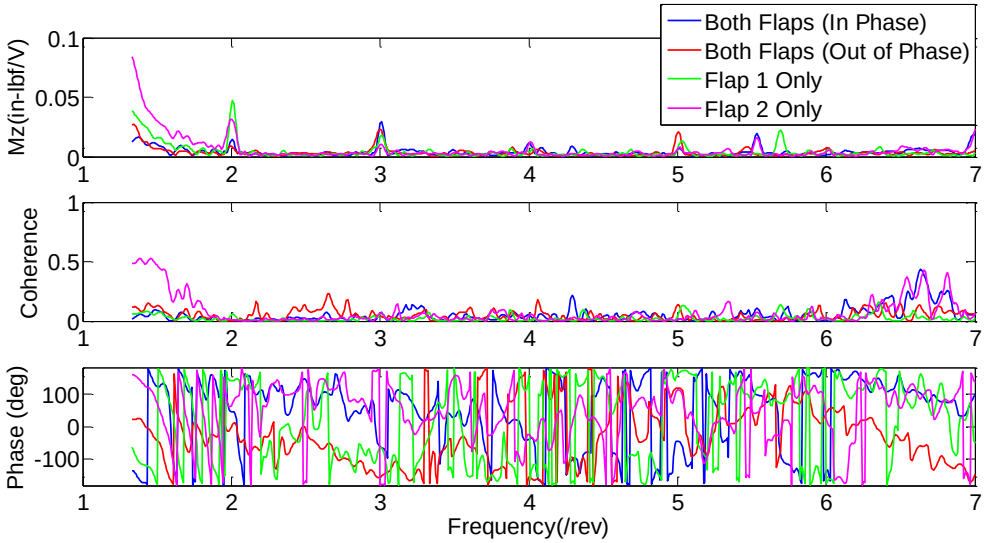

Figure F-24: Hub Torque (M_z) to Input Voltage Transfer Function

F.5 Conclusion

Finally, a summary of different issues experienced in the experimental analysis of dual active flaps is provided along with possible corrections that can be made for future experiments. The issues are listed in the order of their importance.

Issue 1: Baseline vibration in hub loads measurement

Since the tests were done in hover condition, it was expected that the vibratory loads in the absence of any flap motion (baseline vibratory loads) would be very small. However, during the experiments, it was noticed that the baseline vibratory loads were of the same order of magnitude as the expected response loads due to flap motion (for a torsionally stiff blade fabricated for these experiments).

Possible Causes

a) *Ground Effect*: The tests described in this thesis were conducted in the spin test stand located in Aerospace Department at the University of Michigan. The rotor blades have a diameter of 10ft and the blades are located at a height of 7.5ft above the ground. The standard recommended distance between the blades in spin test stand and ground plane in order to avoid ground effect is around 1.5D (15ft in the current setup). As a result of close proximity of the blades to the ground, the blades experience large unsteady motion of air. Even though the setup includes a bell mouth around the spin test stand and a wire mesh above it in order to smoothen the flow coming on to the rotor blade, hub loads still showed sufficient vibratory amplitude.

b) *Proximity to walls around the room*: As mentioned earlier, the spin test stand is enclosed in a closed room. Hence, there is a significant amount of reflection of the vortices generated by blade motion from the four walls enclosing the room. Preliminary analysis performed at GT using CFD (see Figure F-25) showed that the 4/rev vibratory loads are generated due to walls around the spin test stand. The amplitude of vibratory load corresponding to 4/rev frequency shown in Figure

F-25 ($\Delta C_T \sim 0.075x10^{-3}$, that is, $\Delta F_Z \sim 7.1$ lbf) is very close to the value obtained experimentally at 1336 RPM ($\Delta F_Z \sim 6.0$ lbf).

Corrections:

1) Increasing the height of the spin test stand above the ground can result in some improvement in the baseline vibratory loads. The increase in vibratory loads at the hub due to proximity to the ground plane can be investigated in more details using RCAS.
2) The four walls around the room lead to the recirculation of air inside the room. It is difficult to quantify the effect of these four walls using aeroelastic codes like RCAS and AVINOR. However, the effect of walls can be determined using CFD as demonstrated in the results shown in Figure F-25. Thus, in order to minimize these effects, it is important to perform these experiments in open conditions or in a wide wind tunnel. However, before performing any experiment, it is always useful to quantify the baseline vibration using CFD and experimental analysis.
3) One way to reduce the recirculation of air in the test stand room is to keep both the doors open in spin test stand room. (provided it is safe to do it)

Cost Analysis

The main sources of vibration are the four walls enclosing the spin test stand and proximity to ground. Hence moving the spin test stand to a new facility would be useful. However, before finalizing the facility, detailed analysis need to be conducted to determine baseline vibration in the test facility and expected vibratory loads from the flap motion. In the current setup, the only possible way to minimize baseline vibration is to perform the experiment with open doors. Increasing the height of the spin test stand

would also be useful in minimizing the baseline vibration. For increasing the height, using a long shaft between motor and blade would be more useful than raising the height of the entire test stand.

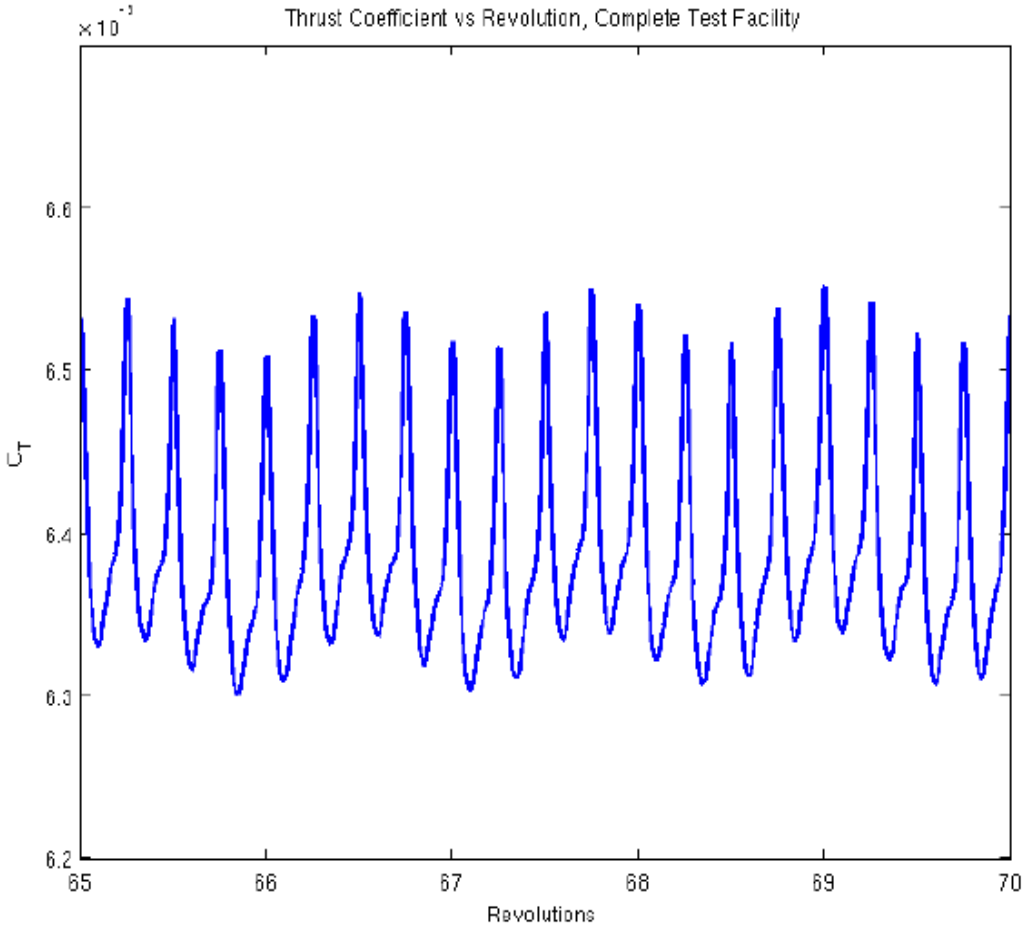

Figure F-25: Variation of C_T for Baseline Conditions [177]

Issue 2: Poor performance of flaps (flap deflection) at high RPM

It was observed during the experiments that the flap deflections decrease significantly (amplitude less than 0.5 deg) when the RPM is above 1000.

Possible causes:

a) Gaps between the airfoil and flap

The flap was designed to have a certain gap between the main blade and the leading edge of the flap in the chordwise direction. However during the manufacturing process, there was small variation in size of these gaps. Also, the analysis performed in CFD to determine the flap-hinge location did not account for gaps along the spanwise direction. Since the flap supports are installed at the ends of the flap, there is some gap between the main blade and the flap in the spanwise direction. Even though an attempt was made to cover up these gaps using E-Glass tabs, it was not exactly flush with the flap. As a result of this, there was a reduction in the flap effectiveness and an increase in the additional aerodynamic forces acting on the flaps which increase with RPM. This can result in a decrease in flap deflection obtained.

b) Large friction at high RPM

During the design process, special care was taken to reduce friction from the flap actuation mechanism. All the supporting parts were fabricated with steel to ensure that there is very little compliance in the system; and flap and its supports can sustain high centrifugal force. However, the reduction in flap deflection indicates that there is a large increase in friction with the increase in RPM (besides the increase in aerodynamic forces against which the flap needs to move).

Correction:

a) In the current setup, it would be difficult to cover up the gaps along the spanwise direction. However, for future flap installation, it would be more suitable to have the flap supported in the middle so that gaps at the end can be minimized.

b) Also, it is important to account for the effect of gaps (in both spanwise and chordwise directions) on the unsteady loads acting on flaps and on reduction in the flap effectiveness. This requires detailed CFD analysis of the flap region in rotating conditions.

c) The use of bearing in the clevis region would be useful for reducing some of the friction effects. However, it was not possible to include the bearing in the current design due to limited space available and size constraint imposed by maximum length of moment arm.

Cost Analysis:

In the short term (1-2 weeks), a better way to cover the gaps in both spanwise and chordwise direction can be designed without getting in contact with flaps. However, before going ahead with that, detailed aerodynamic analysis needs to be performed in order to determine effect of gap size on flap effectiveness. For future active flap experiments, the flap hinge mechanism needs to be redesigned to reduce gaps and include ball bearings in the clevis. In the current flap-actuation mechanism designed, many constraints were imposed due to the requirement of prestress for piezoelectric actuator that was generated using the prestress wire in active flap. However, other actuator available (like Cedrat) can generate required prestress from the actuator frame and hence do not require any external mechanism to generate prestress.

Issue 3: Very small effect of flap motion on vibratory loads at the hub

Flap oscillations at different actuation frequencies led to very small increase in the vibratory loads at the hub at that frequency.

Possible Cause

a) Large torsion stiffness of the blade

The main aim of the experimental analysis was to determine the unsteady *aerodynamic* drag associated with the flap motion. In order to minimize the contribution from blade elasticity to loads generated at the hub (aeroelastic loads), the active blade was designed to be stiff in torsion. The blade designed had a torsional stiffness of 5.88/rev at 1336 RPM. Due to the reduction in flap motion at high RPM (**Issue 1**), the operating RPM was changed to 900 in order to ensure sufficient flap deflection. However, decreasing the RPM caused the blade torsion frequency to become 8.88/rev. Thus, due to the large torsional stiffness of the blade, the twisting moment generated by the active flaps was not sufficient to twist the blade and thereby generate aerodynamic loads.

b) Gap between the airfoil and flap in the spanwise direction.

As discussed previously, the 3D air flow over the gaps can result in reduction in the flap effectiveness. The current 2D codes can only account for gaps in the chordwise directions.

c) Walls enclosing the spin test stand

The spin test stand used for experiments is enclosed inside a room and as a result, there is recirculation of air after reflection from the walls. In the CFD study at GT[177], it was shown that there is approximately 22% reduction in C_T because of the shroud and walls around the spin test stand. The effect of walls on the vibratory loads generated at the hub due to flap oscillations is yet to be quantified.

Correction:

a) Reducing blade torsional stiffness at the root: This can be achieved by using a torsional spring/coupling between the blade root and root attachment on the test stand. This might result in a small increase in radius of the blade. However, the increase in loads using this technique will be due to aeroelastic effects and might be detrimental to original goal of the experiments.

Cost Analysis:

In short term, a torsional spring can be used to reduce torsional stiffness of the blade locally at root. However, for future active flap experiments, blades need to be designed appropriately.

Issue 4: Large variability in results (for similar flap deflection and operating RPM)

Vibratory hub loads generated at the rotor hub showed significant variation in the mean value and amplitude of vibration, even during a single run. During the tests, the data was collected for 150 revolutions in steady state condition at a sampling rate of 1000 samples/sec. In order to analyze the data, this data was split in to 10 sets of 15 revolutions each. The mean value and per rev harmonic loads for each of these intervals were obtained to determine the fluctuations in the test stand hub loads. Results obtained for the mean value of loads indicated the presence of lower order harmonics (less than 1 Hz frequency) in the hub loads.

Possible Causes:

1) This can be attributed to the presence of ground and walls around the spin test stand. It may be possible to capture some of these effects with CFD analysis; however, the analysis needs to be runs for atleast 200 or more revolutions to capture these effects.

Correction:

1) This can also be fixed by using a wide wind tunnel or by performing the tests in open conditions.

Issue 5: Uncontrollable flap deflections

During the experimental runs for the baseline case, the flap position was adjusted to 0 deg at 100RPM and then the RPM was increased to operating RPM (900 RPM). While increasing the RPM, there was small variation in the flap position (between ±1 deg). For the cases where flap was actuated, the input voltage was fixed to 800 V_{p-p} with an offset of 400V in order to maximize the amplitude of flap oscillation. However, due to this input voltage, it was difficult to control the mean value of flap oscillation.

Possible Causes:

a) Due to increase in dynamic pressure with increase in RPM, the aerodynamic forces acting on the flap hinge change. As a result of this, the mean value of the flap position changes with an increase in RPM for the baseline cases.

b) A significant amount of static friction was observed in the flap hinge mechanism. With the same amount of prestress applied (by adjusting the clevis), different flap deflections were obtained (variation of 1-2 deg). Also, the waveform generator used for generating the input signal for active flaps produced small spikes. These spikes also resulted in shift in the mean position of the flap.

c) The range for voltage supply that can be given to the X-frame actuator was fixed by the manufacturer (from 0V to 800V). Thus, in order to maximize the amplitude of flap deflection, complete range of voltage supply had to be utilized. If offset

voltage was varied to adjust the mean position of flap oscillation, it would have resulted in reduction in the amplitude of flap oscillation.

Corrections:

1) Feedback control for controlling flap deflection: In order to accurately control the flap deflection during the tests, a feedback loop is required. In the recent tests with active flaps (at Boeing and Sikorsky), a controller based on HHC algorithm is used to control the flap position.
2) There is a need to minimize static friction in the flap hinge mechanism by appropriate lubrication.
3) There is a need to redesign the flap-actuation mechanism such that higher flap deflection could be obtained. This would allow the controller to control both the mean value and amplitude of flap deflection.

Cost Analysis:

Developing a feedback controller with basic PID approach would be useful in controlling the flap deflection when the flaps are not oscillating. Also, an advanced controller based on HHC would be required to control the flap deflection in rotating conditions.

Issue 6: Decrease in flap deflection with time

Flap deflection was observed to reduce with time during the experimental runs. At full RPM, sufficient flap deflection could only be obtained for less than 2 minutes. After each run, rotor had to be stopped and lubrication had to be applied. In some cases, flap had to be removed from the blade and installed again.

Possible Cause:

a) Loss of lubrication: The increase in friction force can also occur due to the loss of lubrication which occurs because of large centrifugal force.
b) Small deformation of flap supports: The large centrifugal force acting on the flap, can lead to small deformation of the flaps and its support over a period of time. This might cause some components of the flap and its support to get in contact with non-moving parts and rub against each other. This can result in significant increase in friction and reduce the flap deflection.

Correction:

1) Lubrication: During the tests, it was observed that using lubrication after every run helped in reducing the friction effects.
2) Reinstallation of the flaps on active blade: The flap lubrication was effective only for 3-4 runs and after that; even lubrication did not produce any improvement in the flap deflection. In this case, flaps had to be removed from the setup and reinstalled again. This helped in recovering the flap deflection.
3) The need for lubrication needs to be minimized in future tests to ensure longer test time by reducing the number of moving parts and by use of elastic hinges.

Issue 7: Unexpected large 1/rev component in M_z

The experimental results obtained show significant 1/rev component in M_z. Also, this component increased when flaps were oscillated. The amplitude of 1/rev component was larger when the tests were conducted at 2 deg collective setting as compared to tests conducted at 6.5 deg collective.

Issue 8: Decrease in hub load response with increase in flap actuation frequency

Computational results obtained from RCAS and AVINOR showed an increase in vibratory loads with increase in the actuation frequency till it approaches the first torsion frequency. However, the experimental results obtained showed that flaps are effective in generating vibratory loads at the hub only when the actuation frequency is between 2/rev to 4/rev even though a higher amplitude of flap deflection is obtained at higher flap actuation frequencies.

REFERENCES

[1] A. C. Veca. "Vibration Effects on Helicopter Reliability and Maintainability." Sikorsky Aircraft Division, AD-766 307, April, 1973.

[2] R. Heffernan, D. Precetti and W. Johnson. "Vibration Analysis of the SA349/2 Helicopter." NASA, Technical Memorandum 102794, 1991.

[3] G. Reichert. "Helicopter Vibration Control: A survey." *Vertica*, Vol. 5, No. 1, 1981, pp. 1-20.

[4] O. Dieterich. "Application of Modern Control Technology for Advanced IBC Systems." *24th European Rotorcraft Forum*, Marseilles, France, 15-17 September, 1998.

[5] E. Breitbach and A. Buter. "The main Sources of Helicopter Vibration and Noise Emissions and Adaptive Concepts to reduce them." *Journal of Structural Control*, Vol. 3, No. 1-2, June, 1996, pp. 21-32.

[6] H. Strehlow, R. Mehlhose and P. Znika. "Passive and Active Vibration Control Activities in the German Helicopter Industry." *Aerospace Technology Exhibition and Conference (AEROTECH)*, Birmingham, 14-17 January, 1992.

[7] K. S. Brentner and F. Farassat. "Modeling Aerodynamically Generated Sound of Helicopter Rotors." *Progress in Aerospace Sciences*, Vol. 39, 2003, pp. 83-120.

[8] F. H. Schmitz. "Rotor Noise." *Aeroacoustics of Flight Vehicles, Theory and Practice - Vol 1*: Langley Research Center, 1995, pp. 65-49.

[9] B. Edwards and C. Cox. "Revolutionary Concepts for Helicopter Noise Reduction - S.I.L.E.N.T Program." NASA, CR-2002-211650, 2002.

[10] W. Gerstenberger. "The Rotary Round Table: Practical Aspects of Vibration Control." *Journal of the American Helicopter Society*, Vol. 2, No. 3, 1957, pp. 3-4.

[11] R. G. Loewy. "Helicopter Vibrations: A Technological Perspective." *Journal of American Helicopter Society*, Vol. 29, No. 4, 1984, pp. 4-30.

[12] R. L. Bielawa. "Analytical investigation of Helicopter Rotor Blade appended Aeroelastic devices." NASA, Technical Report 166525, 1984.

[13] P. Konstanzer, B. Enenkl, P.-A. Aubourg and P. Cranga. "Recent advances in Eurocopter's Passive and Active Vibration Control." *American Helicopter Society 64th Annual Forum*, Montreal, Canada, April 29-May 1, 2008.

[14] M.-N. H. Hamouda and G. A. Pierce. "Helicopter Vibration Suppression Using Simple Pendulum Absorbers on the Rotor Blade." *Journal of American Helicopter Society*, Vol. 29, No. 1, 1994, pp. 19-29.

[15] R. Ganguli. "Survey of Recent Developments in Rotorcraft Design Optimization." *Journal of Aircraft*, Vol. 41, No. 3, 2004, pp. 493-507.

[16] P. P. Friedmann. "Helicopter Vibration Reduction Using Structural Optimization with Aeroelastic/Multidisciplinary Constraints." *Journal of Aircraft*, Vol. 28, No. 1, 1991, pp. 8-21.

[17] R. Celi. "Recent Applications of Design Optimization to Rotorcraft - A survey." *Journal of Aircraft*, Vol. 36, No. 1, 1999, pp. 176-189.

[18] P. P. Friedmann and T. A. Millot. "Vibration Reduction in Rotorcraft Using Active Control: A Comparison of various Approaches." *Journal of Guidance, Control and Dynamics*, Vol. 18, No. 4, 1995, pp. 664-673.

[19] C. Kessler. "Active Rotor Control for Helicopters: Motivation and Survey on Higher Harmonic Control." *CEAS Aeronautical Journal*, Vol. 1, No. 1, 2011, pp. 3-22.

[20] C. Kessler. "Active Rotor Control for Helicopters: Individual Blade Control and Swashplateless Rotor Designs." *CEAS Aeronautical Journal*, Vol. 1, No. 1-4, 2011, pp. 23-54.

[21] S. P. King and A. E. Staple. "Minimization of Helicopter Vibration Through Active Control of Structural Response." *Rotorcraft Design Operations*, Vol. CP-423, AGARD, October, 1986.

[22] J. T. Pearson, R. M. Goodall and I. Lyndon. "Active Control of Helicopter Vibration." *Computing and Control Engineering Journal*, Vol. 5, 1994, pp. 277-284.

[23] R. C. Cribbs, P. P. Friedmann and T. Chiu. "Coupled Helicopter Rotor/Flexible Fuselage Aeroelastic Model for Control of Structural Response." *AIAA Journal*, Vol. 38, No. 10, 2000, pp. 1777-1787.

[24] A. Z. Lemnios and A. F. Smith. "An Analytical Evaluation of the Controllable Twist Rotor Performance." Kaman Aerospace Corporation, USAAMRDL Technical Report 72-16, May, 1972.

[25] A. Z. Lemnios. "Wind Tunnel Investigation of the Controllable Twist Rotor Performance and Dynamic Behavior." Kaman Aerospace Corporation, USAAMRDL Technical Report 77-10, 1977.

[26] J. Shaw. "Higher Harmonic Blade pitch Control for Helicopter Vibration Reduction: A Feasibility Study." MIT, ASRL-TR-150-1, 1968.

[27] J. Shaw and N. Albion. "Active Control of the Helicopter Rotor for Vibration Reduction." *Journal of American Helicopter Society*, Vol. 26, No. 3, 1981, pp. 32-39.

[28] K. Nguyen and I. Chopra. "Effects of Higher Harmonic Control on Rotor Performance and Control Loads " *Journal of Aircraft*, Vol. 29 No. 3, 1992, pp. 336-342.

[29] E. R. Woods, R. W. Powers, J. H. Cline and C. E. Hammond. "On Developing and Flight Testing a Higher Harmonic Control System " *Journal of American Helicopter Society*, Vol. 30, No. 1, 1985, pp. 223-240.

[30] C. E. Hammond. "Wind Tunnel Results Showing Rotor Vibratory Loads Reduction Using Higher Harmonic Blade Pitch " *Journal of American Helicopter Society*, Vol. 28, No. 1, 1983, pp. 10-15.

[31] K. Nguyen, M. Betzina and C. Kitaplioglu. "Full-Scale Demonstration of Higher Harmonic Control for Noise and Vibration Reduction on the XV-15 Rotor." *American Helicopter Society 56th Annual Forum*, Virginia Beach, Virginia, May 2-4, 2000.

[32] J. Shaw, N. Albion, E. J. Hanker and R. S. Teal. "Higher Harmonic Control: Wind Tunnel Demonstration of Fully Effective Vibratory Hub Force Suppression." *Journal of American Helicopter Society*, Vol. 34, No. 1, 1989, pp. 14-25.

[33] M. Kretz. "Research in Multicyclic and Active Control of Rotary Wings." *Vertica*, Vol. 1, No. 2, 1976, pp. 95-105.

[34] N. D. Ham. "Helicopter Individual-blade Control Research at MIT 1977-1985." *Vertica*, Vol. 11, No. 1-2, 1987, pp. 109-122.

[35] S. A. Jacklin, A. Blaas, D. Teves and R. Kube. "Reduction of Helicopter BVI Noise, Vibration, and Power Consumption Through Individual Blade Control." *Proceedings of the 51st Annual Forum of the American Helicopter Society*, Fort Worth, Texas, May 9-11, 1995.

[36] S. A. Jacklin, A. Haber, G. d. Simone, T. Norman, C. Kitaplioglu and P. Shinoda. "Full-Scale Wind Tunnel Test of an Individual Blade Control System for a UH-60 Helicopter ", *American Helicopter Society 58th Annual Forum*, Montreal, Canada, 11-13 June, 2002.

[37] U. T. P. Arnold and D. Fürst. "Closed loop IBC results from CH-53G flight tests." *Aerospace Science and Technology*, Vol. 9, 2005, pp. 421-435.

[38] V. Giurgiutiu. "Review of Smart-Materials Actuation Solutions for Aeroelastic and Vibration Control." *Journal of Intelligent Material Systems and Structures,* Vol. 11, July, 2000, pp. 525-544.

[39] V. Giurgiutiu. "Active-Materials Induced-Strain Actuation for Aeroelastic Vibration Control." *The Shock and Vibration Digest*, Vol. 32, No. 5, September, 2000, pp. 355-368.

[40] V. Giurgiutiu. "Power and Energy issues in the Induced strain actuation for Aerospace Adaptive Control." *AIAA/ASME/AHS Adaptive Structures Forum*, Salt Lake City, UT, 18-19 April, 1996.

[41] V. Giurgiutiu. "Recent Advances in Smart Material Rotor Control Actuation." *41st AIAA/ASME/ASCE/AHS/ASC Structures, Structural Dynamics and Materials Conference* Atlanta, Georgia, 3-6 April, 2000.

[42] F. Straub. "A Feasibility Study of using Smart Materials for Rotor Control." *Smart Materials and Structures,* Vol. 5, 1996, pp. 1-10.

[43] F. Straub, M. A. Ealey and L. M. Schetky. "Application of Smart Material to Helicopter Rotor Active Control." *SPIE`s Symposium on Smart Structures and Materials*, San Diego, 3-6 March, 1997.

[44] I. Chopra. "Status of Application of Smart Structures Technology to Rotorcraft Systems." *Journal of American Helicopter Society*, Vol. 45, No. 4, 2000, pp. 228-252.

[45] P. P. Friedmann. "Rotary-wing Aeroelastic Scaling and its Implications for Adaptive-materials-based Actuation." *SPIE Conference on Smart Structures and lntegrated Systems,* Newport Beach, California, 1 March, 1999.

[46] O. Dieterich, B. Enenkl and D. Roth. "Trailing Edge Flaps for Active Rotor Control Aeroelastic Characteristics of the ADASYS Rotor System." *American Helicopter Society 62nd Annual Forum*, Phoenix, AZ, May 9-11, 2006.

[47] P. P. Friedmann. "Rotary-Wing Aeroelasticity: Current Status and Future Trends." *AIAA Journal*, Vol. 42, No. 10, 2004, pp. 1953-1972.

[48] P. P. Friedmann, M. de Terlizzi and T. F. Myrtle. "New Developments in Vibration Reduction with Actively Controlled Trailing Edge Flaps." *Mathematical and Computer Modeling*, Vol. 33, 2001, pp. 1055-1083.

[49] P. P. Friedmann. "Vibration Reduction In Rotorcraft Using Actively Controlled Flaps - From Theoretical Concept To Flight Ready Hardware." *AHS 4th*

Decennial Specialists Conference on Aeromechanics, San Francisco, CA, 21-23 January, 2004.

[50] S. Bieniawski and I. Kroo. "Flutter Suppression Using Micro-Trailing Edge Effectors ", *44th AIAA/ASME/ASCE/AHS/ASC Structures, Structural Dynamics, and Materials Conference*, Norfolk, Virginia, April 7-10, 2003.

[51] S. Bieniawski and I. Kroo. "Development and Testing of an Experimental Aeroelastic Model with Micro-Trailing Edge Effectors ", *41st Aerospace Sciences Meeting and Exhibit*, Reno, Nevada, 6-9 January, 2003.

[52] J. Coder, M. Maughmer and P. Martin. "CFD Investigation of Unsteady Rotorcraft Airfoil Aerodynamics: MiTEs and Dynamic Stall." *49th AIAA Aerospace Sciences Meeting including the New Horizons Forum and Aerospace Exposition*, Orlando, Florida, 4-7 January, 2011.

[53] L. Liu, A. K. Padthe and P. P. Friedmann. "A Computational Study of Microflaps with Application to Vibration Reduction in Helicopter Rotors." *50th AIAA/ASME/ASCE/AHS/ASC Structures, Structural Dynamics, and Materials Conference*, Palm Springs, California, 4-7 May, 2009.

[54] A. K. Padthe, L. Liu and P. P. Friedmann. "Numerical Evaluation of Microflaps for On Blade Control of Noise and Vibration." *52th AIAA/ASME/ASCE/AHS/ASC Structures, Structural Dynamics, and Materials Conference*, Denver, Colorado, 4-7 April, 2011.

[55] C. Matalanis, B. Wake, D. Opoku, B.-Y. Min, N. Yeshala and L. Sankar. "Aerodynamic Evaluation of Miniature Trailing-Edge Effectors for Active Rotor Control " *Journal of Aircraft*, Vol. 48, No. 3, 2011, pp. 995-1004.

[56] P. Anusonti-Inthra, F. Gandhi and M. Frecker. "Design of a Conformable Rotor Airfoil using Distributed Piezoelectric Actuation." *ASME International Mechanical Engineering Congress*, Washington, D.C., 15-21 November 2003.

[57] S. Saito, N. Kobiki and Y. Tanabe. "Application of an Active Device for Helicopter Noise Reduction in JAXA." *Fluid Dynamics Research*, Vol. 42, No. 1, 2010, pp. 1-24.

[58] J. P. Rodgers. *Development of an Integral Twist-Actuated Rotor Blade for Individual Blade Control*. PhD Dissertation, Massachusetts Institute of Technology, Boston, 1999.

[59] D. Thakkar and R. Ganguli. "Active Twist Control of Smart Helicopter Rotor - A Survey." *Journal of Aerospace Sciences and Technologies*, Vol. 57, No. 4, August 2005, pp. 1-20.

[60] H. Monner, J. Riemenschneider, S. Opitz and M. Schulz. "Development of Active Twist Rotors at the German Aerospace Center (DLR) ", *52nd AIAA/ASME/ASCE/AHS/ASC Structures, Structural Dynamics and Materials Conference*, Denver, Colorado, 4-7 April, 2011.

[61] I. Chopra. "Review of State of Art of Smart Structures and Integrated Systems " *AIAA Journal*, Vol. 40, No. 11, 2002, pp. 2145-2187.

[62] S. Shin. *Integral Twist Actuation of Helicopter Rotor Blades for Vibration Reduction*. PhD Dissertation, Massachusetts Institute of Technology, Boston, MA, August, 2001.

[63] D. Kumar, B. Glaz, J. Mok, P. P. Friedmann and C. Cesnik. "Determination of Optimum Camber Distribution in Rotating wings with Deformable Airfoils for Vibration Reduction and Performance Enhancement using Surrogate Modeling." Proceedings of *European Rotorcraft Forum*, Paris, France, 7-9 September, 2010.

[64] C. K. Maucher, B. A. Grohmann, P. Jänker, A. Altmikus, F. Jensen and H. Baier. "Actuator Design for the Active Trailing edge of a Helicopter Rotor Blade." *33rd European Rotorcraft Forum*, Kazan, Russia, 11-13 September, 2007.

[65] C. E. S. Cesnik, S. Shin and M. L. Wilbur. "Dynamic Response of Active Twist Rotor Blades." *Smart Materials and Structures*, Vol. 10, 2001, pp. 62-76.

[66] C. E. S. Cesnik and S. J. Shin. "On the Modeling of Integrally Actuated Helicopter Blades." *International Journal of Solids and Structures*, Vol. 38, 2001, pp. 1765-1789.

[67] C. E. S. Cesnik and S. J. Shin. "On the Twist Performance of a Multiple-cell Active Helicopter Blade." *Smart Materials and Structures*, Vol. 10, No. 1, 2001, pp. 53-61.

[68] S. Shin, C. E. S. Cesnik, W. K. Wilkie and M. L. Wilbur. "Design and Manufacturing of a Model-scale Active Twist Rotor Prototype Blade." *Journal of Intelligent Material Systems and Structures*, Vol. 19, No. 12, 2008, pp. 1443-1456.

[69] S. Shin, C. E. S. Cesnik and S. R. Hall. "Closed Loop Control Test of the NASA/Army/MIT Active Twist Rotor for Vibration Reduction." *Journal of American Helicopter Society*, Vol. 50, No. 2, 2005, pp. 178-194.

[70] R. Palacios and C. E. S. Cesnik. "Cross-Sectional Analysis of Nonhomogeneous Anisotropic Active Slender Structures." *AIAA Journal*, Vol. 43, No. 12, July, 2005, pp. 2624-2638.

[71] C. E. S. Cesnik and R. Palacios. "UM/VABS Release 1.35, User Manual." 2008.

[72] R. Palacios and C. E. S. Cesnik. "Geometrically Nonlinear Theory of Composite Beams with Deformable Cross Sections." *AIAA Journal*, Vol. 46, No. 2, 2008, pp. 439-450.

[73] G. L. Ghiringhelli, P. Masarati and P. Mantegazza. "Characterisation of Anisotropic, Non-Homogeneous Beam Sections with Embedded Piezo-Electric Materials." *Journal of Intelligent Material Systems and Structures*, Vol. 8, No. 10, October, 1997, pp. 842-858.

[74] G. L. Ghiringhelli, P. Masarati and P. Mantegazza. "Analysis of an Actively Twisted Rotor by Multibody Global Modeling." *Composite Structures*, Vol. 52, 2001, pp. 113-122.

[75] S. Glukhikh, E. Barkanov, A. Kovalev, J. Riemenshcneider and P. Wierach. "Design of Helicopter Rotor Blades with Actuators Made of a Piezomacrofiber Composite." *Mechanics of Composite Materials*, Vol. 44, No. 1, 2008, pp. 57-64.

[76] F. Hoffmann, S. Opitz and J. Riemenschneider. "Validation of Active Twist Modeling Based on Whirl Tower Tests." *American Helicopter Society 65th Annual Forum*, Grapevine, Texas, 27-29, May, 2009.

[77] T. H. Brockmann and R. Lammering. "Beam Finite Elements for Rotating Piezoelectric Fiber Composite Structures." *Journal of Intelligent Material Systems and Structures*, Vol. 17, 2006, pp. 431-448.

[78] C. E. S. Cesnik, R. S. Park and R. Palacios. "Effective Cross section Distribution of Anisotropic Piezocomposite Actuators for Wing twist." *Proceedings of SPIE*, Vol. 5056, 2003, pp. 21-32.

[79] M. K. Sekula, M. L. Wilbur and W. T. Yeager. "Aerodynamic Design Study of an Advanced Active Twist Rotor." *American Helicopter Society 4th Decennial Specialist Conference on Aeromechanics* San Francisco, California, January 21-23, 2004.

[80] M. K. Sekula, M. L. Wilbur and W. T. Yeager. "A Parametric Study of the Structural design of an Advanced Active Twist Rotor." *American Helicopter Society 61st Annual Forum*, Grapevine, Texas, June 1-3, 2005.

[81] M. L. Wilbur and M. K. Sekula. "The Effect of Tip Geometry on Active-Twist Rotor Response ", *American Helicopter Society 61st Annual Forum*, Grapevine, Texas, 1-3 June 2005.

[82] W. Johnson. "CAMRAD-II Comprehensive Analytical Model of Rotor Aerodynamics and Dynamics." Johnson Aeronautics, Volume II: User's Manual, 1984.

[83] R. P. Thornburgh, A. R. Kreshock and M. L. Wilbur. "Structural Optimization of Active-Twist Rotor Blades." *American Helicopter Society, 67th Annual Forum*, Virginia Beach, VA, 3-5 May, 2011.

[84] J. Mok. *Design Optimization for Active Twist Rotor Blades*. PhD Dissertation, University of Michigan, Ann Arbor, Michigan, 2010.

[85] C. E. S. Cesnik, J. Mok, A. Parekh and S. Shin. "Optimization Design Framework for Integrally Twisted Helicopter Blades." *45th AIAA/ASME/ASCE/ASC Structures, Structural Dynamics and Materials Conference*, Palm Springs, California, 19-22 April, 2004.

[86] C. E. S. Cesnik, J. Mok, J. A. Morillo and A. S. Parikh. "Design Optimization of Active Twist Rotor Blades." *30th European Rotorcraft Forum*, Marseilles, France, 2005.

[87] P. Masarati, M. Morandini, J. Riemenschneider, P. Wierach, S. Gluhih and E. Barkanov. "Optimal design of an Active Twist 1:2.5 Scale Rotor Blade." *European Rotorcraft Forum*, Florence, Italy, September 13-15, 2005.

[88] A. Kovalos, E. Barakanov and S. Gluhihs. "Active Twist Model Rotor Blades with D-Spar Design." *Transport*, Vol. XXII, No. 1, 2007, pp. 38-44.

[89] E. Barakanov, S. Gluhih and A. Kovalev. "Optimal Design of the Active Twist for Helicopter Rotor Blades with C-Spar." *Mechanics of Advanced Materials and Structures*, Vol. 15, No. 3-4, 2008, pp. 325-334.

[90] B. Glaz, P. P. Friedmann and L. Liu. "Vibration Reduction and Performance Enhancement of Helicopter Rotors Using an Active/Passive Approach." *49th AIAA/ASME/ASCE/AHS/ASC Structures, Structural Dynamics, and Materials Conference*, Schaumburg, IL, 7-10 April, 2008.

[91] J. Zhang, E. C. Smith and K. W. Wang. "Active-Passive Hybrid Optimization of Rotor Blades with Trailing Edge Flaps." *Journal of the American Helicopter Society*, Vol. 49, No. 1, 2004, pp. 54-65.

[92] P. P. Friedmann and D. Hodges. "Rotary Wing Aeroelasticity -A Historical Perspective and Some Current Trends." *44th AIAA/ASME/ASCE/AHS Structures, Structural Dynamics, and Materials Conference*, Norfolk, Virginia, 7-10 April, 2003.

[93] A. Datta and W. Johnson. "An Assessment of the State-of-the-art in Multidisciplinary Aeromechanical Analyses." *AHS Specialist's Conference on Aeromechanics*, San Francisco, CA, 23-25 January, 2008.

[94] W. Johnson and A. Datta. "Requirements for Next Generation Comprehensive Analysis of Rotorcraft." *AHS Specialist's Conference on Aeromechanics*, San Francisco, CA, 23-25 January, 2008.

[95] M. E. Gunduz. *Software Integration for Automated Stability Analysis and Design Optimization of a Rotor Blade*. PhD Dissertation, Georgia Institute of Technology, Atlanta, GA, 2010.

[96] B. Glaz. *Active/Passive Optimization of Helicopter Rotor Blades for Improved Vibration, Noise, and Performance Characteristics*. PhD Dissertation, University of Michigan, Ann Arbor, 2008.

[97] B. Glaz, P. P. Friedmann, L. Liu, D. Kumar and C. E. S. Cesnik. "The AVINOR Aeroelastic Simulation Code and its Application to Reduced Vibration Composite Rotor Blade Design." *50th AIAA/ASME/ASCE/AHS/ASC Structures. Structural Dynamics, and Materials Conference*, Palm Springs, California, 4-7 May, 2009.

[98] J. Ku, V. Volovoi and D. Hodges. "Multilevel-Multiphase Optimization of Composite Rotor Blade with Surrogate Model." *48th AIAA/ASME/ASCE/AHS/ASC Structures, Structural Dynamics, and Materials Conference*, Honolulu, Hawaii, 23-26 April 2007.

[99] L. Li, V. Volovoi and D. Hodges. "Cross-Sectional Design of Composite Rotor Blades." *Journal of the American Helicopter Society*, Vol. 53, No. 1, 2008, pp. 240-251.

[100] A. S. Khalid. *Development and Implementation of Rotorcraft Preliminary Design Method using Multidisciplinary Design Optimization*. PhD Dissertation, Georgia Institute of Technology, Atlanta, Georgia, December, 2006.

[101] K. B. Collins. *A Multi-fidelity Framework for Physics based Rotor Blade Simulation and Optimization*. PhD Dissertation, Georgia Institute of Technology, Atlanta, Georgia, 2008.

[102] K. K. Saijal, R. Ganguli and S. R. Viswamurthy. "Optimization of Helicopter Rotor Using Polynomial and Neural Network Metamodels." *Journal of Aircraft*, Vol. 48, No. 2, 2011, pp. 553-566.

[103] S. R. Viswamurthy and R. Ganguli. "Optimal Placement of Piezoelectric Actuated Trailing-Edge Flaps for Helicopter Vibration Control." *Journal of Aircraft*, Vol. 46, No. 1, January-February, 2009, pp. 244-253.

[104] D. Patt, L. Liu and P. P. Friedmann. "Rotorcraft Vibration Reduction and Noise Prediction Using a Unified Aeroelastic Response Simulation." *Journal of the American Helicopter Society*, Vol. 50, No. 1, 2005, pp. 95-106.

[105] D. Patt, L. Liu and P. P. Friedmann. "Simultaneous Vibration and Noise Reduction in Rotorcraft Using Aeroelastic Simulation." *Journal of the American Helicopter Society*, Vol. 51, No. 2, 2006, pp. 127-140.

[106] L. Liu, P. P. Friedmann, I. Kim and D. S. Bernstein. "Rotor Performance Enhancement and Vibration Reduction in Presence of Dynamic Stall Using Actively Controlled Flaps." *Journal of the American Helicopter Society*, Vol. 53, No. 4, 2008, pp. 338-350.

[107] J.-S. Kim. *Design and Analysis of Rotor Systems with Multiple Trailing edge Flaps and Resonant Actuators*. PhD Dissertation, Pennsylvania State University, Pennsylvania, 2005.

[108] S. R. Viswamurthy and R. Ganguli. "Using the Complete Authority of Multiple Active Trailing-edge Flaps for Helicopter Vibration Control." *Journal of Vibration and Control*, Vol. 14, No. 8, 2008, pp. 1175-1199.

[109] U. Dalli and Ş. Yüksel. "Identification of Flap motion parameters for Vibration reduction in Helicopter rotors with Multiple active Trailing edge flaps." *Shock and Vibration*, Vol. 18, No. 5, 2010, pp. 727-745.

[110] K. Noburu, S. Saito, T. Fukami and T. Komura. "Design and Performance Evaluation of Full Scale On-board Active Flap System." *American Helicopter Society 63rd Annual Forum*, Virginia Beach, Virginia, May 1-3, 2007.

[111] M. V. Fulton. "Aeromechanics of the Active Elevon Rotor." *American Helicopter Society 61st Annual Forum*, Grapevine, Texas, June 1-3, 2005.

[112] E. F. Prechtl. *Design and Implementation of a Piezoelectric Servo-Flap Actuation System for Helicopter Rotor Individual Blade Control*. PhD Dissertation, Massachusetts Institute of Technology, Boston, 2000.

[113] B. K. S. Woods, C. S. Kothera, J. Sirohi and N. M. Wereley. "Pneumatic Artificial Muscles for Trailing Edge Flap Actuation: A Feasibility Study." *Smart Materials and Structures*, Vol. 20, No. 10, 2011, pp. 1-15.

[114] F. Straub, D. K. Kennedy, D. B. Domzalski, A. A. Hassan, H. Ngo and T. S. Birchette. "Smart Material-actuated Rotor Technology – SMART." *Journal of Intelligent Material Systems and Structures*, Vol. 15, April, 2004, pp. 249-260.

[115] F. Straub, R. A. Vaidyanathan, T. S. Birchette and B. H. Lau. "SMART Rotor Development and Wind Tunnel Test." *35th European Rotorcraft Forum*, Hamburg, Germany, 22-25 September, 2009.

[116] P. Lorber, J. O'Neill, B. Hein, B. Isabella, J. Andrews, M. Brigley, J. Wong, P. LeMasurier and B. Wake. "Whirl and Wind Tunnel Testing of the Sikorsky

Active Flap Demonstration Rotor." *American Helicopter Society 67th Annual Forum*, Virginia Beach, VA, May 3-5, 2011.

[117] H. Mainz, B. G. van der Wall, P. Leconte, F. Ternoy and H.-M. d. Rochettes. "ABC Rotor Blades: Design, Manufacturing and Testing." *31st European Rotorcraft Forum*, Florence, Italy, September 13-15, 2005.

[118] Y. Delrieux, A. L. Pape, P. Leconte, P. Crozier, B. Gimonet and H.-M. d. Rochettes. "Wind-Tunnel Assessment of the Concept of Active Flaps on a Helicopter Rotor Model." *American Helicopter Society 63rd Annual Forum*, Virginia Beach, VA, May 1-3, 2007.

[119] E. F. Prechtl and S. R. Hall. "Design of a High Efficiency, Large Stroke, Electromechanical Actuator." *Smart Materials and Structures*, Vol. 8, 1999, pp. 13-30.

[120] N. A. Koratkar and I. Chopra. "Analysis and Testing of Mach-Scaled Rotor with Trailing-Edge flaps." *AIAA Journal*, Vol. 38, No. 7, 2000, pp. 1113-1124.

[121] B. Roget and I. Chopra. "Wind Tunnel testing of Rotor with Individually Controlled Trailing-Edge Flaps for Vibration reduction." *Journal of Aircraft*, Vol. 45, No. 3, May-June, 2008, pp. 868-879.

[122] J. H. Milgram, I. Chopra and F. Straub. "Rotors with Trailing Edge Flaps: Analysis and Comparison with Experimental Data." *Journal of the American Helicopter Society*, Vol. 43, No. 4, 1998, pp. 319-332.

[123] S. Dawson, F. Straub, E. Booth and M. Marcolini. "Wind Tunnel Test of an Active Flap Rotor : BVI Noise and Vibration Reduction." *51st Annual Forum of the American Helicopter Society*, Fort Worth, Texas, May, 1995.

[124] M. V. Fulton and R. Ormiston. "Small-Scale Rotor Experiments with On-blade elevons to Reduce Blade Vibratory Loads in Forward Flight." *American Helicopter Society 54th Annual Forum*, Washington, DC, May 20-22, 1998.

[125] L. R. Centolanza and E. C. Smith. "Induced-Shear Piezoelectric Actuators for Active Twist Rotor Blades." *43rd AIAA/ASME/ASCE/AHS/ASC Structures, Structural Dynamics, and Materials Conference*, Denver, Colorado, 22-25 April, 2002.

[126] J. W. Clement, D. Brei, A. J. Moskalik and R. Barrett. "Bench-top Characterization of an Active rotor blade Flap system incorporating C-block Actuators." *AIAA/ASME/ASCE/AHS/ASC Structures, Structural Dynamics, and Materials Conference and Exhibit, 39th, and AIAA/ASME/AHS Adaptive Structures Forum*, Long Beach, CA, April 20-23, 1998.

[127] S. R. Hall and E. F. Prechtl. "Development of a Piezoelectric Servoflap for Helicopter Rotor Control." *Smart Materials and Structures*, Vol. 5, 1996, pp. 26-34.

[128] F. Straub, H. Ngo, V. R. Anand and D. B. Domzalski. "Development of a Piezoelectric Actuator for Trailing edge Flap Control of full scale Rotor Blades." *Smart Materials and Structures*, Vol. 10, 2001, pp. 25-34.

[129] T. Lee and I. Chopra. "Design of Piezostack-driven Trailing-edge Flap Actuator for Helicopter Rotors." *Smart Materials and Structures*, Vol. 10, 2001, pp. 15-24.

[130] H. Ghiasi, D. Pasini and L. Lessard. "Optimum Stacking Sequence Design of Composite Materials Part I: Constant Stiffness Design." *Composite Structures*, Vol. 90, No. 1, 2009, pp. 1-11.

[131] H. Ghiasi, K. Fayazbakhsh, D. Pasini and L. Lessard. "Optimum Stacking Sequence Design of Composite Materials Part II: Variable Stiffness Design." *Composite Structures*, Vol. 93, No. 1, 2010, pp. 1-13.

[132] Z. Gürdal, S. IJsselmuiden and J. v. Campen. "Composite Laminate Optimization with Discrete Variables." *Encyclopedia of Aerospace Engineering*: John Wiley & Sons, Ltd, 2010.

[133] G. J. Kennedy and J. J. R. A. Martins. "A Laminate Parametrization Technique for Discrete Ply Angle Problems with Manufacturing Constraints." *Structural and Multidisciplinary Optimization*, 2012.

[134] G. J. Kennedy and J. J. R. A. Martins. "A Regularized Discrete Laminate Parametrization Technique with Applications to Wing-Box Design Optimization." *53rd AIAA/ASME/ASCE/AHS/ASC Structures, Structural Dynamics and Materials Conference*, Honolulu, Hawaii, 23 - 26 April, 2012.

[135] S. Murugan, R. Ganguli and D. Harursampath. "Surrogate based Design Optimization of Composite Airfoil Cross section for Helicopter Vibration Reduction." *The Aeronautical Journal*, Vol. 116, No. 1181, 2012, pp. 709-725.

[136] S. D. Guido, H. J. M. Geijselaers and A. d. Boer. "Continuous-Discrete Variable Optimization on Composite using Kriging Surrogate Model." *16th International Conference on Composite Structures*, Porto, Portugal, June 28-30, 2011.

[137] J. N. Kudwa. "Overview of the DARPA Smart Wing Project." *Journal of Intelligent Material Systems and Structures*, Vol. 15, 2004, pp. 261-267.

[138] S. Kota, J. Hetrick, O. Russel, D. Paul, E. Pendleton, P. Flick and C. Tilmann. "Design and application of compliant mechanisms for morphing aircraft structures." *Proceedings of SPIE*, Vol. 5054, No. 24, 2003, pp. 24-33.

[139] M. J. Santer and S. Pellegrino. "Topology Optimization of Adaptive Compliant Aircraft Wing Leading Edge." *48th AIAA/ASME/ASCE/AHS/ASC Structures, Structural Dynamics & Materials (SDM) Conference* Honolulu, Hawaii, 23-26 April, 2007.

[140] L. Saggere and S. Kota. "Static Shape Control of Smart Structures Using Compliant Mechanisms " *AIAA Journal*, Vol. 37, No. 5, May 1999, pp. 572-578.

[141] F. Gandhi and P. Anusonti-Inthra. "Skin Design studies for Variable Camber Morphing Airfoils." *Smart Materials and Structures*, Vol. 17, 2008, pp. 1-8.

[142] O. K. Rendinotis, L. N. Wilson., D. C. Lagoudas and M. M. Khan. "Development of a Shape-Memory-Alloy Actuated Biomimetic Hydrofoil." *Journal of Intelligent Material Systems and Structures*, Vol. 13, 2002, pp. 35-49.

[143] J. D. Bartley-Cho, D. P. Wang, C. A. Martin, J. N. Kudwa and M. N. West. "Development of High-rate, Adaptive Trailing Edge Control Surface for the Smart Wing Phase 2 Wind Tunnel Model " *Journal of Intelligent Material Systems and Structures*, Vol. 15, 2004, pp. 279-291.

[144] F. Gandhi, M. Frecker and A. Nissly. "Design Optimization of a Controllable Camber Rotor Airfoil." *AIAA Journal*, Vol. 46, No. 1, 2008, pp. 142-153.

[145] S. Thepvongs, C. E. S. Cesnik, R. Palacios and D. A. Peters. "Finite-State Aeroelastic Modeling of Rotating Wings with Deformable Airfoils." *American Helicopter Society 64th Annual Forum*, Montreal, Canada, April 29-May 1, 2008.

[146] S. Thepvongs, J. R. Cook, C. E. S. Cesnik and M. J. Smith. "Computational Aeroelasticity of Rotating Wings with Deformable Airfoils." *American Helicopter Society 65th Annual Forum*, Grapevine, Texas, May, 2009.

[147] P. J. Röhl, D. Kumar, P. Dorman, M. Sutton and C. Cesnik. "A Composite Rotor Blade Structural Design Environment for Aeromechanical Assessments in Conceptual and Preliminary Design." *68th American Helicopter Society International Annual Forum*, Fort Worth, Texas, 1-3 May, 2012.

[148] P. J. Röhl, P. Dorman, M. Sutton, D. Kumar and C. Cesnik. "A Multidisciplinary Design Environment for Composite Rotor Blades." *53rd AIAA/ASME/ASCE/AHS/ASC Structures, Structural Dynamics and Material Conference*, Honolulu, Hawaii, 23 - 26 April 2012.

[149] D. Kumar, C. Cesnik, P. J. Röhl and M. Sutton. "Optimization Framework for the Dynamic Analysis and Design of Active Twist Rotors." *68th American Helicopter Society International Annual Forum*, Fort Worth, TX, 1-3 May, 2012.

[150] D. Kumar and C. Cesnik. "New Hybrid Optimization for Design of Active Twist Rotor." *54th AIAA/ASME/ASCE/AHS/ASC Structures, Structural Dynamics, and Materials Conference*, Boston, MA 8-11 April, 2013.

[151] D. Kumar and C. Cesnik. "New Strategy for Design of Composite Rotor Blade with Active Flaps." *American Helicopter Society 69th Annual Forum and Technology Display*, Phoenix, Arizona May 21-23, 2013.

[152] D. Kumar and C. Cesnik. "Performance Enhancement in Dynamic Stall Condition using Active Camber Deformation." *American Helicopter Society 69th Annual Forum and Technology Display*, Phoenix, Arizona, May 21-23, 2013.

[153] P. J. Röhl, P. Dorman, M. Sutton, C. E. S. Cesnik and D. Kumar. "IXGEN- A Modeling Tool for the Preliminary Design of Composite Rotor Blade." *AHS Future Vertical Lift Design Conference* San Francisco, 18-20 January 2012.

[154] H. Saberi, M. Khoshlahjeh, R. Ormiston and M. Rutkowski. "Overview of RCAS and Application to Advanced Rotorcraft Problems." *AHS 4th Decennial Specialist Conference on Aeromechanics*, San Francisco, California, January 21-23, 2004.

[155] R. Palacios. *Asymptotic Models of Integrally-Strained Slender Structures for High-Fidelity Nonlinear Aeroelastic Analysis*. PhD Dissertation, University of Michigan, Ann Arbor, 2005.

[156] "RCAS User Manual." 2011.

[157] W. G. Bousman. "Aerodynamic Characteristics of SC1095 and SC1094 R8 Airfoils." NASA, TP-2003-212265, December, 2003.

[158] K. Deb, A. Pratap, S. Agarwal and T. Meriyan. "A Fast and Elitist Multiobjective Genetic Algorithm: NSGA-II." *IEEE Transactions on Evolutionary Computation*, Vol. 6, No. 2, 2002, pp. 182-197.

[159] D. R. Jones, M. Schonlau and W. J. Welch. "Efficient Global Optimization of Expensive Black Box Functions." *Journal of Global Optimization*, Vol. 13, 1998, pp. 455-492.

[160] A. Forester, A. Sobester and A. Keane. *Engineering design via Surrogate Modeling: A Practical Guide*. AIAA: John Wiley and Sons, Ltd, 2008.

[161] N. V. Queipo, R. T. Haftka, W. Shy, T. Goel, R. Vaidyanathan and P. K. Tucker. "Surrogate based Analysis and Optimization." *Progress in Aerospace Sciences*, Vol. 41, 2005, pp. 1-28.

[162] J. Sacks, W. J. Welch, T. J. Mitchell and H. P. Wynn. "Design and Analysis of Computer Experiments." *Statistical Science*, Vol. 4, No. 4, 1989, pp. 409-435.

[163] S. N. Lophaven, H. B. Nielsen and J. Sondergaard. "A Matlab Kriging Toolbox, version 2.0." Informatics and Mathematical Modeling, Technical Report IMM-TR-2002-12, 2002.

[164] B. Glaz, P. P. Friedmann and L. Liu. "Helicopter Vibration Reduction throughout the Entire Flight Envelope Using Surrogate-Based Optimization." *Journal of American Helicopter Society*, Vol. 54, No. 1, 2009, pp. 12007-1-12007-15.

[165] C. E. S. Cesnik, S. Shin, W. K. Wilkie, M. L. Wilbur and P. H. Mirick. "Modeling, Design and Testing of the NASA/ARMY/MIT Active Twist Rotor Prototype Blade." *American Helicopter Society 55th Annual Forum* Montreal, Canada, May 25-27, 1999.

[166] K. Deep, K. P. Singh, M. L. Kansal and C. Mohan. "A Real coded Genetic Algorithm for solving Integer and Mixed-integer Optimization Problems." *Applied Mathematics and Computation*, Vol. 212, No. 2, 2009, pp. 505-518.

[167] D. A. Peters, M. A. Hsieh and A. Torrero. "A State Space Airloads Theory for Flexible Airfoils." *American Helicopter Society 63rd Annual Forum*, Phoenix, AZ, May, 2006.

[168] D. A. Peters and C. J. He. "Finite State Induced Flow Models Part II: Three-Dimensional Rotor Disk." *Journal of Aircraft*, Vol. 32, No. 2, March-April, 1995, pp. 323-333.

[169] L. A. Ahaus. *An Airloads Theory for Morphing Airfoils in Dynamic Stall with Experimental Correlation*. PhD Dissertation, Washington University in St. Louis, Saint Louis, Missouri, May, 2010.

[170] J. Martin and T. Simpson. "Use of Kriging Models to Approximate Deterministic Computer Models." *AIAA Journal*, Vol. 43, No. 4, 2005, pp. 853-863.

[171] R. Palacios and C. E. S. Cesnik. "Low-Speed Aeroelastic Modeling of Very Flexible Slender Wings with Deformable Airfoils." *49th AIAA/ASME/ASCE/AHS/ASC Structures, Structural Dynamics, and Materials Conference*, Schaumburg, IL, 7-10 April 2008.

[172] A. Forester, A. Sobester and A. Keane. *Engineering Design via Surrogate Modeling : A Practical Guide*. John Wiley and Sons, Ltd, 2008.

[173] M. J. Sasena. *Flexibility and Efficiency Enhancements for Constrained Global Design Optimization with Kriging Approximations*. PhD Dissertation, University of Michigan, Ann Arbor, 2002.

[174] S. R. Hall, T. Tzianetopoulou, F. Straub and H. Ngo. "Design and Testing of a double X-frame Piezoelectric Actuator." *Proceedings of SPIE*, Vol. 3985, 2000.

[175] J.-L. Petitniot, H.-M. d. Rochettes and P. Leconte. "Experimental Assessment and Further Development of Amplified Piezo Actuators for Active Flap Devices." *Actuator 2002, 8th International Conference on New Actuators*, Bremen, Germany, 10-12 June, 2002.

[176] E. R. Muir, L. Liu, P. P. Friedmann and D. Kumar. "Effect of Piezoelectric Actuator Hysteresis on Helicopter Vibration and Noise Reduction." *Journal of Guidance, Control and Dynamics,* Vol. 35, No. 4, 2012, pp. 1299-1311.

[177] J. Cook and M. J. Smith. "Effect of Testing Facility" *Personal Communication,* Georgia Institute of Technology, March, 2010